THE UNIVERSITY OF QUEENSLAND

AUSTRALIA

MULTI-SCALE PERMEABILITY OF COAL FRACTURES AND CLEATS

Julia Busse

Dipl. Geo-Ecologist (M.Sc. eq.)

A thesis submitted for the degree of Doctor of Philosophy at

The University of Queensland in 2017

School of Civil Engineering

Abstract

Coal is characterised by its unique microstructure made up of a porous matrix intersected by a network of face and butt cleats. Together with mining-induced fractures and faults caused by geological activities, these small scale cleats provide the principal source of permeability for groundwater and gas flow within a coal seam. The coal seam permeability plays a crucial role in mine stability, minability, gas well performance, and seam drainage behaviour. Therefore, a fundamental understanding of the fracture and cleat characteristics is essential for safe and efficient coal mining and coal seam gas production.

Due to the various structural parameters of coal varying widely in size, the permeability of coal is highly scale-dependent. This thesis investigates the permeability of coal fractures and cleats on the example of Bowen Basin coals over a range of scales. The investigation of permeability is carried out using field studies, laboratory work, and numerical modelling. The relationship between permeability results gathered across scales is investigated to determine the Representative Element Volume and thus the smallest volume over which a measurement can be made that will yield a value representative of the whole.

Field work has been undertaken at the Hail Creek Coal Mine in Central Queensland, Australia. A Heat Pulse Flow Meter, a downhole wireline tool, was utilised to test for permeability of macro-scale (metres to kilometres) fractures frequently associated with fault structures intersecting the coal measures at the mine site. Coal samples were taken for subsequent laboratory work. Laboratory investigations of permeabilities cover the meso-scale (centimetres to decimetres). The coal samples taken at two coal seams, the Elphinstone and the Hynds seam, were tested for permeability in a triaxial cell using the constant head test method. Based on Computer Tomography scans of the coal, the samples were numerically reconstructed to allow for investigations on the micro-scale (millimetres to centimetres). A unique image processing workflow was developed to extract and statistically describe the key structural parameters of the network of butt and face cleats present in a two-dimensional image. A Lattice-Boltzmann-based code was utilised for simulating fluid flow and estimating permeabilities within the three-dimensional cleat network on a range of subsample volumes. The correlations of results across scales are investigated and up-scaled to the Representative Element Volume using a power-averaging approach.

Permeability heterogeneities are observed at each scale. Using the average numerical data, a trend is found that shows an increase in permeability with an increase in scale. The numerical investigation of the permeability for different subsample volumes over a micro-scale found average permeability values in the range of 0.38 mD to 6.77 mD for the Elphinstone coal, and 0.21 mD to 9.01 mD for the Hynds coal. The laboratory values, investigating permeability over a meso-scale, span 0.023 mD to 1.408 mD for the Elphinstone seam, and 0.011 mD to 20.62 mD for the Hynds seam. Finally, the largest range in permeability has been obtained from the field work, which measured permeability at the macro-scale, also referred to as field-scale. These permeability values vary between 0.17 mD and 70.46 mD for the Elphinstone seam, and between 3.04 mD and 88.31 mD for the Hynds seam.

The variation between the field work and laboratory results shows that the permeability of coal is governed by two main systems: coal cleats and coal fractures. Laboratory values are representing the bulk measurement of the micro-scale cleat permeability, while field-scale values represent the macro-scale at which permeabilities are governed by larger coal fractures. To capture the heterogeneity of permeability of coal within this dual scale system, investigations have therefore to be focused on the scale of the intended use of the respective study.

Declaration by author

This thesis is composed of my original work, and contains no material previously published or written by another person except where due reference has been made in the text. I have clearly stated the contribution by others to jointly-authored works that I have included in my thesis.

I have clearly stated the contribution of others to my thesis as a whole, including statistical assistance, survey design, data analysis, significant technical procedures, professional editorial advice, and any other original research work used or reported in my thesis. The content of my thesis is the result of work I have carried out since the commencement of my research higher degree candidature and does not include a substantial part of work that has been submitted to qualify for the award of any other degree or diploma in any university or other tertiary institution. I have clearly stated which parts of my thesis, if any, have been submitted to qualify for another award.

I acknowledge that an electronic copy of my thesis must be lodged with the University Library and, subject to the policy and procedures of The University of Queensland, the thesis be made available for research and study in accordance with the Copyright Act 1968 unless a period of embargo has been approved by the Dean of the Graduate School.

I acknowledge that copyright of all material contained in my thesis resides with the copyright holder(s) of that material. Where appropriate I have obtained copyright permission from the copyright holder to reproduce material in this thesis.

Publications during candidature

Journal publications

- Busse, J., de Dreuzy, J. R., Galindo Torres, S., Bringemeier, D., Scheuermann, A. (2017) Image processing based characterisation of coal cleat networks, International Journal of Coal Geology, Vol 169, pp 1–21, DOI: http://dx.doi.org/10.1016/j.coal.2016.11.010
- Busse, J., Galindo Torres, S., Scheuermann, S., Li, L., Bringemeier, D. (2016) Micro-Scale Flow Simulations and Permeability Estimation of Cleat Networks in Coal, *Applied Mechanics and Materials*, Vol. 846, pp. 42-47, 2016, DOI: 10.4028/www.scientific.net/AMM.846.42
- Busse, J., Scheuermann, A., Paillet, F., Bringemeier, D., Li, L. (2016) Field performance of the Heat Pulse Flow Meter: Experiences and Recommendations*, Journal of Applied Geophysics,* Vol. 126, pp 158-171, DOI: http://dx.doi.org/10.1016/j.jappgeo.2016.01.021
- Busse, J., Scheuermann, A., Bringemeier, D., Hossack, A., Li, L. (2016) In-situ coal seam and overburden permeability characterisation combining downhole flow meter and temperature logs*, Contemporary Trends in Geoscience. The Journal of Uniwersytet Slaski,* Vol. 5 (1), pp 1 -17, DOI: 10.1515/ctg-2016-0001

Conference publications

- Busse, J., de Dreuzy, J.R., Scheuermann, A., Bringemeier, D., Galindo Torres, S., Davy, P., Li, L., Poster Detection and description of fracture networks in coal samples for micro-scale flow simulations, *26th General Assembly of the International Union of Geodesy and Geophysics (IUGG), Prague, Czech Republic*, 22. June – 02. July 2015.
- Busse, J., Scheuermann, A., D. Bringemeier, Li, L. (2014) Tracing groundwater flow paths in a coal mine by means of geophysical and borehole flow data, *Conference contribution to Interdisciplinary Responses to Mine Water Challenges, Xuzhou, China*, 18.-22. August 2014.
- Busse, J., Scheuermann, A., Galindo-Torres, S., D. Bringemeier, Li, L. (2014) In-situ and laboratory measurements of coal matrix and cleat permeability, *Conference contribution to UNSAT 2014 - Unsaturated soils: Research and applications, Sydney, Australia*, 02.-04. July 2014.

Publications included in this thesis

J. Busse, S. Galindo Torres, A. Scheuermann, L. Li, D. Bringemeier (2016) Micro-Scale Flow Simulations and Permeability Estimation of Cleat Networks in Coal, *Applied Mechanics and Materials*, Vol. 846, pp. 42-47, 2016, DOI: 10.4028/www.scientific.net/AMM.846.42 – incorporated in part as chapter 7.

Contributor	Statement of contribution
J. Busse (Candidate)	Developed and ran numerical modelling (80%) Wrote and edited paper (85%)
S. Galindo Torres	Developed numerical modelling (20%) Wrote and edited paper (8%)
A. Scheuermann	Wrote and edited paper (3%)
L. Li	Wrote and edited paper (1%)
D. Bringemeier	Wrote and edited paper (3%)

Busse, J., Scheuermann, A., Paillet, F., Bringemeier, D., Li, L. (2016) Field performance of the Heat Pulse Flow Meter: Experiences and Recommendations, Journal of Applied Geophysics, Vol. 126, pp 158-171, DOI: http://dx.doi.org/10.1016/j.jappgeo.2016.01.021 - incorporated in part as chapter 4.

Contributor	Statement of contribution
J. Busse (Candidate)	Planning of field campaign (70%) Field measurements (80%) Wrote and edited paper (75%)
A. Scheuermann	Wrote and edited paper (5%)
F. Paillet	Field measurements (15%) Wrote and edited paper (12%)
D. Bringemeier	Planning of field campaigns (20%) Field measurements (5%) Wrote and edited paper (5%)
L. Li	Planning of field campaigns (10%) Wrote and edited paper (3%)

Busse, J., de Dreuzy, J. R., Galindo Torres, S., Bringemeier, D., Scheuermann, A. (2017) Image processing based characterisation of coal cleat networks, International Journal of Coal Geology, Vol 169, pp 1–21, DOI: http://dx.doi.org/10.1016/j.coal.2016.11.010 - incorporated in parts as chapter 6.

Contributor	Statement of contribution
J. Busse (Candidate)	Developed image processing method (80%) Wrote code (90%) Wrote and edited paper (85%)
J.R. De Dreuzy	Developed image processing method (18%) Edited code (10%) Wrote and edited paper (8%)
S. Galindo Torres	Developed image processing method (2%)
D. Bringemeier	Wrote and edited paper (2%)
A. Scheuermann	Wrote and edited paper (5%)

Busse, J., de Dreuzy, J.R., Scheuermann, A., Bringemeier, D., Galindo Torres, S., Davy, P., Li, L., Poster Detection and description of fracture networks in coal samples for micro-scale flow simulations, 26th General Assembly of the International Union of Geodesy and Geophysics (IUGG), Prague, Czech Republic, 22. June – 02. July 2015 – incorporated in part in chapter 6.

Contributor	Statement of contribution
J. Busse (Candidate)	Developed image processing method (80%) Wrote code (90%) Wrote and edited poster (90%)
J.R. De Dreuzy	Developed image processing method (16%) Edited code (10%) Wrote and edited poster (5%)
A. Scheuermann	Wrote and edited poster (1%)
D. Bringemeier	Wrote and edited poster (1%)
S. Galindo Torres	Developed image processing method (2%)
S. Davy	Developed image processing method (2%)
L. Li	Wrote and edited poster (1%)

Contributions by others to the thesis

Dr Alexander Scheuermann advised on all aspects of the design of the thesis and critically reviewed all material. Dr Sergio Andres Galindo-Torres advised on all aspects of the design of the thesis and critically reviewed all material. Dr Detlef Bringemeier advised on all aspects of the design of the thesis critically reviewed all material.

Statement of parts of the thesis submitted to qualify for the award of another degree

None.

Acknowledgements

I want to express my gratitude to my advisory team, Dr Alexander Scheuermann, Dr Sergio Galindo Torres and Dr Detlef Bringemeier, as well as Prof Ling Li for giving me the opportunity to work on this project and supporting my research throughout the process.

The University of Queensland has provided me with a well-equipped work environment to conduct my PhD studies using a wide range of techniques and instruments.

I acknowledge the help of the staff of RioTinto Coal Australia at the Hail Creek Mine, especially Alex Hossack and Matt Mafu. I have learned a lot from Dr Fred Paillet, who introduced me to the Heat Pulse Flow meter.

The technicians at the School of Civil Engineering have made laboratory work a pleasure. I thank Jennifer Speer, Shane Walker, Stewart Matthews, Christopher Russ, Ruth Donohoe and Sebastian Quintero Olaya.

My research stay at Geosciences Rennes was a success thanks to the guidance of Dr Jean Raynald de Dreuzy.

My time as a PhD candidate has been brightened by the presence of my peers and good friends Patrick Schmidt, Moritz Schwing, Max Kumm, Jurij Karlovsek, Flavien Sciortino and my favourite scientist Tamara Kolbe.

Special thanks go to my friends Auri and Maria who inspire me each in their own special ways and always keep their door open for me. I am happy about the love and support of Robin and am looking forward to our next adventures.

Keywords

coal permeability, cleat geometry, flow in fractures, fluid flow modelling, image processing, multi-scale quantification

Australian and New Zealand Standard Research Classifications (ANZSRC)

ANZSRC code: 040603, Hydrogeology 60%

ANZSRC code: 040309, Petroleum and Coal Geology, 10%

ANZSRC code: 090599, Civil Engineering not elsewhere classified, 30%

Fields of Research (FoR) Classification

FoR code: 0905, Civil Engineering, 80%

FoR code: 0406, Physical Geography and Environmental Geoscience, 20%

Table of Contents

Table of Figures

List of Tables

Nomenclature

Symbol	Parameter	Unit
a	Aperture	[m], [mm]
α	Power law exponent alpha	
c_s	Speed of sound	[m/s]
CT-Scans	X-ray Computed Tomography Imaging	
d	Diameter	[m]
e	particle velocity LBM	
f	particle distribution function LBM	
f_{eq}	equilibrium Boltzmann-Maxwell distribution function	
$f_i(x,t)$	density function LBM	
g	Gravitational acceleration	[m/s^2]
h	Height	[m]
h	Piezometric head	[m]
K	Hydraulic conductivity	[m/day], [m/s]
k	Permeability	[m^2], [mD]
l	Sample length	[m]
LBM	Lattice Boltzmann Method	
p	Number of subsamples of each supersample	[-]
P	Pressure	[N/m^2]
Q	Volumetric flow rate	[m^3/s]
q	Volumetric flux	[m/s]
REV	Representative Element Volume	
s	Spacing	[m], [mm]
T	Transmissivity	[m^2/day]
TN	True North	
t	Time	
u	Pore water pressure	[kPa]
v	Flow velocity	[m/s]
u_d	Backpressure bottom	[kPa]
u_u	Backpressure top	[kPa]
V_a	Average flow velocity	[m/s]
x	Lattice position LBM	
x	Radius of cone of depression	[m]
γ	Surface tension	[mN/m]
γ_W	Specific weight of water	[N/m^3]
δt	Time step	
η	Dynamic viscosity	[kg/ms]
θ	Contact angle	[°]
λ	relaxation time due to particle collision	
ρ	Fluid density	[kg/m^3]
σ_c	Confining stress	[kPa]
φ_c	Cleat porosity	[-]
φ_{LBM}	Ratio of cleat volume to bulk volume	[-]
φ_m	Matrix porosity	[-]

1. Introduction

1.1 MOTIVATION AND BACKGROUND

Australia is the world's leading coal exporter and a large consumer of coal, which provides about 85% of the country's electricity production (International Energy Agency, 2008). However, coal mining in Australia has been increasingly subjected to criticism with serious concerns about the impact of a mining operation on the surrounding environment, the carbon footprint of coal mines and CO_2 emission from burning coal (NSW Department of Planning, 2008).

The operation of coal mines is vulnerable to a range of risks linked to the extraction of groundwater as well as mining induced change of flow paths provided by faults, fractures and coal seams. Permeability is one of the most important geotechnical parameters. The permeability is causative for the ability of any fluid phase (either as gas phase or liquid phase or both phases together at partly saturated conditions) to flow through the coal seam and surrounding rocks.

Coal seam permeability is underpinned by not only large-scale fault and fracture zones within the porous media but also small-scale cleat structures in the coal seam (Wold & Jeffrey, 1999). Therefore, fluid flow processes and thus permeabilities in coal are highly scale-dependent. While gas desorption and diffusion also concern the micro-scale, an investigation of groundwater flow within the medium must focus on the scales of the cleat and fracture system. This constitutes the need to understand permeability of coal across multiple scales.

- **Micro-scale:** micrometre to centimetre
- **Meso-scale:** centimetre to decimetre
- **Macro-scale:** meter to kilometre range

Besides fluid flow, permeability also controls the strength and deformation behaviour of coal and therefore directly affects the following fields:

- Wall and spoil designs that consider elevated pore water pressures in compartmentalised zones resulting from faults, gouge and ancillary structures
- The design of cut-offs beneath dams on permeable foundations

- The design of the clay layer for a liner for waste dumps
- The need for water tolerant explosives used in strip blasts
- Assessment of the quantity of water that will flow toward excavations and the control of the drilling of horizontal drain holes
- Fluid flow in coal seam gas reservoirs and the requirement of a high cleat density to improve permeability
- The selection of a method for well completion (Ali et al., 2008), along with information regarding the primary cleat direction and its relationship to present in-situ horizontal stresses
- Whether commercial levels of coal seam gas production can be reached

Mining impact

- The impact on drainage in open pit mining, especially when the mine is adjacent to river or aquifer systems
- The extent of drawdown of both surface water and ground water, that can influence groundwater-dependent ecosystems
- Minimization of greenhouse gas emissions
- Formation of fault systems resulting from coal seam gas production on regional scales

1.2 THESIS OBJECTIVES

The importance of the permeability for all these aspects in mining and coal seam gas production triggers the presented study, which focuses on the scale dependent flow of water in coal seams. The realistic characterization of fluid flow in heterogeneous reservoir rock has been a long standing problem in reservoir engineering, however, it is needed to allow for the proper assessment and management of risks (Cnudde & Boone, 2013).

During the exploration of coal resources, coal qualities and quantities are examined by drilling of boreholes for coal sampling and logging of coal seam depth and thickness. These investigations include the identification and description of defects and larger geological structures that govern the flow. On the field-scale, permeability tests like pumping tests, water pressure tests, and recovery tests, are done to obtain estimates of

rock mass permeability. On the meso-scale, laboratory tests like a falling head or constant head tests can be conducted, and on the micro-scale image processing methods are used.

However, geophysical logging campaigns and the retrieval of a large number of reservoir samples are not economically efficient and laboratory experiments to measure permeabilities are time-consuming (Norouzi Apourvari & Arns, 2015). Fracture occurrence is difficult to measure and analyse, mainly because of the high range in size from microscopic to cavernous (Şen, 1995) and it remains difficult to draw a picture of the geometry of fractures and the interconnections between them. The need for a better representation of fracture characteristics during permeability measurements has been pointed out by Huy et al. (2010). Samples usually taken through boreholes are smaller than the Representative Element Volume (REV) scale necessary for permeability testing. The fundamental concept of the REV states that there is a scale below which individual heterogeneities and discrete features can be ignored (Bear, 1972). It is widely accepted that permeability as the key parameter that controls multi-phase mass and energy flow in porous and fractured media is spatially variable on all scales. The scale effect on permeability is still debated (Illman, 2006), as well as the choice of the most suitable conceptual model to describe flow in fractured media (Neuman, 2005).

A multi-scale approach combining permeability data from different scales is tested here. The research presented in this thesis combines field and laboratory data with numerical simulations to receive permeability values that are representative for the reservoir across scales. The field-scale (or macro-scale) is covered by measurements with the Heat Pulse Flow Meter. The meso-scale is investigated using constant head tests in a triaxial cell. For the micro-scale, permeability data is obtained through computational modelling for millimetre to centimetre volumes. The simulation of flow experiments based on X-Ray Computed Tomography Imaging, referred to herein as CT-scans, allows a flexible parameter choice, is cost-efficient, and above all, gives a non-invasive insight into the structure of the coal. To date, small-scale simulations of fluid flow in fractures have been based on synthetically generated fracture networks (Schwarz & Enzmann, 2013). Using the data from CT-scans obatined from image processing, this project uses a real fracture network as the basis for the simulation.

Figure 1-1 gives an overview on the methods used for permeability investigations on the different scales. By combining the results from this range of scales, up-scaling relations between permeabilities are investigated.

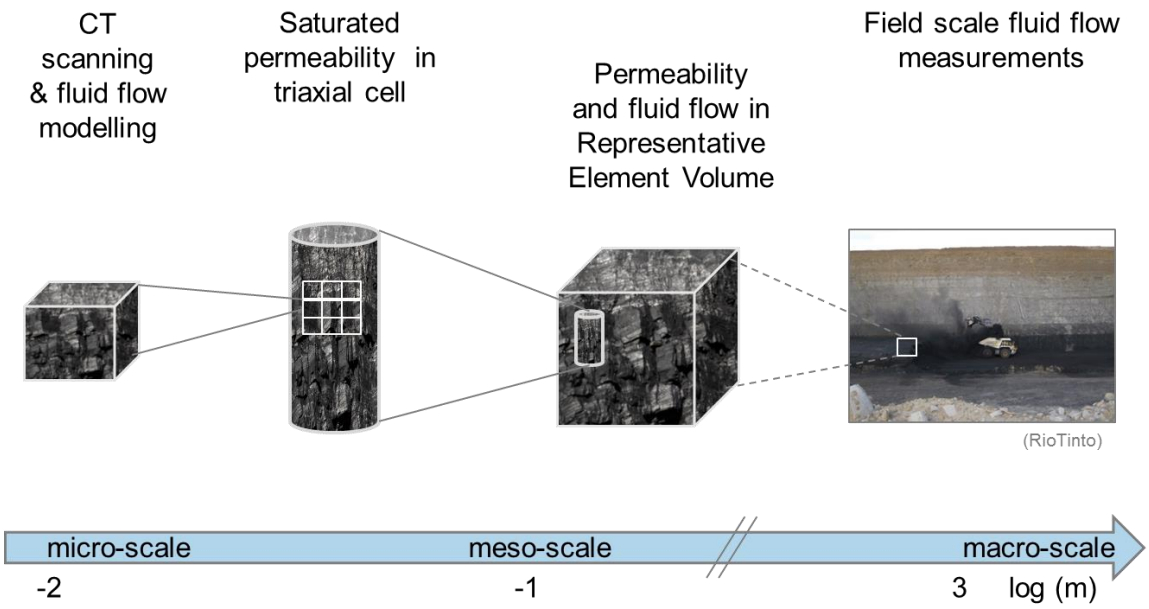

Figure 1-1 Overview of methods used along different scales

The three main thesis objectives can therefore be summarised as follows:

1. **Measurement of permeabilities across a range of scales using field, laboratory and modelling approaches**
2. **Establishment of relationships between permeabilities measured across scales and identification of the scale effects on coal permeability**
3. **Identification of REV for coal permeability**

1.3 THESIS OUTLINE

To achieve the research objectives, an integrated approach has been designed combining field testing, lab testing and numerical simulations. The research is based on experimental flow measurements and computations at different scales.

The thesis is structured in ten chapters, including this introductory chapter. Chapter 2 introduces the literature review related to the topic of the thesis. Coal composition, coal structure, as well as typical porosities and permeabilities found in earlier studies are presented. Field and laboratory methods to quantify structure and parameters influencing fluid flow are introduced. An introduction to modelling of fluid flow in fractured media discusses common modelling approaches. In the following, the literature review focuses on scales relevant to fluid flow in coal and presents different up-scaling methods.

The field site subject to field investigations and location of sampling is introduced in chapter 3. The geological and hydrogeological set-up of the Hail Creek coal mine located

in Central Queensland, Australia, is presented with a focus on the properties of the two coal seams that are investigated and sampled, Elphinstone and Hynds coal seam. For an easy distinction, all results for the Elphinstone seam are plotted in a blue colour scheme, for the Hynds seam in green throughout the thesis. The chapter concludes with the permeabilities that have been documented in earlier studies. Field testing using the Heat Pulse Flow Meter allow for in-situ insight into flow behaviour along boreholes and the derivation of field-scale permeability. The instrument and the logging campaigns are presented in chapter 4.

Core samples from the coal seam, over- and interburden were taken at the field site and are subsequently prepared for CT-scans and triaxial cell tests. Chapter 5 reports on the laboratory permeability testing. Coal sample permeability is examined with tests in a triaxial cell under saturated conditions. A subsequent structural characterisation of the coal is presented in chapter 6. Using SEM and CT-scans the inner structure of one sample for each of the coal seams, Elphinstone and Hynds, is revealed and characterised based on two-dimensional images. Helium pycnometry and mercury intrusion are used to measure porosity and specific gravity. The output of the non-invasive imaging of the structural composition of coal samples serves as a basis for the modelling of the flow in coal cleats.

The numerical modelling is introduced in chapter 7. The cleat network is reconstructed in three dimensions and the fluid flow through the artificial samples is simulated, taking the flow governing properties into account. Through the partition of the artificial sample into smaller blocks, a range of micro-scale results are obtained. The relations across these micro-scales are tested with an upscaling approach that uses power averaging of the permeabilities of the subsamples and compares them to the permeabilities of the supersamples.

Chapter 8 focuses on the relations of permeabilities across scales. Permeability values gained in the modelling of the different sized artificial blocks, and the permeability test results from the laboratory and the field are reviewed. The results on the different scales are discussed and scale factors are deduced. Chapter 9 discusses the methods used to obtain data and the limitations of the work. Finally, in chapter 10 conclusions are drawn and recommendations for future work are given.

2. Literature Review

2.1 INTRODUCTION

The literature review addresses the state of the art in the fields relevant to the thesis topic. Coal composition, coal structure, as well as typical porosities and permeabilities found in earlier studies are presented. Field and laboratory methods to quantify structure and parameters influencing fluid flow are introduced. An introduction to the modelling of fluid flow in fractured media presents common modelling approaches. In the following, the literature review focuses on scales relevant to fluid flow in coal and presents different up-scaling methods.

As the term cleat refers to opening-mode fractures in coal beds, relevant research on fracture mechanics and hydraulics of other geo-materials (e.g. sandstone, crystalline rocks) has been reviewed, and is presented in the following. Where literature results are based on coal investigation the term *cleats* is used for the characteristic systematic joint sets which do not cut clastic facies adjacent to coal layers, field-scale fractures in coal seams are called *coal fractures*. For all other geo-materials, the term *fracture* is used.

A focus lies on the background relevant to the imaging of the structure of fractured rock by means of CT-scans. Further, common field and laboratory methods to examine permeability are reviewed. Approaches to the multi-scale problematic of hydrogeological questions and its modelling were studied. In the following, commonly used parameters for describing the hydraulic characteristic of a coal sample are introduced.

According to Darcy's law, presented in equation 2-1, the relationship between the rate of flow, Q [m^3/s], through a porous media fully saturated with water is proportional to the cross-sectional area, A [m^2], the pressure difference between top and bottom, dh [m], and inversely proportional to the length of the sample, dl [m]. The coefficient of proportionality is the hydraulic conductivity represented as, K [m/s]. Equation 2-2 is used to calulate i, a value that incorperates dh and dl into one value.

$$Q = -K\,A\,i \qquad (2\text{-}1)$$

$$i = \frac{dh}{dl} \qquad (2\text{-}2)$$

The intrinsic permeability, k [m^2], is a parameter that depends only on the properties of the solid and is determined using equation 2-3 with the hydraulic conductivity, K [m/s], the gravitational acceleration, g [m/s^2], the fluid density, ρ [kg/m^3], and viscosity, μ [kg/ms], of water at 25°C (0.000891 kg/ms).

$$k = \frac{K\,\mu}{\rho\, g} \qquad (2\text{-}3)$$

The intrinsic permeability, k, is often given in milliDarcy [mD]. 1 Darcy = 0.9869233 μm^2. Conversion to m^2, therefore, is done by multiplying the permeability value in mD with $9.869233*10^{-16}$. For reasons of simplification, in the following the term permeability is used when referring to the intrinsic property of the material. Permeability is heterogeneous and anisotropic, i.e. the permeabilitiy varies in the different directions and depends on facies changes and lithological variability (Figure 2-1).

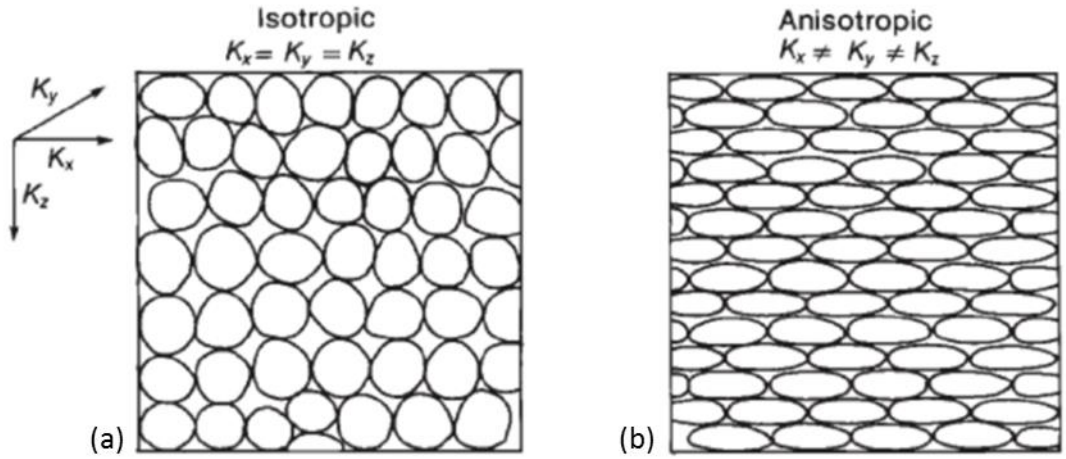

Figure 2-1 a. Isotropy and b. anisotropy in a porous medium (Fetter, 2000)

Permeability k can therefore be expressed as a tensor as shown in equation 2-4

$$\mathrm{k} = \begin{pmatrix} k_{xx} & k_{xy} & k_{xz} \\ k_{yx} & k_{yy} & k_{yz} \\ k_{zx} & k_{zy} & k_{zz} \end{pmatrix} \qquad (2\text{-}4)$$

Another useful parameter is the transmissivity, which incorporates the height of the zone of interest, i.e. a facies, a coal seam or a fracture. Transmissivities of a coal seam are usually given in [m^2/day]. The transimissivity T [m^2/day] is related to the hydraulic conductivity, K [m/day], of each zone with a zone height, z [m], as shown in equation 2-5.

$$T = K\, z \qquad (2\text{-}5)$$

2.2 COAL CHARACTERISTICS

2.2.1 Coal composition

Coal is a chemically complex three-dimensional cross-linked network of macro-molecules consisting of a mixture of plant remains. The formation of coal occurs over millions of years by a complex process known as coalification or carbonification. The process begins with diagenesis of plant material by bacteria as it subsides into the earth. The peat then forms lignite which at temperatures above 100 °C (approximately 1000 m depth) undergoes thermal metamorphosis into coal. The process of carbonification that forms coal as plant material subsides into the earth's crust is illustrated in Figure 2-2. The inorganic constituents of coal are commonly referred to as mineral matter. Minerals occur as finely disseminated particles throughout the coal matrix or as distinct non-coal inter-beds such as coal fractures and cleats (Serra, 1983).

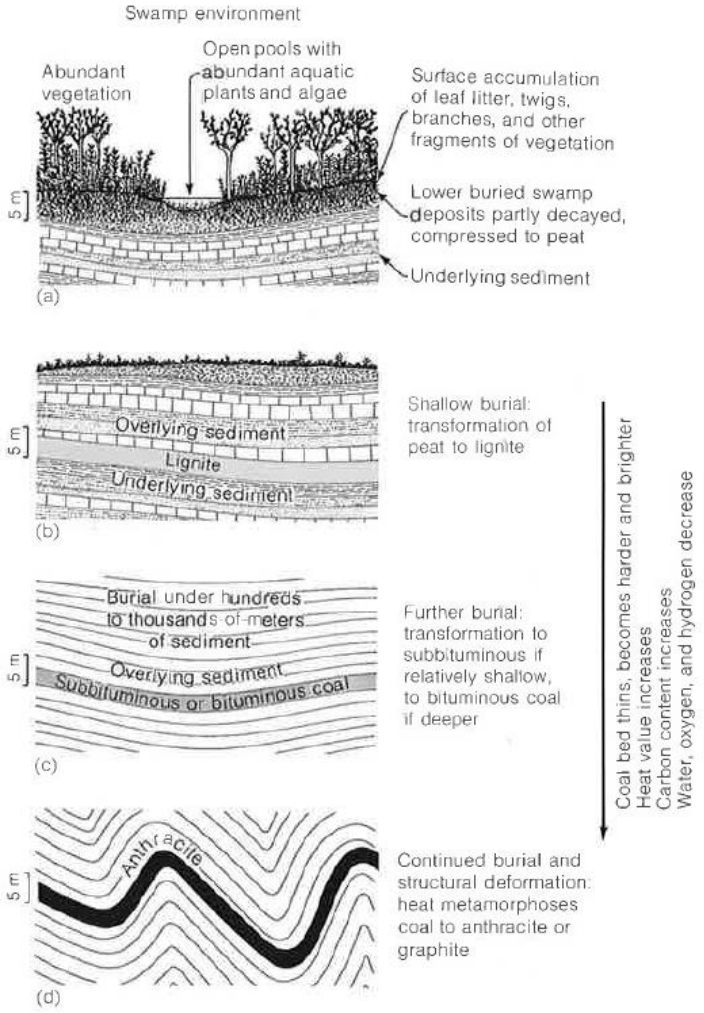

Figure 2-2 Coalification and progress of rank development as described by (Serra, 1983): a. surface accumulation of organic material and peat genesis, b. shallow burial transforms peat to lignite, c. further burial transforms lignite to subbituminous or bituminous coal, d. continued burial with increased pressure and heat drives transformation to anthracite or graphite

2.2.1.1 Coal rank

The extent of carbonification (Figure 2-2) is described by rank with high ranked coals having undergone longer periods of high temperature and pressure, thus containing greater fixed carbon content and greater structural ordering. The ranks, in ascending order are peat, lignite, sub-bituminous, bituminous, and anthracite as the highest ranked coal (Kural, 1994).

2.2.1.2 Coal type

The properties of coal are determined by the type of organic matter and plant material, and the extent to which this has been altered biochemically. The type of coal is assessed through a variety of petrographic methods to determine the coal composition in relation to distinct organic and inorganic components.

The components known as lithotypes are visually determined without the use of a microscope. The main lithotypes are summarised below (O'Keefe et al., 2013):

- **Vitrain:** A bright, shiny, homogenous component of coal mainly composed of vitrinite. Vitrain is made from the bark plant material and formed under drier conditions than the other lithotypes.
- **Durain:** The dullest component of coal has a granular texture and is a heterogeneous material made from macerals of inertinite and exinite. Durain is believed to have formed in peat deposits below water level.
- **Clarain:** Bright but less so than vitrain, it has a banded heterogeneous structure having formed in conditions in-between those of vitrain and durain formation.
- **Fusain:** Fibrous, black and opaque, fusain is believed to originate from fossilised charcoal.

The micro-components of these lithotypes are termed macerals and are analogous to minerals. They are determined visually with the help of a microscope (Figure 2-3). The main maceral groups are

- **Vitrinite:** a highly reactive maceral which has a large influence on coal fluidity. It has a reflective, glassy appearance made from cellular plant material and a box-shaped cellular structure. Vitrinite has a high calorific value (24 to 28 MJ/kg).
- **Inertinite:** made from fossilised charcoal, is a highly oxidised component of coal.

- **Liptinite (exinite):** a reactive maceral formed from decayed leaf matter, spores, pollen, algae, resins and waxes. The structure of liptinite is generally that of the fossilised plant material from which it originates. The maceral has the highest calorific value and is also rich in hydrogen (Tyson, 2006).

These maceral are further distinguished in sub maceral groups, as shown in Table 2-1. An example of this is semi-fusinite, a sub maceral of inertinite.

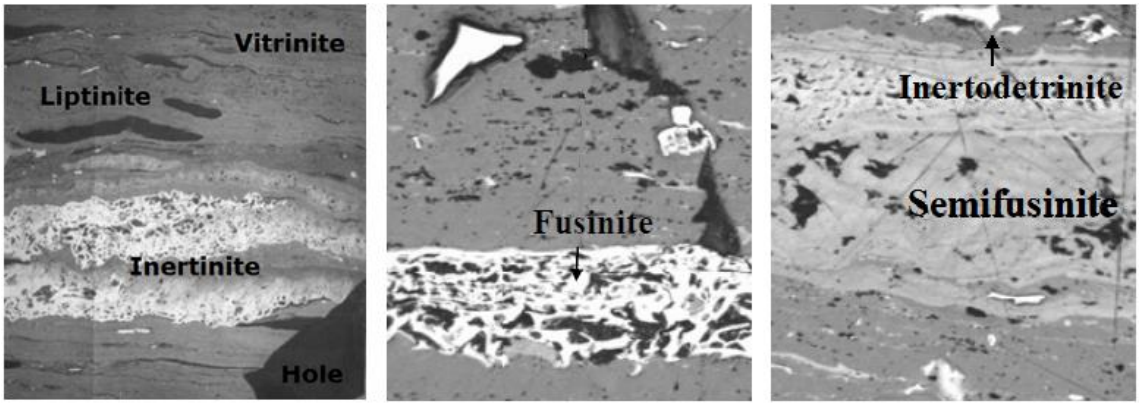

Figure 2-3 Coal macerals (Esterle, 2012)

Table 2-1 Coal maceral group and their origin (Tyson, 2006)

Maceral Group	Maceral	Origin
Vitrinite	Telinite	Cellular structure of wood, leaf and root tissue
	Collinite	Structure less, infilling gel
	Vitrodetrinite	Unidentified cell fragments
Liptinite	Sporinite	Spore and pollen cases
	Cutinite	Waxy coating of leaves and stems
	Suberinite	Cork, tissues, bark and root walls
	Resinite	Resin bodies
	Alginite	Algal tests
	Liptodetrinite	Unidentified liptinite fragments
	Fluorinite	Lenses/layers, possibly plant essential oils
	Bituminite	Wisps of groundmass, from lipids
	Exudanite	Veins of expelled bitumen-like material
Inertite	Fusinite	Charred wood and leaf tissue
	Semi-fusinite	The transition stage between vitrinite and fusinite [21]
	Macrinite	Charred gel material
	Micrinite	Charred liptinitic material
	Scleronite	Fungal remains
	Inertodetrinite	Unidentified inertinite fragments

2.2.2 Coal structure

Coal is highly heterogeneous, being built up of a solid, comparatively impermeable, matrix that is penetrated by cleats and coal fractures formed during coalification and/or subsequent deformation (Laubach et al., 1998). Besides larger scale coal fractures, the

coal structure is characterised by systematic joint sets which do not cut clastic facies adjacent to coal layers. These small scale structures are called cleats (Dron, 1925) and are caused by the interdependent influences of desiccation, lithification, coalification and tectonic stress (Ali et al., 2008). The cleats account for most of the permeability and porosity of a coal seam. The cleats, on a larger scale in conjunction with fissures, joints and coal fractures, represent the main flow paths for producing gas stored in coal seams and contain most of the movable water (Clarkson & Bustin, 2011). Besides the shape of coal fractures and cleats, their cementation, filling and weathering are factors influencing permeability. In the subsurface, over geologic time, carbonate minerals, quartz, or other cement forming minerals (kaolinite, illite, smectite) may precipitate on the cleat and coal fracture walls, often closing apertures and reducing permeability of cleat and coal fracture networks (Laubach et al., 1998).

The complex nature of coalification leads onto the complexity of the molecular coal structure. Coal is made of complex hydrocarbons with a mixture of aromatic, carboxylic, carbonyl, aliphatic, alkene, ether, heteroaromatic and hydroaromatic groups. The subject of the macromolecular coal structure is covered in detail by van Krevelen (1993) and Mathews & Chaffee (2012).

2.2.2.1 Cleat orientation

The cleats are distinguished by their orientation into two types, face cleats and butt cleats. Face cleats are dominant and are directed perpendicular to the bedding plane. The fewer orthogonal butt cleats generally terminate when they encounter face cleats. Typical structural dimensions are illustrated in Figure 2-4. Face cleats are considered extensional (mode 1) fractures and are aligned with the maximum principal stress that was present during the coalification process. The non-persistent butt cleats in-between are resulting from the relaxation of the original stress field (Scholtes, Donze, & Khanal, 2011).

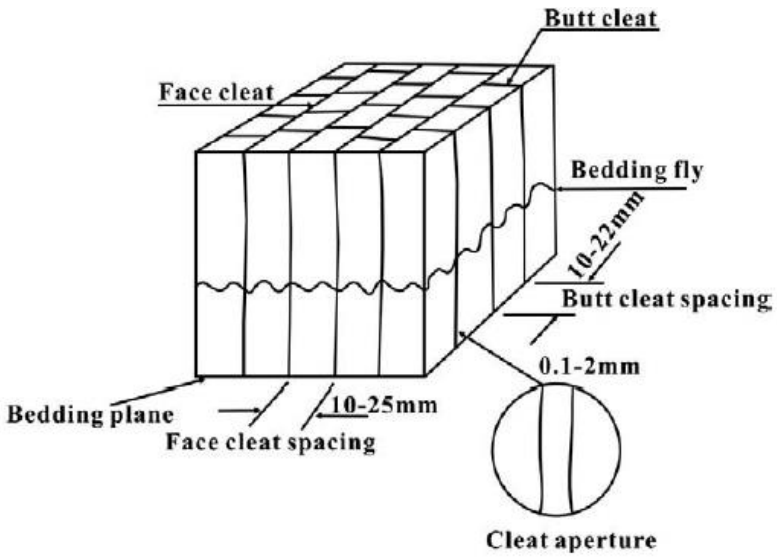

Figure 2-4 Coal structure (Wang, Massarotto, & Rudolph, 2009)

Deviations of the model of orthogonal butt and face cleats shown in Figure 2-4 have for example been reported in a study by de Haan (1999), where angles within 30° and 90° between cleats have been described. Wolf et al. (2008) found major cleat angles of 85° in Polish coal samples. Laubach et al. (2004) showed that open cleats are not necessarily aligned or more permeable in certain directions relative to the stress field. In fact, the orientation of open natural cleats depends on the relative stiffness of the fracture and host material. Knowledge of cleat orientation is useful for the design of roadway and longwalls on the coal mine site. To reduce kinematic wedge formation, cleat orientations ideally are at a moderate angle to both face cleats and butt cleats (Blacka & MacGregor, 2014).

2.2.2.2 Cleat length and size

Cleat length is a critical property for network connectivity and therefore strongly influences mechanical properties and flow behaviour in the system (Darcel et al., 2003; Galindo-Torres et al., 2015). Analysis of Walker Creek Coals from the Bowen Basin using CT-scans by Permana (2012) revealed cleat lengths ranging from 0.5 mm to 15 mm in length. No distinction between butt and face cleats was made in this study, but it was noted that smaller cleats are only present on the bright vitrine bands, while larger cleats are continuous through the dull coal bands. Master cleats that are present besides butt and face cleats and traverse the various coal lithotypes within a seam have also been observed by Esterle et al. (2011).

Gamson & Beamish (1992) studied coal type microstructures and gas flow behaviour of Bowen Basin coal for economic coal seam gas retrieval from the low permeability coal seam. They found micrometre-sized fractures (micro-fractures) and cavities (micro-

cavities) that are present besides micro-pores and the cleat network. These microstructures which vary in width from 0.05 to 20 µm are thought to have a significant effect to overall permeability, especially for gas diffusion at the micro-pore level and laminar flow at the cleat level. The micro-fractures are associated with bright coals, while the micro-cavities are associated with dull coal layers.

2.2.2.3 Cleat aperture

Aperture between fracture walls has been discussed as one of the main influencing parameters for flow in fractures. Fracture apertures cover a wide scale range as their variation is influenced by mechanical and chemical actions in the system (Bonnet et al., 2001). Philip et al. (2005) numerically investigated the effect of diagenesis on the initial flow properties of fracture systems, especially with respect to diagenetic effects on the connectivity of the fracture network. The results indicated that fracture permeability is more sensitive to fracture patterns and connectivity than aperture. The most commonly applied relation between aperture and permeability is the cubic law (Witherspoon, Wang, Iwai, & Gale, 1979).

Weniger et al. (2016) analysed a set of 17 different coals and found a maximum cleat aperture of 2 mm, and a minimum of 2 µm (median 29 µm). Similar apertures have been measured in polished surface analyses for two samples from Turkey by Karacan & Okandan (2000). Cleat aperture was found in the range of 40–60 µm (mean value 47.1 µm) and 10–30 µm (mean value 20.2 µm). Cleat aperture of Bowen Basin coals have been found in the range from 0.3 mm to 1.5 mm in a CT-scan analysis by Permana (2012).

2.2.2.4 Cleat spacing

The distribution of cleats is highly variable with intensely cleated bands and less intensely cleated bands. This distribution is captured by the measure of the spacing between the cleats. Characteristic sizes of cleat spacing are reported between 10 – 25 mm by Wang et al. (2009).

The abundance of cleating is related to vitrinite content, mineral matter content and tectonic activity of the reservoir (Ali et al., 2008). According to Law (1993), spacing is inversely related to coal rank, with low ranks being highly cleated. With increasing coal rank, a decreasing average cleat spacing is apparent. The processes leading to the formation of cleats are still debated. Shrinkage and coal bulk volume changes associated with loss of porosity due to dehydration and devolatilisation during the coalification are discussed. Dawson & Esterle (2010) found that for specific vitrain layers, the cleats could

be spaced as closely as less than a millimetre apart. Further, the spacing of the cleats tended to be proportional to cleat height for given types of cleats. For example, vitrain layers that confined smaller cleats, as well as larger master cleats which traversed multiple coal layers have been observed.

Pattison et al. (1996) investigated Bowen basin coals and found face and butt cleat spacings in a range from 1 mm to 100 mm, with typical spacing of 1 mm to 10 mm in bright lithotypes and 5 mm to 20 mm in dull lithotypes (see chapter 2.2.1 on coal types). Based on the variation in cleat density, dull coal is observed to have greater strength than bright coal (Scholtes et al., 2011).

2.2.2.5 Topology of cleat systems

In each case, cleat geometry or cleat shape can be described as a function of frequency, aperture, size, orientation relative to current in situ stresses, the degree of their connectivity and porosity (Close, 1993). These geometric parameters will affect cleat permeability. Long & Witherspoon (1985) claimed that fracture length, density and flow rate are interrelated. Networks with longer fracture lengths and lower fracture densities exhibit higher connectivities and therefore higher permeabilities than those formed of shorter fracture lengths with higher densities.

Most research has been done on orthogonal cleat systems, e.g. by Robertson & Christiansen (2008) who assumed a system of cubic matrix blocks. However, different structure systems can be distinguished (Nick et al., 1995). A variety of cleat patterns in Permian Queensland coals have been described by Pattison et al. (1996) that deviate from the orthogonal structure. Turner (2015) identified four groups of cleat morphologies based on CT-scans and core photographs (Figure 2-5b).

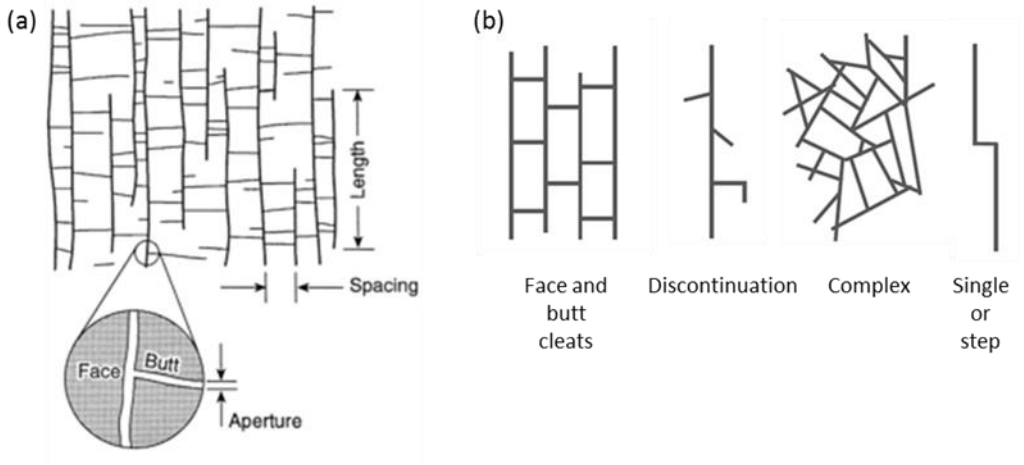

Figure 2-5 a. Schematics of orthogonal cleat system (Laubach et al., 1998), b. Cleat systems as described by Turner (2015)

2.2.3 Coal porosity

Porosity, φ, is calculated using equation 2-6 and is defined as the ratio of voids, Vv, to the total volume, V, of a rock mass.

$$\Phi = \frac{V_v}{V} \qquad (2\text{-}6)$$

Fractured or cleated rock formations are made up of two porosity systems: the primary matrix porosity, φ_m, formed between the grains and given by equation 2-7 and the secondary porosity, φ_c, due to open cleats and given by equation 2-8. The total of φ_m and φ_c represent the total porosity.

$$\Phi_m = \frac{Matrix\ void\ volume}{Total\ bulk\ volume} \qquad (2\text{-}7)$$

$$\Phi_c = \frac{Cleat\ void\ volume}{Total\ bulk\ volume} \qquad (2\text{-}8)$$

While insignificant, primary porosities and permeabilities occur in the coal matrix, cleats and coal fractures account for the secondary porosity and permeabilities. These cleats and coal fractures contribute to varying extents to the anisotropic and heterogeneous nature of coal permeability (Singhal, 2008).

Gamson et al. (1993) examined coal microstructures and defined cleat and matrix porosity within coal that are responsible for fluid flow. Void space associated with the original plant fragments, and cavities associated with pore space separating particles are summed up under matrix porosity. Matrix porosity has been classified as follows: micro-pores (< 2 nm), meso-pores (2 to 50 nm) and macro-pores (> 50 nm) (Gamson, Beamish, & Johnson, 1996). Pore diameters in the matrix are found in the range of 0.5 nm to 1.0 nm and somewhat larger for the cleat system with diameters from approximately 10 nm to 10 µm (Paterson, 1986).

While the matrix of coal typically consists of micro-pores so small that it has no effective permeability, the cleat porosity is estimated between 0.5 and 2.5% (Laubach et al., 1998). Cleat porosities found in the San Juan Basin at typical depths and confining pressure ranges from 0.19 to 0.59 % (Gash et al., 1992) to 2.8 % (Puri, Evanoff, & Brugler, 1991). Cleat porosities incorporated as input parameters during permeability modelling range from 1 to 5% (Jalal & Mohaghegh, 2004). For example, Gong et al. (2014) used a matrix porosity of 0.1% and a porosity of 1% for the cleats.

Kural (1994) states that the porosity of a coal sample has a parabolic relationship to the carbon content of the sample (Figure 2-6) and the coal rank. Coking coals with carbon content around 89% are found to have the lowest porosities of around 2% to 3%. However, the porosity of coals can be higher than 22% for low rank (lignite and sub-bituminous) coals and higher than 10% for anthracites (coals with very high carbon content).

Flores (2013) distinguishes between macro-pores and meso-pores when relating size distributions to coal rank. The percentage total volume of micro-pores increases and that of macro-pores decreases from lignite to anthracite coals (Figure 2-7). For many coal systems the porosity of cleats is found to be dependent on the stress field and therefore the depth (Barton et al., 1995).

A standard methodology to measure coal porosity is helium and mercury porosimetry where the amount of gas injected into a sample equals the fraction of the total volume that is occupied by pores (Mahajan & Walker, 1978). Most of the coal measures along the East coast of Australia have little to no primary porosity. Approximately 75 % of eastern Australian coals are in characterised by meso- and micropores (< 50 nm) (Faiz & Aziz, 1992).

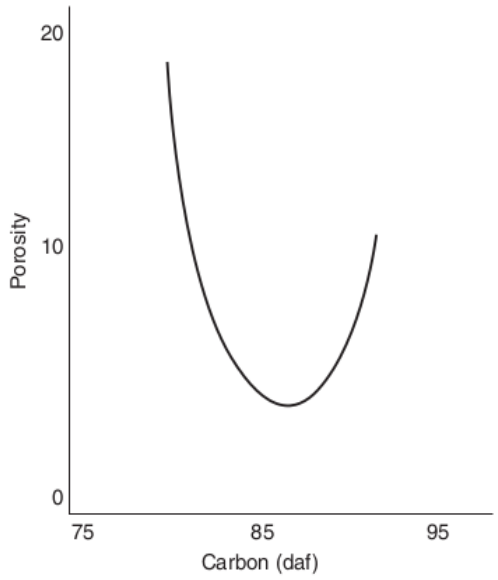

Figure 2-6 Relationship between porosity and carbon content (Speight, 2005)

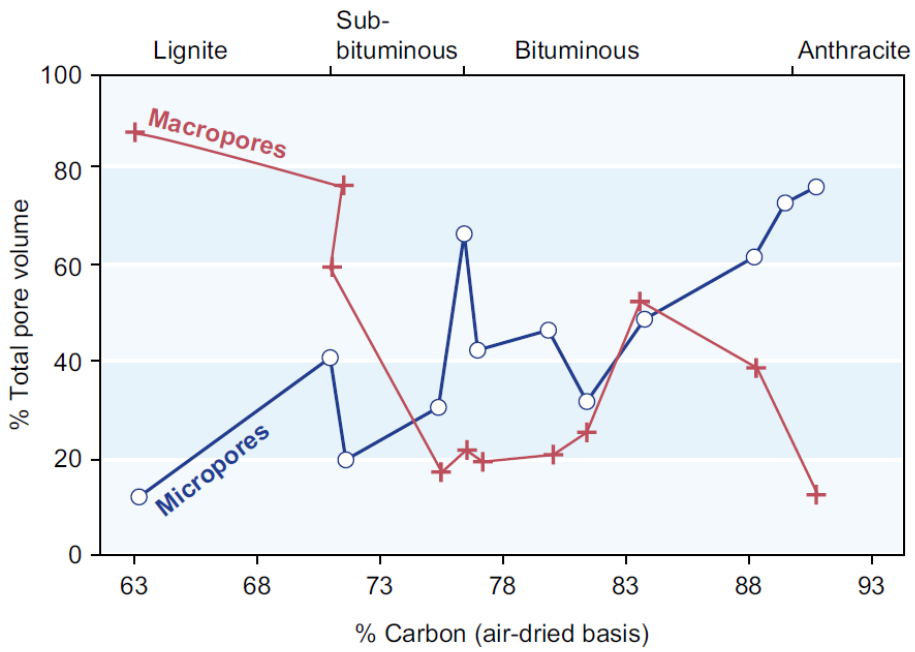

Figure 2-7 Relationship between macro- and micro- porosity and rank (Flores, 2013)

2.2.4 Coal permeability

The permeability of coal is divided in cleat and matrix permeability. Both are introduced in the following. Generally, natural and artificial cleats and coal fractures play a greater role in coal permeability than the coal matrix (Esterle et al., 2011). For a comprehensive discussion of permeability of coal across scales, the reader is referred to chapter 2.5.6.

2.2.4.1 Matrix permeability

Matrix permeability represents the average over a wide range of pore sizes in coal: micro-pores of less than 2 nm; meso-pores of between 2 nm and 50 nm; and macro-pores larger than 50nm, but generally excludes the effects of cleats (Massarotto et al., 2008).

Single-phase flow of gas occurs through the coal matrix by the mechanism of diffusion, whereas viscous or Darcy flow describes the two-phase water and gas flow through the cleats and coal fractures. Gas flow is considered to be pressure driven in the cleats and coal fractures and concentration driven through the coal matrix. It is modelled using Fick's law. Coal is both a source and reservoir rock for gas, making it unique regarding fluid flow. Biogenic gas is generated during early stages of the burial, and thermogenetic gas during later burial. Because of its high density, significant volumes of gas can be stored even under low reservoir pressures. Gas sorption causes the matrix to swell significantly, causing permeabilities to decrease. Accordingly, permeability will increase during desorption due to an increase in cleat aperture under shrinking of the matrix (Clarkson & Bustin, 2011). Significant permeability change has been observed during the production of

coal bed methane and CO_2 injection (Pekot & Reeves, 2002). Thus, matrix permeability is a function of both the effective stress and the coal swelling or shrinkage due to gas desorption and absorption. A change of permeability as a response to changes in pressure has for example been examined by Robertson & Christiansen (2008).

The matrix permeability of coal is typically very low resulting in poor fluid conductivity. Absolute water permeability in the order of 10^{-5} mD has been reported for an anthracite plug from Qinshui Basin, China, by Han et al. (2010). Adeboye (2011) examined the matrix permeability of varying rank coals from Western Canada Sedimentary Basin and obtained matrix permeability in the order 10^{-2} to 10^{-5} mD. For coals from the Bowen Basin, Australia, the matrix permeability has been measured in the range of 10^{-3} mD to 1 mD, which is one to three orders of magnitude less than bulk permeability tests that includes the effects of cleats (Massarotto, Rudolph, et al., 2008). These extremely small values result in a commonly used assumption of the matrix to be effectively impermeable.

2.2.4.2 Cleat permeability

Cleats account for most of the permeability and major parts of the porosity of the coal system and serve as the main pathways inside the matrix. The groundwater flow through cleats is controlled by various geometrical factors: cleat aperture, height, spacing (evenly or unevenly, closely or largely), surface roughness, area, filling and porosity, as well as the distribution and interconnection of the cleats (Legrand, 1979).

Cleat permeability will be affected by these geometric parameters, as well as the degree of mineralisation. Un-mineralised (open) cleats or larger joints can be present in any seam and will represent the primary flow pathways, particularly for high permeability seams. The presence of only a few of these larger, un-mineralised joints might result in a greater permeability than a dense network of low porosity mineralised cleats or coal fractures.

The degree of mineralisation of cleats is a function of burial conditions, the amount of CO_2 present (for calcite mineralisation) and depth. Even highly mineralised cleats will have a much greater permeability (or porosity) than the matrix itself. The filling of cleats in the coals from the Bowen Basin have been analysed by Beeston (1986). Face cleats of coals from the studied field sites are filled with authigenic clays: pure illite or illite-chlorite mixtures. Carbonates (calcite, ferroan calcite, ankerite and siderite) are the main mineralisation component of butt cleats and joints. Mineralised and unmineralised cleats occur (Nick et al., 1995).

Due to the structure of perpendicular butt and face cleats, the permeability of coal is anisotropic (Massarotto et al., 2003). The ratio of the two horizontal to the vertical permeability has been the subject of field-scale studies, e.g. through pumping test presented in Weeks (1969), and on the laboratory scale by various researchers (e.g. Mavor & Robinson, 1993; Gash et al., 1992; Massarotto et al., 2003). In the field, the coal seams are often inclined, and the permeability components, therefore, deviate from the theoretical horizontal layout.

Highest permeability values occur parallel to the face cleats, which are by definition longer than the butt cleats. If the cleat structure does not extend through the bedding plane, the bed-normal permeability can be almost non-existent (Gash et al., 1992). Comparing the permeability in the direction of face cleats to those found in the direction of the butt cleats, typical permeability anisotropy ratios vary from 2:1 to 4:1 (Clarkson & Bustin, 2011). Stress distribution has a large impact, with cleats parallel to the maximum stress tending to be open, while those perpendicular to this direction are rather closed. Permeability is therefore inversely related to normal stress and less cleats and coal fractures are found with increasing depths (Singhal, 2008). Dmyterko (2014) investigated matrix and cleat permeability of the Leichhardt Seam, Rangal Coal Measures, Bowen Basin for blocks of coal sized 15 mm and 40 mm and found that there is a minor anisotropy between face and butt cleats and major anisotropy between horizontal permeabilities and permeabilities perpendicular to the bedding plane. Gash et al. (1992) investigated the variability of permeabilities with direction for coal samples of the San Juan Basin of New Mexico, USA and found similar results. The results of both studies are summarized in Table 2-2.

Table 2-2. Directionality of permeability of samples (Dmyterko, 2014 and Gash et al., 1992)

Coal seam	Sample size	Direction	Permeability	
			from [mD]	to [mD]
Leichhardt, Bowen Basin	15 mm cube	Face cleats	0.30	11.38
		Butt cleats	0.20	10.93
		Perpendicular to bedding	0.10	4.70
Leichhardt, Bowen Basin	40 mm cube	Face cleats	0.67	16.67
		Butt cleats	0.60	11.77
		Perpendicular to bedding	0.43	6.67
Fruitland, San Juan Basin	Coal core:	Face cleats	0.60	1.70
	10.16 cm length	Butt cleats	0.30	1.00
	8.9 cm diameter	Perpendicular to bedding	0.01	--

2.2.4.3 Influences on permeability

Permeability as a function of cleat aperture is strongly affected by changes in effective stress as well as matrix swelling. Coal naturally is quite compressible. Its cleats, as well as the coal matrix, are subject to deformation under pressure (Clarkson & Bustin, 2011). Compressibility of coals has for example been studied by Harpalani (1999), who defines different types of compressibility. Bulk compressibility is the fractional change in bulk volume per unit change in pressure and has been found to be $7.25*10^{-6}$ MPa^{-1}. The fractional change in pore volume per unit change in pressure is called pore volume compressibility and has been measured with $6.53*10^{-3}$ MPa^{-1}. Finally, matrix compressibility is defined as the fractional change in volume of solid material per unit change in pressure and given with a value of $1.31*10^{-4}$ MPa^{-1}. Cleat compressibility of coals has been studied by Turner (2015) who cites a number of studies with compressibility values ranging from $2.8*10^{-2}$ MPa^{-1} to $5.36*10^{-1}$ MPa^{-1}. Given these values, the permeability of coal is pressure dependent (Wang et al., 2009). It is currently not well understood whether cleats are open at depth or open up due to the release of stress during exhumation (Ting, 1977). Hysteresis behaviour has been observed on repeated compression-decompression cycles by Suuberg, Deevi, & Yun (1995) who concluded that coal behaves like a macromolecular material under dynamic stressing conditions.

Coal is characterised by a high Poisson's ratio with a mean of 0.346 (Szabo, 1981). Young's moduli of coal increase with increasing coal ranks. Pan et al. (2013) experimentally found values from 2.5 to 5.5 GPa. Because a large proportion of flow occurs through cleats and coal fractures, changes of relative permeabilities take place with a change of cleat and coal fracture aperture and therefore during dewatering and change of reservoir pressure (Clarkson & Bustin, 2011).

Massarotto et al. (2003) observed horizontal and vertical permeability anisotropy ratios (PAR) using a True Triaxial Stress Coal Permeameter on large cubic coal samples. The work included the testing of effective permeabilities to helium, nitrogen and methane and sorption-induced permeability changes as well as research on coal anisotropy and anisotropic stress effects on permeability at different in situ stress levels and pore pressures. Meng and Li (2013) found in their triaxial cell tests on high-rank coal that cleats and coal fractures close during stress and do not re-open during recovery. This fact allows for the testing of the flow behaviour in cleated samples taken in the field within laboratory experiments.

Lama & Bodziony (1998) pointed out that laboratory permeability data are often lower by 1 to 3 orders of magnitude as compared to in situ test results. This is because cleats are not filled with gas and water after removal from the site. The presence of gas is reducing the water conductivity. However, samples are usually degassed and fully water saturated in laboratory tests. A fact that should be taken into account within the analysis.

2.3 QUANTIFICATION OF COAL PROPERTIES

Due to its importance for ground stability for engineering purposes as well as for the ability to store and transmit the resources water, oil and gas, the testing of permeability of soil media has a long tradition. In the following, field tests, laboratory methods and image processing methods used to quantify coal structure and derive permabilities are presented.

Classical Logging Methods in the Field have the advantage that they show the behaviour under in-situ conditions. Many different techniques to determine the permeability in situ have been used. However, different types of permeability testing yield different results. The specifics and combinations of testing are further explained by Clarkson & Bustin (2011). Laboratory testing allows to test for characteristics, e.g. permeability, under controlled conditions and has a long tradition in hydrogeological and engineering applications (for example Fetter, 2000).

Due to the dependency of flow in fractured medium to geometric features like the orientation, spacing, aperture and length of the fractures, it is essential to map structure and pattern of fractures in a hard rock aquifer. Mapping can be done using aerial photographs and remote sensing to study outcrops, as well as borehole surveys (Singhal, 2008). X-ray computed tomography (CT) scanning of coal allows for a non-destructive insight into a coal structure through acquisition of projection images from three different directions. The application of this 3D imaging and analysis technique is on the rise for the investigation of internal structures of a large variety of materials in geosciences (Cnudde & Boone, 2013).

2.3.1 Field methods

2.3.1.1 Borehole hydraulic testing

Classical field methods to determine in-situ permeability are pumping tests, slug-tests, and packer tests. They are solved using analytical solutions, like the Thiem or Theis equation (Price, 2009). During a pumping tests, the drawdown of the groundwater level in observation wells around the pumped borehole is measured over time. At the end of a

pumping test, the rate of recovery of the groundwater surface is observed to allow conclusions about aquifer properties. In a slug-test, the groundwater level is suddenly changed for example by the introduction of a cone into the well, and the response of the groundwater level is observed (see e.g. Fetter, 2000). Packer testing is one of the most effective ways to measure permeabilities locally. Sections of the borehole are isolated using packers and the mentioned hydraulic tests are conducted for the isolated zone (Paillet, Hess, Cheng, & Hardin, 1987).

Hydraulic tests with artificially changed pressures in freshly drilled boreholes can falsify the resulting permeabilities. In the near well zone, skin effects result in a local increase of the permeability caused by the opening of fractures (positive skin) or in decreasing permeability values (negative skin) as an effect of void filling and the coating of borehole walls during the drilling process (Sevee, 1991).

2.3.1.2 Geophysical logging

Besides these permeability measurement methods, a wide range of geophysical methods are commonly used to characterise aquifers (Figure 2-8).

Kirsch (2006) demonstrates the use of geophysics for the detection and delineation of groundwater resources. Caliper logs that present the borehole diameter [cm] and absolute and relative temperature logs [°C] are used in the determination of in- and outflow zones. Pressure logs [bar], Natural gamma ray emissions [API], Resistivity [Ohm meter], Density [grams/cc], Sonic logs [m/s] give information about lithological features. Furthermore, optical and acoustic televiewer are in use to image borehole walls.

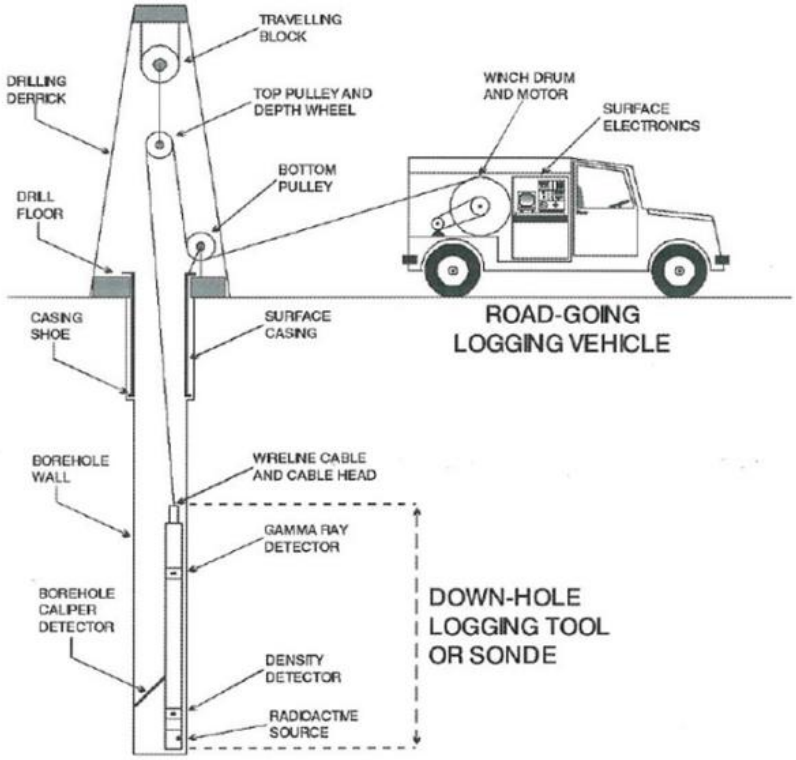

Figure 2-8 Typical wireline logging setup (Groenland, 2007)

Different methods are available to derive a profile of the groundwater flow directions and velocities. Groundwater streams inside the borehole are detected and quantified to allow conclusions on the zoning of the flow within the aquifer along the borehole. Monier-Williams et al. (2009) provide an overview of the different methods used for flow logging to obtain information about the hydrogeological properties of deep geological sites. Based on different principles impeller flow meter and electromagnetic flow meter (Molz et al., 1994), or the tracking of a heat pulse (Hess, 1986; Paillet, 1998) are in use to quantify flow in boreholes. Dilution logging captures a flow based on conductivity measurements (Pitrak et al., 2007). The principles of heat pulse flow logging used as part of this study are further explained in chapter 4.

While these flow logging methods allow a detection of in- and outflow zones along the borehole, the nature and extent of smaller coal fractures and cleats often remain poorly defined. Traditionally, coal seam gas reservoirs have been characterised using density, gamma ray and resistivity logs. However, these logs might be influenced by the presence of secondary minerals.

A more precise coal fracture and cleat characterisation in the field has been done by an integration of resistivity logs and acoustic logs by Ali et al. (2008). Apertures have been

calculated based on the resistivity of open coal fractures and cleats filled with conductive mud.

2.3.2 Laboratory methods

2.3.2.1 Porosity

Using core samples taken in the field, the porosity of a geo-material is obtained either by the injection of gas or liquids to fill the pore spaces and determine the changes in weight or volume. Common methods are mercury porosimetry and helium pycnometry (Dmyterko, 2014).

2.3.2.2 Permeability

Laboratory measurements of coal samples collected during coal exploration give an approximation to the anisotropic and heterogeneous conductive behaviour of the seam they were taken from. Due to significant changes of the ambient stress and the resulting structure alteration to the coal structure during sampling. Characteristics present under natural stress conditions cannot be captured. Common laboratory test are presented in

Table 2-3, along with the equations 2-9 and 2-10 used to derive hydraulic conductivity K [m/s] in these methods. The conversion to permeability is done as shown in equation 2-3.

Table 2-3. Overview of commonly used lab methods to test hydraulic conductivity / permeability

Method	Principle
Constant head test	A constant volume of water streams upwards through a soil sample under a constantly maintained head $K = \frac{Q}{t}\,\frac{1}{A}\,\frac{l}{h}$ [m/s] (2-9) K – hydraulic conductivity [m/s], Q - rate of flow [m^3/s], t – time [s], A - cross section [m], h - constant head [m], l – length of sample [m] (Hölting & Coldewey, 2005)
Falling head test	The volume of water passes through a soil sample under changing head, used for smaller conductivities $K = \frac{A_r}{A}\,\frac{1}{t}\,\ln(\frac{h_1}{h_2})$ [m/s] (2-10) K – hydraulic conductivity [m/s], A_r – cross section of tube [m^2], A – cross section of sample, l –length of sample, t – time [s], h_1 –head at beginning [m], h_2 – head at end [m] (Hölting & Coldewey, 2005)
CT-scans	Provides a comprehensive detailed view of the sample without cutting, information on particle and mineral grain size and shape, mineral associations, porosity and matrix density can be calculated and visualised, X-rays to observe and distinguish the different densities in a sample. (Golab et al., 2013)

2.3.2.3 Strength testing

While the test of hydraulic conductivity can be performed using a triaxial cell, the use of triaxial cells to test rock core specimen and their response to pressure is common in rock mechanics and geotechnical engineering since the 1960's (Hoek & Franklin, 1967). The test involves the placement of a cylindrical sample inside a cylinder filled with a fluid and the sample enclosed by a membrane. Hydraulic pressure in the cell is elevated to a desired level and kept constant throughout the measurement. Vertical stresses are applied until the sample fails under the load. Vertical stresses at failure are used to plot Mohr's circle and attain shear parameters (Price, 2009).

Parameters obtained from the test may include the angle of shearing resistance, cohesion and undrained shear strength, stress paths (p, q and s, t), as well as shear stiffness, compression index and permeability (Rees, 2013). The physical interaction between hydraulic and mechanical processes is referred to as hydro-mechanical coupling. Due to its pores and fractures, which are filled with water or air, a geological medium responds to changes in external stresses or internal fluid pressures with deformation with consequential changes in permeability (Rutqvist & Stephansson, 2003).

2.3.2.4 Limitations of laboratory testing of coal

The unique structure of coal poses some limitations to the use of cores for laboratory testing. Samples that do not span above the average cleat spacing cannot provide useful permeability data. Therefore, depending on the cleat spacing, a minimum diameter of 20 mm to 30 mm for small spaced samples and a minimum diameter of 40 mm for large space coal needs to use. Ideally, a true triaxial cell should be used, to capture the directional permeability along the directions of face and butt cleats. Further, desorption and adsorption processes will influence the process, which influences the choice of fluid used for the tests (Massarotto, Rudolph, et al., 2008).

2.3.3 Structural image analysis

2.3.3.1 Image acquisition

X-ray computed tomography scanning (CT-Scans) of coal samples allows a non-destructive insight into a sample through the acquisition of projection images from three different directions. The interior of the sample is represented depending on their X-ray attenuation. By stacking slices of two-dimensional imagery, a three-dimensional data set is obtained. Coal matrix and pore spaces filled with air or liquid can be distinguished, as the X-ray attenuation is primarily a function of the energy, density and atomic number of the

material (Ketcham & Iturrino, 2005). Hounsfield (1973) has first developed the widely used radiological imaging technique for medical use.

The three commonly used scanning systems are shown in Figure 2-9: the LCAT industrial system, a commercial medical system, and a GSECARS synchrotron-based micro-tomography facility.

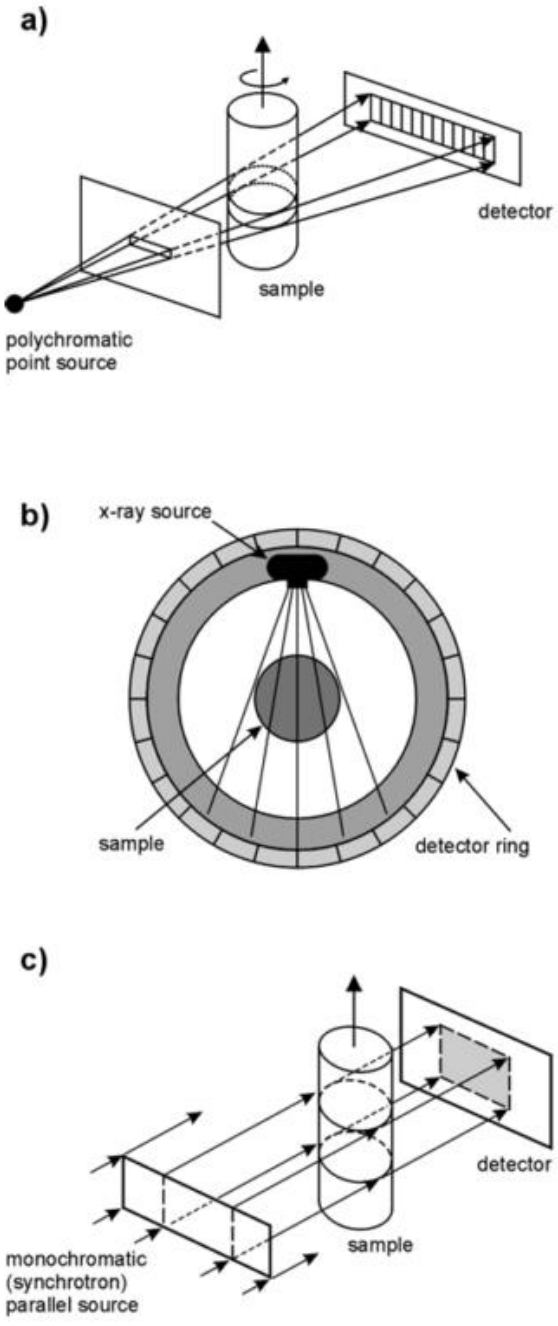

Figure 2-9 Tomography setup of different systems commonly used: a. LCAT industrial system, b. commercial medical system, and c. GSECARS synchrotron-based micro-tomography facility (Wildenschild & Sheppard, 2013)

The infiltration of samples with a high attenuation agent, e.g. potassium iodide (KI), can help making pore spaces visible in the scanning process. In cases, where a chemical analysis of the sample properties is planned, distilled water is an alternative. To replace air pockets in the sample, the flooding should take place under vacuum conditions (Ketcham & Iturrino, 2005).

Depending on the spatial resolution provided by the scanning system used, two primary scales of observation of porous structures have been described in the literature. An overview of the different systems used in hydrogeology has been provided by Wildenschild et al. (2002). Micro-scans at scale from 5 to 20 µm voxel resolution have been gained for samples of up to a few cm in diameter and used in modelling processes, for example by Knackstedt et al. (2001). Using medical scanners, samples of up to 15 cm diameter have been depicted with a resolution of 100 to 1000 µm. A large number of studies utilised a micro-focal source on an intermediate scale in the 50 to 100 µm range, which compares to the scale of a petrographic thin section (Ketcham & Iturrino, 2005).

The resolution of the scanning instruments is the main constraint for pore-scale simulations. The choice of a bigger field of view may cover a bigger volume of sample but also exhibit a lower resolution. In a porous medium, the effect of micro-pores would be underestimated. Further, the resolution of the system influences the segmentation process, where micro- and macro-pores or, in a fractured medium, fracture and matrix are distinguished (Norouzi Apourvari & Arns, 2015).

2.3.3.2 Image processing and analysis

The quality of an image is largely a function of the system used to acquire it. However, a well-thought-out subsequent image processing can highly improve the usability of the image to analyse certain features in the picture. Usually, image processing comprises of several stages. The aim of the image enhancement process is the preparation of the picture for the particular application. Imaging defects that might be present due to imperfect illumination, an inadequate viewpoint or imperfect detectors are corrected. For instance, through the use of filters, noise in the pictures can be reduced, the focus can be re-adjusted by sharpening or de-blurring and contrasts improved.

To improve their visual appearance and the possibility to measure features and structures present in a CT image of a coal sample, image processing tools are available and described in the literature. To distinct objects of a picture, its features need to be well defined either in terms of brightness, colour, edges or a combination of these features

(Russ, 1999). The characteristics of interest are brightness, location, orientation, neighbour relationships, alignment or arrangement of features (e.g. image transformation into Hough space as introduced by Hough in 1962), number and sizes of features, their perimeter, shapes and fractal dimensions.

Segmentation processes help to reduce the information in the image according to the question, that is, only relevant features will be looked at. To facilitate the distinction of elements in an image, contrasts can be adjusted and colours equalised using thresholds fitted to the relative problem. Particularly helpful and widely used is a binarisation of the image based on a certain threshold on its greyscale (Gonzales, Woods, & Eddins, 2004).

A grayscale image is turned into a binary image by choosing a gray level in the original image as threshold and turning every pixel value depending on their relative position to the threshold into black or white. Once binarised, the black and white images allow for a simple feature extraction and further processing, e.g., logical operations, feature connection through erosion and dilation, skeletisation, edge detection (Gonzales et al., 2004).

Quantitative measuring of image features can be classified into two categories: feature-specific and global or scene-based (Russ, 1999) and are given in Table 2-4.

Table 2-4 Classification of image feature measurement methods

Measurements	Parameter
Feature specific measurements	Size (volume, surface area, length)
	Position
	Density
	Topology / Connectivity
	Shape parameters
Global scene based measurements	Volume fraction of selected phase counting voxels
	Surface area per unit volume of boundary

Minimising an object to its skeleton, that is, the midline, pixel with only a single touching neighbour are representing end points, more than two neighbours are branch points. The skeleton illustrates topological as well as geometrical shape properties as length and direction. Pixels with only a single touching neighbour are representing end points, more than two neighbours are branch points (Figure 2-10) (Pratt, 2001).

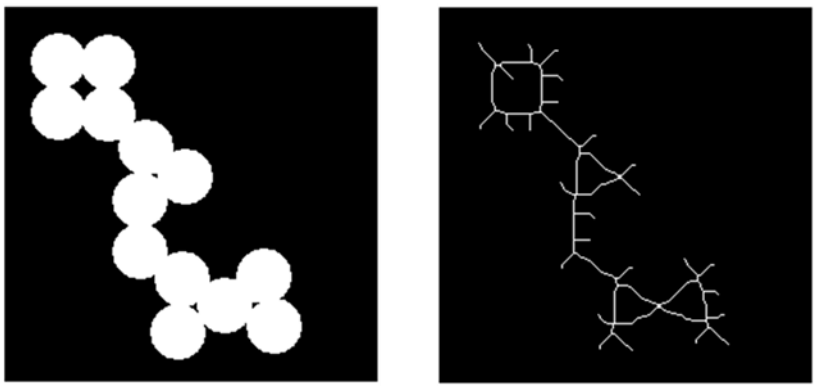

Figure 2-10 Object and its skeleton (www.mathworks.com, 2015)

The Euclidean distance is a metric measure to compute distances between objects in an image. Computing the Euclidean distance one can determine the distance from each cell to the next non-zero element (Deza & Deza, 2009). For Cartesian coordinates, the Euclidean distance between two points a and b in an n-dimensional space is calculated by equation 2-11.

$$ED(a,b) = ED(b,a) = \sqrt{\sum_{i=1}^{n}(b_i - a_i)^2} \qquad (2\text{-}11)$$

2.3.3.3 Cleat structure investigation based on CT - imaging

The use of digital mapping can greatly improve the statistical accuracy associated with the characterisation of discontinuities (Elmouttie & Poropat, 2011). Fractures, cleats and the variation of occurrence through the length of a cored coal sample can be detected by CT imaging, and parameters like size, aperture and cleat connectivity can be quantified.

Karacan & Okandan (2000) did a study based on CT-scans and polished surface analysis on coals from north-western Turkey focused on the gas productivity of the coal. They investigated the distribution of minerals, cleat morphology, cleat density and apertures. Interactions between matrix and cleats were deduced based on the examination of cleat surfaces. Mazumder et al. (2006) used CT-scans to describe cleat orientations and cleat aperture and spacing in coal samples. The approach has been extended to deduce coal density and the distribution of inorganic material (Klawitter, Collins, & Esterle, 2013). Wolf et al. (2008) compared cleat angle distributions from drilling cutting to cleat orientation distributions from CT-scans from coal blocks of the same seams. Weniger et al. (2016) quantified cleat aperture, spacing, height, and frequency data from images using optical microscopy of scanned polished sections and derived permeability related to aperture and spacing based on the cubic law.

The usefulness of CT-scans for the testing and calibration of image and network-based models of multiphase flow has been pointed out (Kumar et al., 2010). The fluid flow through a single CT-scanned fracture has been modelled using computational fluid dynamics by Petchsingto and Karpyn (2009). An innovative integrated application combining CT-scan based material characterization and process monitoring is promising to give an insight into the influence of heterogeneous rock properties like porosity, hydraulic conductivity and diffusivity on fluid transport processes and geo-mechanical properties (Cnudde & Boone, 2013). To be used as an input for flow or mechanical models, the physical properties of the coal structure require an appropriate statistical description. The characterization of fractured rock has been pointed out as the most challenging problem that hydrogeology currently faces (Faybishenko et al., 2000). Nowadays, the common approach for the modelling of fluid flow in fractures is to generate random artificial sets of fractures based on commonly known distributions (De Dreuzy, Davy, & Bour, 2001).

Prediction of transient processes like flow and transport in geo-materials based on system information remains a challenge. Kasteel et al. (2000) have described effective solute transport at the centimetre scale by taking the spatial structure of the millimetre scale into account. The absorption coefficients from CT-scans were used to distinguish bulk density which serves as a proxy for the local hydraulic properties. Bai et al. (2015) modelled the generation of coal fines, small particles frequently found in coal seams, in single micro-scale cleats. To model mass transport within the porous matrix of coal as part of bio-conversion of coal to methane, Pant et al. (2015) used CT-scans with a 5 to 10 nm and 2 to 10 µm resolution. Capturing fluid flow using CT-scans fails due to the nature of the methods that allows to capture characteristics at a certain moment. Hirono et al. (2003) have approached a description of fluid flow within deformed rock using images taken in certain time intervals, e.g. after 150, 210 and 270 minutes, after flooding and comparing them to the initial state.

2.4 FLUID FLOW IN FRACTURED MEDIA

2.4.1 Fracture reservoir types

Fractures are discontinuities within a rock mass that are developing as a response to stress (Bonnet et al., 2001). Therefore the permeability of fractured rocks is epigenetic, that is, caused by external influences.

In principle, three different simplified fracture reservoir types can be considered (Figure 2-11). For the reservoir type represented in Figure 2-11a the solid matrix is treated as impermeable (e.g. Hamzehpor et al., 2009) and flow takes place in fractures only. Another approach to describe fractured reservoirs is a double porosity system (Figure 2-11b), with liquid flow occurring in the host rock and the fractures (Barenblatt et al., 1960). In a double porosity medium, the interaction between the fracture and the matrix is a process to be looked at when describing fractured rock system (Faybishenko, Witherspoon, & Benson, 2000). In a so-called heterogeneous system, as shown in Figure 2-11c, the cleats are filled and the fracture permeability is reduced.

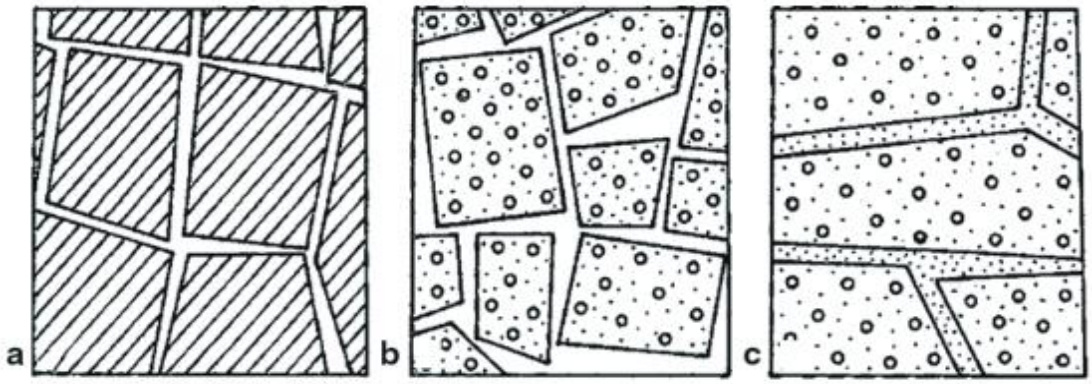

Figure 2-11 Fracture reservoir types: a. Purely fractured medium, b. Double porosity medium, c. Heterogeneous medium (Singhal, 2008)

Even in a granular medium, the flow of fluids is generally focused along a few dominant pathways, a phenomenon called flow channelling that occurs on all scales (Tsang & Neretnieks, 1998). Aquifers that are dominated by the occurrence of fractures are highly heterogeneous at multiple scales (Bonnet et al., 2001). A comparison of the flow characteristics in granular and fractured media is found in Table 2-5.

Table 2-5 Hydraulic features of porous and fractured aquifers (after Singhal, 2008)

Aquifer Characteristic	**Aquifer Type**	
	Porous medium	**Fractured medium**
Effective Porosity	Mostly primary	Mostly secondary through joints and fractures
Isotropy	Rather isotropic	Mostly anisotropic
Homogeneity	Rather homogeneous	Less homogeneous
Flow	Laminar	Rapid and turbulent
Recharge	Dispersed	Dispersed with local point recharge
Flow prediction	Darcy's law applies	Darcy's law applies in tensorial form
Head variations	Minimal	Moderate
Water quality variations	Minimal	Greater

Numerous field observations have shown that single fractures are organized in networks with preferential flow paths (Tsang & Neretnieks, 1998). Identification and proper description of the dominating flow channels is critical to describe the flow in fractured

systems. Intrinsic permeabilities in fractured porous media has been found to be greater of up to two orders of magnitude than in the porous matrix (DeAngelis et al., 1984). The interconnected network of fractures is described by the percentages of fractures, the degree of their connectivity and resulting conductivity.

2.4.2 Influence of fracture characteristics on flow and permeability

Single phase flow is mainly controlled by the topology and morphology of the rock structure. Further complexity arises for multi-phase flow, which is also affected by the saturation and distribution of fluids within the structure, as well as by fluid-fluid interactions (Norouzi Apourvari & Arns, 2015).

It is widely claimed that fracture aperture and flow rate are interrelated by a cubic relationship (Witherspoon et al., 1979). Park et al. (2004) found a positive correlation between fracture density and hydraulic conductivity measured in single-hole hydraulic tests.

Aperture between fracture walls has been discussed as one of the main influencing parameters for flow in fractures. Fracture apertures cover a wide scale range, their variation is influenced by mechanical and chemical actions in the system (Bonnet et al., 2001). A study of carbonates by Lucia (1983) found that permeability increases with the cube of the fracture aperture and varies with the inverse of the fracture spacing.

Besides aperture, other fracture characteristics play an important role in the fluid flow, and can be more dominant whether flow can occur. Non-parallelism of walls and the wall roughness lead to friction losses. It has been shown by Neuville et al. (2010) that, depending on the orientation of the hydraulic gradient relative to heterogeneities in wall roughness, the flow can be either enhanced or inhibited. With increasing temperature fracture permeability is found to reduce as a result of thermal expansion of the rock that causes fractures to reduce. Finally, cementation, filling and weathering are factors influencing fracture permeability (Singhal, 2008).

The relationship between in-situ stress and fluid flow in fractures has been studied by Barton et al. (1995) who noted that depending on the orientation in the stress field few active fractures serve as the primary flow conduits. The porosity of fractures is strongly dependent on the stress field and therefore the depth. With increasing temperature fracture permeability is found to decrease as a result of thermal expansion of the confined rock that causes fracture apertures to reduce (Singhal, 2008). Philip et al. (2005) numerically investigated the effect of diagenesis on the initial flow properties of fracture

systems, especially with respect to diagenetic effects on the connectivity of the fracture network. The results indicated that fracture permeability is more sensitive to fracture patterns and connectivity than aperture.

Long & Witherspoon (1985) claimed that fracture length, density and flow rate are interrelated. Networks with longer fracture lengths and lower densities exhibit higher connectivities and therefore higher permeabilities than those formed of shorter fracture lengths with higher densities. That permeabilities are more sensitive to fracture patterns and connectivity than aperture has been confirmed by Philip et al. (2005). Park et al. (2004) found a positive correlation between fracture density and hydraulic conductivity measured in single-hole hydraulic tests. However, other studies show that fracture geometry is not directly correlated to hydraulic parameters of the fractured rocks. The correlation between fracture density and transmissivity has been found to be non-existent or difficult to generalize. Moreover, interpolation of fracture geometry between boreholes, as well as their connectivity are subject to questioning (Neuman, 2005).

While for many coal fracture systems the porosity of fractures is found to be dependent of the stress field and therefore the depth (Barton et al., 1995; Laubach et al., 2004) showed that open fractures are not necessarily aligned or more permeable in certain directions relative to the stress field. In fact, the orientation of open natural cleats and coal fractures depends on the relative stiffness of the cleats and fractures and the host material.

2.4.3 Mathematical models for flow in fractured media

The modelling of groundwater systems that are highly heterogeneous has been an active area of research, with a significantly increasing number of studies and publications on flow and transport processes in fractured systems within the last three decades. A wide range of methods that can capture the heterogeneity of hydraulic parameters like hydraulic conductivity and storage coefficients has been developed (Figure 2-12).

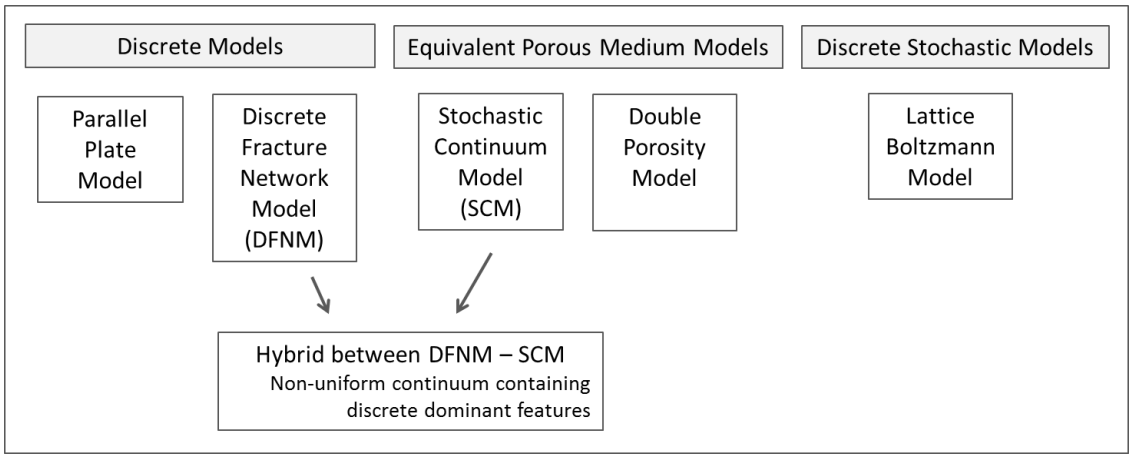

Figure 2-12 Concepts for flow modelling

Discrete Models and Equivalent Porous medium models are generally based on Darcy's law. Due to computational limitations, the fractured or porous medium is homogenized at a meso-scale before modelling the flow within. At the fracture scale some models take the Naiver-Stoke equations into account. These equations describe the incompressible flow of Newtonian fluids (see e.g. Munson, Young, & Okiishi (1990).

For Discrete Models the equations are either solved explicitly for a plate model (Poisson equation) or by using the linear network theory for a capillary model. Equivalent Porous Medium Models are assuming a random porous medium. The Lattice-Boltzmann Model is a Discrete Stochastic Model based on the Boltzmann equation for a gas. The choice of the most suitable conceptual model describing flow in a fractured medium strongly depends on the considered problem and is still a subject of debate (Neuman, 2005).

Unforeseen or unidentified uncertainty may have a major effect on the ability to predict the fluid flow in fractured rock mass and therefore significant safety implications. Even relatively small numbers of stochastically generated structures can produce large uncertainty in percolation parameters like the equivalent permeability (Ji, Park, & Lee, 2011). Moore (2006) found that the calibration of hydrogeological models based on insufficient data can lead to errors in excess of 100% in predictions of transport times.

2.4.3.1 Parallel Plate Model

The simplest conceptual models to describe the flow in fractures are the Parallel Plate Model. The Parallel Plate Model is a simplified representation of a fracture two plain parallely arranged plates with a constant aperture (Figure 2-13). At the scale of a single fracture, flow patterns are influenced by the fracture aperture variability and the roughness of the facing aperture surfaces.

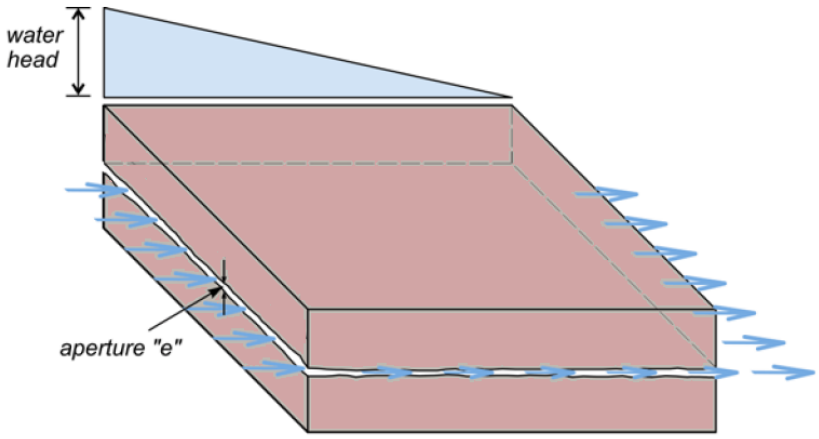

Figure 2-13 Parallel Plate model of a single, isolated fracture (Kong et al., 2015)

The cubic law provides an estimation of the flow rate per unit fracture length. The cubic law can be derived easily for laminar flow conditions within sufficiently open fractures assuming the fracture walls are impermeable (e.g. Moreno et al., 1988; Singhal & Gupta, 1999).

Darcys law for flow in a single fracture can be written as equation 2-12. Equation 2-13 is used to calulate the hydraulic gradient i, a value that incorperates dh and dl:

$$V = -K_f\, i \qquad (2\text{-}12)$$

$$i = \frac{dh}{dl} \qquad (2\text{-}13)$$

The hydraulic conductivity, K_f, [m/s] of the fracture is related to the fractures aperture, a [m], the specific weight of water, γ_w [N/m^3], and its viscosity, μ [kg/s m] as shown in equation 2-14.

$$K_f = \frac{\gamma_w\, a^2}{12\mu} \qquad (2\text{-}14)$$

Combining the equations 2-12 and 2-14 to equation 2-15 allows the calculation of the average velocity of fluid flow, v_a, within the fracture.

$$v_a = \frac{\gamma\, a^2}{12\mu}\, i \qquad (2\text{-}15)$$

The cubic law gives the volumetric flow rate, Q_f [m^3/s], per unit fracture width as presented in equation 2-16.

$$Q_f = \frac{\gamma\, a^3}{12\mu}\, i \qquad (2\text{-}16)$$

Analytical models have been used to calculate flow in fractures and cleats whose geometry has been quantified. Philip et al. (2005) suggest the parallel plate model to calculate the permeability, k [m^2] of a fracture of continuous aperture, a [m], for a simulated fracture network as presented in equation 2-17.

$$k_i = \frac{a^2}{12} \qquad (2\text{-}17)$$

Pan & Connell (2012) developed a simple model for an idealised coal cleat system. With the aperture, a [m], being comparably small to the spacing, s [m], the permeability, k [m^2], of each fracture can be calculated using equation 2-18.

$$k_j = \frac{a^3}{12\ s} \qquad (2\text{-}18)$$

Huy et al. (2010) estimated fracture aperture width of coal core samples and the carbon dioxide gas permeability in the core. They found that overall permeability is dominated by the fracture aperture, a [m], more than the length, l [m], and suggest equation 2-19 to calculate the overall permeability, k [m^2], for a coal core of diameter, d [m], with n fractures.

$$k = \frac{1}{3\ \pi\ d^2} \sum_{j=1}^{n} a_j^3\ l_j \qquad (2\text{-}19)$$

2.4.3.2 Double Porosity Model

The Double or Dual Porosity Model assumes two regions within a sample: a matrix of low permeable blocks intersected by highly permeable fractures (Singhal, 2008). Fluid flow from the blocks into the fractures follows the internal pressure gradients.

2.4.3.3 Equivalent Porous Models

Equivalent Porous Models are based on the concept that a discontinuous rock mass behaves mathematically like a porous medium if the considered volume is large enough so that the REV of the material characterized by effective hydraulic parameters can be defined. These models have been the first approach to capture the flow behaviour in fractured media at a time, when the characterization of fractures and matrix properties was still technically limited (e.g., Long et al., 1982; Bear, 1972). Equivalent medium approaches for fluid flow in fracture represent individual fracture properties like position, size and aperture using deterministic and stochastic methods (Elmouttie & Poropat, 2011).

2.4.3.4 Discrete Fracture Network Models

Discrete Fracture Models (DFNM) represent each fracture individually and explicitly. The geometry and interconnection of fractures are considered explicitly. Therefore, DFNMs are a more natural approach to describe fluid flow within fracture networks. In recent years, discrete representations of fracture networks are more common and find wide use in mining engineering, civil geo-mechanics, as well as hydrogeological studies (e.g. Cvetkovic et al., 2004; McLaren et al., 2012; Gong et al., 2014; Lorig et al., 2015). Software has been developed to model DFN to represent discontinuities (e.g. cleats and coal fractures) more realistically. Growing computing resources allow to capture all relevant structures in a volume of interest (Elmouttie & Poropat, 2011).

Fracture network models generally assume the matrix to be impermeable with the flow being conducted through a network of cracks with uniform apertures. They require detailed deterministic or statistic information on the fracture geometry, which calls for a comprehensive research design (Neuman, 2005). Uncertainties are associated to the modelling process, especially inherent uncertainty due to the explicit requirements of the modelling process (Jing, 2003). DFNMs are usually constructed based on the statistical parameters mapped in the field that describe the fracture geometry. Field sampling based methods like core logging and exposure mapping (e.g. scan line or window mapping) are used. Inherent biases must be corrected, especially estimates of fracture density (or frequency) and trace lengths (Mauldon, 1998).

2.4.3.5 Stochastic Continuum Models

Stochastic Continuum Models (SCM) employ stochastic principles to obtain representative parameters. They can be extended from small-scale studies to large-scale problems (van der Heijde et al., 1988). The fractured rocks are treated as a non-uniform continuum whose transmissivities obtained using in-situ field tests are described as a random but correlated field (Neuman, 2005).

This approach aims to describe the hydraulic behaviours of a system as an average of the available data. Therefore, small data sets often result in high uncertainties, which is expressed by the fundamental concept of the Representative Element Volume (REV) (Bear, 1972). The concept of REV states that there is a scale below which individual heterogeneities and discrete features can be ignored. It has been shown, that continuum models are only valid for high-density fracture networks with uniform aperture distribution and non-uniform orientation distribution (J C S Long et al., 1982).

The common approach for the modelling of fluid flow in fractures is to randomly generate artificial sets of fractures based on commonly known distributions (De Dreuzy et al., 2001). Stochastic analysis like Monte Carlo simulations are often used for the analysis of flow and transport through fractured rock. Due to their random nature, multiple realisations are required, which makes this approach computationally expensive. Galindo-Torres et al. (2015) examined randomly generated two-dimensional fracture networks and showed that the connectivity and average conductivity of the individual fractures are related to the macro-conductivity and hence can be described by universal functions based on percolation theory.

2.4.3.6 Hybrid of DFN and SCM

As we have seen, DFN models characterizes the flow along individual pathways, whereas in SCM hydraulic properties of the medium are averaged. To take advantages of both DFNM and SCM, a hybrid model of a non-uniform continuum containing a number of deterministic fractures has been developed to describe the flow through the system depending on the matrix permeability as well as on the fracture network (Neuman, 2005). Properties are described either deterministic or stochastic.

Several possible choices of model simulations are presented by Dershowitz & Einstein (1988). An often used example of DFN for rock mass simulations is the Baecher DFN model (Baecher, Lanney, & Einstein, 1977).This model is based on the statistical description of rocks and assigns certain distributions to relevant geometrical parameters. Fractures are represented by circular disks. Random centre points are assigned to these disks following Poisson distributions. Radii are assigned following log-normal distributions, while disk (i.e. fracture) orientations are based on weighted frequency distributions and aperture size distribution are neglected. The approach has been evolved by Cacas et al. (1990). They applied a Fisher von Mises distribution of fracture orientation and classify different families of orientation. Fracture apertures are characterised by lognormal distributions. Differences that might be present for the characteristic distributions have to be taken into account for different rock types. Matthäi & Nick (2009) introduced a fracture-matrix-flux ratio and showed that the relative permeability depends on the transfer at the fracture-matrix interface, which is a function of water saturation, water breakthrough, and interface structure.

This method of building DFN models is widely used to date, however, it generalises network characteristics to some extent as it may underrepresent the connectivity of the fracture system. DFN approaches for coal have for example been used by Deisman et al.

(2010) and Scholtes et al. (2011). The comprehensive consideration of all characteristic features of the geometry of coal structure and the connectivity of the cleat network is relatively new. While the DFN model of Gao, Stead, & Kang (2014) consists of three orthogonal discontinuities to represent face cleats, butt cleats and bedding planes, but they did not include independent orientation statistics for the cleats. Jing et al. (2016) included this parameter to mimic the geological formation of the cleat network.

2.4.3.7 Lattice-Boltzmann based model for flow in fractured media

The Lattice-Boltzmann Method is based on the idea that macroscopic behaviour of a fluid system is generally not very sensitive to the underlying microscopic fluid particle behaviour (Kadanoff, 1986). Instead of tracking the movement of each single particle, the behaviour of the fluid system is described as a collective averaged macroscopic flow behaviour. Due to these features, the Lattice Boltzmann received much attention for flow simulation at the pore scale (Norouzi Apourvari & Arns, 2015).

Lattice Boltzmann simulations of fluid flows are both used for flows with simple geometries, like cavity flows or around circular cylinders, and flows with more complex geometries. Turbulent flows in industrial applications have been subject to studies, as well as complicated multi-phase and multi-fluid flows. The method is represented by the Boltzmann equation, which represents simplified, fictitious molecular dynamics in which space, time and particle velocities are all discrete (Tu et al., 2007). The Boltzmann equation is given in equation 2-20

$$\frac{\partial f}{\partial t} + e * \nabla f = \frac{f - f^{eq}}{\lambda} \qquad (2\text{-}20)$$

with f being a particle distribution function, e the particle velocity, λ the relaxation time due to particle collision and f_{eq} the equilibrium Boltzmann-Maxwell distribution function. The particle velocity space, e, can be discretised into a small set of discrete vectors, and along each velocity direction, e_i, at the lattice is, therefore, represented by equation 2-21.

$$f_i(x + e_i\delta t, t + \delta t) - f_i(x, t) = -\frac{1}{\tau}[f_i(x, t) - f_i^{eq}(x, t)] \qquad (2\text{-}21)$$

with $f_i(x,t)$ being the density function, e_i the velocity, x the lattice position, t the time, $\tau = \lambda/\delta t$ the relaxation parameter and δt the time step.

The macroscopic density, ρ, and flow velocity, v, can be defined in terms of the particle distribution function as equation 2-22 and 2-23.

$$\rho = \sum_i f_i \qquad (2\text{-}22)$$

$$\rho * v = \sum_i f_i * e_i \qquad (2\text{-}23)$$

On the microscopic scale the flow is dependent on the topology of the pore structure, as well as on the morphology of the obstacles (McClure et al., 2010), which can be accessed using micro-scale simulations. With the Lattice Boltzmann Method (LBM) many microscopic features, such as the tortuosity, can be quantified with enough accuracy. But perhaps the most useful feature of the method is its ability to impose many types of boundary conditions, which permits the calculation of the full permeability tensor in three dimensions that accounts for the anisotropy of the material, as represented by equation 2-24.

$$\begin{pmatrix} k_{xx} & k_{yx} & k_{zx} \\ k_{xy} & k_{yy} & k_{zy} \\ k_{xz} & k_{yz} & k_{zz} \end{pmatrix} = k_{LBM} \qquad (2\text{-}24)$$

In a permeability tensor, the diagonal terms represent the flow in the direction of the pressure drop. The off-diagonal terms represent the flow perpendicular to the pressure drop. In an isotropic case, where permeability is equal in all directions, permeability can be expressed as a scalar. For a highly heterogeneous and anisotropic medium like coal, the tensorial form of the permeability is more applicable.

The LBM has been used to simulate fluid flow in synthetically generated fractures by several authors. Madadi & Sahimi (2003) have simulated fluid flow in a two-dimensional synthetically generated model of fracture network with rough, self-affine surfaces and systematically varied the geometrical parameters of the model to investigate their effect on the permeability. Similarly, Eker & Akin (2006) simulated fluid flow in two-dimensional synthetically created fractures using different fractal dimensions, anisotropy factors, and mismatch lengths. Ghaffari, Nasseri, & Young (2011) studied synthetic fracture networks in rock mass and the effect of variating connectivity patterns on fluid flows.

The fluid flow in a complex real, thus mechanically induced, rock joint structure has been studied using the Lattice Boltzmann method and the resulting permeabilities showed a good correlation to the laboratory results (Ghaffari et al., 2011).

Three-dimensional flow in complex geometries that are similar to the cleat geometries in coal has been calculated with the Lattice Boltzmann Model by Succi, Foti, & Higuera (1989). To describe coal seam gas desorption and diffusion, Jin et al. (2013) treated coal

as a dual porosity medium of a porous matrix coupled with a fracture network and focused on the fluid flow in the porous matrix. They used LBM simulations to simulate micro-scale fluid flow through a number of numerically generated realisations of fractal pore structures to represent the coal matrix.

For simulations of flow within a real coal cleat network, the Lattice Boltzmann method has been used by Jing et al. (2016). They performed numerical simulations based on lattice Boltzmann method on cleat network realisations to evaluate coal permeability. They used coal μ X-ray CT data for the acquisition of structural parameters and built discrete fracture networks to reconstruct representative coal images based on the obtained parameters. Xue et al. (2015) used the Lattice Boltzmann method to model flow of gas and water in coal and coupled the results with an analysis of a discrete element method that describes deformation, failure and fracturing of solid coal under stress to simulate outbursts of coal and gas.

2.5 SCALING OF FRACTURED SYSTEMS

2.5.1 Scales

The major challenge to model the properties of an aquifer lies in the heterogeneity of the pore voids. For example, a coal sample of a diameter of few centimetres can only give limited information on the large-scale hydraulic properties of coal seams. Therefore the permeability values depend on the scale they are obtained at, and multiple scales have to be considered (Figure 2-14).

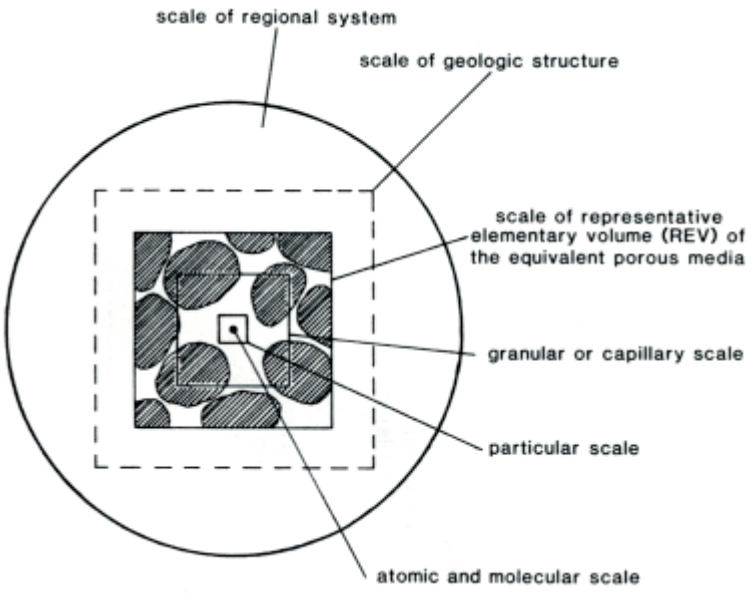

Figure 2-14 Scales of a hydrogeological system (Singhal, 2008)

Spatial scales of pore voids can range from micrometre (micro pores in clays) up to several kilometres (rock caverns in limestone and sandstone). Usually high resolutions and detailed mathematical descriptions can be achieved at the measurement scale, but limitations in computational resources require models to be up-scaled to a larger scale so that the analysis of coal properties and the computation of fluid flow in coal seams at field-scale is feasible for practical applications for example in reservoir engineering, hydrogeology, environmental engineering and CO_2 sequestration (Fu et al., 2011).

2.5.2 Scale definition and practical constraints

Aggregating small scale descriptions of microscopic processes into continuous hydrodynamic equations on a larger field-scale is traditionally done by the application of averaging procedures (Bear, 1972; Bear, 1979). The resulting model requires fewer field data than a comparable problem of the same size, but has also several drawbacks as explained by van der Heijde (1987). Assumptions made on a microscopic level may not necessarily reflect the groundwater system on a macroscopic scale. By averaging the data, some information about the real condition is lost. Furthermore, characteristics like geological heterogeneities or long term recharge effects that only become influential on larger scales might be missed.

While field studies may capture structures and flow in fractures over kilometres, the investigations with laboratory instruments capture scales in the cm to dm range. Mapping of the fractures in a sample of rock or a hard rock aquifer serves as the basis to undertake a simulation of the flow within fracture networks. However, in field observations only the fractures that intersect the boreholes are directly accessible, while in laboratory tests a sample of limited size is often considered as the representation of a bigger picture.

The constraints given by the resolution of the instruments used can be dealt with by using dual scale and three scale approaches. The variation of reservoir properties is captured on their respective scale. For the dual scale approach the medium is divided into the micro-scale and the macro-scale. The structure and behaviour on each scale investigated separately, and the results are merged (Norouzi Apourvari & Arns, 2015). These attempts are examples of the technique of upscaling.

A major task in the modelling of flow and transport in fractured media is therefore the description of heterogeneities on different scales. This process involves selecting parameters used in the model and distinguishing between variables that are constant across discrete intervals and that behave differently on different scales (Beck, 1985). The

advantages of computer simulations versus field and laboratory tests are their repeatability, the freedom to change boundary conditions and, once implemented, the relative cost efficiency.

The definition of micro-, meso- and macro-scale highly depends on the subject of each study. Each of the scales shown in Figure 2-14 may itself be subdivided into these categories. For the structure of coal, the definition given in Figure 2-15 has been used for the modelling of mass transport within the porous matrix (Pant et al., 2015).

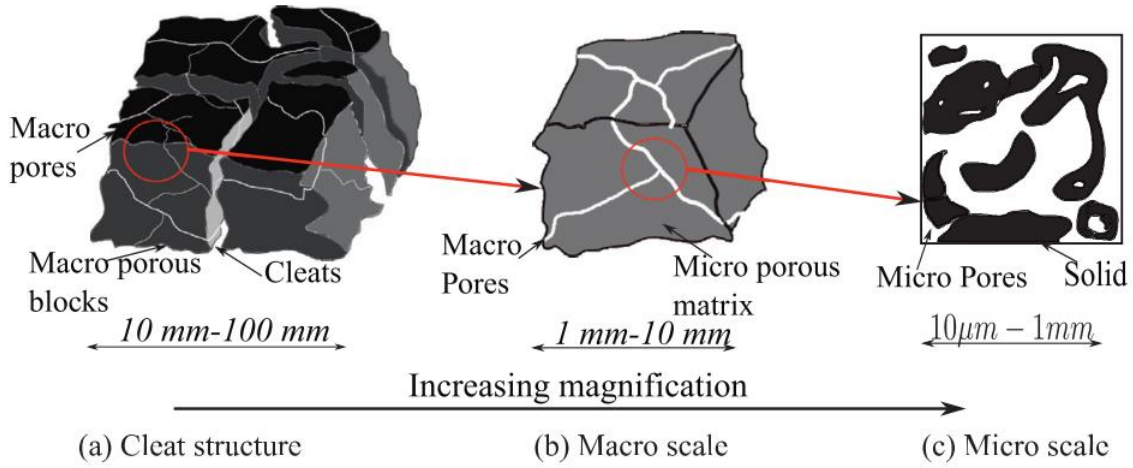

Figure 2-15 Illustration of internal structure of coal at different length scales defined as a. cleat structure scale, b. macro-scale, c. micro (Gamson et al., 1996)

2.5.3 Up-scaling of reservoir properties

Most pore-scale studies have been carried out on homogeneous porous material. A small subset of a homogeneous material can be considered as representative for the whole (Olafuyi et al., 2006). However, heterogeneity is a fundamental characteristic of nature and defining for the behaviour of fractured media and flow and transport within. Heterogeneity appears on all scales of observation and has effects on all sorts of physical phenomena, including a large range of hydrogeological parameters like dispersivity, breakthrough, and solute distribution curves and porosities (Sánchez-Vila, Carrera, & Girardi, 1996).

Up-scaling attempts to find the REV scale that it is representative for the behaviour of the medium as a whole (Bear, 1972). Any property of the medium can vary among the scales of the sample volume (Figure 2-16). While a small volume of the sample fails to capture the heterogeneity of the material and is highly affected by small-scale variations, an increase of the volume will lead to a stabilisation of the measured property. The volume where the measured property is relatively insensitive to small changes in volume and location is defined as the REV scale (Nordahl & Ringrose, 2008).

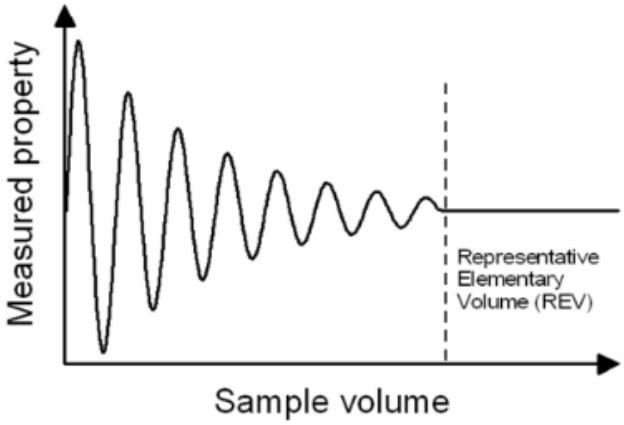

Figure 2-16 Variation of a measured property along scales of the sample volume (Nordahl & Ringrose, 2008)

For questions concerning reservoir characterisation, many different length scales have to be taken into account. The smallest scale of interest is the pore scale in the range of micrometre to centimetres. Samples are usually taken in a centimetre to decimetre range, the so-called core scale. Field instruments allow the investigation of reservoir characteristics and flow behaviour on a scale of metres to sub-kilometres. Usually, cleat network reconstruction on larger scales (metres to kilometres) combines seismic, well logging, outcrop analysis, and coring data. This type of quantitative field data are expensive and not always available (Jing et al., 2016). Satellite methods can provide basin wide data of kilometres to hundreds of kilometres.

REVs can be identified for each of these scales. Once a REV is reached for a scale, a further increase of the volume leads to oscillation of the measured property again. In Figure 2-17 this is shown for permeability. By including information from each length scale, the heterogeneity of a system can be represented. Statistical information at each scale is collected and then used to generate multi-scale stochastic networks as for example done for porous media by Jiang, Dijke, Sorbie, & Couples (2013).

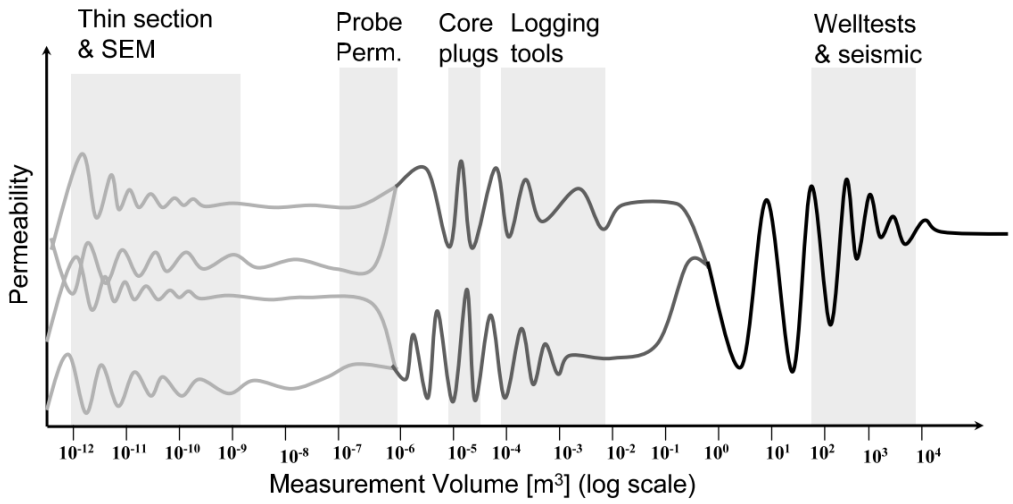

Figure 2-17 Different scales of REV related to sedimentological heterogeneities with the methodology used for investigation on each scale (Nordahl & Ringrose, 2008)

2.5.4 Up-scaling of permeability

Up-scaling is an active research topic with a focus on the question how to upscale non-additive properties such as the permeability (Norouzi Apourvari & Arns, 2015). Many upscaling techniques for permeability have been derived, some are based on different averaging methods, while others are flow-based (Odsæter, 2013).

While the spatial variation of permeability is widely accepted, the scale effect in permeability is still under debate. Based on field measurements Illman (2006) showed that permeability of fractured rock increases with scale, along with the fracture connectivity that is the controlling parameter. Collecting data from a large range of sources, a general trend of permeability increasing with scale from the laboratory scale to the field-scale is apparent, with a stabilisation at regional scales in the kilometre range (Figure 2-18).

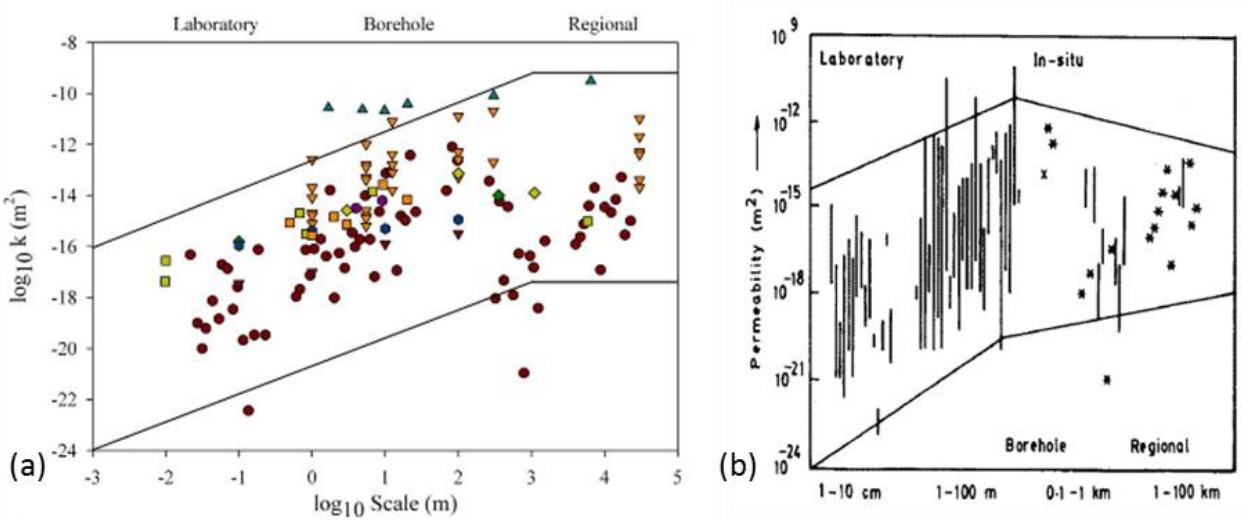

Figure 2-18 Permeability (k) data collected at different fractured field site plotted against measurement scale of two different studies (a. Illman, 2006; b. Clauser, 1992)

2.5.4.1 Averaging methods

Matheron (1967) showed that large-scale permeabilities equal the geometric average of local values. He proposed that the effective permeability, $k_{effective}$, is between the arithmetic mean and the harmonic mean of the local point values, expressed as equation 2-25.

$$k_{harmonic} \leq k_{effective} \leq k_{arithmetic} \quad (2\text{-}25)$$

The arithmetic mean of n permeability values is expressed as equation 2-26.

$$k_{arithmetic} = \frac{\sum_{i=1}^{n} k_i}{n} \quad (2\text{-}26)$$

The harmonic mean of the local values is expressed as equation 2-27.

$$k_{harmonic} = \frac{n}{\sum_{i=1}^{n} \frac{1}{k_i}} \quad (2\text{-}27)$$

Gutjahr, Gelhar, Bakr, & MacMillan (1978) proposed that the $k_{effective}$ is related to the geometric mean, the dimensionality, n, of the medium and the variance of the logarithm of k that is represented by σ_Y^2 and shown in equation 2-28.

$$k_{effective} = k_{geometric}\left[1 + \left(\frac{1}{2} - \frac{1}{n}\right)\sigma_Y^2\right] \quad (2\text{-}28)$$

This has been extended by Gelhar & Axness (1983) to equation 2-29.

$$k_{effective} = k_{geometric}\, e^{\left[1+\left(\frac{1}{2}-\frac{1}{n}\right)\sigma_Y^2\right]} \quad (2\text{-}29)$$

However, Sánchez-Vila et al. (1996) observed that the large-scale values often exceed the geometric average of the small-scale values. An extension of these averages is the power average, $k_{power\ average}$, that has been proposed for permeability upscaling by Desbarats (1992) as equation 2-30

$$k_{power\ average} = \left(\frac{\sum_{i=1}^{n} {k_i}^{\alpha}}{n}\right)^{\frac{1}{\alpha}} \quad (2\text{-}30)$$

with α being the power average exponent and k_i the permeability of each of n fractures. For the harmonic and arithmetic mean α respectively equals to -1 and 1. For the geometric mean α equals to 0 and the power average can be expressed as the exponential of the arithmetic means of the logarithms of k_i using equation 2-31.

$$k_{power\ average} = exp^{\left(\frac{\sum_{i=1}^{n} \ln(k_i)}{n}\right)} \quad (2\text{-}31)$$

The increase in permeability with increasing scales is attributed to the higher likelihood of high permeability zones included within the area of investigation. For a single fracture, the aperture determines the permeability, for a network of fractures a high connectivity increases the permeability further (Sánchez-Vila et al., 1996). This trend might further be biased by the use of different techniques capturing the features, but it is difficult to measure permeability with the same instrument at multiple scales (Illman, 2006). Neuman (1988) states that a REV scale might not exist for the permeability of fractured media and hydrogeological properties may vary erratically on all scales that are shown in Figure 2-17.

All statistical methods that are used to infer the properties of discontinuities like cleats and fractures from the observed sample to the overall population are subject to uncertainties. Total uncertainty is defined as the sum of both the stochastic variability and the inherent uncertainty. Stochastic variability represents the variability in characteristics of the medium. The inherent uncertainty arises from methodical errors, i.e. over- or under-representation of cleats due to method (Elmouttie & Poropat, 2011).

2.5.4.2 Spatial interpolation

Traditional stochastic approaches often involve the up-scaling of point hydraulic parameter estimates (Renard & De Marsily, 1997) and the interpolation between sampling points based on geo-statistic methods like Kriging. Here, the interpolated values are modelled by a Gaussian process with a given spatial statistical correlation. Interpolation between measured permeability data is done according to a spatial statistical correlation (De Marsily et al., 2005). Data are typically obtained through slug or pumping tests. Unless there is a sufficient number of sampling data points, the resulting map (e.g. of the permeability) can only treat the medium to be homogenous (Tsang & Neretnieks, 1998; Chen et al., 2000). Although a relatively large number of densely distributed data is required, this geostatistical approach has its advantage that it provides an insight into the uncertainty of the data, e.g. through the mapping of the variance of the measured values in the field, and therefore makes the design for data collection easier. It is simple, computationally inexpensive and is available in many user-friendly codes like Surfer or ArcView (Illman, 2013).

2.5.4.3 Random field simulations

Heterogeneity fields like permeability are commonly realised using random field simulations (Deutsch & Journel, 1998), such as the spectral simulation, the sequential Gaussian conditional simulation and fractal approaches (Kentwell et al., 1999). To represent the heterogeneity of an aquifer, a large number of equally likely realizations of permeability are generated. Based on random function models, all realisations share the same pattern of spatial variability, and are subsequently solved numerically for flow or transport. The output of this approach are probability distributions of the variables of interest, for example permeability (Gómez-Hernández & Wen, 1998). However, it has been pointed out by Journel & Deutsch (1993) that the results of flow simulations, which are performed on multiple random field realisations based on multi-Gaussian distributions are very similar.

2.5.4.4 Inverse modelling

Deterministic or stochastic inverse modelling has been applied to hydrogeological data like hydraulic heads, geophysical data or borehole flow (Paillet et al., 2012; Klepikova et al., 2013). One possibility is hydraulic tomography, which refers to the relatively new method of inverse modelling of data gained in multiple cross-hole pumping or injection tests. Water is sequentially extracted or injected and the corresponding pressure monitored. Others (e.g. Martin & Frind, 1998) calibrate the layers in a stratigraphic or geological model to pumping tests or other data. The corresponding responses are monitored and subsequently analysed with an inverse algorithm (e.g. Yeh & Liu, 2000).

2.5.5 Fracture characteristics across scales

As already shown in chapter 2.4, permeability of a fractured medium is highly dependent on the geometry of the fracture network. Laubach (1997) found that orientations of fractures are scale invariant. This has been confirmed by Ortega & Marrett (2000), who also noted that frequencies of micro-fractures are reproduced by the larger macro-fractures contradicting earlier studies that found micro-fractures to be more abundant than macro-fractures (Laubach & Milliken, 1996). Properties like the size or aperture distribution of fractures have been subject of many studies and are found to be scale invariant. Different mathematical laws have been employed to describe the statistical distributions of fracture properties. While scale-limited laws (log-normal and exponential distributions) have been found to well describe some of the properties of fracture systems, power laws

or fractal geometry are more promising to provide accurate descriptions for fracture systems.

A fractal is a self-similar pattern that displays at every scale. Fractal geometry has first been described by Mandelbrot (1983) and the concept has found wide application to describe natural phenomena. For many objects that show scaling behaviour fractal geometry is well suited as a descriptor. For fractal geometries no homogenization scale or representative elementary volume exist (Bonnet et al., 2001). Fracture networks with fractal correlations have for example been investigated by Darcel et al., 2003)

The functions that are mostly used to fit data sets of fracture properties are shown in Figure 2-19. To distinguish between the distributions, data over more than one order of magnitude are necessary (Bonnet et al., 2001).

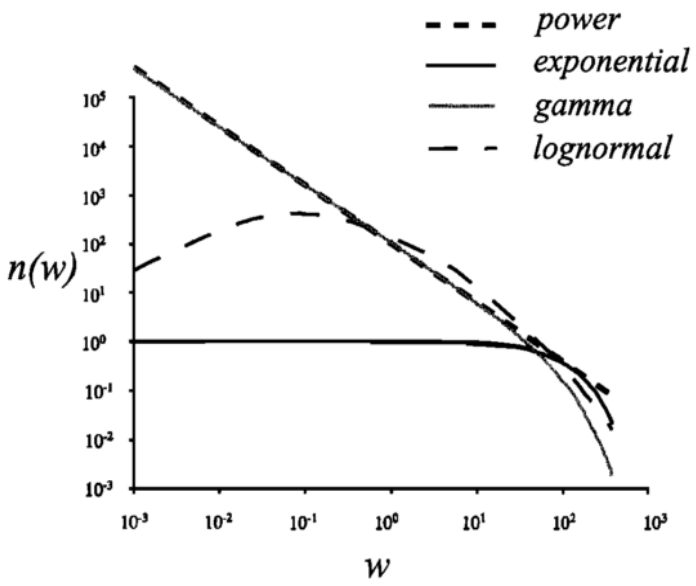

Figure 2-19 The four most commonly used functions to fit fracture shape parameters (Bonnet et al., 2001)

2.5.5.1 Length distribution

Cleat or fracture length is a critical property for network connectivity and therefore strongly influences mechanical properties and flow behaviour in the system (Galindo-Torres et al., 2015). The characteristics of fracture length distribution are required as an input to discrete fracture networks to model physical properties of fractured rocks (Chilès, 2005; Ghaffari et al., 2011). This parameter typically has been found to follow a truncated power law distribution with a tall head and a long tail by Walsh & Watterson (1993). A power law distribution has the general form shown in equation 2-32

$$n(w) = i\, w^{-c} \qquad (2\text{-}32)$$

with n being the number of occurrences in w the fracture property, i being a coefficient of proportionality, and c the power law exponent. For self-similar fracture patterns, the power law exponent reflects a fractal dimension. In most cases, c represents the length distribution coefficient and is independent from the fractal dimension (Bonnet et al., 2001).

Others (e.g. Rouleau & Gale, 1985) have used a lognormal distribution to describe fracture length distributions. Lognormal distributions may appear if a power law distributed data set is incomplete and upper and lower ends are cut off (Einstein & Baecher, 1983). In order for a lognormal distribution to reflect reality a characteristic length scale in the system imposed by a boundary needs to be present (Odling et al., 1999). The lognormal distribution is given by equation 2-33

$$n(w) = \frac{1}{w\sigma\sqrt{2\pi}} exp^{-\left(\frac{\ln w - M_{lm}{}^2}{2\sigma^2}\right)} \qquad (2\text{-}33)$$

with the M_{lm} being the logarithmic mean, and σ the standard deviation of w the fracture property. Furthermore, for non-parallel fractures the total length in the region is an indicator of connectivity (Dershowitz, 1984).

On larger scales the exponential law has been found to be descriptive. The size of discontinuities in continental rocks (Priest & Hudson, 1981; Nur,1982) and near mid-oceanic ridges (Carbotte & Macdonald, 1994) are following exponential distributions. The law contains a characteristic length scale parameter. The length can be limited either by a present physical boundary or by the deformation process being in an early stage when fracture nucleation dominates over fracture elongation (Bonnet, 1997).

2.5.5.2Aperture distribution

Compared to studies on fracture length, there are relatively few studies on the distributions of the aperture. Aperture has been found to follow a gamma law distribution, that is a power law with an exponential tail by Bonnet et al. (2001). Madadi & Sahimi (2003) approximated the distribution of fracture apertures in a rock by log-normal distributions. Power laws have been found to best represent fracture aperture distributions measured by means of scan lines perpendicular to the fractures by Ortega & Marrett (2000). The physical causes of power law scaling and variation in exponent and fractal dimension are open for further research.

2.5.5.3 Spacing

The distribution of cleats is highly variable with intensely fractured bands and less intensely fractured bands. This distribution is captured by the measure of the spacing between the fractures. Characteristic sizes of cleat spacing are between 10 – 25 mm (Wang et al., 2009). Dawson and Esterle (2010) found that for specific vitrain layers, the cleats could be spaced as closely as less than a millimetre apart. Furthermore, the spacing of the cleats tended to be proportional to fracture height for given types of cleats. For example, a vitrain layer that confined smaller cleats, as well as larger master cleats which traversed multiple coal layers have been observed.

2.5.5.4 Size

While fracture size often (e.g. Hooker et al., 2013) refers to length and height, it is defined as the area of the fracture face (length and aperture) for the two-dimensional study in chapter 6. Fracture-size distribution has been found to either being centred onto a specific value with fewer smaller or larger values present (Priest & Hudson, 1976) or are scale-independent for example in power-law size distributions (Ortega et al., 2006).

2.5.6 Up-scaling of structural characteristics and permeability of coal

The complexity of a coal seam constitutes of the inherent cleat structure introduced in chapter 2.2.1 as well as of large-scale fractures that may exist on the field-scale. The permeabilities associated with fault structures and hydraulic fractures that have been induced by well-stimulation are significantly higher than the permeability of joints, cleats, micro-cleats and matrix and dominate the flow behaviour. Modelling the structures and resulting flow behaviours on these different scales and merging the results to receive a complete picture of the fracture characteristics has been subject to several studies.

Scholtes et al. (2011) have done a case study on the scale effects on the strength of coal using a DFN. As long as the DFN density remains constant with a uniform distribution or if discontinuities are absent in the considered medium, the maximum strength of the material remains constant across all scales.

Gong et al. (2014) have used Discrete Fracture Modelling to simulate fluid flow on two scales: the core scale and the reservoir scale. The large-scale fractures have been characterised using seismic and image logs. Small scale cleat structures are represented by a model of perpendicular face and butt cleats. The authors estimated the permeability of the large-scale fractures based on the equivalent plate model. In a dual scale model like this, assumptions have to be made for each scale. While the matrix of coal is often

assumed to be impermeable, permeabilities can be computed for the cleats. For the field-scale simulation, the matrix permeability can then take the values of the cleat system.

Jing et al. (2016) modelled fluid flow in micro-scale coal samples with a maximum side length of 4.1 mm. They found directional permeabilities due to the underlying structure of the cleat network that result in different system scaling effects. Generally, permeabilities are increasing with increasing sample size, with different variation of the increase for different directions. The modelled permeability values range from 100 mD to 300 mD, and are therefore up to two magnitudes larger than the values for coal permeability found in the literature (chapter 2.2.4). This study showed that in direction of the longer face cleats the percolation thresholds are lower and permeabilities constantly increase with increasing domain size. In butt cleat direction, the variation of the permeability gradually decreases. They conclude that scaling has a stronger effect on the modelling results for permeability than on porosity, due to its dependence on a range of parameters, as for example connectivity, percolation threshold, cleat size, aperture and spacing.

The most comprehensive study on coal permeability upscaling has been done by Massarotto et al. (2008). The study on Bowen Basin coal found that core sample matrix permeability, which excludes the effect of cleats, is one to three orders of magnitude less than bulk permeability gained in borehole tests that includes the effects of cleats. Matrix permeability has been measured in the range of 0.001 mD to 0.1 mD (Enever & Hennig, 1997; Gash et al., 1993) and represents the average over a wide range of pore sizes in coal: micro-pores of less than 2 nm; meso-pores of between 2 and 50nm; and macro-pores larger than 50nm, but generally excludes the effects of cleats.

Massarotto et al. (2008) further investigated scale-up factors that might be used to derive average in-situ permeabilities based on lab data. The coal used in the tests was sampled at the Upper Newlands seam, Rangal coal measures. The Permian aged coal with average thicknesses of 2 m to 6 m is extracted in an underground operation at the Newlands coal mine, 60 km North East of the Hail Creek Mine. In true triaxial tests the authors tested cubes of 40 mm, 80 mm and 200 mm side length. The resulting up-scaling factors for the permeability are shown in Table 2-6. The data given for the block C has been derived by measuring the permeability along the face and butt cleats. After cutting the block down into eight blocks of each 40 mm side length an average of the face cleat permeability was determined. In the table, the average of the eight sub-samples of 40 mm is given for the face and butt cleats. All results measured for face cleats (FC) and butt cleats (BC) are shown in Figure 2-20.

Table 2-6 Up-scaling factors for lab-derived permeability of coal samples with different side lengths (Massarotto, Rudolph, et al., 2008)

Block	Permeability [mD]			Up-scaling factor (size to size)		
	40 mm Block	80 mm Block	200 mm Block	40 to 80	40 to 200	80 to 200
A	4.9	19.5		4:1		
B	0.5	0.23	4.8	0.46:1	9.6:1	20.9:1
C avg. Face	1.49	5.3		3.6:1		
C avg. Butt	0.38	2.1		5.5:1		
A,B & C avg.	1.82	6.78	4.8	3.7:1	2.6:1	0.6:1

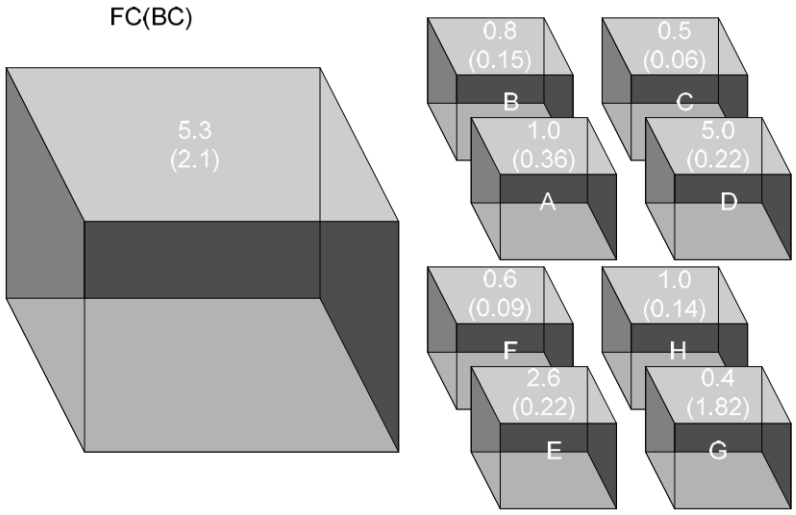

Figure 2-20 Lab-derived permeability of samples and sub-samples for face cleats (FC) and butt cleats (BC) as tested in a true triaxial test cell by (Massarotto, Rudolph, et al., 2008)

Factors have also been derived for up-scaling laboratory measurements of coal permeability to represent field-scale permeability. In Table 2-7 the laboratory k_{mean} refers to the average of the permeability of face and butt cleats. The average permeability given for the field results reflects the fact that field measurements capture an average of the horizontal permeability. Only results for the Bowen Basin are reported here from Massarotto et al. (2008). The average lab-derived value is 4.3 mD, the field data account for an average of 6.6 mD, which leads to an average up-scaling factor of 1:53.

Table 2-7 Up-scaling factors for lab- and field-derived permeability of coal (Massarotto, Rudolph, et al., 2008)

Field	Permeability [mD]			Up-scaling factor
	laboratory		field	
	k_{max}	k_{mean}	k_{mean}	
Dawson River, Bowen Basin	2.3	2.0	2.0	1:1
	2.3	2.0	7.8	3.9:1
Fairview, Bowen Basin	1.8	1.3	10	7:1
Bowen Basin average	6.4	4.3	6.6	1.53:1

2.6 CONCLUSIONS

Due to its high relevance in engineering applications, permeability estimation, and mapping of flow in fractures has been subject to a number of studies, approaching the question from different directions in laboratory and field studies.

The anisotropy and heterogeneous permeability field is influenced by the complex interaction of different parameters such as the geometry of the fractures and the occurrence of large scale flow channels, saturation level, and ambient stresses, as well as the general flow direction. The identification and proper description of the matrix and cleats is, therefore, critical for flow modelling.

The unique structure of coal as well as faults and fractures on the field-scale influence the permeability on different scales (Figure 2-21). A multi-scale approach is necessary to capture these permeabilities. Besides a range of field-scale methods, commonly used laboratory tests to investigate permeability and porosity have been reviewed. Constant head tests in a triaxial cell allow for controlled boundary conditions. Studies using the non-invasive technique of CT-scans have been done on several materials to describe the inner structure. Processes changing the structure have been observed, and the flow in a single fracture has been modelled. However, studies on complex multi-scale fluid flow based on CT-scans have not been found. Furthermore, the actual coal structure is much more complex than the typically used model of perpendicular face and butt cleats idealises.

Besides other methods, the statistical distributions of fracture properties and permeabilities are used for the up-scaling of fractured rock heterogeneity. Based on the importance of permeability in all sorts of engineering practice, further work on up-scaling of coal permeabilities has been recommended by Massarotto et al. (2008). Finding meaningful up-scaling relationships can contribute to a sounder and more cost efficient classification of reservoirs.

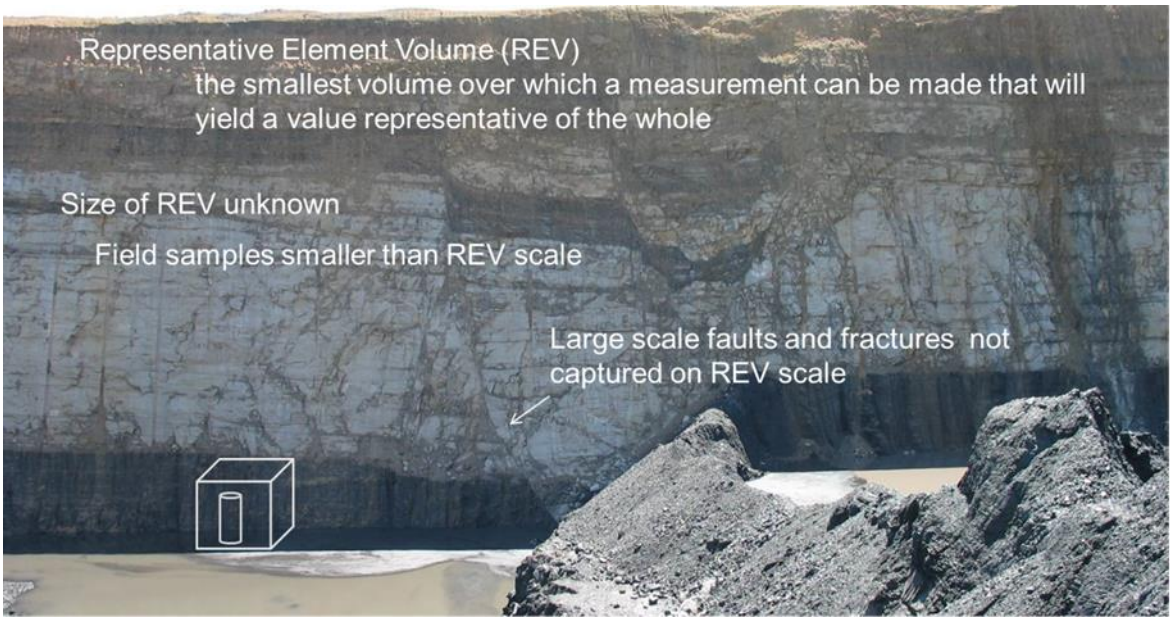

Figure 2-21 Elphinstone seam at the Hail Creek mine and the structures that influence permeability on different scales (photo by Holwell, 2007)

3. Hail Creek Field Site

3.1 INTRODUCTION

The field work and coal sampling has been done at the Hail Creek Mine in Central Queensland. Here, one of the largest coal reservoirs of Australasia is mined, consisting of up to 970 million tonnes of coking coal (Central Queensland University, 2003). The mine has been chosen for field work and sampling, as it can be considered a typical example of the Bowen basin coal geology. Generally, the structural parameters of the coal are comparable to those who have undergone coalification under similar conditions in other parts of the world, which makes the outcome of this study transferrable to other sites. Furthermore, the relatively easy accessibility and the well set up infrastructure at the mine were beneficial to the execution of the field work. In the following, the mine and its geological and hydrogeological set up are introduced.

Hail Creek Mine is located at the East Coast of Australia, 120 km south West of Mackay (21°28'48"S 148°22'41"E) and operated by Rio Tinto Coal Australia (Figure 3-1). Currently, eight million tonnes of coking coal are extracted annually by open cut mining from two seams; the Elphinstone seam, with an average thickness of 6.4 metres and the Hynds seam, averaging 8.3 metres in thickness. An underlying third coal measure with no economic value is the Fort Cooper seam (Clarke, 2007). The seams form part of the Hail Creek syncline (Figure 3-2).

In 2015 coal was extracted from the shallower parts at the north-western flank of the syncline. Underground mining may take place in future in the central part of the syncline. During the years 2012 to 2015, the feasibility of such an underground mine was subject to planning investigations (Clarke, 2007).

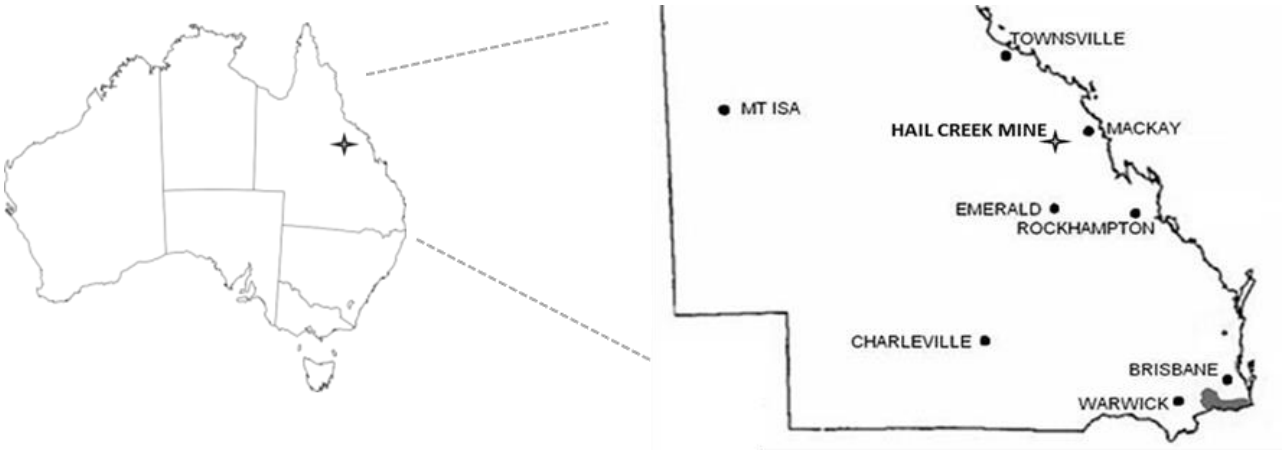

Figure 3-1 Location of Hail Creek Mine in Central Queensland (www.ehp.qld.gov.au)

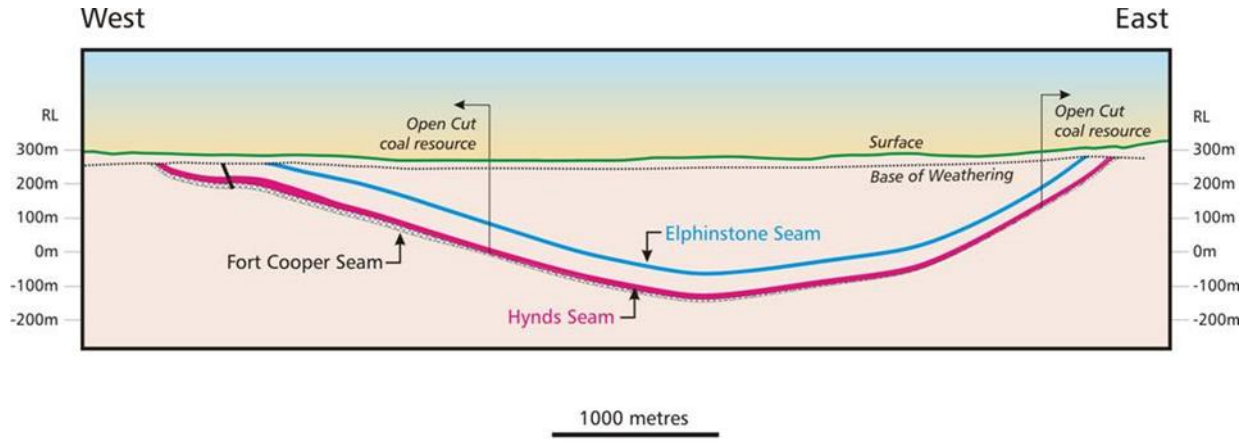

Figure 3-2 Schematic West – East section through the Hail Creek Syncline (Holwell, 2007).

3.2 GEOLOGY

The Hail Creek Syncline is part of the Bowen Basin which extents 600 km in north - south direction and has an east – west extent of 250 km. The distance between the eastern and western limbs of the relatively shallow open syncline fold structure reaches a maximum of about 7 km. The syncline has a length of approximately 32 km and the syncline axis plunges to the south-southeast (Figure 3-3). Strata on the western limb of the syncline dip at approximately 4° to 8°, while the dip on the eastern limb is steeper with an average of 18° (Stadter & Hair, 2014).

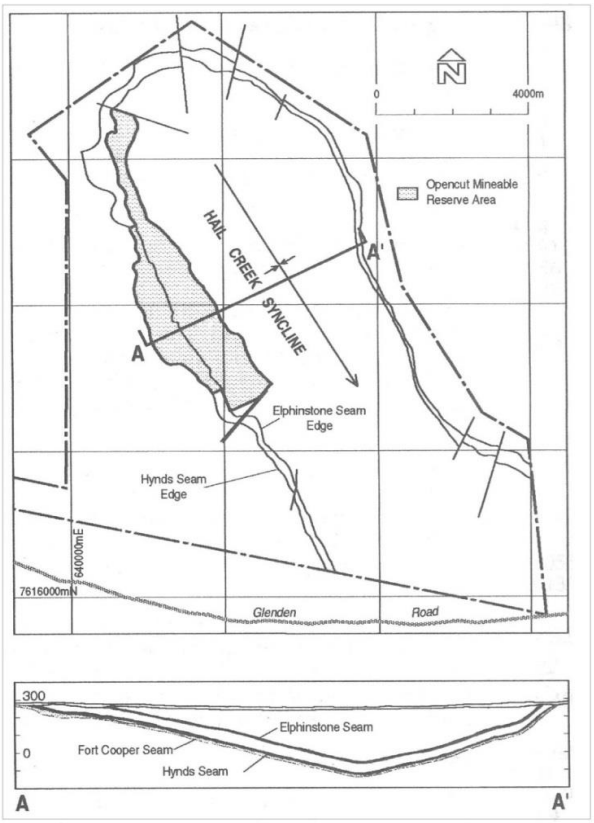

Figure 3-3 Alignment of Hail Creek syncline in relation to the open pit (Rio Tinto, 2010)

3.2.1 Lithostratigraphy

The syncline is built of sedimentary strata of Permian and Triassic age and covered by a relatively thin layer of quaternary alluvials, consisting of clay, sandy clay, and paleo-channel fills of sand and gravel.

The Triassic-Permian sequence comprises from youngest to oldest:

- Rewan Group of Triassic age which is characterised by the absence of coal and consists of lithic sandstone, pebbly lithic sandstone, green to reddish brown mudstone and minor volcanilithic pebble conglomerate
- Rangal Coal Measures comprising the Elphinstone coal seam, with an average thickness of 6.4 metres (m) and the Hynds coal seam, averaging 8.3 m in thickness. Maximum depth of the seams along the syncline axis are approximately 300 m for the Elphinstone seam and 450 m for the Hynds seam. The seams are divided by an interburden of mudstone, silt- and sandstones that increases in thickness from 25 m up to 94 m in a northerly direction (Clarke, 2007). The Rangal Coal Measure are underlain by the
- Fort Cooper Coal Measures which consist of lithic sandstone, conglomerate, mudstone, carbonaceous shale, coal, tuff and tuffaceous mudstone, and the

- Moranbah Coal Measures which include labile sandstone, siltstone, mudstone, coal, and conglomerate (Stadter & Hair, 2014).

3.2.2 Fault structures

Major normal faults are found in the coal resource area east of the Hail Creek syncline. Less significant faulting and low angle thrusting occur in the far north and south-east of the syncline (Golder Associates Pty Ltd, 2013). Although these small scale faults do not cause significant dislocation of strata, they appear to increase the permeability locally resulting in higher groundwater yields (King, 2009). Figure 3-4 and Figure 3-5 provide faults projections for the Elphinstone and Hynds seam based on the latest fault and intrusive model for the Hail Creek Mine (Blacka & MacGregor, 2014). Nominal fault frequency varies between 85 m/fault in the South to 650 m/fault in the North. Faults range in sizes and occur both as normal and thrust faults. In the ongoing mining process, five thrust faults have been intersected as compared to fourteen normal faults. The displacement of thrust faults is typically one metre, but can add to several metres (Clarke, 2007). Normal faults display 1 m to 28 m throw, with an average of 7.5 m. A more complex, but yet unmapped fault geometry and morphology is assumed. Blacka & MacGregor (2014) suggest the presence of multiple fault splays, bifurcations, ramps, sympathetic faults and structural disturbances.

3.2.3 Dykes and Sills

Permeability of the coal seams in the Hail Creek Mine is further influenced by the occurrence of dykes and sills resulting from volcanic intrusion. The area has been subject to two episodes of volcanic intrusion, which formed the Nebo Volcanic Complex. Mt Gotthardt, immediately west of the Hail Creek syncline is formed by a cretaceaous granodiorite. Basaltic plugs, dykes and sills in the area have been formed during tertiary volcanic intrusions and form the limits to the mined coal seams to the north and south of the Hail Creek Mine (Stadter & Hair, 2014). Together with the faults, they are mapped in Figure 3-4 and Figure 3-5.

Dykes in the open-cut area range from less than a metre to several metres thickness. Many of them are basalts. They are typically sub-vertical and penetrate the coal seam, as well as the strata above and below the seam. As a result, zones of heat affected coal of several metres to tens of metres thickness occur. Both, groups of several smaller dykes, as well as single thicker dykes are present, mainly with a NNE-SSW strike. Sills are occurring in the Elphinstone and the Hynds coal seam. Locally, thin lenses are replacing

the coal seams locally. The sills present are non-magnetic, and usually comparably flat dipping. Local heat alteration of the coal due to dykes and sills results in localised pinching and swelling of the coal which results in the local variation of the seam thickness (Blacka & MacGregor, 2014).

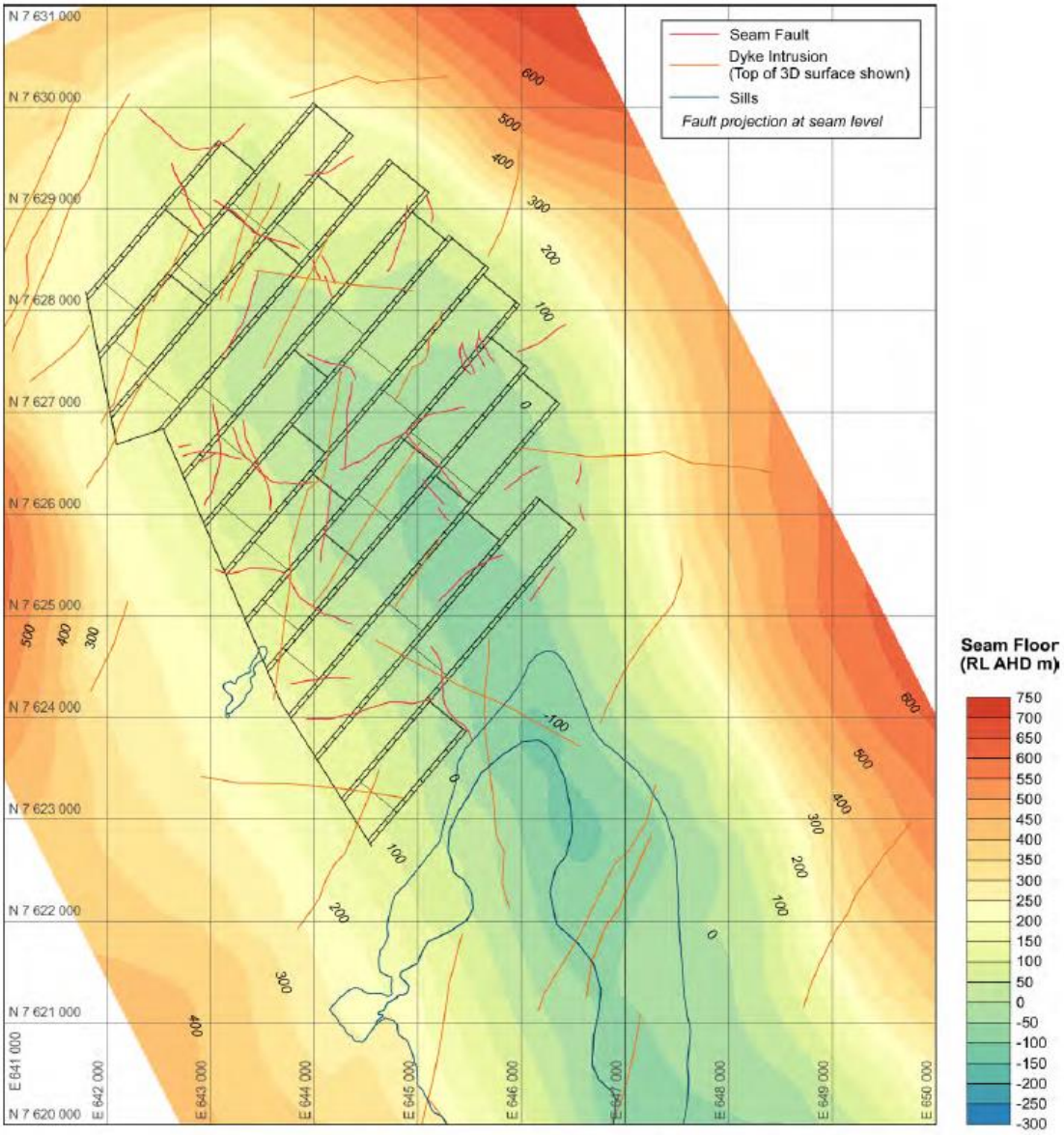

Figure 3-4 Faults, dykes and sills occurring in the Elphinstone seam (Blacka & MacGregor, 2014)

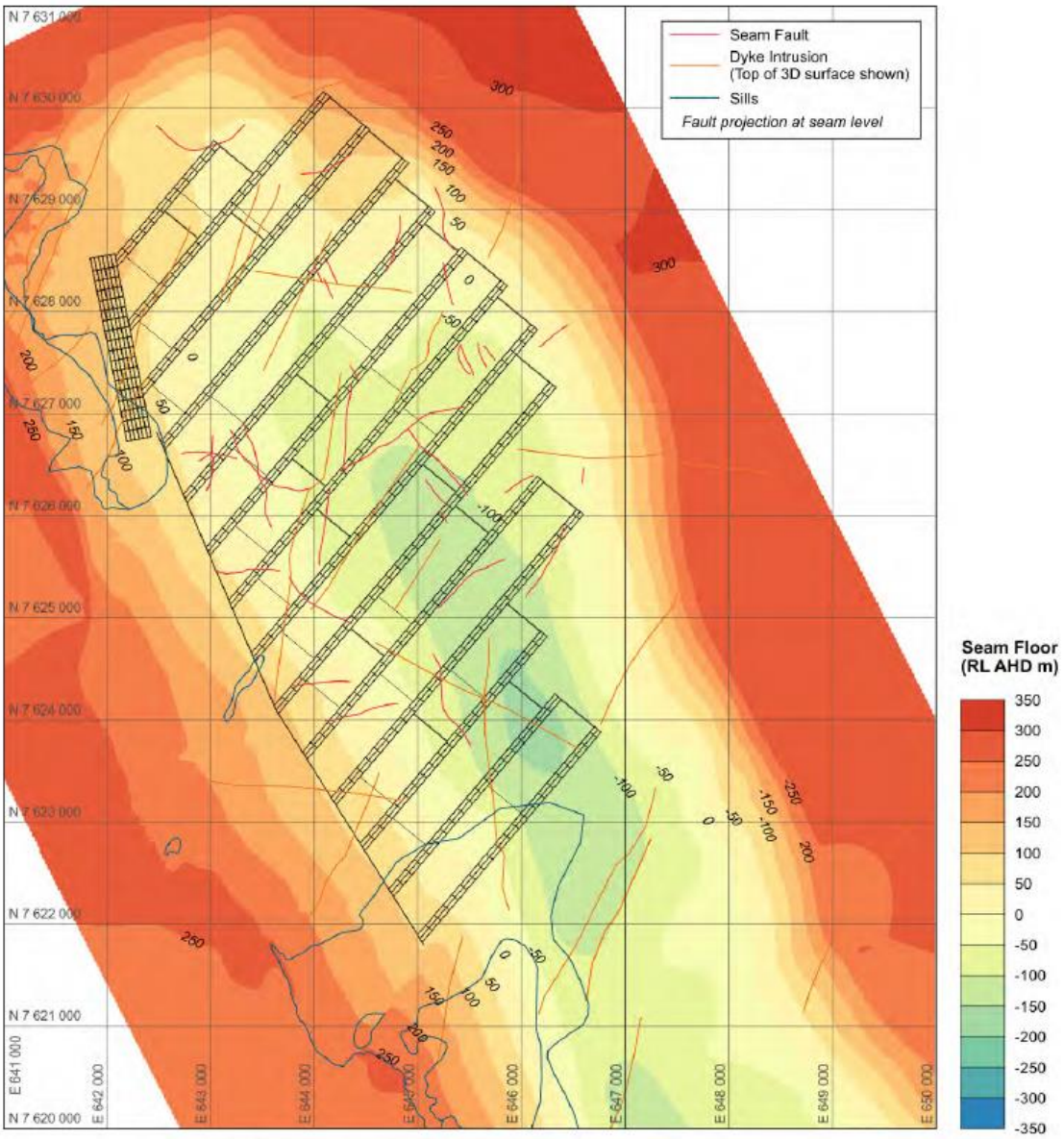

Figure 3-5 Faults, dykes and sills occurring in the Hynds seam (Blacka & MacGregor, 2014)

3.2.4 Coal characterisation

3.2.4.1 Coal quality

The Elphinstone seam is made up of bright-banded coal that is interbedded with thin stone bands towards the bottom of the seam. The Hynds seam is intersected by a band of tuffaceous claystone which separates an upper layer of bright banded coals from dull banded coal in the lower half. The basal section of the Hynds seam is very dull, shaly coal interbedded with thin stone bands.

With the present crucible swell numbers (CSN) larger than five, both seams classify as hard coking coal. The vitrinite contents (vitrinite %) in the Rangal coal measures are with percentages between 45 and 65 lower in comparison to other coalfields in the Bowen

Basin. The vitrinite reflectance (R_0Max) is the parameter used to determine the coals rank. The older Hynds seam is a slightly higher rank coal, with higher vitrinite levels, a more acidic ash chemistry and therefore higher coke strength after reaction (CSR). With its lower rank, the Elphinstone seam has higher fluidity. The maximum fluidity value is expressed in dial divisions per minute (MF [ddpm]). There is a decreasing trend in rank from south to north across the western margin of the syncline for both seams. The Hynds seam has a feed ash content of around 25%, while for the Elphinstone seam it is around 20%. The Hynds seam on average yields 10% less coal than the Elphinstone seam (Holwell, 2007). Information about average seam qualities are summed up in Table 3-1.

Table 3-1 Average seam qualities of Hail Creek coals at 8.5% ash product (Holwell, 2007)

Coal Type	Vitrinite [%]	R_0Max	CSN	MF [ddpm]	CSR
Elphinstone Seam	45-55	1.25	5-7	300-700	50-60
Hynds Seam	55-65	1.35	6-8	200-400	60-70

3.2.4.2 Cleat mineralisation

Cleats in the Rangal coal measures of the Bowen basin have been found to be mineralised during formation as a result from tectonic processes, as for example the large sill intrusions to the north and south of the Hail Creek mine. Face cleats are dominated by authigenic clay minerals, predominantly pure illite with fewer occurrences of ammonium illite, chlorite and kaolinite mixtures. Butt cleats are dominated by carbonates. These are dominated by calcites that are comprised of ferroan calcite, ankerite, and siderite (Faraj, Fielding & Mackinnon, 1996).

3.2.4.3 Cleat directions

Based on acoustic scanning data Blacka & MacGregor (2014) determined main directions of face cleats in the field. Face cleats are striking N-S to NNE-SSW in the northern and central mining area of the Hail Creek operation. Towards the south of the open-cut mine, the cleat directions change towards NE to NW. Fewer data are available for butt cleats. They generally follow the common model with a strike direction that is orthogonal to the face cleats as introduced in chapter 2.2.2, however, with a deviation of cleat angles.

A strike direction rosette for the cleats in Elphinstone seam, taken from the report of Blacka & MacGregor (2014), is shown in Figure 3-6a. The preferential strike is in the range of 340˚ - 010˚ relative to north and is assumed to represent face cleats. A secondary strike in the range 040˚ - 070˚ relative to north represents the butt cleats.

The Hynds seam shows a larger overall variability in cleat directions (Figure 3-6b). Furthermore, the butt cleats are better developed as compared to the Elphinstone seam. The rose plot reveals a spread of cleat occurrences ranging from 330˚ - 070˚ with a preferred strike in the range 040˚ TN - 070˚TN.

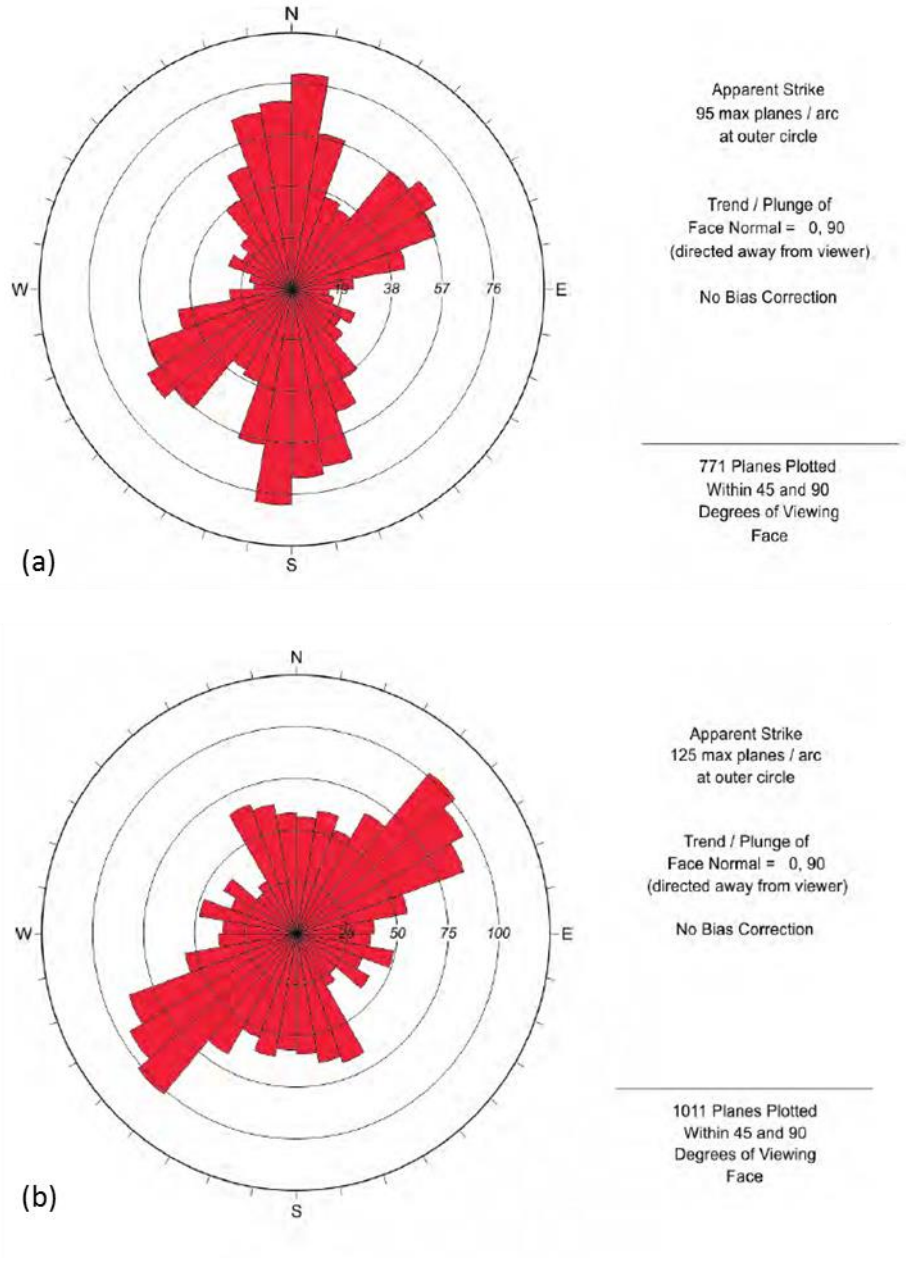

Figure 3-6 Rose plot of cleat directions occurring in a. the Elphinstone seam and b. the Hynds seam (Blacka & MacGregor, 2014)

3.3 HYDROGEOLOGY

3.3.1 Groundwater occurrence

Following the syncline and influenced by the drainage due to the pit operation, the main flow direction of shallow groundwater and surface water is southeast (Golder Associates Pty Ltd, 2013)**.** Figure 3-7 shows the groundwater levels above Australian Height Datum and indicated flow directions measured in coal exploration boreholes in 1980 and 2009. In comparison, the latter data show a draw-down of the groundwater table of approximately 5 m to 15 m in proximity to the open-cut operations (King & Hair, 2009).

The Rangal Coal Measures behave hydraulically like a fractured aquifer system with the Elphinstone and Hynds seams being the main aquifer units (Stadter & Hair, 2014).

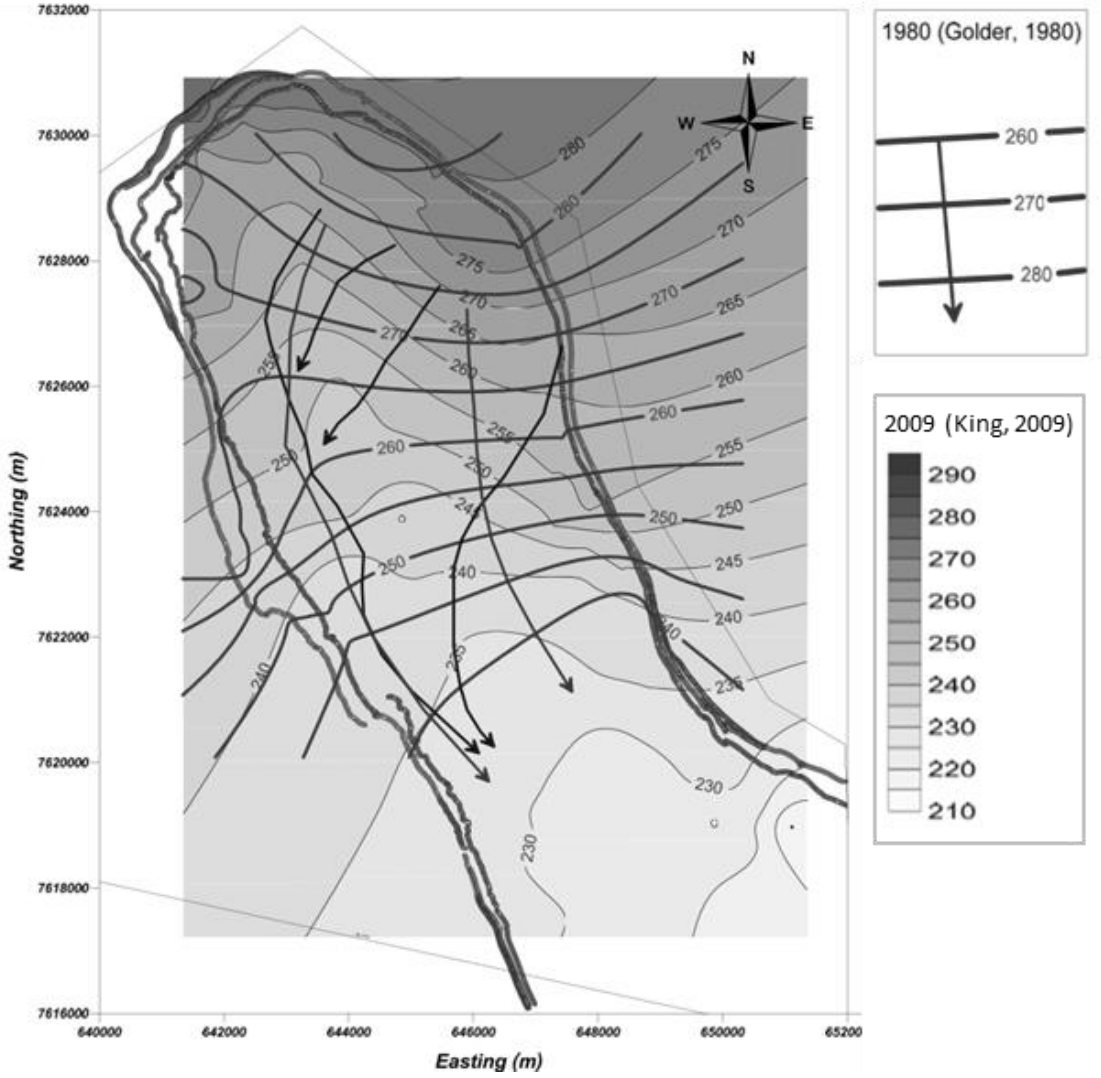

Figure 3-7 Groundwater levels in m above sea level and indicated flow directions (taken from King, 2009, based on data from Golder, 1980)

3.3.2 Permeability data determined in earlier studies

A summary of former hydrogeological investigations implemented in the area has been completed by Stadter & Hair (2014) and includes data which span four decades (i.e. Golder Associates Pty Ltd, 2013). These data include results from pumping tests, falling head tests, constant-head tests, heat pulse vertical flow meter tests, falling head packer tests, and constant rate injection packer tests that are dating back until 1973. The spatial distribution of borehole data is irregular, with few data points in the syncline centre, where the seams are deepest, and comparably many data in the west margin of the syncline where open cut mining is taking place. The results are depicted in Figure 3-8.

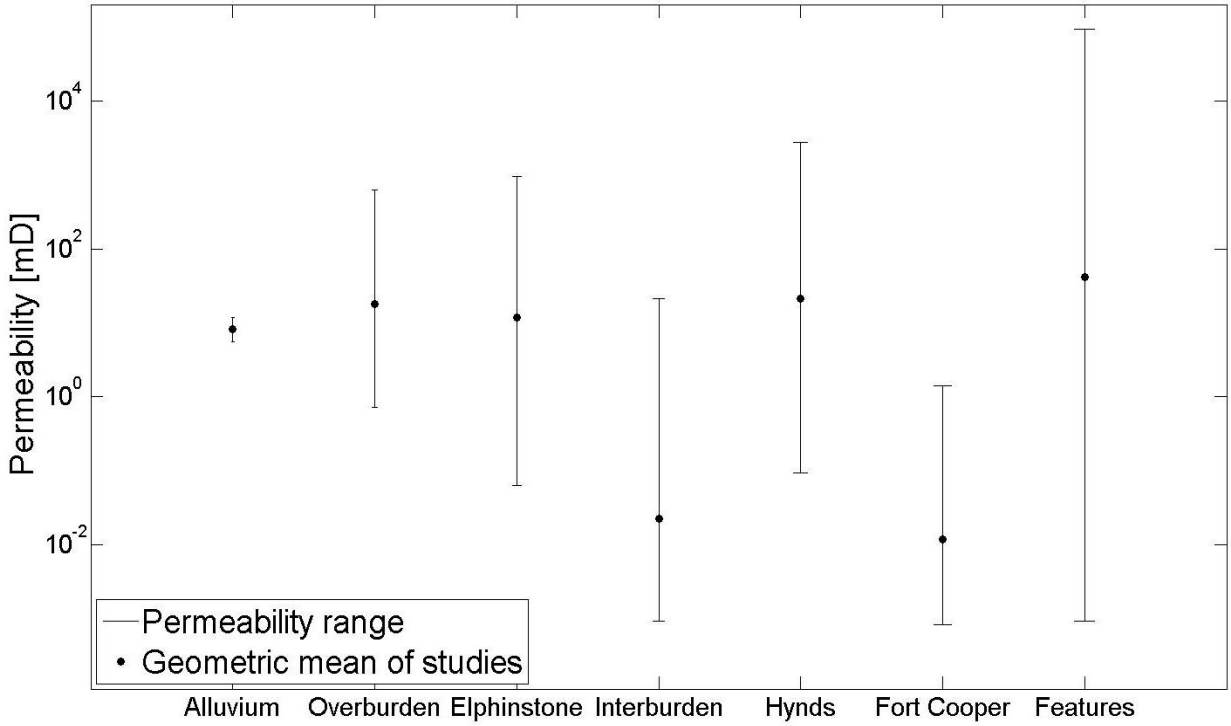

Figure 3-8 Ranges of permeability for geological units at Hail Creek Mine (based on Stadter & Hair, 2014)

Permeabilities of the rock mass generally decrease with depth from 18 mD in the overburden to a minimum of 0.01 mD in the Fort Cooper Seam. Areas of increased permeability occur locally in jointed and faulted sandstone with hydraulic conductivities of up to 95079 mD mainly following the northwest to southeast orientated axis (Stadter & Hair, 2014). The permeability anisotropy of both, Elphinstone and Hynds seam is found to be larger than 10:1. The maximum permeability is found in the NE-SW orientation, that is, perpendicular to the syncline axis. Minimum permeability is found along the axis of the syncline in the NW-SE orientation (Stadter & Hair, 2014). Results for the two coal seams subject to this study are listed in Table 3-2. The measured permeabilities span a range from 10^{-8} to 10^{3} mD.

Table 3-2 Permeabilities of Elphinstone and Hynds seam obtained in earlier studies (Stadter & Hair, 2014)

Test method	Elphinstone k from [mD]	k to [mD]	Hynds k from [mD]	k to [mD]
In-situ test	0.063	95079.204	0.0920	2777.595
Interference test	0.092	91.874	0.0920	73.713
Packer test	8.867		0.0001	
Heat Pulse Flowmeter	1.709	3.846		

The measured permeabilities span a huge range from 10^{-8} to 10^{3} mD. While there is a range of resulting values across the different methods, there is also a big variability within each method. For example, the data given for the in-situ testing range from 0.063 mD to 95079.204 mD. It is surprising that a single permeability method allows to measure permeability in the field over almost seven orders of magnitude and can still provide data with three numbers after the digit. Therefore, it has to be concluded that the accuracy of these results from several campaigns over four decades is questionable.

3.4 CONCLUSION

The Hail Creek field site has been well investigated by numerous studies in the past. This chapter summarised the main information collected at the site. The studies provide important data to compare the results of the presented thesis.

Permeability measurements at Hail Creek Mine have been undergone using a range of different methods. The documented results range from 0.063 mD to 95079.2 mD for the Elphinstone seam, and even wider for the Hynds seam with permeabilities from 0.0001 to 2777.6 mD. The large range of values measured suggests a large spatial variability that is connected to the structure of the coal seams. Large scale coal fractures provide preferential pathways and can increase the measured permeabilities locally.

However, the wide-ranging results might also indicate that the methods used to derive these permeabilities could have an influence on the result. With different techniques used to derive permeabilities, such as interference tests, packer tests and Heat Pulse Flowmeter measurements, an experimental bias cannot be ruled out. Furthermore, interpretation errors might have occurred due to the possibly subjective judgement on how to interpret the field data by the different personnel that have undergone the investigations over four decades.

4. Field testing and sampling

4.1 INTRODUCTION

In July 2013, and October/ November 2013 field campaigns have been carried out at the Hail Creek Mine site. The measurements have been performed by the author of this thesis. A Heat Pulse Flow Meter was used at the Hail Creek Mine extension site with the aim to get an overview of the groundwater flow system. The method has been chosen over other geophysical measuring instruments, because it is relatively easy to use in the field and can be used in boreholes of varying diameters. The probe can be positioned with high precision at any depth of interest and provide local estimates of permeability. For the data analysis, powerful solvers are available. The high sensitivity of thermistors allows the capture of low flowrates with a high measuring accuracy (Busse et al., 2016). To assess the hydraulic subsurface characteristics the logging campaign covered a wide area of the adjacent extension site.

The instrument, the logging technique and data analysis are introduced in the following (chapter 4.2). In chapter 4.2.5 the measured permeabilities are presented. The sampling of coal cores done during the campaigns is documented in chapter 4.3.

4.2 HEAT PULSE FLOW METER FIELD TESTING

4.2.1 Flow logging principle

Flow meter measurements have been widely used to quantify flow along borehole profiles and to draw conclusions about the underlying hydraulic characteristics of aquifers. A review of flow meter techniques is given by Monier-Williams (2009). A range of downhole flow meters has been developed based on different principles. These are for instance impeller flow meter, heat pulse flow meter and electromagnetic flow meter (Molz et al., 1994).

Heat pulse flow meter data deliver information on the fluid flow along the borehole and allows further quantification of in- and outflows, as well as transmissivities of the rock formations and geological structures intersected by the borehole. Using this instrument, the vertical borehole flow is measured by collecting in- or outflow related data along the undisturbed borehole profile intersected by high permeable zones. Heat pulse flow

measurements have been used for estimating fracture transmissivity since the mid-eighties (Hess, 1986; Paillet et al., 1987).

The measurements for this study have been carried out using the heat pulse flow meter HFP 2293 (Mount Sopris Instruments Co, Inc), a wireline-tool that captures flow rates as small as 0.113 l/min. The working principle is based on a heat grid that raises the temperature of the borehole fluid in the vicinity of the grid creating a temperature spike which moves upwards or downwards along the borehole profile (Figure 4-1). A diverter, which is a disk-shaped rubber element to seal the fluid flow against the borehole walls, is used to direct the flow past the heat grid. The change of the temperature signal is detected by thermistor sensors that are situated above and below this grid. The time, Δt, which the temperature peak takes to travel the distance, ΔL, from the grid to one of the thermistors is measured and converted into a flow rate, q, using a calibration factor, c by equation 4-1.

$$q = c\frac{\Delta L}{\Delta t} \qquad (4\text{-}1)$$

The calibration Is further explained in chapter 4.2.3. To estimate transmissivity and far field hydraulic head, flow rates are recorded down hole at two different water levels in a borehole. Usually, measurements are taken under ambient and stressed conditions, but two different stressed conditions can be used as well.

The measuring of the rate of vertical flow allows

- The identification of flow zones provided by faults, fractures, coal fractures and cleats,
- An estimation of relative hydraulic gradients, an analytical solution of transmissivity and hydraulic head for the flow zones (Davis and De Wiest, 1966),
- The identification and distinction of individual geologic units or fractures in the borehole,
- An identification of potential flow conduits, and
- Subsequent numerical modelling and hydrogeological mapping.

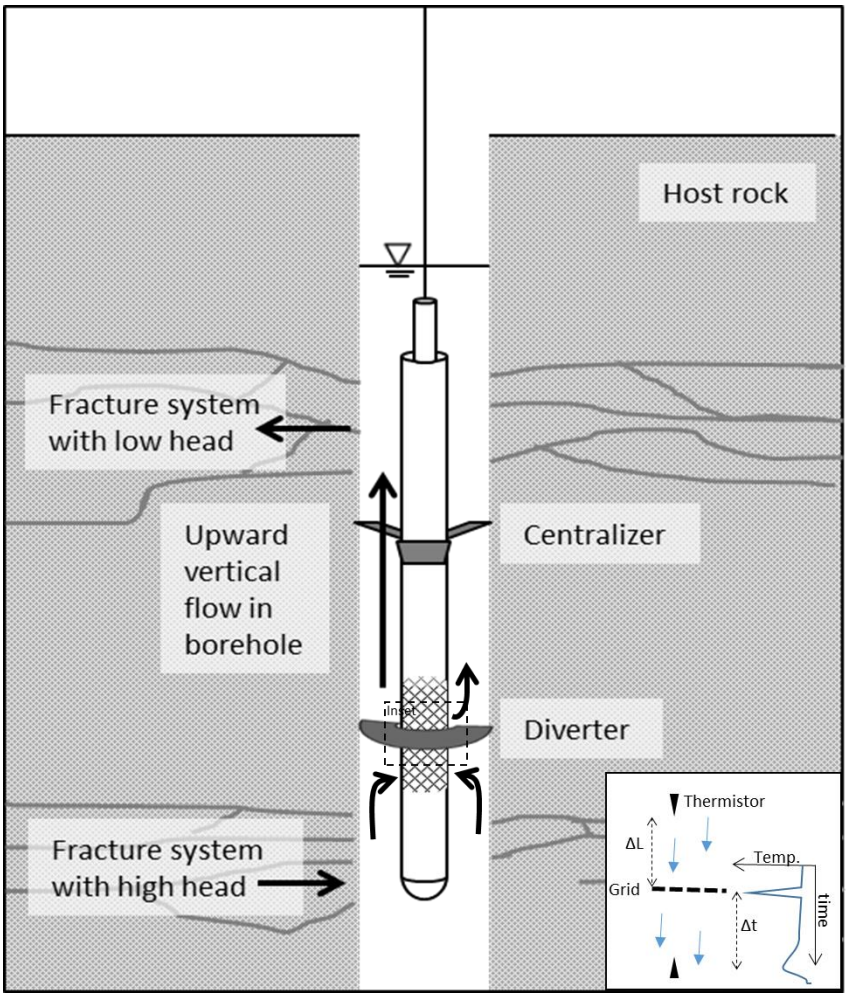

Figure 4-1 Working principle of heat pulse flow meter

Plots of the results give an insight into the flow conditions along the borehole. Negative values represent downward flow. Positive values account for upward flow. Where the vertical flow changes abruptly, discrete in- or outflow zones are concluded. A mass balance over all in- and outflow is carried out. Depending on its part on the total flow, a percentage of transmissivity for each in- or outflow zone can be estimated.

The flow in a borehole is driven by two parameters: transmissivity of the conductive zone (rock or fracture) and head difference between the borehole and the far field head in the conductive zone. Using an inverse modelling approach, transmissivities and far field heads for each conductive zone are calculated (Paillet, 1998). To solve the borehole flow equation for a certain transmissivity, borehole vertical flow values for two different head values are needed. These are obtained by field testing under ambient and stressed conditions. In an iterative process the total transmissivity of the rock profile intersected by the borehole and the head for each fracture that fits the given values are approached.

4.2.2 Field set-up

The set-up of the borehole flow meter equipment is pictured in Figure 4-2. A thorough Job Hazard Assessment has been conducted in accordance with the health and safety standards at Hail Creek Mine before the start of the campaign. The system was run from the tray of a truck, which required the use of a taller tripod. It was operated by one person standing next to the vehicle monitoring the output data on a laptop and operating the winch to position the probe downhole (Figure 4-2).

Figure 4-2 Set up of instruments at the site

The probe was lowered into a borehole and stationed at each point of interest. Measurements were repeated three times at a point. After the flow along the profile has been measured under ambient conditions, the measurement was repeated with water from a water tank fed to the bore at constant rate (Figure 4-3). The initial idea of gravity feeding the water into the borehole was given up in favor of a simple pumping system to keep the flow rates stable over time. A manual flow meter was added to the set up between tank and borehole to monitor injection rates.

Figure 4-3 Injection test

At the Hail Creek mine field site the boreholes are cased to a depth between 24 m and 49 m below which the borehole is open. Depending on the depth of the coal seams the total borehole depths vary from 141 m to 396 m.

4.2.3 Calibration

As discussed in a separately published review on the field campaigns that focuses on the usability of the tool (Busse et al., 2016), both a laboratory and a field calibration are needed. The heat pulse flow meter was calibrated by the manufacturer Mt. Sopris off-site and based on several data points where the slightly nonlinear relation between inverse pulse travel time and flow rate through the probe measurement section can be captured. The tool specific calibration factor c (equation 4-1) is incorporated into the instruments internal flow rate calculation.

During the field testing, further calibration was done. A diverter with a size fitting the respective borehole diameter was used, however, it is assumed that even when the diverter is used, a certain quantity of flow bypasses along the borehole walls. To calibrate under field conditions, water was fed into a borehole at known constant rates and the flow rate measured with a manual flow meter. These measurements were compared with the flow rates measured by the heat pulse flow meter. The results were plotted and a regression line fitted to the points in the graph. The slope of the regression line is the calibration factor which was applied to the data records. The use of a bypass factor to

account for differences between the flow measured by the heat pulse flow meter and the known pumping rate at the top of the profile has been suggested by Paillet (2004).

4.2.4 Data analysis

In the following, the data analysis is described using the representative borehole 10087D that has been logged at the Hail Creek mine site.

4.2.4.1 Flow profile and delineation of zones

Based on the data collected at the site, flow rates were determined in the form of a flow profile for each borehole. A plot of the flow data is generated and used to detect in- and outflow zones along the borehole profile.

The delineation of individual zones is based on the vertical flow rate that has been detected with the flow meter. Any sudden changes in the vertical flow rate of the borehole fluid or changes of flow direction indicate an inflow or outflow from the borehole into the surrounding formation. To verify these hydraulically active zones, logs generated based on other geophysical methods that indicate possible inflow locations, e.g. caliper log, were used. This way, the thickness of each individual zone can be defined with accuracy close to the centimetre. Figure 4-4 shows the flow profile of borehole 10087D.

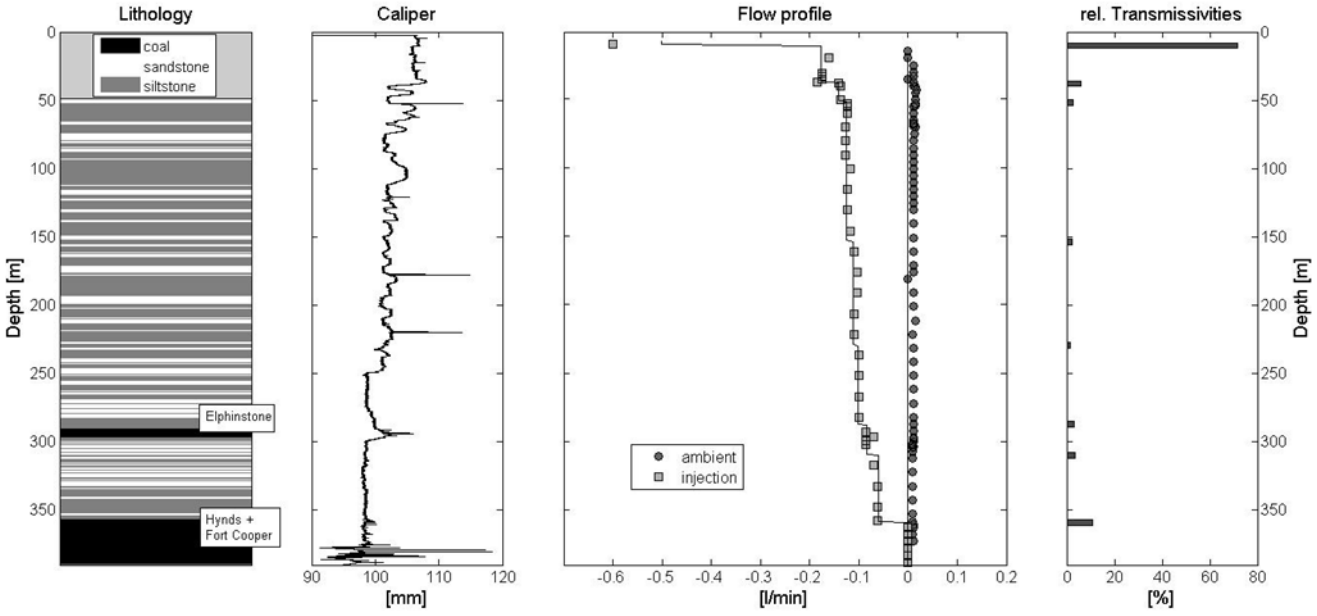

Figure 4-4 Flow profile 10087D

The flow profile reveals issues of data scatter. The individual data points all come with data scatter, that is, measurement error. The critical interpretation issue is to decide which differences between adjacent points are real shifts in flow, and which are just measurement errors. This results in the important conclusion that the flow meter has a

dynamic-range problem. That is, it is hard to see the small inflow/outflow zones in the presence of larger zones because the smaller steps in the profile get lost within the scatter. Therefore, the dynamic range is set at a little less than two orders of magnitude below the highest transmissivity zone. This fact has been demonstrated by Paillet (2004).

4.2.4.2 Mass balance

Based on the principle of mass balance, the average borehole flow rate is calculated for each zone that is delimited by the fractures. The difference of the vertical flow between the zones indicates the amount of in- or outflow to or from the section of the borehole. An overall in- and outflow mass balance is calculated to verify the data. Depending on its part on the total flow, a percentage of transmissivity for each fracture can then be estimated. An example of the mass balance is given in Table 4-1. This approach to flow data analysis has first been published by Molz et al. (1989).

Table 4-1 Mass balance for borehole flow in borehole 10087D

Zone no.	From	To	Ambient			Injection			Diff. Ambient-Injection	% Trans-missivity
			above	below	flow	Above	below	flow		
8	10.00	10.00	0.00	0.00	0.00	-0.60	-0.17	-0.43	0.430	71.7
7	37.28	38.28	0.00	0.00	0.00	-0.17	-0.14	-0.04	0.035	5.9
6	50.38	53.40	0.00	0.00	0.00	-0.14	-0.12	-0.02	0.015	2.5
5	146.10	161.22	0.00	0.00	0.00	-0.12	-0.11	-0.01	0.013	2.2
4	221.67	236.78	0.00	0.00	0.00	-0.11	-0.10	-0.01	0.008	1.3
3	282.13	292.21	0.00	0.00	0.00	-0.10	-0.08	-0.02	0.018	3.0
2	302.28	317.40	0.00	0.00	0.00	-0.08	-0.06	-0.02	0.022	3.6
1	357.70	359.70	0.00	0.00	0.00	-0.06	0.00	-0.06	0.064	10.6
Σ					0.00			-0.17	0.60	100.8

4.2.4.3 Modelling using FWRAP

Transmissivities are subsequently modelled with the program FWRAP written by Paillet (1998). The general model approach is the identification of zone transmissivity with the difference between inflows under two different flow conditions. The FWRAP method uses a transient solution that reaches the outer boundary after a specified number of time steps. That is, FWRAP can be applied to fully non-steady conditions and is designed to follow the evolution of flow to the steady state. Paillet uses non-dimensional scaling to define an optimum time step. This is done internally to provide the best compromise between reducing finite difference errors (small time step) and approach to infinite time (large time step). Thus FWRAP does not require a radius of investigation estimate. The radius is effectively built in by the specified number of time steps. Furthermore, the radius is scaled to be larger for larger values of diffusivity (ratio of T to S) for each fracture. The code

identifies an optimum non-dimensional time step based on borehole diameter, transmissivity and storage coefficient for the computation involving a specified number of steps - usually 1000. The optimum non-dimensional step was verified by comparison with results from straddle packer tests performed at the U.S. Geological Survey Mirror Lake fractured rock study site where crystalline rock is present, as well as other locations with karst and sandstone geologies. The dimensional radius of influence increases in rough proportion to the transmissivity and thus to the size of a particular fracture.

The concept of the original code is that each fracture flow node is treated as an ideal aquifer responding to a slug test. Every flow node simply responds to the difference between the water level in the borehole and the water level feeding the fracture at its outer edge. This approach works for as many nodes as the user wants to specify, and it is fully non-steady. A challenge with this method is the numerical bookkeeping. The computation has to remember every one of the slug responses at every previous time step as they all affect the water level in the fracture where it meets the borehole. This approach is based on the slug-test solution presented by Cooper et al. (1967).

Figure 4-5 shows a fully penetrating well in a confined aquifer with the parameters needed for the solution for the radial flow towards the borehole. The solution for the radial flow (Q) of groundwater into a borehole is derived under the following assumptions (Batu, 1998):

- The aquifer is horizontal and of constant thickness.
- The aquifer is homogeneous and isotropic, and its boundaries go to infinity.
- The piezometric head surface is horizontal before pumping (or injection).
- Flow in the aquifer follows Darcy's law.
- As the piezometric head declines, water is instantaneously removed from storage.
- Well is pumped at a constant rate.
- Flow is symmetric around the axis of the well.

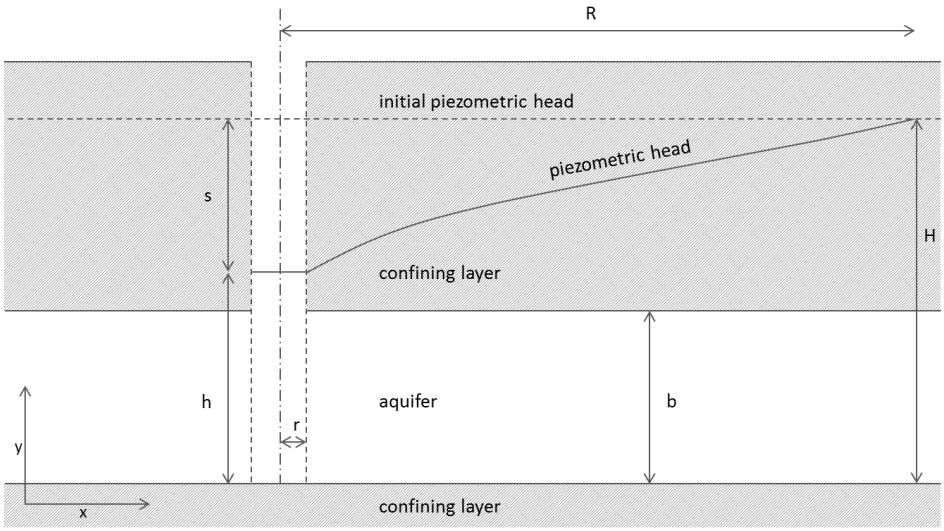

Figure 4-5 Fully penetrating well in a confined aquifer

To calculate the whole surface area providing water to the well, the cross-sectional area, A, in Darcy's law (equation 2-1) is replaced by equation 4-2

$$A = 2\pi bx \qquad (4\text{-}2)$$

where b is the height of the aquifer [m], and x the radius of the cone of depression [m]. The hydraulic gradient, i, is given with the slope of the piezometric head surface, y [m] in equation 4-3

$$i = \frac{dy}{dx} \qquad (4\text{-}3)$$

Following Darcys law, the rate of flow, Q [m^3/s] is calculated as shown in equation 4-4, which can be solved for the piezometric head difference dy as given in equation 4-5.

$$Q = 2\pi kbx \, \frac{dy}{dx} \qquad (4\text{-}4)$$

$$dy = \frac{Q}{2\pi kb} \, \frac{1}{x} \, dx \qquad (4\text{-}5)$$

Integration of the equation 4-5 leads to equation 4-6.

$$y = \frac{Q}{2\pi kb} \, lnx \pm C \qquad (4\text{-}6)$$

The boundary conditions for the confined aquifer as shown in Figure 4-5 are

y = H (piezometric head at outer edge of producing zone), x = R (outer boundary)

y = h (piezometric head in well), x = r (radius of borehole)

The equation for the aquifer surface of the cone of depression therefore is represented by equation 4-7

$$H - h = \frac{Q}{2\pi kb}(lnR - lnr) \quad (4\text{-}7)$$

Hence the discharge, Q, into a confined aquifer from a fully penetrating well is shown as equation 4-8

$$Q = \frac{2\pi kb(H - h)}{lnR - lnr} \quad (4\text{-}8)$$

which can be written as equation 4-9.

$$Q = 2\pi T\ (H - h) \ln\left(\frac{R}{r}\right) \quad (4\text{-}9)$$

Based on this equation, Paillet (1998) demonstrated that drawdown depends on both the transmissivity, T and head difference, H - h.

The term ln(R/r) can be treated as constants. The measured inflow is proportional to the product of transmissivity and the head difference; it depends not only on the transmissivity of the formation but also on pressure gradients. Since each fracture might be fed by a different, far field aquifer, these far field hydraulic head values need to be obtained to calculate the transmissivity. That is why two subsequent sets of data need to be collected under two different hydraulic conditions: ambient and stressed conditions. The latter can be achieved either through injection or pumping.

The difference between the two flows Q^a (ambient) and Q^s (stressed) is directly proportional to the fracture transmissivity (Molz et al., 1994) as shown in equation 4-10.

$$Q^s - Q^a = 2\pi T\ (h^a - h^s)\ ln\left(\frac{R}{r}\right) \quad (4\text{-}10)$$

Knowing the water levels in the borehole h^a and h^s under both conditions, this equation can be solved for T and a quantitative estimation of the transmissivity is obtained.

The mathematical derivation shows that two different quasi-steady flow profiles and the associated borehole water levels are sufficient to eliminate the dependence of the piezometric head H on the outer edge of the producing zone.

The water level in an open borehole that is connecting n different inflow/outflow zones with a certain transmissivity T can be assumed as the average of the n individual hydraulic

heads weighted by their transmissivity. Given steady conditions, the sum of all inflow and outflow equals to zero and can be expressed as equation 4-11.

$$\sum Q^a = \sum 2\pi T\,(H - h^a)\,ln\left(\frac{R}{r}\right) = 0 \qquad (4\text{-}11)$$

Treating π and ln(R/r) as constants, this can be rearranged to equation 4-12.

$$\sum TH = h^a \sum T \qquad (4\text{-}12)$$

The flow in a borehole is driven by two parameters: transmissivity of the rock and head difference between the borehole and the far field aquifer, which feeds the fracture. Both parameters are variables of the underlying formula. The transmissivity value does not change, but to solve the equation, two different values for the head are obtained during the field work through ambient and injection testing. As transmissivities are quantitatively known from the former mass balance analysis, as well as h^a, the far field head H given with respect to the open borehole water level for each producing zone can be calculated using a trial and error approach.

The FWRAP software is designed to calculate the transmissivity and head of each fracture in exactly this approach. Input parameters are the number of fractures in the borehole, the diameter of the borehole, the total well depth, the water level under the ambient condition, the ambient flow and injection/pumping flow above each fracture, the water head change in the borehole between the ambient condition test and the injection test, and a factor of the percentage of the total transmissivity for each fracture.

In an iterative process, the total transmissivity in the borehole and the head for each fracture that fit the given values are approached. The program calculates the water flow and head in each zone, the transmissivity for each fracture, as well as the mean square difference between the measured and modelled values. The iteration continues until the error is small enough to be accepted by the user. This model method solves simultaneously for both permeability and hydraulic head. Permeability is a very local property in a fracture flow system, whereas the hydraulic head says something about where the fracture flow path is ultimately connected. The latter attribute may be ultimately more meaningful than a small sample of local permeability values. And, in particular, provides information at the large kilometre size scale while making measurements at what is the meso-scale of just the borehole radius of influence.

4.2.4.4 Results for example borehole 10087D

At borehole 10087D, the ambient groundwater level was at 13.54 m below surface, under injection of 0.6 l/min depth to groundwater decreased to 0.215 m. Eight in- and outflow zones along the logged profile have been detected, including a breakage in the casing at around 10 m below surface.

The transmissivities decrease with depth, with a maximum of 0.0387 m^2/day to a minimum value of 0.0057 m^2/day. The total transmissivity for the borehole 10087D is 0.054 m^2/day. Under ambient condition, no flow has been detected. The far field heads are calculated with 13.54 m.

As introduced in equation 2-4 hydraulic conductivity K [m/day] is deduced from transmissivity T [m^2/day] measurements and the thickness estimate z of each zone [m]. The permeability k is then derived from the hydraulic conductivity as introduced in equation 2-3. The permeability values measured in borehole 10087D are ranging from 0.08 mD to 82.69 mD and are presented with the measured data in Table 4-2.

Table 4-2 Transmissivities of zones captured at borehole 10087D

Zone no.	Depth [m]		Thick-ness [m]	Part of T_{total}	Transmissivity T [m^2/day]	Hydraulic Conductivity K [m/day]	Permeability K [mD]	Head [m]
	from	to						
8	10.00	10.50	0.5	71.7	0.0387	0.077	82.69	13.54
7	37.28	38.28	1	5.9	0.0032	0.003	3.42	13.54
6	50.38	53.40	3.02	2.5	0.0014	0.003	0.50	13.54
5	146.10	161.22	15.12	2.2	0.0012	$7.9*10^{-5}$	0.08	13.54
4	221.67	236.78	15.11	1.3	0.0007	$4.63*10^{-05}$	0.05	13.54
3	282.13	292.21	10.08	3.0	0.0016	$1.59*10^{-04}$	0.17	13.54
2	302.28	317.40	15.12	3.6	0.0019	0.003	0.13	13.54
1	357.70	359.70	2	10.6	0.0057	$2.85*10^{-03}$	3.04	13.54

4.2.5 Permeability data obtained in the field

Altogether ten boreholes were logged. Their locations are shown in Figure 4-6. An overview of the Heat Pulse Flow Meter tests is shown in the following Table 4-3. Based on the relations introduced in the literature review (chapter 2.1), the hydraulic conductivity K for each zone in [m/day] is calculated based on the transmissivity T [m/day] over the height h [m] of the inflow/outflow zone (equation 2-4).

The permeability k [μm^2] is based on the hydraulic conductivity K [m/day], the gravitational acceleration g [m/s^2], the fluid density ρ [kg/m^3] and dynamic viscosity η [kg/ms] of water at 25°C (0.000891 kg/ms) (equation 2-3). The intrinsic permeability k is expressed in milliDarcy [mD].

Figure 4-6 Location of logged boreholes at Hail Creek extension site (Google Maps, 2014)

Table 4-3 Transmissivities T and intrinsic permeabilities K for each geological unit

Bore ID	Depth Tested [m] below ground		Zone Thickness [m]	Transmissivity [m^2/d]	Intrinsic Permeability [mD]
	Top	Bottom			
10075D	8.58	9.07	0.49	0.43	937.49
	48.89	49.39	0.50	0.52	1111.04
	50.40	53.42	3.02	0.20	70.75
10079P	79.63	82.86	3.23	0.19	62.84
	107.86	109.87	2.01	0.19	100.98
	139.10	141.62	2.52	0.1	42.39
	211.18	211.69	0.51	0.04	83.79
	24.18	24.69	0.51	0.11	230.42
10082D	42.82	43.33	0.51	0.01	20.95
	67.00	67.51	0.51	0.01	20.95
10086P	26.61	28.21	1.60	0.175	116.85
	10.00	10.50	0.50	0.0387	82.69
	37.28	38.28	1.00	0.0032	3.42
	50.38	53.40	3.02	0.0014	0.50
10087D	146.10	161.22	15.12	0.0012	0.08
	221.67	236.78	15.11	0.0007	0.05
	282.13	292.21	10.08	0.0016	0.17
	302.28	317.40	15.12	0.0019	0.13
	357.70	359.70	2.00	0.0057	3.04
	46.35	47.36	1.01	0.783	828.20
10200R	56.43	56.93	0.50	1.323	2826.74
	79.60	80.10	0.50	0.54	1153.77
	329.48	329.99	0.51	0.027	56.56
	40.30	41.31	1.01	0.9	951.96
	79.10	81.11	2.01	0.3	159.45
10214R	136.03	141.06	5.038	0.09	19.08
	198.50	202.53	4.03	0.18	47.72
	239.30	241.32	2.02	0.03	15.87
	33.25	33.75	0.50	14.415	30799.25
10215R	151.14	161.22	10.08	0.465	49.28
	260.97	268.02	7.05	0.465	70.46
	332.00	335.75	3.75	0.31	88.31

All borehole profiles show decreasing transmissivities with depth. The highest transmissivities are found in the overburden. Where all the injected water is lost into the overburden, no transmissivity values could be obtained for the Elphinstone, Hynds, and Fort Cooper seams. After consulting geophysical data provided by Rio Tinto (e.g. caliper log, sonic logs, density logs) geological units were attributed to their respective depth along the borehole profile. An overview of transmissivities and permeabilities by geological unit is is given in Table 4-4. For the two coal seams subject to this study, the intrinsic permeability results are shown in Table 4-5. The intrinsic permeabilities measured in the Elphinstone seam are within a range between 0.17 mD and 70.46 mD, as compared to a range of 3.04 mD to 88.31 mD in the Hynds seam. Therefore, on the field-scale the deeper Hynds seam may comprise of zones with higher permeability than the Elphinstone seam.

Table 4-4 Transmissivities T and intrinsic permeabilities K for each geological unit

Bore ID	Overburden		Elphinstone		Interburden		Hynds		Fort Cooper	
	T [m^2/d]	k [mD]	T [m^2/d]	k [mD]	T [m^2/d]	k [mD]	T [m^2/d]	k [mD]	T [m^2/d]	k [mD]
10075D	0.430	937.49	--	--	--	--	--	--	--	--
10079P	1.100	1345.61	--	--	0.1000	42.39	0.0400	83.79	--	--
10082D	0.130	272.31	--	--	--	--	--	--	--	--
10086P	0.175	116.85	--	--	--	--	--	--	--	--
10087D	0.045	86.73	0.0016	0.17	0.0019	0.13	0.0057	3.04	--	--
10094D	--	--	--	--	--	--	--	--	--	--
10111P	--	--	--	--	--	--	--	--	--	--
10200R	2.646	4808.71	--	--	--	--	--	--	0.027	56.56
10214R	1.470	1178.20	0.0300	15.87	--	--	--	--	--	--
10215R	14.88	30848.53	0.4650	70.46	--	--	0.3100	88.31	--	--

Table 4-5 Permeabilities derived for Elphinstone and Hynds seam using Heat Pulse Flowmeter

Bore ID	Depth		Length	Elphinstone	Hynds
	from [m]	to [m]	[m]	k [mD]	k [mD]
10079P	211.18	211.69	0.51	--	83.79
10087D	282.13	292.21	10.08	0.17	--
10087D	357.70	359.70	2.00	--	3.04
10214R	239.30	241.32	2.02	15.87	--
10215R	260.97	268.02	7.05	70.46	--
10215R	332.00	335.75	3.75	--	88.31

4.3 FIELD SAMPLING HAIL CREEK MINE

Core samples were taken from the coal seams as well as from the silt- and sandstone formations above and in between the coal. To avoid core drying, the samples were wrapped in plastic wrap and duct tape to prevent oxidation and stored in airtight bags in a cool environment. Core drying is to be avoided due to the potential of additional fracture development that may significantly alter core permeability (Roy & Pyrak-Nolte, 1995). One drawback in the use of laboratory tests for the estimation of the permeability, which is related to the fracture aperture by the cubic law (Witherspoon et al. 1980), is the risk of damage to the fractures during drilling and extraction or even the formation of new cleat spaces. Careful handling, therefore, is essential. Another obstacle arises from the fact that the core recovery from intensely fractured intervals may be poor, and therefore the present samples do not represent these zone (Stumm, 2001).

The samples available for subsequent laboratory testing with their respective depth are displayed in Figure 4-7. The experiments in the laboratory, as well as the scanning that are subject to discussion in the following chapter 5. , have been applied to coals from the Elphinstone and Hynds seams. Samples of the Fort Cooper seam have not been tested,

due to the high content of sand- and siltstone. The samples tested are summarised in Table 5-2 in the next chapter.

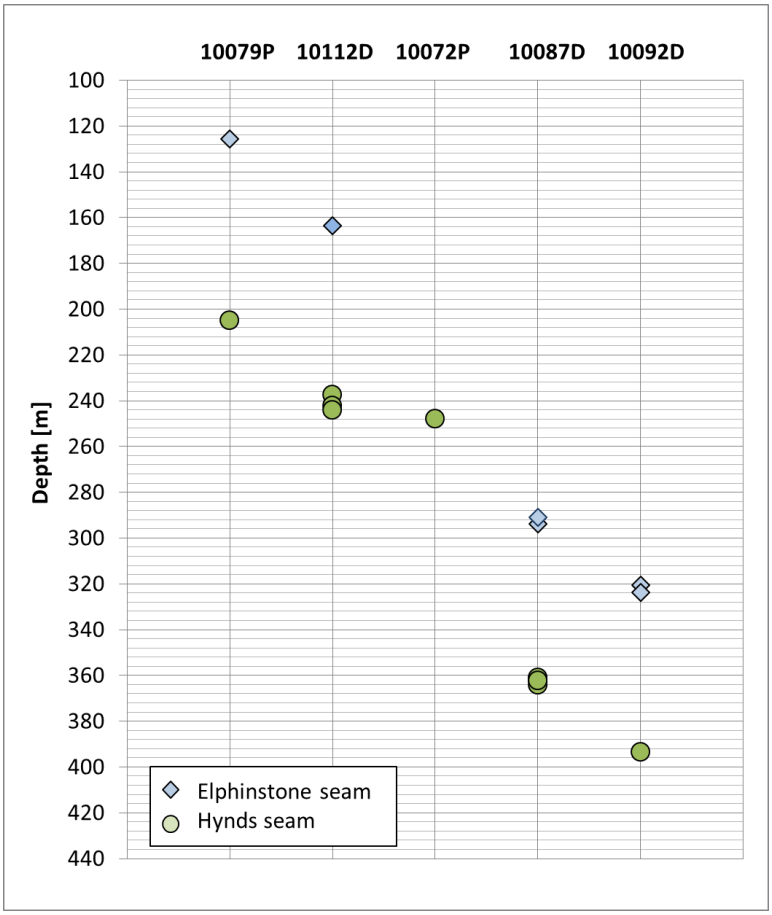

Figure 4-7 Coal samples taken at from different boreholes at Hail Creek Mine with their respective depth [m]

4.4 CONCLUSION

Intrinsic permeability value measured at Hail Creek Mine site range from 86.73 mD to 30848.53 mD in the overburden, one measurement each delivered values for the interburden (0.13 mD) and Fort Cooper seam (56.56 mD). A slightly greater range of values has been found for the Elphinstone seam than for the Hynds seam: from 0.17 mD to 70.46 mD in the Elphinstone and from 3.04 mD to 88.31 mD in the Hynds seam.

The values follow the same pattern as found by Golder Associates Pty Ltd (2013) with descending transmissivities in higher depths, however, the results presented in this thesis are around one magnitude higher. Intrinsic permeability reported by Golder Associates Pty Ltd (2013) range from less than $9.0*10^{-4}$ to 92,057 mD in the overburden, 0.06 to 8.61 mD in the Elphinstone Seam and less than $1.3*10^{-4}$ to 2.16 mD in the combined Hynds and Fort Cooper Seams (see chapter 3.3.2).

All tests presented in this chapter have been conducted with the Heat Pulse Flowmeter and analysed by the PhD candidate, so experimental bias and interpretation errors can be excluded. The relatively large range of permeability values measured in the coal is instead assumed to be characteristic of the highly structured material. Locally increased permeabilities are associated with local discontinuities provided by coal fractures, faults, dykes, and sills. These large scale discontinuities influence the permeability results on the field-scale.

In the following, permeability of coal on smaller scales are presented. Laboratory testing of core samples provide permeability data on the meso-scale (chapter 5), and numerically obtained data give and insight on the structure and permeability on the micro-scale (chapter 6. and chapter 7). The comparison of the permeability data across these scales will provide an insight on the structural influences that are present at each scale (chapter 8).

5. Laboratory testing

5.1 INTRODUCTION

The samples taken at the Hail Creek Mine during the field campaigns have been tested for permeability in the laboratory of the Geotechnical Engineering Centre at the University of Queensland. A triaxial cell has been used for the system to provide controlled conditions. Twenty-nine samples of the Elphinstone and the Hynds seam have been tested. The test set-up and the results are presented in the following sections. The aim of those measurements is to provide experimental data on a meso-scale, which can be used to compare to results from the field measurements and numerical studies.

5.2 PERMEABILITY TESTING IN TRIAXIAL CELL

The hydraulic conductivity of coal samples was examined by triaxial cell testing under controlled hydraulic and mechanical conditions. The application of stresses to induce deformation is not part of the research. A triaxial testing system manufactured by Wille Geotechnik (2013) was used in this research that can apply static axial loads up to 100 kN and confining pressures of up to 2 MPa (Figure 5-1).

Figure 5-1 Triaxial testing system (Wille Geotechnik, 2013)

5.2.1 Testing principle

Permeability testing is done under standard triaxial stress conditions. In theory, the test set up equals that of a constant head permeameter under saturated conditions and is following the principles of Darcy (1856) (see chapter 2.1 and 2.3.1). Figure 5-2 shows the set up with the sample placed inside the triaxial cell. Using a membrane, the sample is isolated from water that fills the cell body using a membrane. The test is run under fully saturated conditions: all void spaces in the sample are saturated with de-aired, de-ionised water. The stresses applied to the sample during the test are displayed in Figure 5-3.

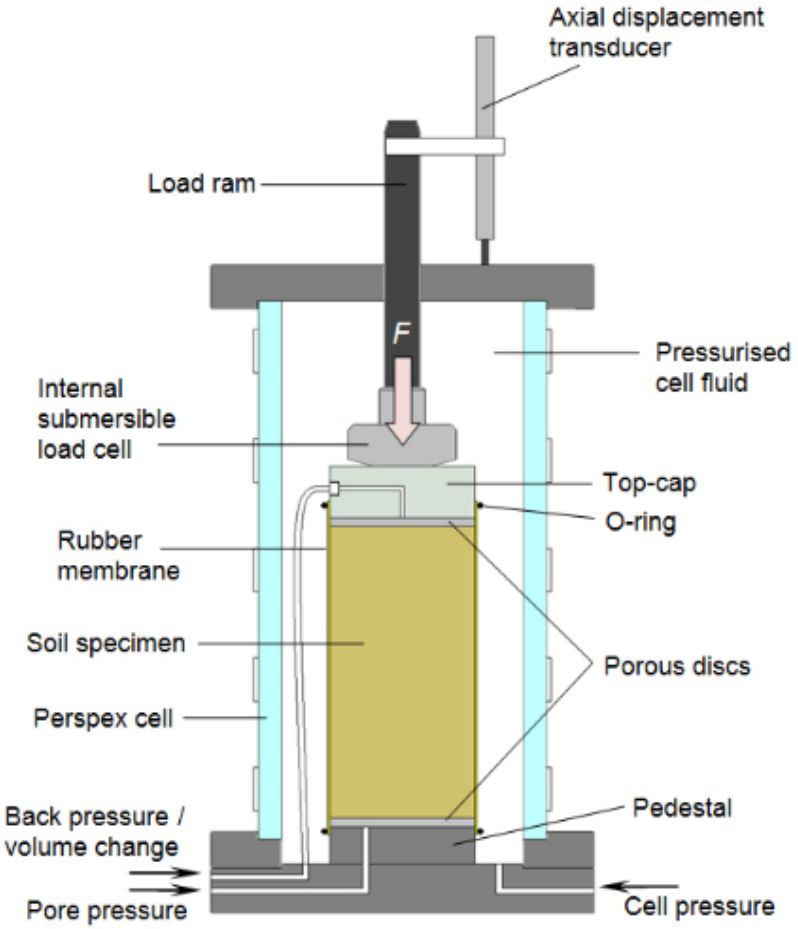

Figure 5-2 Constant head permeability test in triaxial cell (Rees, 2013)

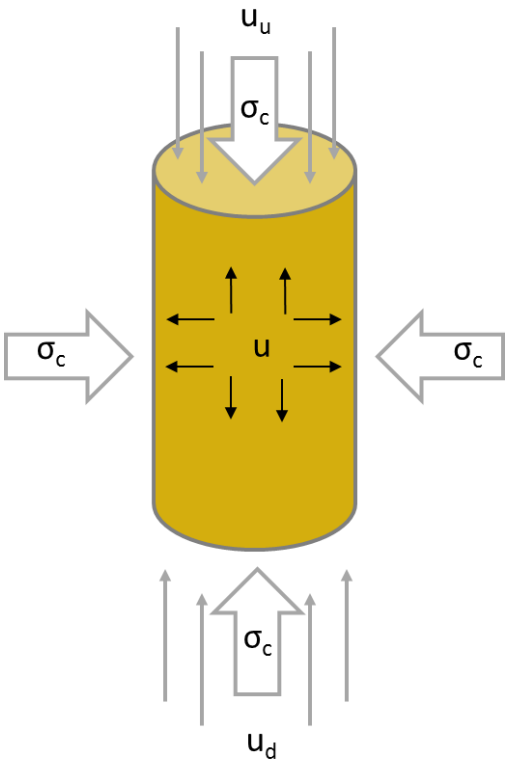

Figure 5-3 Stress components applied onto sample

The pressure applied to the cell fluid surrounding the specimen is called the confining stress σ_c [kPa]. With equal stress applied from all direction, isotropic stress conditions are present within the cell. The pressure inside the fully saturated sample is the pore water pressure, u [kPa]. It is approximated by the average of the backpressure applied at the top, u_u [kPa], and the backpressure applied at the bottom, u_d [kPa], shown in equation 5-1.

$$u = \frac{u_u - u_d}{2} \qquad (5\text{-}1)$$

Effective stress, σ' [kPa], is the difference between the applied confining stress, σ_c, and the pore water pressure, u, as shown in equation 5-2.

$$\sigma' = \sigma - u \qquad (5\text{-}2)$$

The hydraulic head, h, is determined by the pressure difference over the length of the coal sample, l [m], using equation 5-3.

$$h = \frac{u_u - u_d}{l} \qquad (5\text{-}3)$$

The coefficient of permeability, k [m^2], in the vertical direction is calculated by equation 5-4

$$k = \frac{Q\,\mu}{A\,h\,\rho\,g} \qquad (5\text{-}4)$$

with Q, being the mean flow rate in [m^3/s] through the coal specimen with an area A [m^2]. μ represents the viscosity of water which at 25˚C equals to 0.000891 kg/ms. The density of water ρ at 25˚C is 997 kg/m^3. Gravity g is 9.81 m/s^2. The permeability k is converted from m^2 to mD by dividing the values by $9.869233*10^{-16}$.

5.2.2 Test set-up

Both ends of the cylinder shaped sample have to be parallel. The coal cores from the field are cut in cylinders of around 7 cm length. Care has to be taken due to the very brittle nature of the material. The samples have been wrapped in duct tape and placed into a plastic pipe of equal diameter before cutting to prevent breakage and structural changes (Figure 5-4).

(a)  (b) 

Figure 5-4 a. Coal sample and b. sample cutting

The sample preparation includes the following steps: measurement of the weight, length and diameter of sample and the saturation of the sample under vacuum conditions for several days before the test. For the saturation as well as the actual test de-ionised and de-aired water has been used (Figure 5-5).

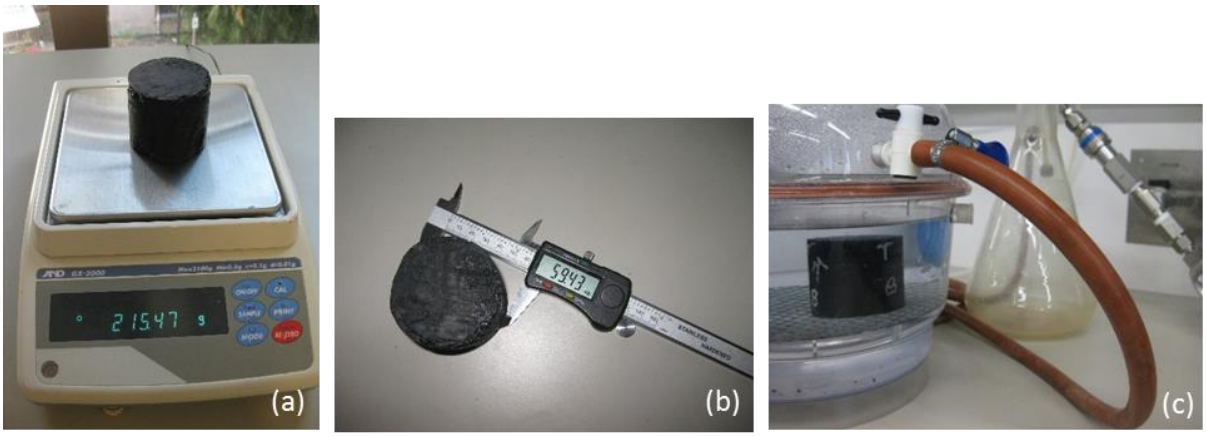

Figure 5-5 a. Sample weighing, b. measurement and c. saturation

Testing coal samples in conventional triaxial cells for soils is not standard and trivial. A discussion on the limitations of the method is found in chapter 9.2.

The set-up is explained in detail in the following. For the mounting of the sample and the test run, the following procedure was applied, based on Murray (2002) as well as suggestions by the manufacturer of the triaxial cell.

The equipment is checked for cleanliness and all valves closed. The cover of the cell body is lifted. Porous stone and filter paper are placed on the base pedestal. A rubber membrane is placed over base pedestal and fixed with two O-Rings. The membrane is rolled down around the base pedestal while the coal sample is put in place. The porous stone and rubber membrane have been soaked in water beforehand.

In case the diameter of the sample is smaller than the diameter of the base pedestal a small amount of impermeable clay (kaolin type eckalite 1) is smeared on the edge between both to prevent the membrane from breaking along the sharp edge. The permeability of kaolin is low and depends on various chemical parameters like the pH of the solution or clogging (Li, Katsumi, Inui, & Takai, 2013), and varies in the range of 10^{-3} to 10^{0} mD. To rule out any influence on the results the set-up has been tested without the clay lining, which showed no change in the measured permeability values.

The membrane is carefully rolled up along the sample. Potential air pockets from between the membrane and the specimen are removed by lightly stroking upward. No further water shall be inserted between the specimen and the membrane. Filter paper, porous stone and top loading cap are placed on top of the sample and fixed with two O-Rings. The two tubes that serve at the top outlets are connected to the base. A vacuum can be applied to the sample to seal the membrane tight around the sample (Figure 5-6).

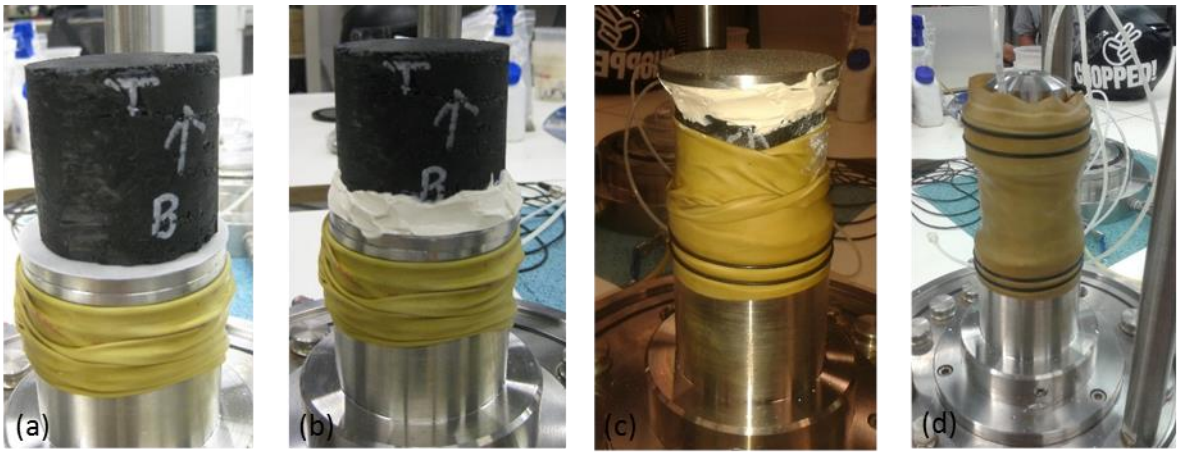

Figure 5-6 a. Sample placement on pedestal with filter stone and filter paper, b. and c. application of kaolin to smoothen edges for membrane fitting, d. connection of top outlets

The cover of the cell body is closed using screws at the top. A clean surface is essential to prevent leakages. The loading piston is slowly moved to the top of the sample until it slightly touches the sample and is fixed in this position. Next, the cell is carefully placed onto the machine and fixed via a stamp attached to the top beam. The stamp height can be adjusted manually after the triaxial machine is turned on.

The cell is filled with de-aired and de-ionised water. Three pressure controller are used: one for the cell pressure, one for top and backpressure each. All tubes connecting the pressure controller with the cell are filled with water, and the sample and cell are de-aired. The system is fitted with a pore pressure sensor.

The test is run using the Wille GeoSys system. The computer is connected to the triaxial cell and the volume pressure controller. Input parameters are the length of the sample [m], the diameter of the sample [m], cell pressure (confining pressure) [kPa], as well as the backpressure at the top and bottom of the sample. Furthermore the general test parameters of the initial deviator [kN/m^2], stress rate [kN/m^2/min] and recording interval [s] need to be set.

The first stage of the test is saturation, where backpressure at top and bottom of the sample are set to the same value to fully saturate the sample by disolving air in water. Once equilibrium is reached, the actual permeability testing is started. Therefore the backpressure at the bottom is increased to induce a flow within the sample.

Data analysis is based on the Darcy equation. The system monitors the hydraulic head [m] resulting from the pressure difference between top and bottom of the sample, as well as the flow Q [ml/min] over time. Once an equilibrium between inflow at the bottom and outflow at the top is reached, the hydraulic conductivity, K, and permeability, k, can be

calculated. For the permeability calculation parameter values at a temperature of 25˚C are chosen: a viscosity of 0.000891 kg/ms, and a density of 0.997 kg/m^3.

Testing of coal samples of the four boreholes 10079P, 10112D, 10087D and 10092D was done, each for the Hynds and the Elphinstone coal seam. The samples having a diameter of 59 mm to 83 mm and lengths in the range of 33 mm to 94 mm.

Three different hydraulic heads were applied on each sample for the permeability determination to test for repeatability of the results. To keep the fracture geometry undisturbed, the effective stress was not changed. Taking these considerations into account, the test setup shown in Table 5-1 has been used.

Table 5-1 Testing conditions for permeability measurements

Test name short	Cell pressure [kPa]	Backpressure bottom [kPa]	Backpressure top [kPa]	Effective Stress [kPa]
low	222.5	170	185	45
mid	230	170	200	45
high	245	170	230	45

The density of the samples is determined after the permeability testing. The samples are dried for 72 hours in a vacuum oven at 105˚C to remove all free water. The samples are weighted, and density is calculated as the ratio of weight to the volume. An overview of the coal samples that have been tested is given in Table 5-2.

Table 5-2 Coal core samples tested for permeability in triaxial cell

Bore ID	Sample short	Depth From [m]	Depth To [m]	Length [m]	Diameter [m]	Weight [kg]	Density [kg/m^3]
10072D	13 1/3	247.82	247.89	0.0697	0.0598	0.2558	1306.40
	13 2/3	247.89	247.96	0.0663	0.0605	0.2502	1311.00
	13 3/3	247.82	247.89	0.0851	0.0833	0.6131	1322.97
10079P	4 1/2	125.81	125.90	0.0882	0.0592	0.3011	1241.17
	4 2/2	125.92	126.00	0.0809	0.0836	0.7465	1681.51
	5 1/2	204.87	204.94	0.0700	0.0838	0.4790	1241.51
	5 2/2	204.94	205.02	0.0803	0.0598	0.2740	1213.00
10087D	11 1/3	290.80	290.86	0.0552	0.0594	0.2085	1363.19
	12 1/3	293.91	293.96	0.0511	0.0609	0.2128	1430.29
	12 2/3	293.96	294.02	0.0511	0.0609	0.2132	1432.64
	12 3/3	294.02	294.09	0.0731	0.0608	0.2884	1356.95
	14 2/3	360.96	361.03	0.0693	0.0609	0.2953	1463.95
	14 3/3	361.03	361.10	0.0717	0.0608	0.3006	1445.36
	15 1/3	361.57	361.66	0.0941	0.0609	0.3720	1358.85
	15 2/3	361.66	361.74	0.0746	0.0595	0.2792	1345.67
	17 2/2	364.23	364.30	0.0740	0.0610	0.3084	1426.23
10092D	2 2/3	320.65	320.72	0.0686	0.0610	0.2839	1416.29
	2 3/3	320.74	320.72	0.0430	0.0611	0.1653	1310.85
	3 1/3	323.91	323.96	0.0461	0.0610	0.1775	1318.56
	3 2/3	323.96	324.01	0.0516	0.0611	0.1968	1300.45
	3 3/3	324.03	324.09	0.0598	0.0610	0.2451	1401.49
	6 1/2	393.28	393.34	0.0693	0.0610	0.2925	1445.87
	6 2/2	393.34	393.41	0.0704	0.0612	0.2860	1381.86
	7 1/1	393.60	393.66	0.0617	0.0609	0.2300	1279.77
10122D	23 1/1	163.72	163.78	0.0622	0.0610	0.2769	1523.25
	24 1/1	237.59	237.66	0.0723	0.0602	0.2563	1246.33
	25 1/1	242.47	242.54	0.0600	0.0600	0.2690	1585.71
	26 2/3	244.23	244.27	0.0374	0.0590	0.1501	1472.13
	26 3/3	244.28	244.32	0.0400	0.0606	0.1526	1325.87

5.2.3 Permeability data obtained in the lab

The results of the permeability testing in the triaxial cell are summarised in Table 5-3. The terms low, mid, and high are referring to the pressure conditions as introduced in Table 5-1. Furthermore, an average permeability is given. The in-situ depth, as well as the density of the material based on the sample diameter and volume are listed.

Plotting the permeability data against the sampling depth shows no apparent relation (Figure 5-7a), neither does the plot of the measured permeability values and the densities (Figure 5-7b). No relationship between sample size and result can be recognised (Figure 5-8).

Table 5-3 Permeability results obtained in triaxial cell tests

Bore ID	Sample short	Depth From [m]	Depth To [m]	Elphinstone k [mD] Low	Elphinstone k [mD] Mid	Elphinstone k [mD] High	Elphinstone k [mD] Average	Hynds k [mD] Low	Hynds k [mD] Mid	Hynds k [mD] High	Hynds k [mD] Average
10072D	13 1/3	247.82	247.89					0.024	0.017	0.014	0.018
	13 2/3	247.89	247.96					0.014	0.011	0.009	0.011
	13 3/3	247.82	247.89					0.043	0.053	0.053	0.050
10079P	4 1/2	125.81	125.90	0.429	0.430	0.525	0.460				
	4 2/2	125.92	126.00	0.025	0.026	0.019	0.023				
	5 1/2	204.87	204.94					8.722	4.929	3.597	5.749
	5 2/2	204.94	205.02					9.620	9.707	10.08	9.801
10087D	11 1/3	290.80	290.86	11.350	0.982	1.019	4.450				
	12 1/3	293.91	293.96	0.130	0.112	0.085	0.109				
	12 2/3	293.96	294.02	0.060	0.043	0.052	0.052				
	12 3/3	294.02	294.09	0.743	0.641	0.615	0.666				
	14 2/3	360.96	361.03					0.968	0.736	0.653	0.786
	14 3/3	361.03	361.10					0.189	0.176	0.161	0.176
	15 1/3	361.57	361.66					1.371	1.304	1.427	1.367
	15 2/3	361.66	361.74					0.561	0.522	0.517	0.533
	17 2/2	364.23	364.30					0.078	0.069	0.057	0.068
10092D	2 2/3	320.65	320.72	0.143	0.138	0.098	0.126				
	2 3/3	320.74	320.72	0.056	0.055	0.054	0.055				
	3 1/3	323.91	323.96	0.094	0.092	0.091	0.092				
	3 2/3	323.96	324.01	0.152	0.160	0.176	0.163				
	3 3/3	324.03	324.09	0.089	0.082	0.074	0.082				
	6 1/2	393.28	393.34					0.172	0.148	0.137	0.153
	6 2/2	393.34	393.41					0.147	0.162	0.123	0.144
	7 1/1	393.60	393.66					0.397	0.542	0.542	0.494
10122D	23 1/1	163.72	163.78	0.059	0.045	0.038	0.047				
	24 1/1	237.59	237.66					19.940	21.210	20.720	20.620
	25 1/1	242.47	242.54					0.523	0.460	0.414	0.466
	26 2/3	244.23	244.27					0.944	0.944	0.815	0.901
	26 3/3	244.28	244.32					3.186	2.740	3.729	3.218

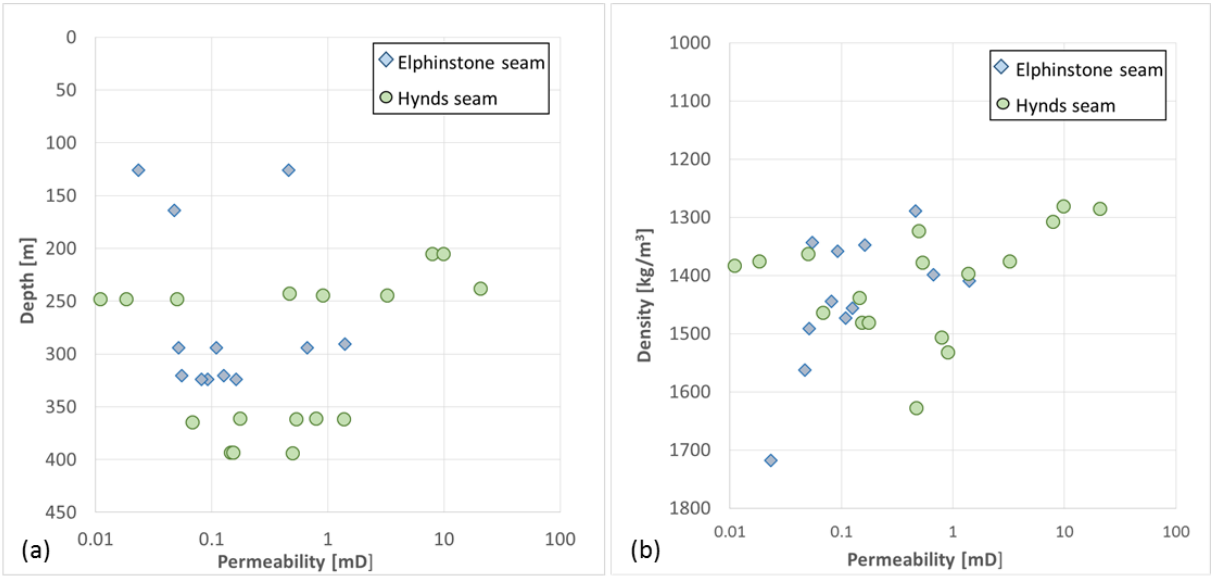

Figure 5-7 a. Permeabilities [mD] derived in laboratory tests plotted against their sampling depth [m] and b. their density [kg/m^3]

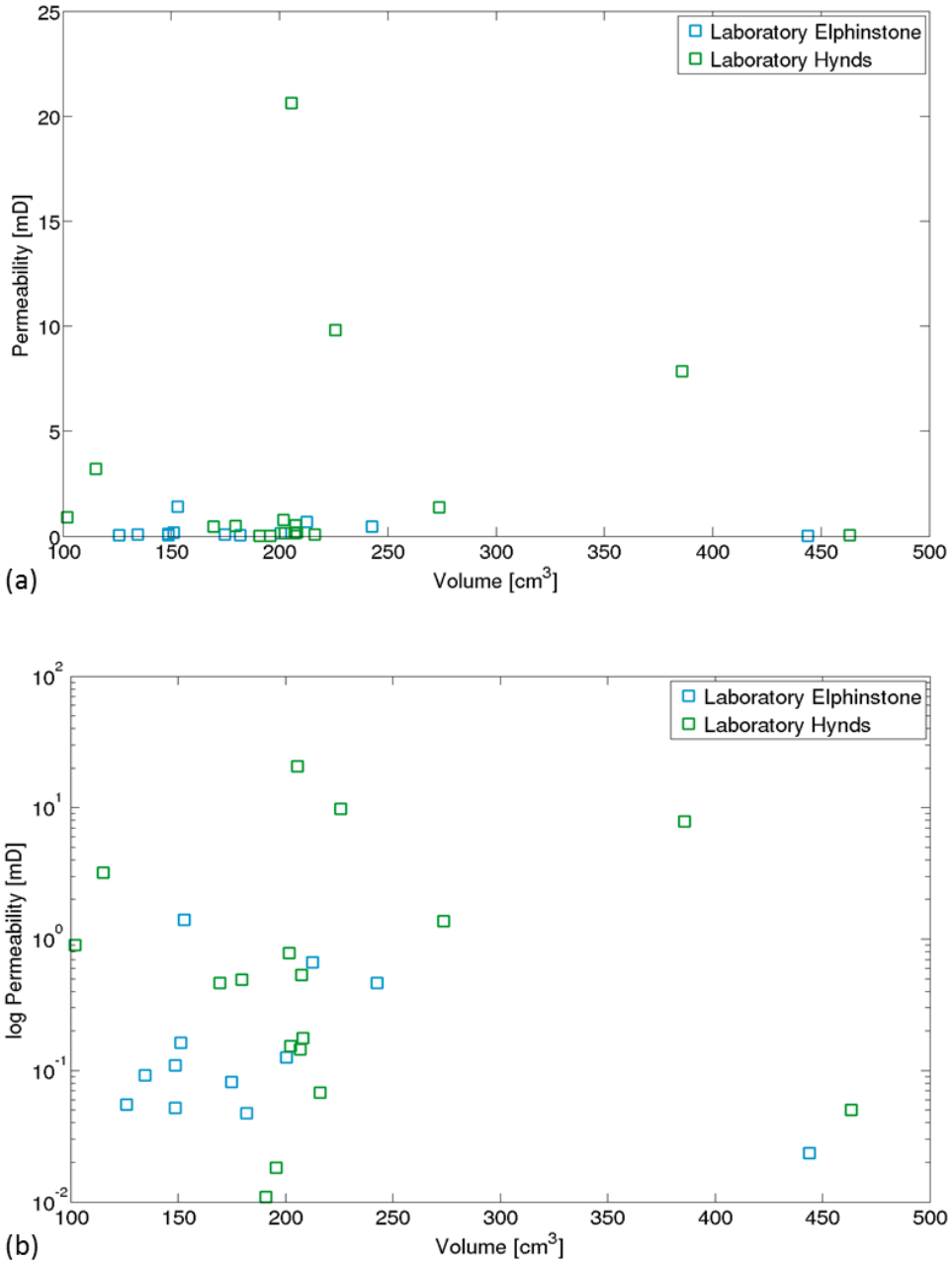

Figure 5-8 a. Permeability [mD] and b. Logarithmic scaled permeability [mD] over sample volume [cm^3]

5.3 CONCLUSION

As for the field measurements (chapter 4.2.5), the range of permeability values measured in the laboratory is greater for the Hynds seam than for the Elphinstone seam. While for the Elphinstone seam values from 0.023 mD (sample 4 2/2) to 1.408 mD (sample 11 1/3) have been obtained, the results for the Hynds seam are in the range of 0.011 mD (sample 13 2/3) to 20.62 mD (sample 24 1/1). The laboratory results are generally smaller than the data retrieved using the Heat Pulse Flow Meter. Compared to field results of 0.17 mD to 70.46 mD, the laboratory data for samples of the Elphinstone seam are at least one order of magnitude smaller (0.023 mD to 1.408 mD).

It is assumed, that the meso-scale that is covered by these laboratory tests does include the influence of cleats, but does neglect the influence of large-scale coal fractures and other large-scale continuities. The lowest laboratory results for the Hynds samples are two orders of magnitude smaller than the minimum field data of the Hynds seams (3.04 mD), while the maximum laboratory value of 20.64 mD is in the same order of magnitude as the maximum field value of 88.31 mD. No relation between density and sampling depth to permeabilities could be established in the laboratory testing. This supports the assumption that the permeability on this scale is largely influenced by the presence and structure of cleats.

The results of these tests provide a data set which is used for comparison with results from numerical permeability tests. These tests are based on CT-scans which are introduced in the next chapter.

6. Coal structure characterisation

6.1 INTRODUCTION

A characterisation of the cleat network serves as the basis for estimating the hydraulic and mechanical seam properties which in turn are fundamental for flow and geo-mechanical modelling in the context of underground coal mining. Cleat and cleat network geometry can be described as a function of frequency, aperture, size, orientation relative to in situ stresses, connectivity and porosity, with mineralised and un-mineralised cleats occurring. To describe these properties, CT-scans of two core samples taken at the Hail Creek Mine are analysed, one of the Elphinstone and the Hynds coal seam each.

A unique image processing workflow method is introduced to extract the key statistical parameters of perpendicular butt and face cleat present in a two-dimensional image. As shown by Laubach et al. (1998), face and butt cleats have different characteristics. For this research project, a method that is distinguishing face cleats and butt cleats by direction has been developed (Busse et al., 2015). Detailed data for both cleat types are presented in the following. The results comprise cleat length, apertures, sizes, intensities, densities, shape parameter, spacing, orientation and connectivity. Therefore, the results are more comprehensive than previous cleat description methods. A paper on the characteristics of three different cleat geometries has been published by the author of this thesis (Busse et al., 2017).

6.2 SAMPLES USED FOR STRUCTURAL AND NUMERICAL ANALYSIS

After coring, the coal has been wrapped in plastic foil and duct tape and stored in a cool environment. Before scanning the samples have been cut into smaller pieces. As a result of the sample handling the azimuthal orientation of the samples as found in-situ is unknown. Identified cleat directions therefore are only relative to each other.

A thorough characterisation of cleat geometry, bulk and cleat porosities and mineralogy was completed for two samples, one from the Elphinstone seam and the other from the Hynds seam. These two samples are subject to the numerical modelling in chapter 7.3 and the analysis of scale effects on permeabilities in chapter 8. Two samples were chosen to represent each of the both main coal seams at Hail Creek Mine. An overview of the samples that have been used for the analysis is given in Table 6-1.

Table 6-1 Cut Coal Samples used in CT-scans

Bore ID	Sample Short	Seam	Depth from [m]	Depth to [m]	Length [m]	Diameter [m]	Weight [g]	Scanning date
10087D	11 1/3	Elphinstone	290.800	290.855	0.055	0.059	208.45	16/12/2013
10087D	15 2/3	Hynds	361.660	361.736	0.075	0.056	279.22	16/12/2013

6.3 CLEAT GEOMETRY CHARACTERISATION BASED ON IMAGE PROCESSING

6.3.1 Scanning set up

CT-scans and fracture quantification analysis are performed on samples taken at boreholes where the Heat Pulse Flow Measurement took place. After scanning, the samples have been tested for permeability in the triaxial cell as described in chapter 5.1. Two coal samples have been scanned at the Centre for Advanced Imaging of the University of Queensland. The samples are around 5 cm and 7 cm long, and are taken from the Hynds and Elphinstone seam at the borehole 10087D for which permeability data have been obtained in the field measurements. Different scanning resolutions have been tested. 500µm was found to be too coarse for the application of the developed model. Scans of a higher resolution of 53 µm have been taken. This higher resolution was obtained with the drawback that the coal samples had to be cut into smaller pieces, due to the maximum loading capacity of the CT-scanner of 800 g.

The CT images are acquired using an Inveon Multimodality PET/CT system (Siemens, Figure 6-1) with an X-ray source with the voltage set to 80 kV and the current set to 500 µA. The scans are performed using 360° rotation with 360 rotation steps with a low magnification and a binning factor of 2. The exposure time is 800 ms with an effective pixel size of 53.3 µm. The CT images are reconstructed using Cobra software (Siemens). The CT-scans are used to visualize fracture networks and model flow pattern. The scanning results in image files from three directions: the axial, sagittal and coronal plane (Figure 6-2).

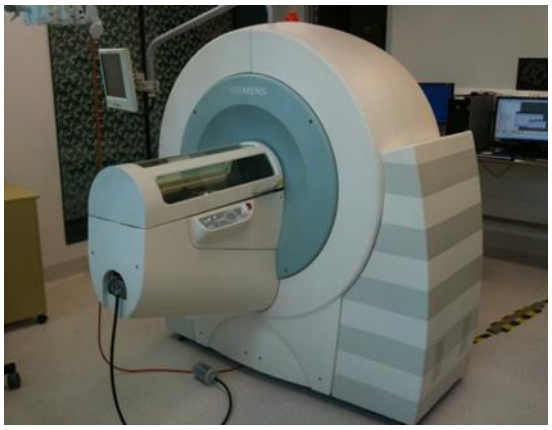

Figure 6-1 CT-scanner at Centre of Advanced Imaging, University of Queensland

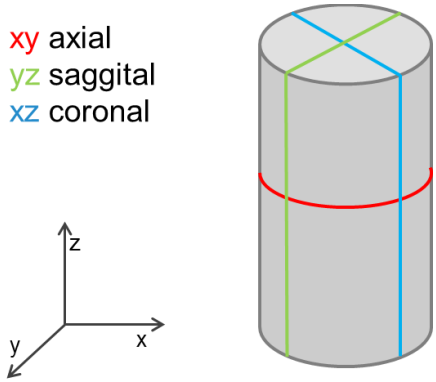

Figure 6-2 Axial, sagittal and coronal planes of coal core sample

6.3.1.1 Sample 11 1/3

Sample 11 1/3 stems from 290.79 m to 290.865 m in the Elphinstone seam at borehole 10087D. It was tested with a lab permeability of 1.4 mD. The density measured based on the dry weight and the volume of the sample is 1363.19 kg/m^3. The axial view for different axial cuts along the sample is shown in the following (Figure 6-3).

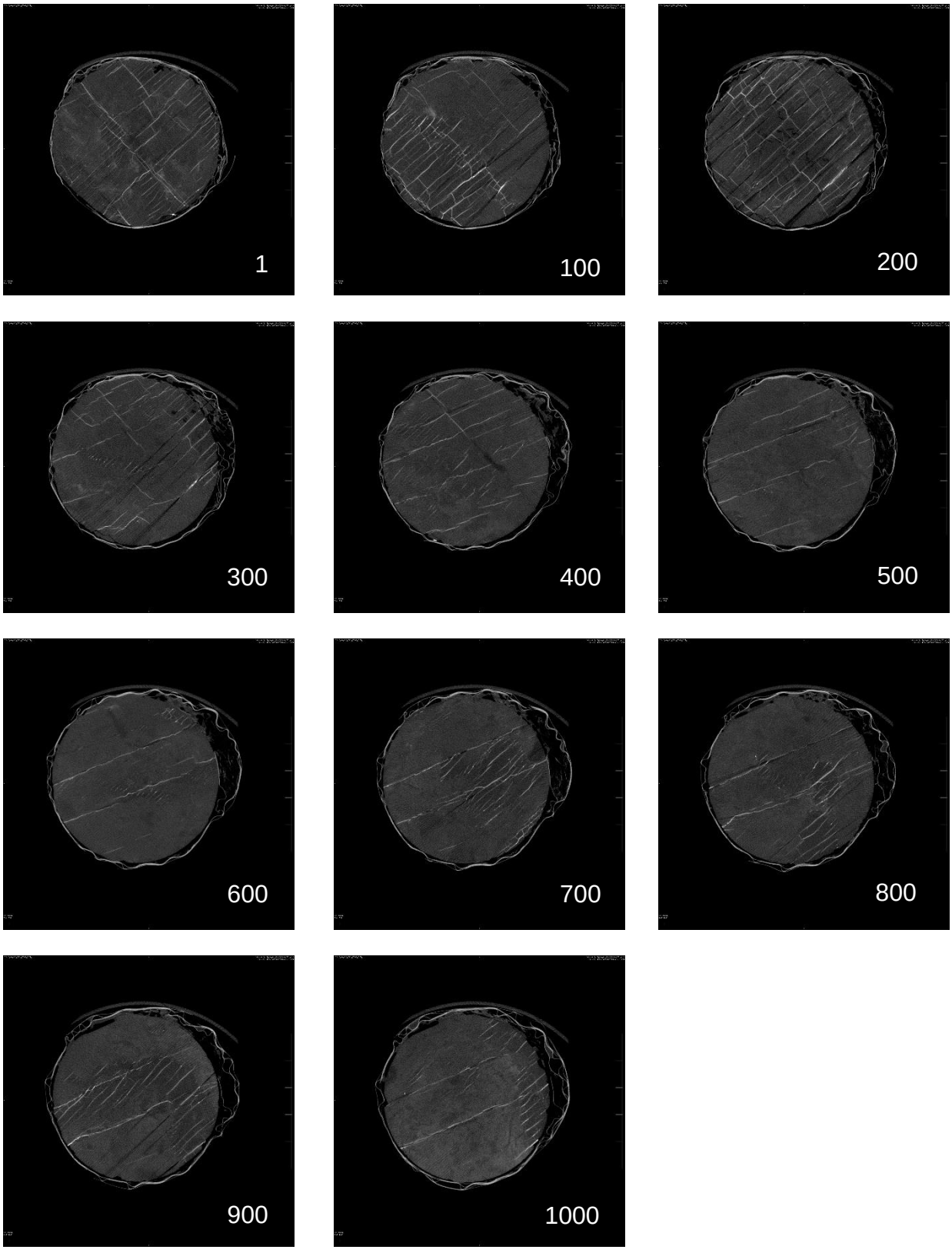

Figure 6-3 A selection of CT- scans of the axial plane showing the structure of sample 11 1/3

6.3.1.2 Sample 15 2/3

A permeability of 0.53 mD has been measured for the sample number 15 2/3 originating from the Hynds seam at borehole 10087D in 361.66 m to 361.736 m depth. The sample is

pervaded by lighter slices that have been identified as fusain (charcoal). The density based on dry weight and volume is 1345.67 kg/m^3. Axial views along the sample 15 2/3 are presented in Figure 6-4.

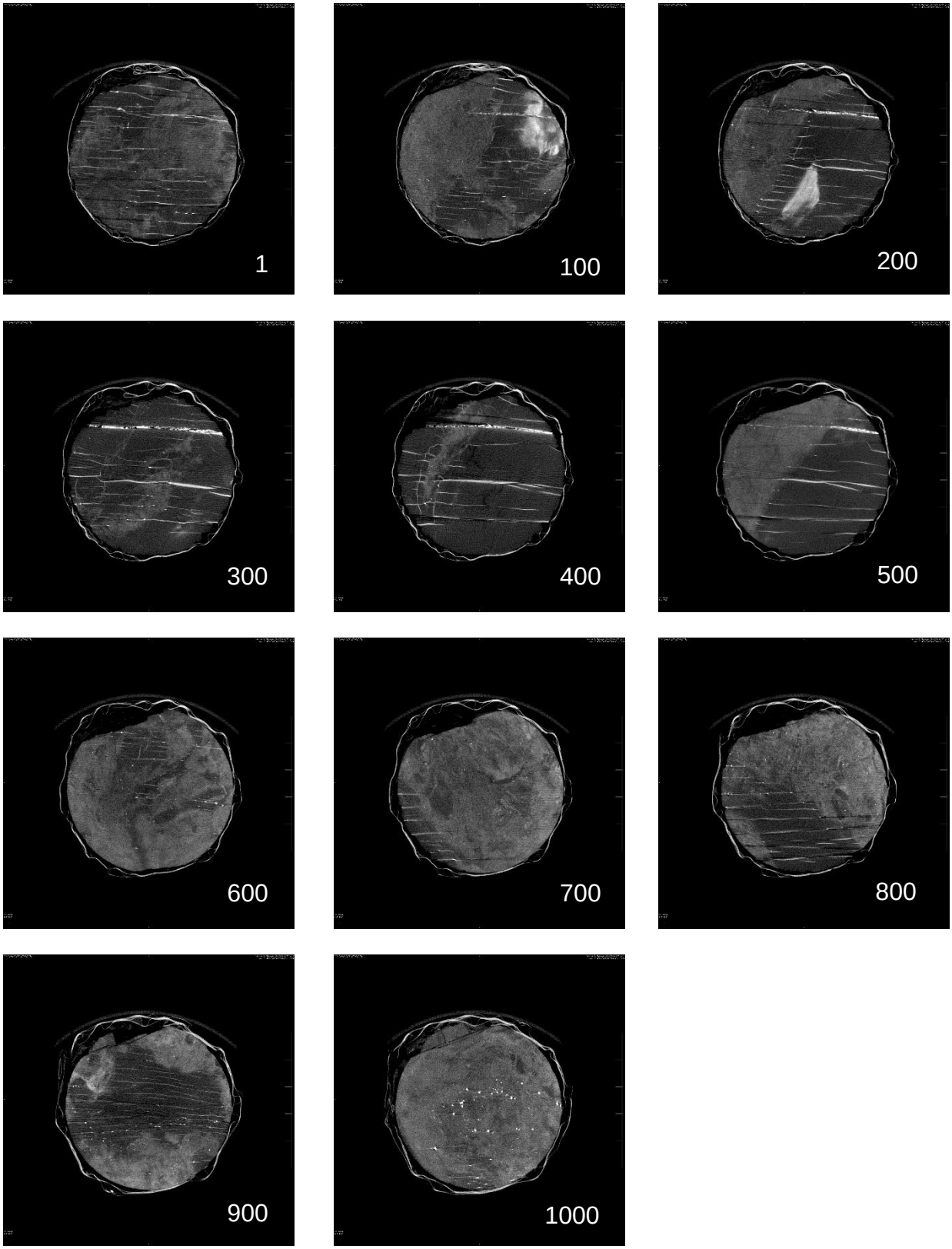

Figure 6-4 A selection of CT- scans of the axial plane showing the structure of sample 15 2/3

6.3.1.3 Comparison of samples

When comparing the scans of sample 11 1/3 of the Elphinstone seam, and 15 2/3 of the Hynds seam (Figure 6-3 and Figure 6-4), a more homogeneous Elphinstone coal and more heterogeneous structure for the Hynds coal is apparent. As a consequence, results from the image analysis and subsequent structure based modelling are more representative for 11 1/3 than for 15 2/3.

6.3.2 Image processing

An algorithm to extract geometric and topologic cleat information from a two-dimensional greyscale image has been developed and implemented in in the MATLAB® environment. The form definition of a cleat in a coal specimen is based on the widely accepted concept of orthogonal network of butt and face cleats with both being aligned normal to the bedding plane (Figure 2-5).

For the study of cleat occurrence and geometry in 2D image processing, a cleat has been defined as a feature that is longer than wide and aligned straight. Gaps in the direction of alignment are closed, when they are smaller as the average cleat aperture in the region of interest.

The feature extraction and statistical analysis follows the workflow illustrated in Figure 6-5. It is noted that all results shown in the following are given in mm based on the fact that each square pixel has a side length of 53 µm. The sample of the Elphinstone seam (sample 11 1/3) which exhibits a network of face and butt cleats is used to demonstrate the details of the image processing steps. The image processing results for this sample, as well as for the Hynds seam are presented in chapter 6.3.4.

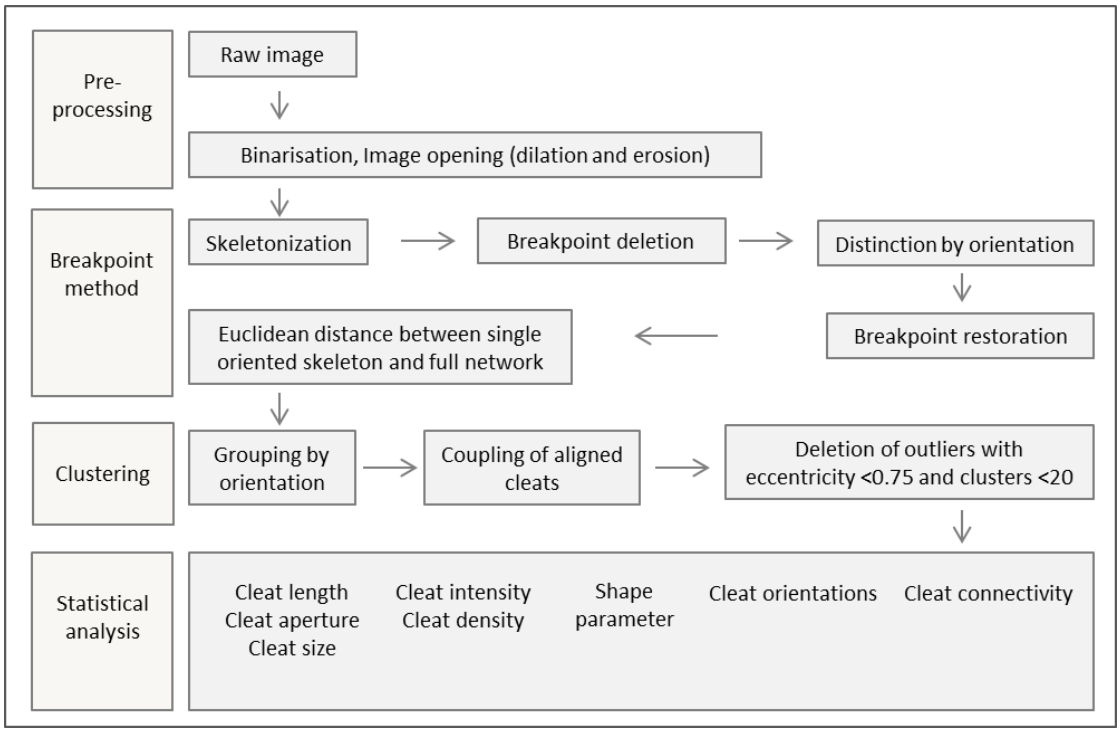

Figure 6-5 Workflow of image processing

6.3.2.1 Pre-processing

The scanning results in image files from three directions: the axial, sagittal and coronal plane (Figure 6-2). The cleat system in sample 11 1/3 is orthogonal to the bedding planes and the axial view with the axial plane parallel to the bedding planes of the coal sample was chosen for this two-dimensional study to best capture the cleat structure with a single image (Figure 6-6a). The image was cropped to reduce the image size and remove the outer rim of the sample image that shows the sample region most disturbed by the sampling preparation (Figure 6-6b). The initial image size before cropping is 2048 x 2048 pixels; afterwards the dimensions are 800 x 800 pixels, showing an image region of 4.24 x 4.24 cm^2.

The distinction between face and butt cleats in each image is made visually based on the concept by Laubach et al. (1998). Face cleats are dominant and perpendicular to the bedding plane. The fewer orthogonal butt cleats generally terminate when they encounter face cleats. Based on this commonly used description, the positively orientated structures (relative to the x-axis of the image) detected in the image represent face cleats, the negatively orientated structures are butt cleats.

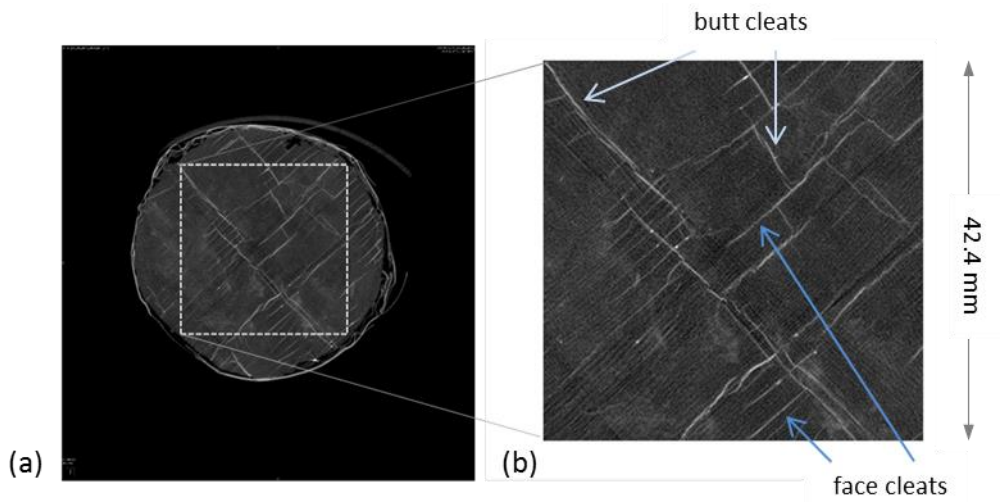

Figure 6-6 a. CT-scan image of coal sample 11 1/3 and b. chosen region of interest

Segmentation processes help to reduce the information in the image according to the question, that is, only relevant features will be looked at. To facilitate the distinction of features in an image, greyscale contrasts can be adjusted, using thresholds fitted to the relative problem. Particularly helpful and widely used is a binarisation of the image based on a certain threshold on its greyscale (Gonzales et al., 2004). A greyscale image is turned into a binary image by choosing a grey level in the original image as threshold and turning every pixel value depending on their relative position to the threshold into black or white. The binarisation threshold is chosen based on the distribution of the grayscale values. The grayscale values of the cropped image are displayed in Figure 6-7a, they are uni-modally distributed. Therefore, the Rosin threshold to distinguish between the present cleats and the matrix (Rosin, 2001) is chosen. Using this method, a straight line is drawn between the histogram peak and the maximum occurring value (Figure 6-7a). The threshold is selected at the point of the histogram that is furthest from the straight line. The threshold value obtained for the Elphinstone sample greyscale image is 92 out of the 255 grayscale values, which equals a grayscale ratio of 0.36. The resulting binarisation of the greyscale image is shown in Figure 6-7b. In this case white pixels may provide information on cleat structure and black pixels are background (matrix).

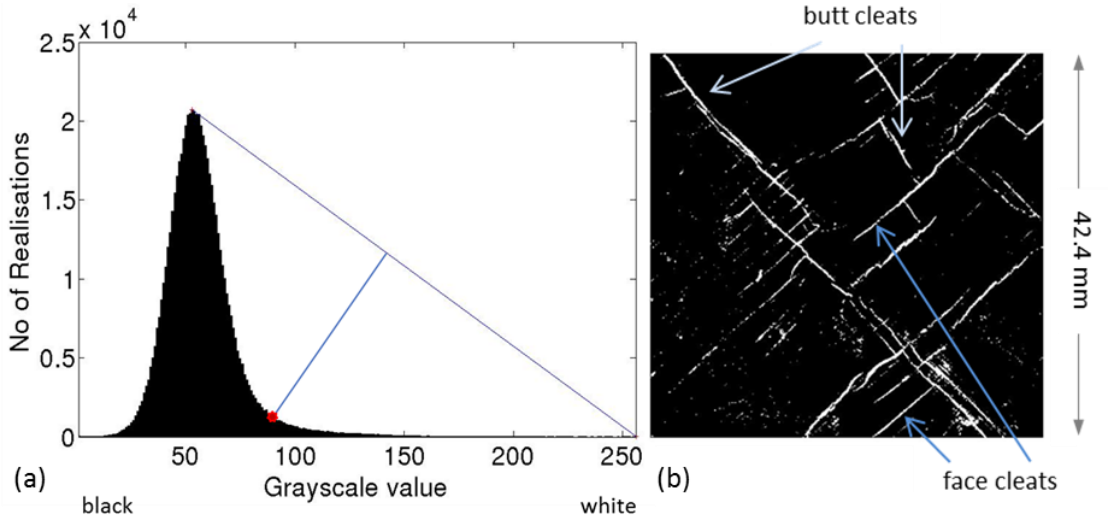

Figure 6-7 a. Plot of grayscale distribution and b. resulting binarised greyscale image of sample 11 1/3

Once binarised, the black and white images allow for a simple feature extraction and further processing, e.g. logical operations, feature connection through erosion and dilation, skeletonisation, edge detection (Gonzales et al., 2004). Single pixels or small pixel clusters in a binary image are frequently considered noise and removed by digital noise filtering. However, filtering was not applied in this case, since it may also partially remove those small clusters that line up perfectly and that represent part of a cleat.

Dilation and subsequent erosion serve to reconnect features that might have been divided in the image acquisition and processing. In the dilation stage the features are thickened with pixels added onto the outside in the form of a defined disk-shaped structuring element with a certain radius. The erosion uses the same filter to delete the outer edge of pixels, with the exemption of the pixels now connecting two features (Figure 6-8). The result of the dilation and erosion on the image of the cleat structure of a sample of the Elphinstone seam is shown in Figure 6-9.

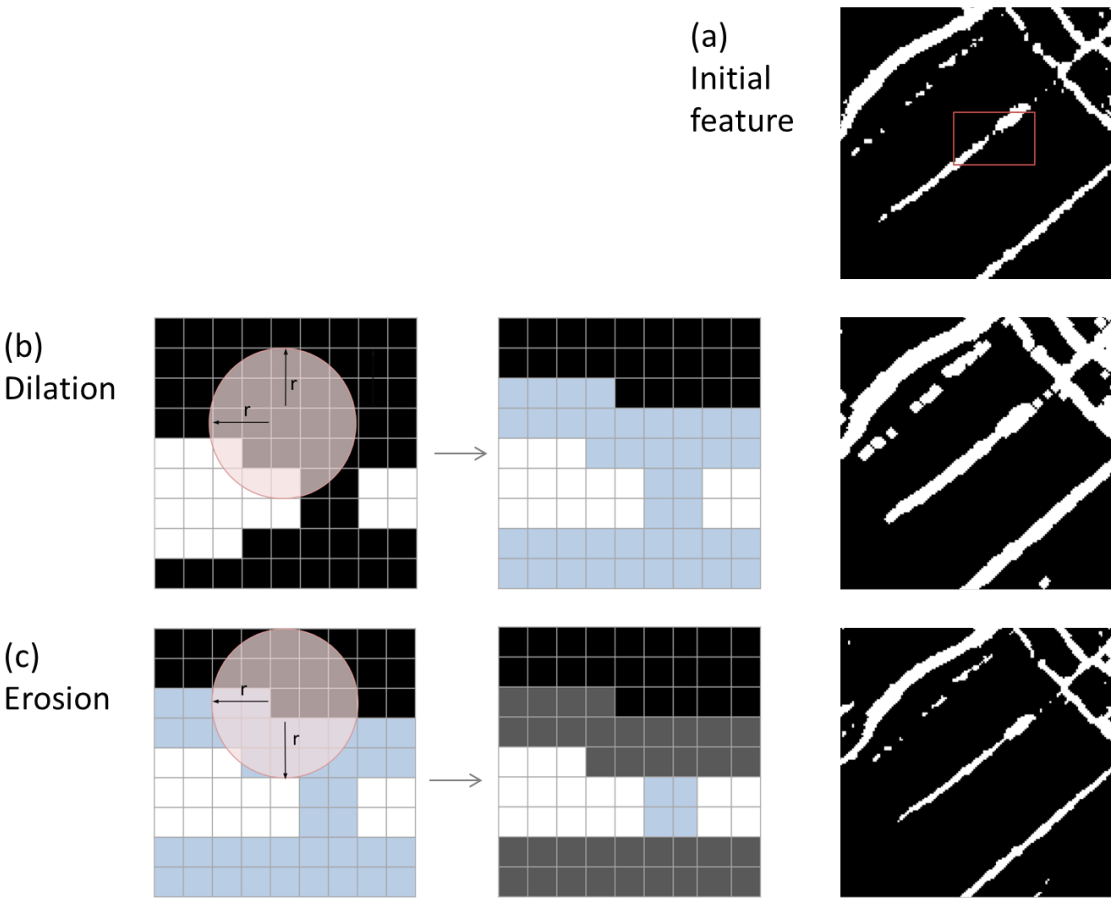

Figure 6-8 a. Initial feature and the principle of b. dilation and c. erosion of image features using a disk-shaped element with radius r

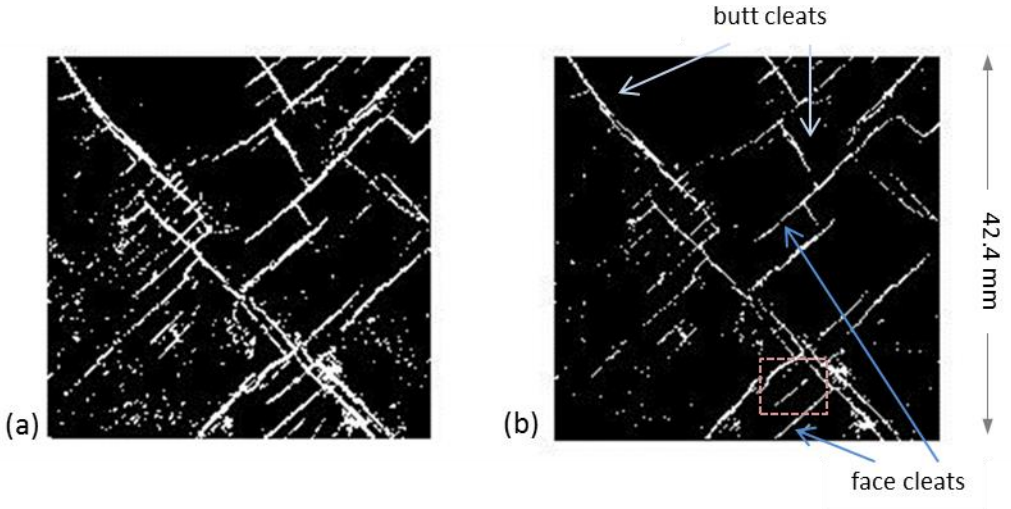

Figure 6-9 Dilated and b. eroded binary image of coal sample 11 1/3 of the Elphinstone seam. The marked area in b is shown in Figure 6-10.

6.3.2.2 Breakpoint method for cleat detection

To extract elements that represent the cleats based on the cleat definition made earlier, the following steps are done on the pre-processed picture. Firstly, the skeleton of each of the elements are displayed and their breakpoints are calculated. Skeletonisation helps to visualise shape properties. In the process, a feature is minimised to its skeleton, i.e. its midline (Figure 6-10). The skeleton illustrates topological as well as geometrical shape properties as length and direction. In the skeleton, pixels with only a single touching neighbour are representing end points, pixels with more than two neighbours are breakpoints (Pratt, 2001). Breakpoints mark a crossing between or a joint of two skeletons. These breakpoints are removed from the binary image to get a set of aligned skeleton sections (Figure 6-11).

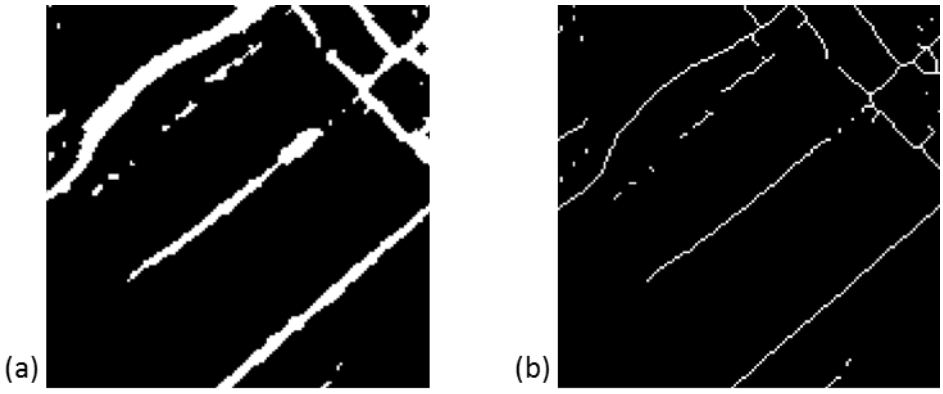

Figure 6-10 Inset of Figure 6-9 with a. features and b. skeletons of the features

Using the MATLAB image processing toolbox (‘regionprops’) the orientations of the skeletons are calculated. Due to the nature of coal cleats being perpendicular to each other the distinction between face and butt cleats can be done (Figure 6-12). Once this distinction is done, the skeleton sections are bridged by filling the breakpoints back into the image. The result is the full skeleton of each cleat. Cleats are by definition relatively straight features with no discontinuation.

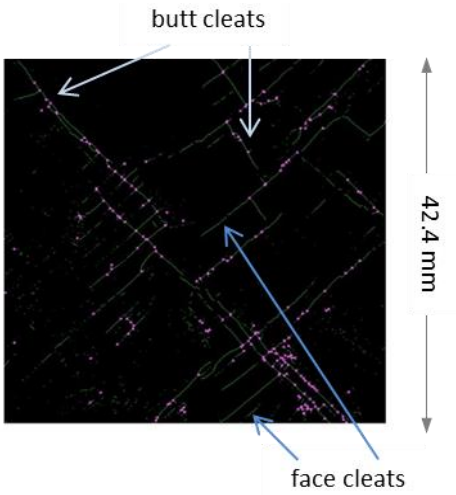

Figure 6-11 Skeletons and breakpoints of the features in the binary image of coal sample 11 1/3

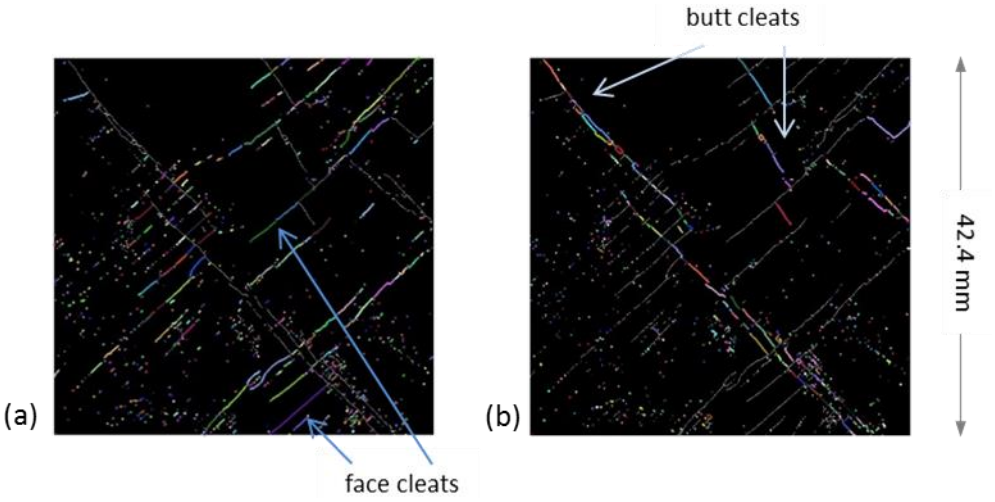

Figure 6-12 Distinction of skeleton sections based on orientation, a. face cleats and b. butt cleats. Each individual skeleton section is identified by a different colour in the binary image of coal sample 11 1/3

In order to get the complete set of shape parameters of the features, the skeletons are overlapped with the inverse of the original binary cleat network using an Euclidean distance function. Face and butt cleats are reconstructed around the skeletons based on the input cleat network. The fitting is done using visual trial and error (Figure 6-13). Computing the Euclidean distance one can determine the distance from each cell to the closest non-zero element (Deza & Deza, 2009). For Cartesian coordinates the Euclidean distance between two points a and b in a n-dimensional space is calculated by equation 6-1.

$$ED(a,b) = ED(b,a) = \sqrt{\sum_{i=1}^{n} (b_i - a_i)^2} \qquad (6\text{-}1)$$

In Figure 6-13a and Figure 6-13b the original binary image (green) is masked with the face and butt cleat features that have been extracted (red). Finally, the reconnected features

that represent the cleat traces of face and butt cleats are extracted (Figure 6-14a and Figure 6-14b) and feature properties are calculated.

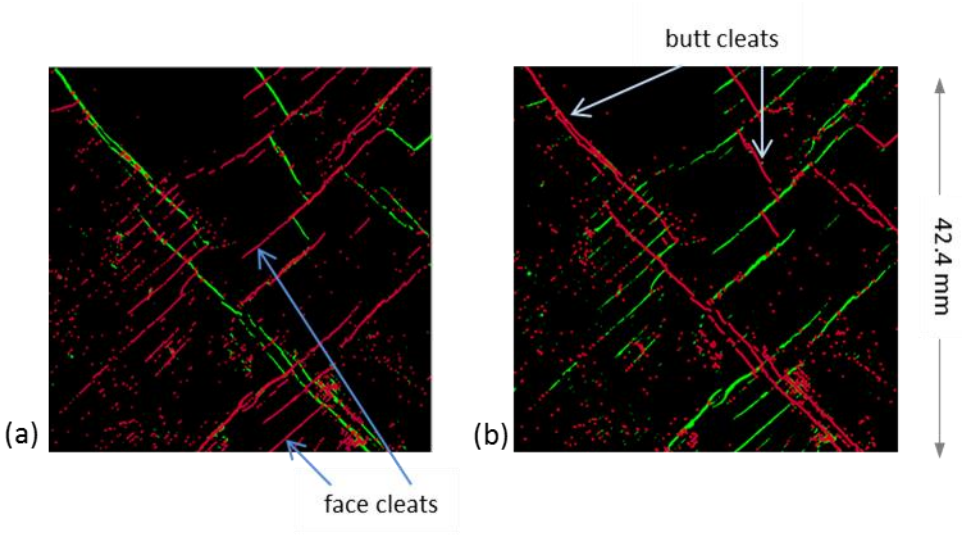

Figure 6-13 Overlap of the original binary image (green) with the extracted, reconnected and grouped features (red) for a. butt cleat and b. face cleat orientation

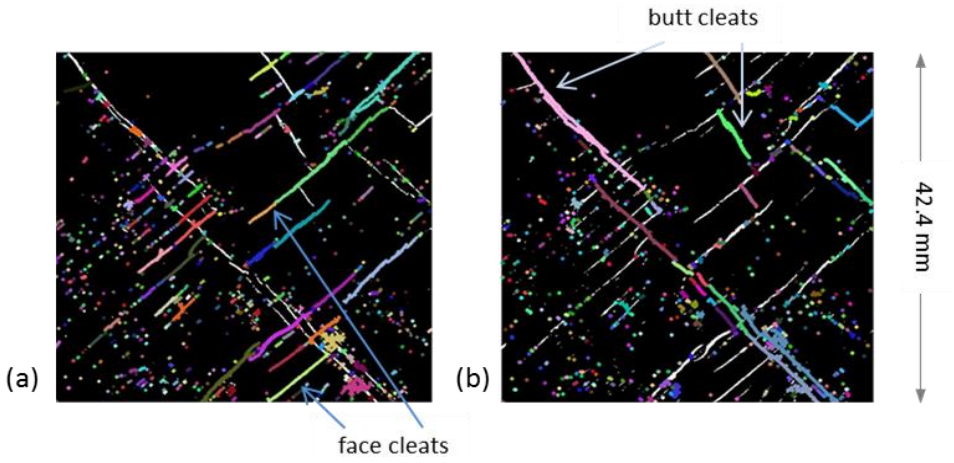

Figure 6-14 Reconnected features present in the sample 11 1/3 for both a. face cleat and b. butt cleat orientations

6.3.2.3 Clustering of reconnected elements

A feature in a grey scale image representing a cleat trace has been defined by the pixel's greyscale values exceeding a defined threshold value and the shape being a cluster of aligned pixels that is longer than wide. To fulfil the latter part of the definition, the features are grouped based on their eccentricity, orientation and position. Eccentricity is deduced by fitting a major and minor axis to each feature and defined as the ratio of the distance between the foci of the ellipse and its major axis length. The principles of major and minor axis length, perimeter and area size are presented in Figure 6-15. The ellipse fitting is based on an ellipse perimeter that has the same normalized second central moment (variance) as the area of a feature.

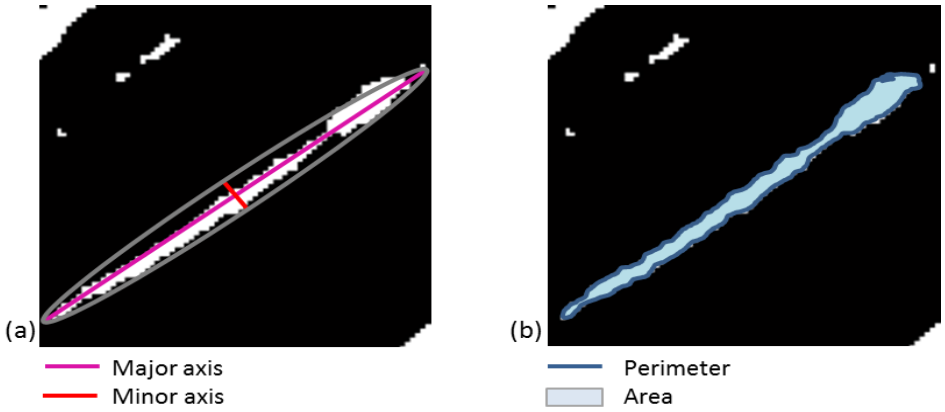

Figure 6-15 Principle of shape parameters used in the study, a. ellipse perimeter that has the same normalized second central moment (variance) as b. the area of a binary image feature

The features that have an eccentricity below 0.75 are not considered as cleats. Eccentricity takes values between 0 and 1, with 0 representing a circle, and 1 a line shape (Figure 6-16).

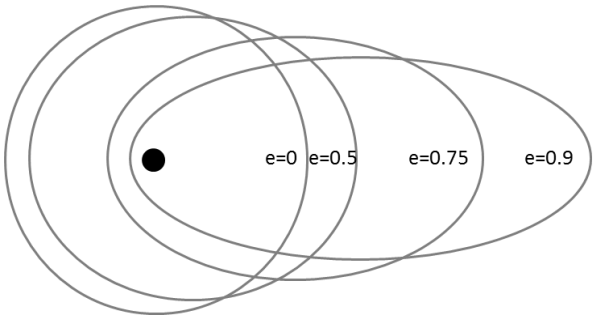

Figure 6-16 Principle of eccentricity (after http://earthobservatory.nasa.gov)

In the next step, gaps between the line-shaped features (those with an eccentricity larger than 0.75) are bridged. Line-shaped features that are aligned along the same axis with a gap between them that is smaller than the average cleat aperture occurring in the image are grouped to one cleat. A line-shaped structuring element with the length of the average aperture is used to fill the gap in the respective direction in an image opening process (dilation and erosion). At this stage, clusters that consist of less than 20 pixels are removed in a final filtering process.

As a result of the image processing and clustering two sets of extracted reconnected features that represent cleats are obtained: a set of face and a set of butt cleats. They are pictured in Figure 6-17.

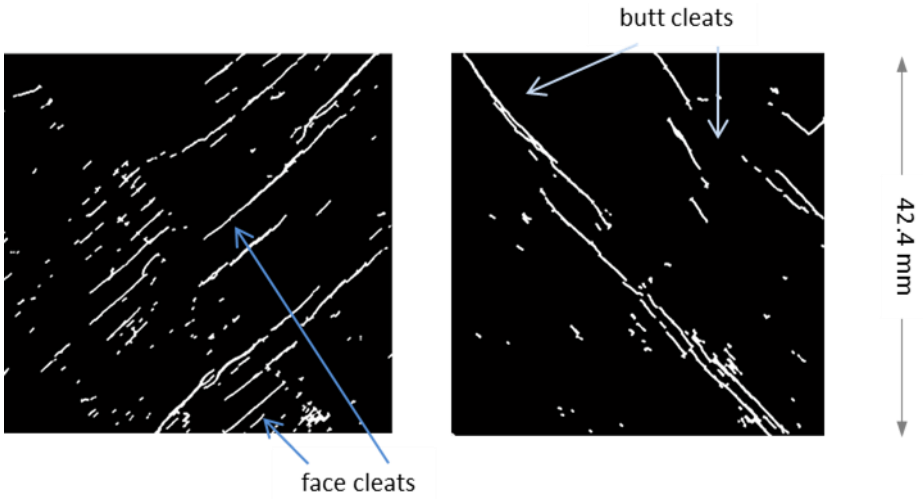

Figure 6-17 Extracted reconnected elements that represent cleats for both orientations

6.3.3 Statistical analysis of cleat properties

The extracted, reconnected line-shaped features are a close approximation of the shape of cleats in the CT-scan images of coal samples and are referred to as cleats throughout the remainder of this chapter. Using the image processing toolbox of MATLAB, geometric properties of all cleats are measured and a range of shape parameters are obtained. Feature specific image properties are sizes like cleat length, apertures and total size distributions.

The intensity and density, shape parameter and cleat spacing are also all measured. Relative orientations are given where a network of face and butt cleats is present. The connectivity of the cleat network is described by the Euler characteristic and the density of intersections. Distributions of cleat properties are both shown in histograms and log-log plots that are fitted with the power law function that describes the distribution best. In the log-log plots the centre of the bins that have been selected are used. An introduction to literature on distribution of fracture and cleat characteristics is given in chapter 2.5.5

6.3.3.1 Cleat length, aperture and size distribution

Cleat lengths extracted from the image are based on the major axis length of the extracted line-shaped features. Cleat apertures extracted from the image are based on the minor axis length (Figure 6-15). While fracture size often (e.g. Hooker et al., 2013) refers to length and height, it is defined as the area of the fracture face (length and aperture) for the present two-dimensional study. Fracture-size distribution have been found to either being centred onto a specific value with fewer smaller or larger values present (Priest & Hudson, 1976) or are scale-independent for example in power-law size distributions (Ortega et al., 2006).

6.3.3.2 Cleat intensity and density

In the presented two-dimensional case the total number of cleats, cleat intensity and density are useful measures to characterize the cleat system (Dershowitz, 1984). The intensity of cleats, given by equation 6-2, is calculated as the sum of the cleat area over the whole image area and is therefore dimensionless. The density is defined as the total number of cleats in the image area and given by equation 6-3.

$$intensity = \frac{cleat\ area}{sample\ area}\ [-] \qquad (6\text{-}2)$$

$$density\ = \frac{nr\ of\ cleats}{sample\ area}\ [mm^{-2}] \qquad (6\text{-}3)$$

6.3.3.3 Cleat shape

A useful parameter to define cleat shape is the ratio of aperture to length, shown in equation 6-4.

$$\frac{aperture}{length}\ [-] \qquad (6\text{-}4)$$

The relation between fracture aperture b and length l has been proposed to follow equation 6-5

$$b = i\ l^{c} \qquad (6\text{-}5)$$

with i being a constant and c varying between 0.5 and 2 (Bonnet et al., 2001).

6.3.3.4 Cleat spacing

The perpendicular spacing between the cleats in the region of interest is determined and average cleat spacing for both orientations is calculated. Following the principle of scanline mapping based on Acoustic Televiewer and Optical Televiewer logs that is used in the field (Jing & Stephansson, 2007) a grid perpendicular to the main features in the image is constructed (Figure 6-9). It consists of a total number g of 31 gridlines in the diagonal case and 17 gridlines in the vertical case with a distance of each 2.65 mm between the lines. The distance between features along the gridlines is measured.

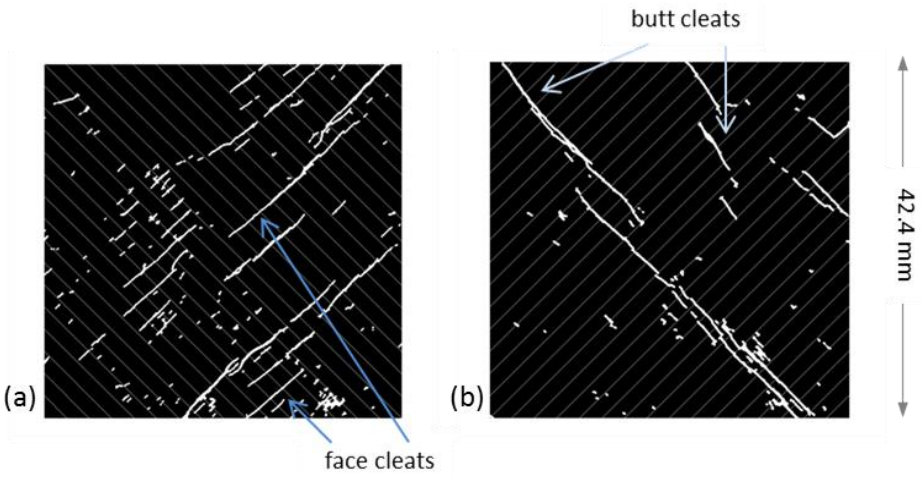

Figure 6-18 Spacing measurements along grid with 2.65 mm distance for a. Face and b. Butt cleats

Quantitative statements of spacing are only meaningful with a scale reference included in the analysis and the method that has been used to measure cleat spacing. Laubach et al. (1998) plotted cleat spacings that represent the averages of all measured spacings having a specific aperture measurement and found cleat spacing to increase linearly with cleat aperture that spanned a particular fractured bed. In this case study the average of spacing and apertures along the gridlines that are shown in Figure 6-18 are used. An illustration of a representative gridline is shown in Figure 6-19.

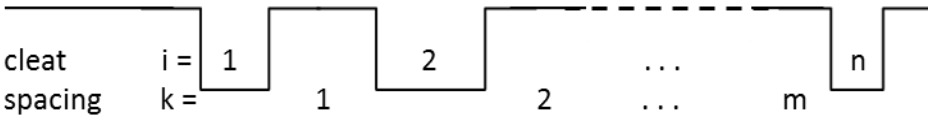

Figure 6-19 Cleats and spacings along gridline

For a representative gridline with a number of cleats, I, of a certain aperture and a number of k spacings of a certain length, the equations 6-6 and 6-7 have been established

$$avg\ spacing = s_{avg} = \frac{\sum_{k=1}^{m} spacing}{\sum_{i=1}^{n-1} nr\ of\ cleats} \quad (6\text{-}6)$$

$$avg\ aperture = \mathrm{b}_{avg} \frac{\sum_{i=1}^{n} aperture}{\sum_{i=1}^{n} nr\ of\ cleats} \quad (6\text{-}7)$$

Displaying the average spacing, s_{avg}, against the average aperture, b_{avg}, in a log-log plot, a power law can be fitted that follows equation 6-8

$$s_{avg} = i\ {b_{avg}}^{-c} \quad (6\text{-}8)$$

with I, being a coefficient of proportionality and c, the power law exponent (Laubach et al., 1998).

As an average over the sum of the gridlines in the image the gridline frequency is defined using equation 6-9.

$$gridline\ frequency = \frac{\sum_1^g nr\ of\ cleats\ along\ gridlines}{\sum_1^g gridline\ length}\ [mm^{-1}] \qquad (6\text{-}9)$$

6.3.3.5 Cleat orientations

Cleat orientations are illustrated using rose plot diagrams. The orientation of each cleat is calculated as the angle from the x-axis of the input image and displayed in fractions of 360 degrees. To illustrate length differences between face and butt cleats, the cleats are weighted by their length in mm. For example a cleat of 10 mm length is counted ten times, a 5 mm long one five times. The cleat orientations show relative orientations of face and butt cleats to each other. The plot is therefore only made for samples where face and butt cleats are present.

6.3.3.6 Cleat connectivity

Long & Witherspoon (1985) show that the degree of interconnection and, therefore, the permeability increases as fracture lengths and densities increase. Using image processing methods, structural connectivity of features can be described using the Euler characteristic. In 2D the Euler characteristic is the total number of features, C, in the image minus the total number of holes, H, in those features and shown in equation 6-10.

$$E = C - H \qquad (6\text{-}10)$$

For a network in which at least one path exists between any two nodes, the maximum number of branches that could be removed without breaking the network into parts is 1 - N. Breaking a single connection increases the Euler characteristic by 1, the addition of a connection decreases it by 1. In other words: the Euler characteristic is a measure of how many connections in a structure can be severed before the structure falls into two separate pieces (Odgaard & Gundersen, 1993). Therefore, depending on the material of interest, a highly connected structure has a negative Euler characteristic of up to several thousand in a volume of 1 cm^3.

Besides the total length of fractures in the region of interest, the density of fracture intersections is a measure for connectivity of a system (Jing & Stephansson, 2007). It is defined by equation 6-11 as the number of cleat intersections per image area.

$$density\ of\ cleat\ intersections = \frac{nr\ of\ cleat\ intersections}{image\ area}\ [mm^{-2}] \qquad (6\text{-}11)$$

6.3.4 Cleat properties

6.3.4.1 Cleat properties Sample 11 1/3

Cleat geometry Sample 11 1/3

Sample number E2 was taken at the Elphinstone seam. The scanned sample is of 7.5 cm length and was taken in a depth of 290.79 to 290.865. The image with an area of 1797.76 mm^2 refers to an in-situ depth of 290.8 m. The image processing workflow has been introduced using this example. Face cleats and butt cleats are present (Figure 6-20).

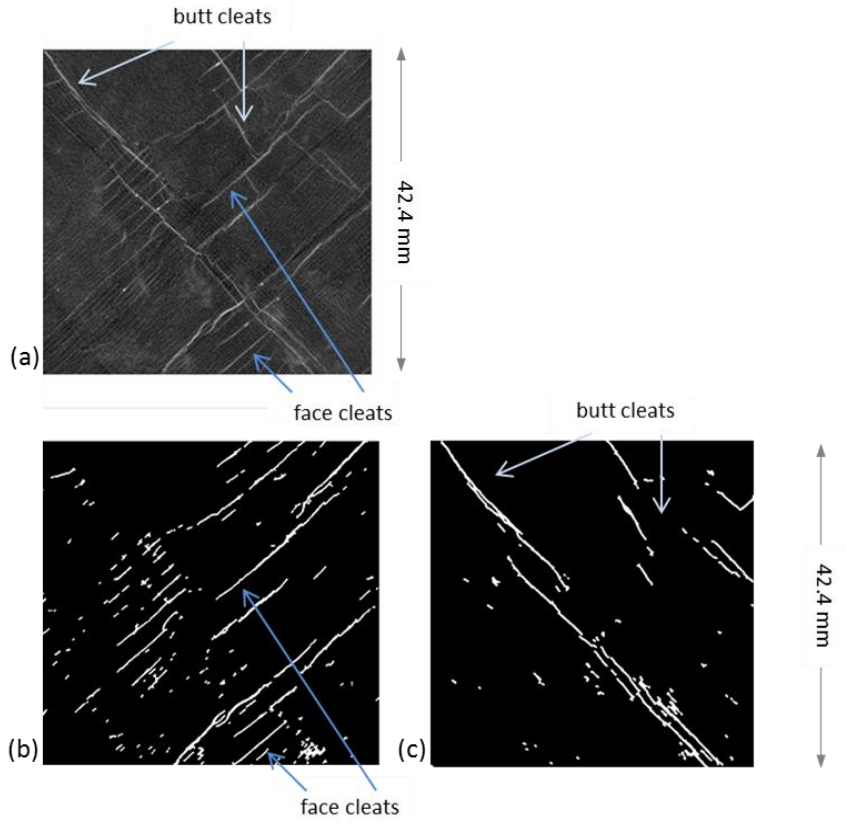

Figure 6-20 a. CT-scan of sample 11 1/3 and binary image of b. face cleats and c. butt cleats after segmentation

Cleat length, aperture, and size distribution Sample 11 1/3

The total number of face cleats is 139; the total number of butt cleats is 60. The total face cleat length sums up to 311.19 mm, for butt cleats to 179.7 mm. The cleat length distribution follows a power law distribution (Figure 6-21a). Looking at the distributions of the aperture, they follow a power law distribution for both cleat types (Figure 6-21b). The total area size of butt cleats in the image is 56.08 mm^2, the face cleats take up 74.90 mm^2. The cleat size distributions are shown in Figure 6-21c.

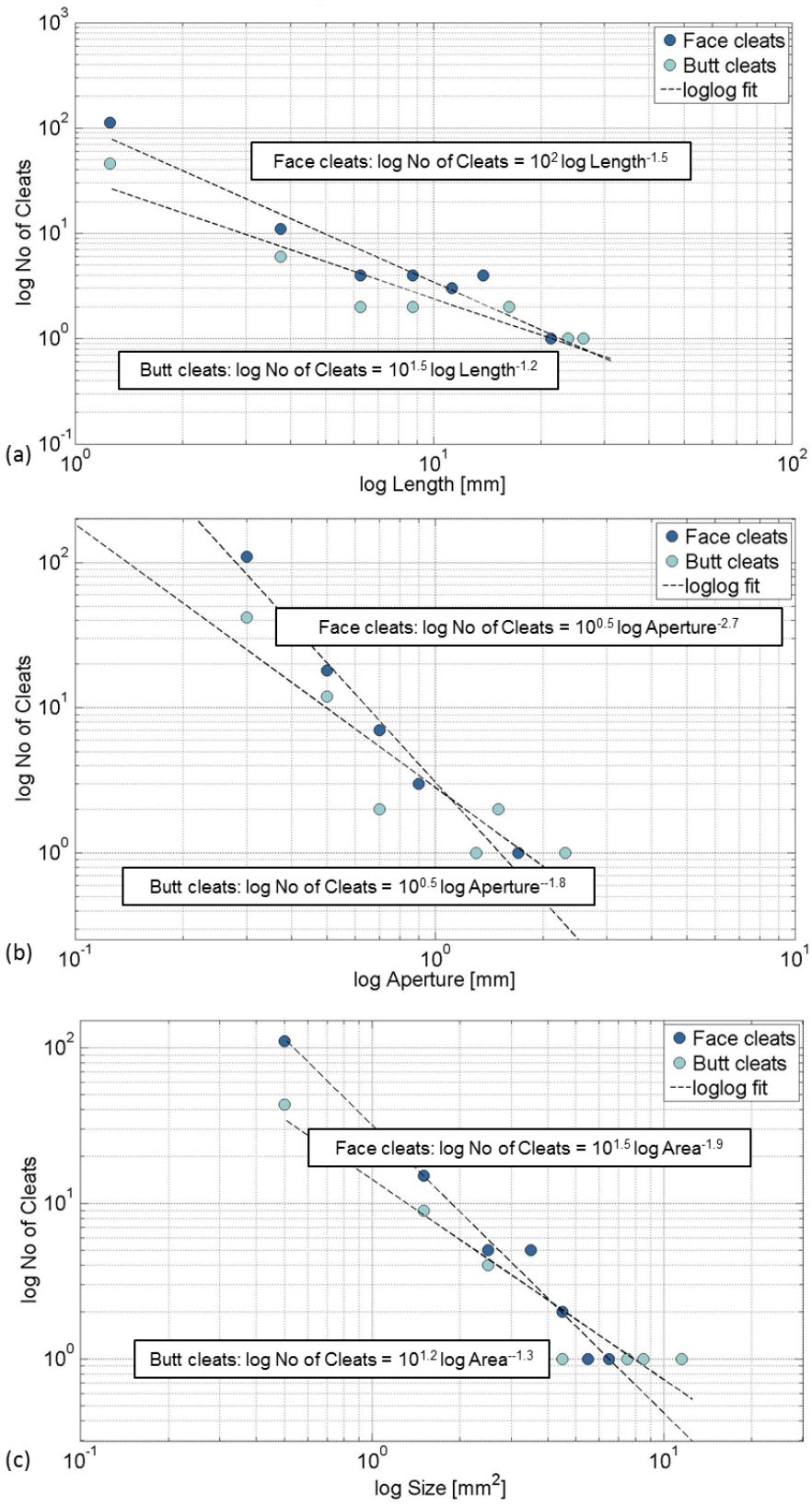

Figure 6-21 log-log plot of a. Length distribution, b. Aperture distribution, c. Size distribution of sample 11 1/3

Cleat intensity and density Sample 11 1/3

Cleat intensity measured for the face cleats is 0.0417, for the butt cleats it is 0.0312. The cleat density of the face cleats is 0.077 mm^{-2} and 0.0334 mm^{-2} for the butt cleats.

Cleat shape Sample 11 1/3

The shape parameters of the sample 11 1/3 is shown in Figure 6-22.

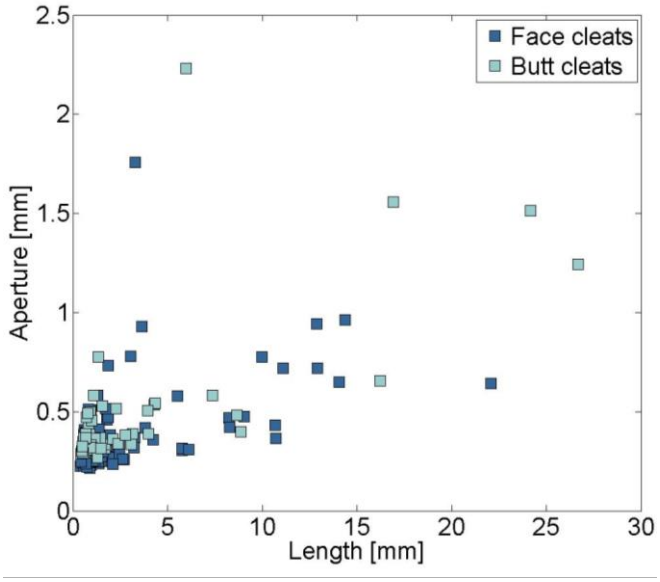

Figure 6-22 Aperture / length ratio

Cleat spacing Sample 11 1/3

For the face cleats a gridline frequency of 0.1477 mm^{-1} has been found, for the butt cleats the gridline frequency is 0.0998 mm^{-1}. The cleat spacing distribution is shown in Figure 6-23. No clear relationship between average spacing and average aperture along the gridlines can be established. The plots (Figure 6-24a and Figure 6-24b) reveal a random distribution of these two parameters when related to each other.

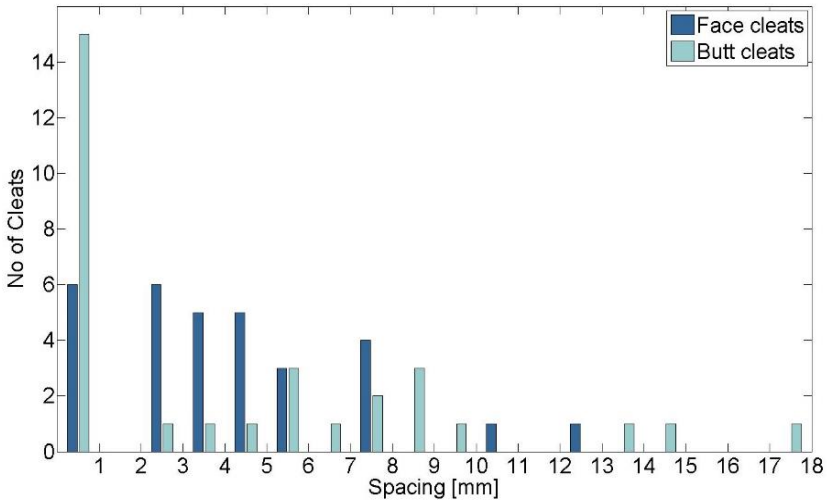

Figure 6-23 Cleat spacing distribution

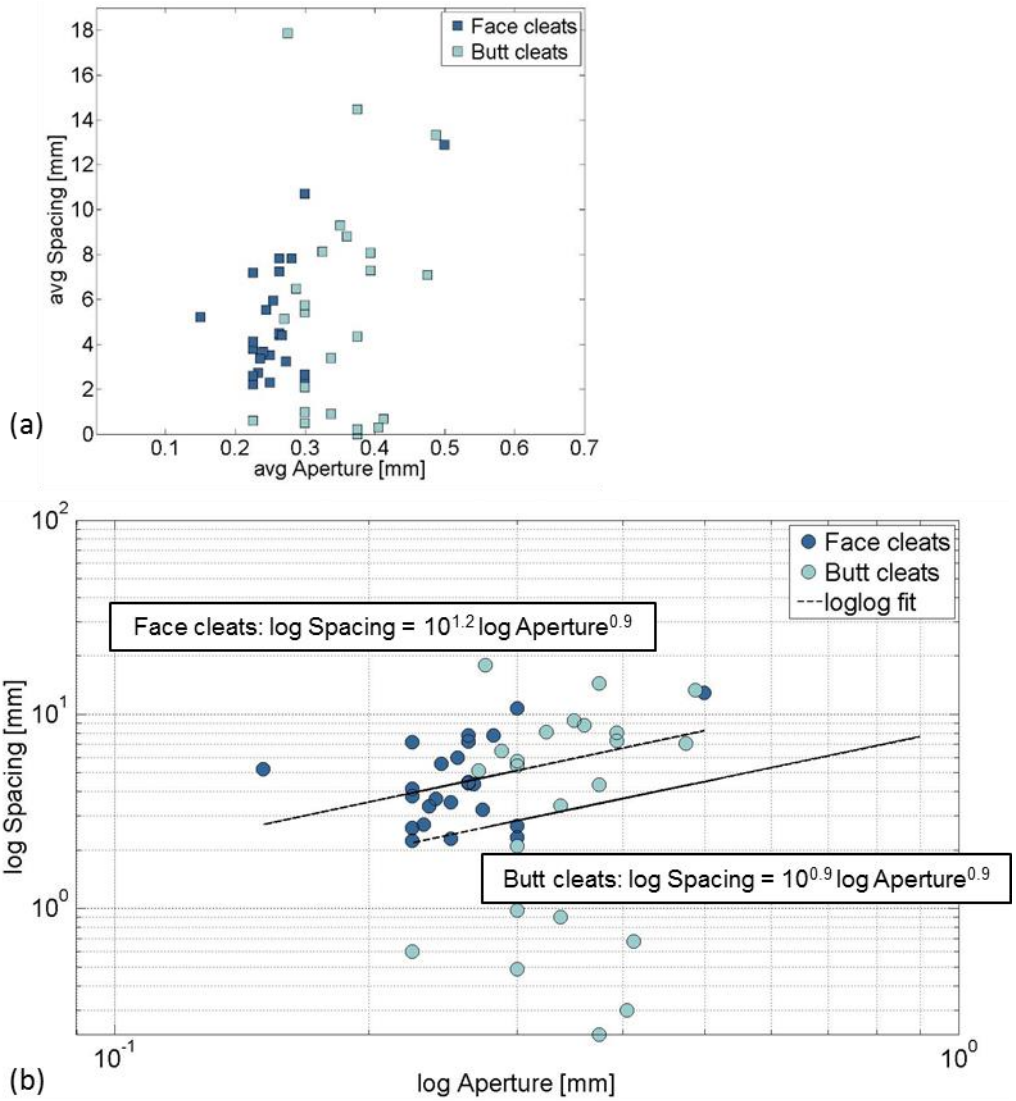

Figure 6-24 a. Ratio between average spacing and average aperture along gridlines, b. log-log plot of spacing against aperture along gridlinesfor sample 11 1/3

Cleat orientation Sample 11 1/3

Sample 11 1/3 is an example of a cleat network with the characteristic perpendicularity between face and butt cleats that has been described by Laubach et al. (1998). The rose plot shows the relative abundance of face cleats compared to the butt cleats (Figure 6-25)

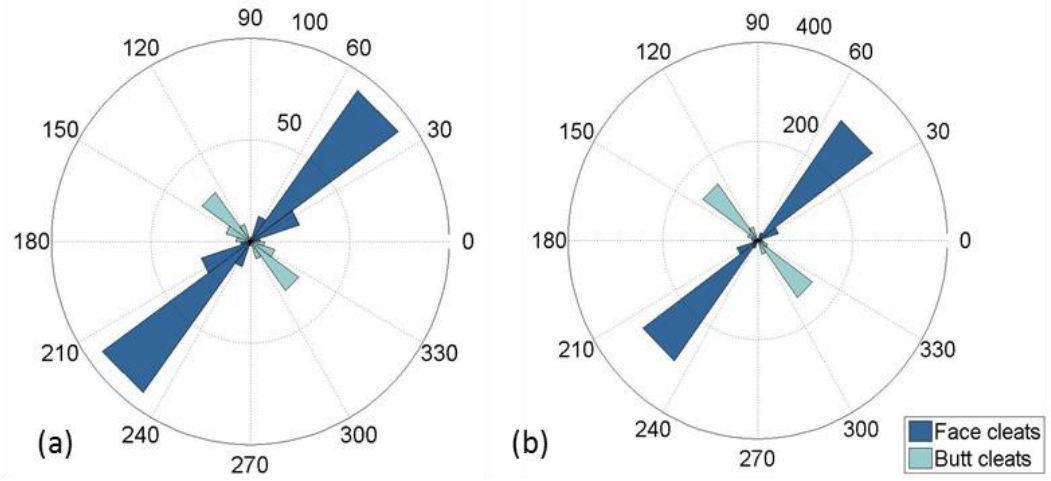

Figure 6-25 Rose plot of cleat orientations of sample 11 1/3: a. Total number, b. Weighted by their length

Cleat connectivity Sample 11 1/3

The network of face and butt cleats is well connected with a density of intersections given by the number of branch points in the image area: 238. The connected elements are shown in Figure 6-26, as well as a table of the occurring Euler characteristics. The negative Euler characteristic is summing up to -12.

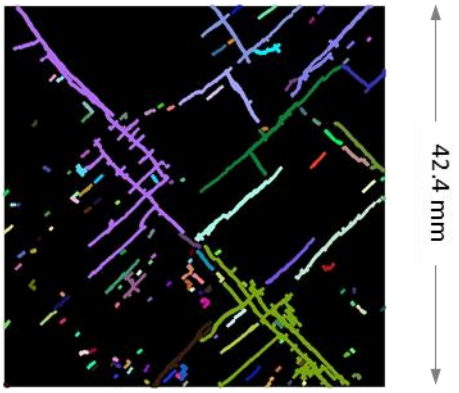

Euler Characteristic	Occurrence
-7	1
-4	2
-1	1
0	2
1	130

Figure 6-26 a. Connected elements distinguished by colours b. Occurrences of Euler characteristic

6.3.4.2 Cleat properties Sample 15 2/3

Cleat geometry Sample 15 2/3

Sample number H1 was taken at the Hynds seam. The scanned sample is of 7.45 cm length and was taken in a depth of 361.66 m to 361.74 m. The image with an area of 1797.76 mm^2 refers to an in-situ depth of 361.69 m. In this sample parallel face cleats, but no butt cleats are visible (Figure 6-27)

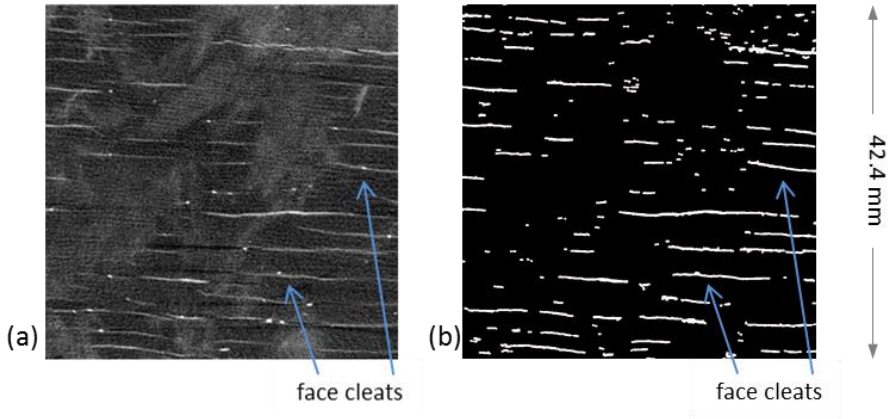

Figure 6-27 a. CT-scan of sample 15 2/3 and b. binary image of face cleats after segmentation

Cleat length, aperture, and size distribution Sample 15 2/3

The total number of the face cleats is 172. The total face cleat length sums up to 412.26 mm. Cleat length distribution can be fitted to a power law distribution (Figure 6-28a). The aperture of the face cleats in sample H1 follows a power law distribution that is shown in the plot in Figure 6-28b. The total area size of face cleats in the image is 103.67 mm^2. The cleat size distribution follows a power law distribution (Figure 6-28c).

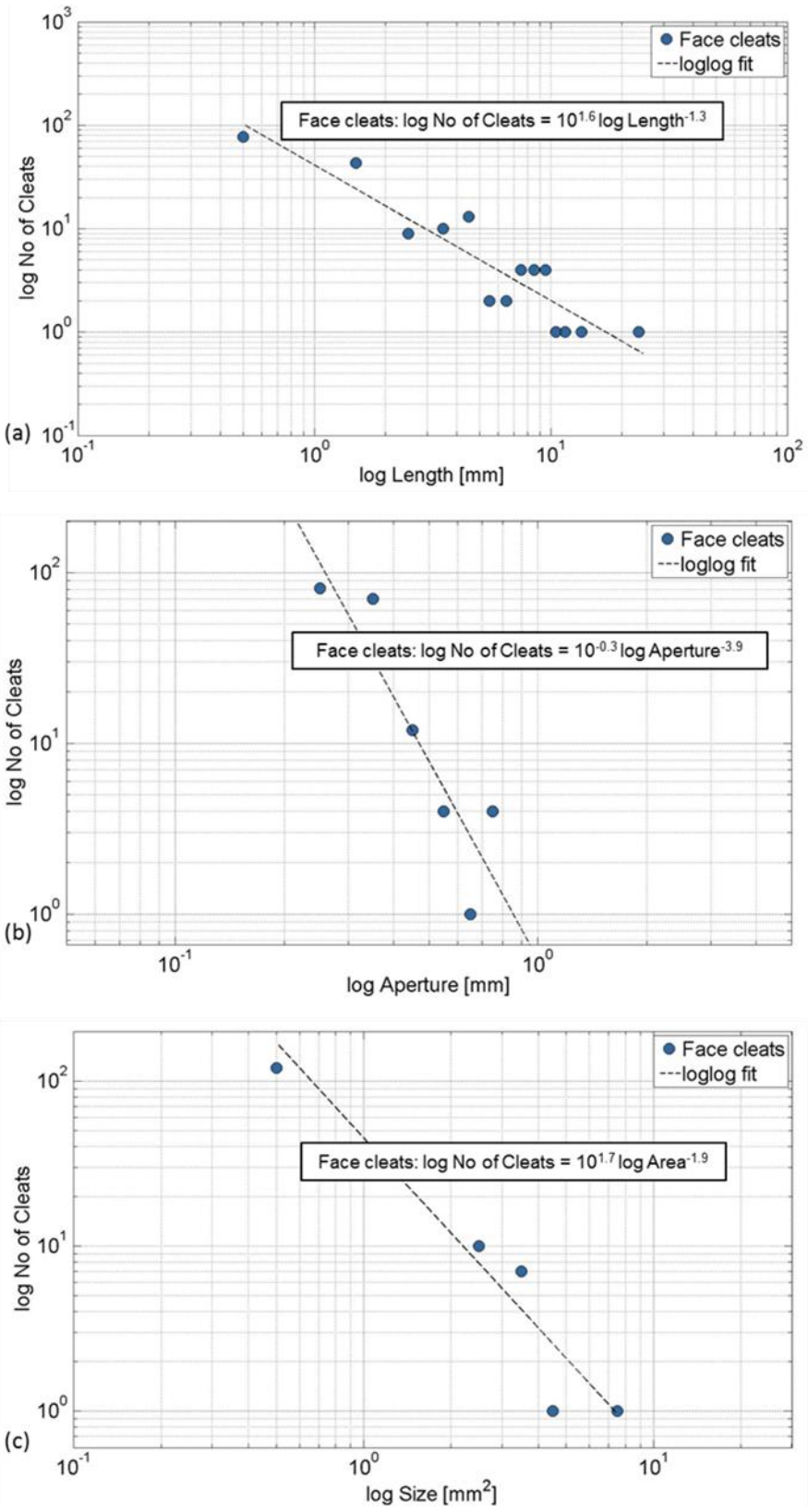

Figure 6-28 log-log plot of a. Length distribution, b. Aperture distribution, c. size distribution of sample 11 1/3

Cleat intensity and density Sample 15 2/3

The cleat intensity of the face cleats is 0.058, and their cleat density is 0.096 mm^{-2}.

Cleat shape Sample 15 2/3

The ratio of aperture and length is shown in Figure 6-29. The aperture vs. length plot shows two main directions of the distributions with some of the very short cleats having longer apertures than average and another set of cleats having larger apertures with increasing lengths.

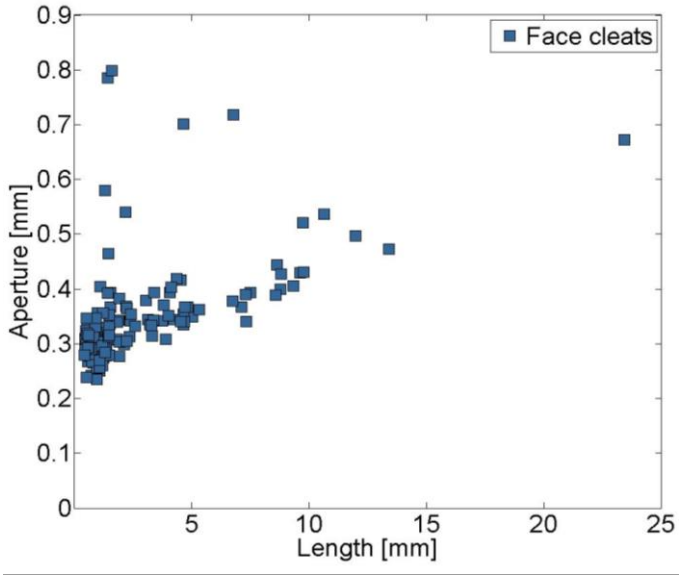

Figure 6-29 Aperture / length ratio

Cleat spacing Sample 15 2/3

The gridline frequency of the face cleats is 0.204 mm^{-1}. The cleat spacing distribution is shown in Figure 6-30. Ratios between average spacing and average apertures (Figure 6-31a and Figure 6-31b) reveal no apparent relationship between these two parameters.

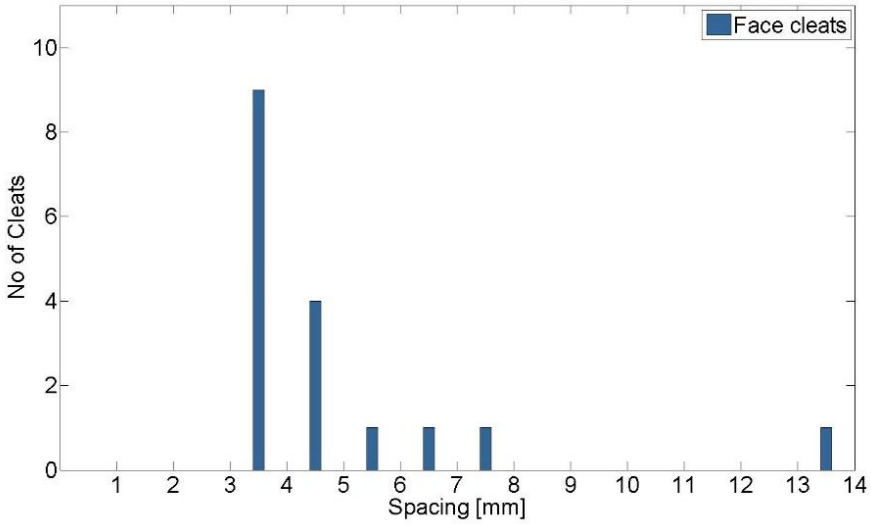

Figure 6-30 Cleat spacing distribution

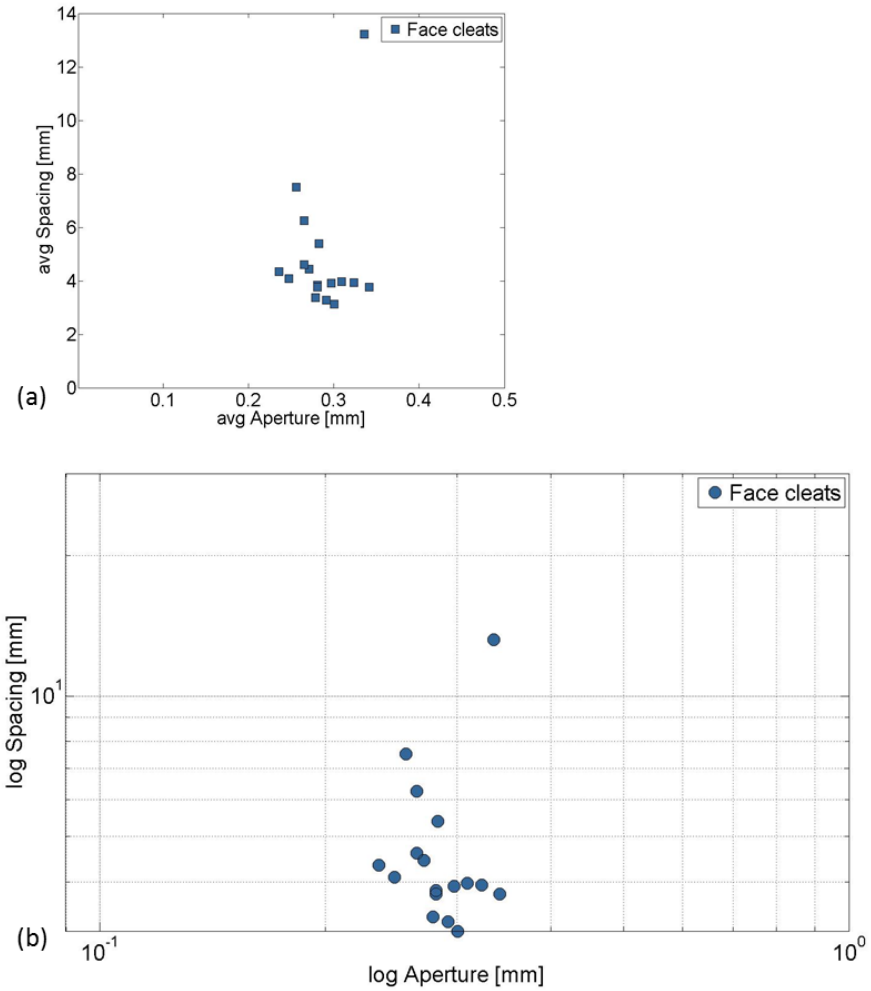

Figure 6-31 a. Ratio between average spacing and average aperture along gridlines, b. log-log plot of spacing against aperture along gridlines for sample 15 2/3

6.4 MINERALOGY AND POROSITY CHARACTERISATION

6.4.1 Testing principle

6.4.1.1 Mineralogy characterisation

Scanning electron microscopy and energy dispersive spectroscopy (SEM-EDS) is used for the characterisation of minerals and their relative abundance. The method is based on the scanning of an electron beam across the sample surface to generate an image based on the emission of secondary electrons, backscattered electrons, and X-rays. The emitted X-ray has an energy characteristic of the parent element. Detection and measurement of emitted X-ray energy permits the analysis of elemental composition (University at Buffallo, 2016).

6.4.1.2 Porosity characterisation

Porosity can be determined using helium pycnometry and mercury porosimetry.

Helium pycnometry is used to measure the density of porous media based on the displacement of gas and the constant relationship between volume V [m^3] and pressure P [N/m^2] that has been described as Boyle's Law and is given in equation 6-12 (Boyle, 1662).

$$P\,V = const. \qquad (6\text{-}12)$$

The pycnometer measures the pressure difference when pressurised helium is flowing from one cell with a defined volume into another cell of a defined volume which contains the sample of the porous medium. The volume of the sample is determined based on the decrease of pressure within the system. The density of the sample is then deducted by its mass divided by its volume (Rude & Strait, 2000). Helium pycnometry has for example been used for testing of coal by Massarotto, Iyer, & Bae (2008).

Mercury Porosimetry is a widely used analytical technique to quantify parameters of a porous material. These parameters could include the total pore volume, pore diameter, surface area, as well as bulk and absolute densities. The technique is based on the intrusion of a non-wetting liquid, that is, a liquid with a contact angle greater than 90° under high pressure into the porous medium. For this study, mercury is used. Using a porosimeter, the pore size can be determined based on the pressure that is needed to force the liquid into a pore against the opposing force of the liquid's surface tension. The volume intruded at each pressure increment is used to determine the pore size distribution. With increasing pressure, the cumulative pore volume increases. Consequently, the total porosity equals to the total volume of the intruded liquid (Abell, Willis, & Lange, 1999). The relationship between the pressure and capillary diameter is based on an extension of the Washburn equation (equation 6-13) that describes capillary flow in a bundle of parallel cylindrical tubes (Washburn, 1921)

$$P = \frac{-4\,\gamma\,cos\theta}{d} \qquad (6\text{-}13)$$

with P being the pressure [N/m^2]. γ denotes the surface tension of the non-wetting liquid [mN/m], which for mercury is 480 mmN/m at 20 °C under vacuum. The contact angle θ [°] between mercury and most solids is between 135° and 142°. The diameter d of the capillary is given in [m].

6.4.2 Test set-up

The two HQ size core samples, 11 1/3 (Elphinstone seam) and 15 2/3 (Hynds seam) (see Table 6-1), were provided to the School of Earth Sciences at the University of Queensland for the investigation of core mineralogy and total core porosity. Scanning electron microscopy and porosity analysis using helium pycnometry and mercury porosimetry were undertaken. The majority of cleats for both samples were found to be mineralised.

6.4.2.1 Mineralogy characterisation

Scanning electron microscopy and energy dispersive spectroscopy (SEM-EDS) was used to determine the relative abundance and textural context of mineral occurrence for core samples i.e. major, moderate and minor mineralisation in the face cleats, butt cleats, and coal matrix. The samples were initially sonicated in ethanol for approximately 6 hours to remove the kaolin surface coating that was residual from the triaxial cell test. This was largely successful, though some core breakage occurred, particularly in 11 1/3. Despite core breakage, two whole coal blocks containing mineralised cleats were extracted from each core sample (four in total) and mounted in epoxy resin. The blocks were then polished and carbon coated before SEM-EDS studies using a low vacuum JEOL6460LA environmental SEM with EDS detector at the UQ Centre for Microscopy and Microanalysis (CMM). All samples were imaged in the bedding plane view. The approximate stoichiometric formula of minerals observed in this study are summarised in Table 6-2. Photographs of the polished epoxy mounted core blocks are shown in Figure 6-32.

Table 6-2 Approximate stoichiometric formulae of minerals found in this study.

Mineral	Formula
Kaolinite	$Al_2Si_2O_5(OH_4)$
Quartz	SiO_2
Illite-K	$K_{1.5}Al(Si_6Al_{1.5})O_{20}(OH)_4$
Ankerite	$(Fe,Ca,Mg)CO_3$
Calcite	$CaCO_3$
Anatase	TiO_2
Apatite	$Ca_5F(PO_4)_3$
Barite	$BaSO_4$
Sulphide	PbS

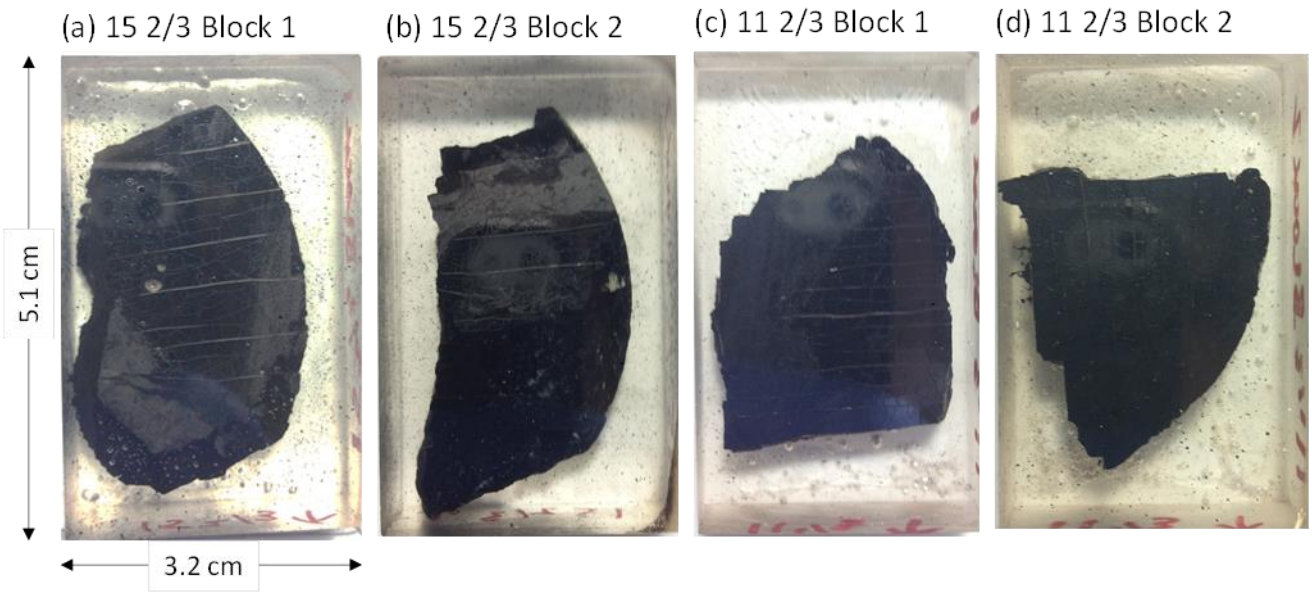

Figure 6-32 Photographs of polished coal blocks from 15 2/3 (a, b) and 11 1/3 (c, d). Note that only Block 1 from 15 2/3 and Block 2 from 11 1/3 have been analysed, though the mineralogy of Block 2 from each sample is not expected to be significantly different

6.4.2.2 Porosity characterisation

Two block samples from each core were prepared for porosity analysis by the following methods (Figure 6-33):

- Matrix/skeletal density via helium pycnometry (Micrometrics AccuPyc 1330);
- Bulk density, meso-, and macropore distribution via mercury porosimetry (Quantachrom Autoscan 60).

Repeated tests were performed for each core in order to determine heterogeneity effects. The total accessible porosity (ϕ) from each sample was determined using equation 6-14:

$$\phi = 100\rho_{Hg}\left(\frac{1}{\rho_{Hg}} - \frac{1}{\rho_{He}}\right) \qquad (6\text{-}14)$$

where ρ_{Hg} and ρ_{He} are the mercury and helium derived densities [g/cm^3], respectively. The mercury intrusion experiments were limited to a cut-off pressure of 55 MPa, as previous investigations have indicated that the coal matrix begins to collapse above this pressure level (Massarotto et al., 2010; Guo, Yao, & Liu, 2014).

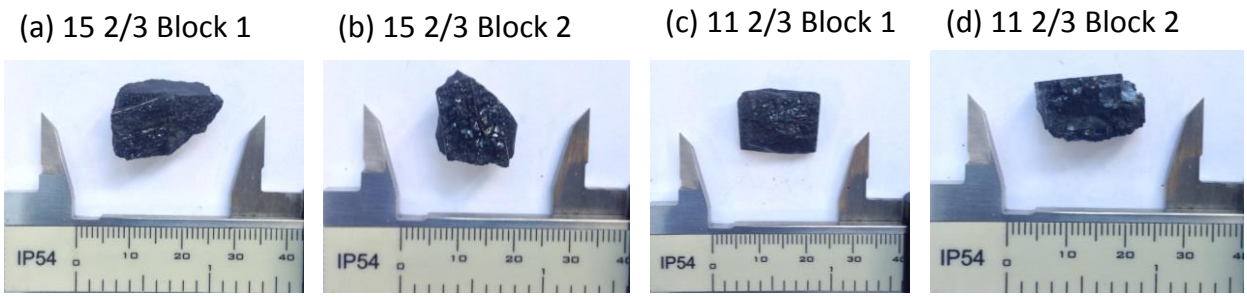

Figure 6-33 Photographs of coal blocks from 15 2/3 (a, b) and 11 1/3 (c, d) used during helium pycnometry and mercury porosimetry experiments.

6.4.3 Core mineralogy

The cleat and matrix mineralogy of 15 2/3 and 11 1/3 is summarised in Table 6-3. Example SEM images of cleat and matrix mineralogy for in 15 2/3 and 11 1/3 are shown in Figure 6-34 and Figure 6-35, respectively. Core mineralogy and the possible modes of occurrence of minerals in fractures are discussed below:

Table 6-3 Summary of major, moderate and trace mineralisation from face cleats, butt cleats and coal matrix.

Sample	Face cleats			Butt cleats			Matrix		
	Majors	**Moderate**	**Minors, trace**	**Majors**	**Moderate**	**Minors, trace**	**Majors**	**Moderate**	**Minors, trace**
15 2/3 Block 1	Kaolinite	N/A	Anatase	N/A	N/A	N/A	Kaolinite	Quartz, ankerite, illite (K)	Apatite, barite
11 1/3 Block 2	Kaolinite	Calcite	Anatase	Calcite, kaolinite	N/A	Anatase	Kaolinite	N/A	Apatite, sulphides

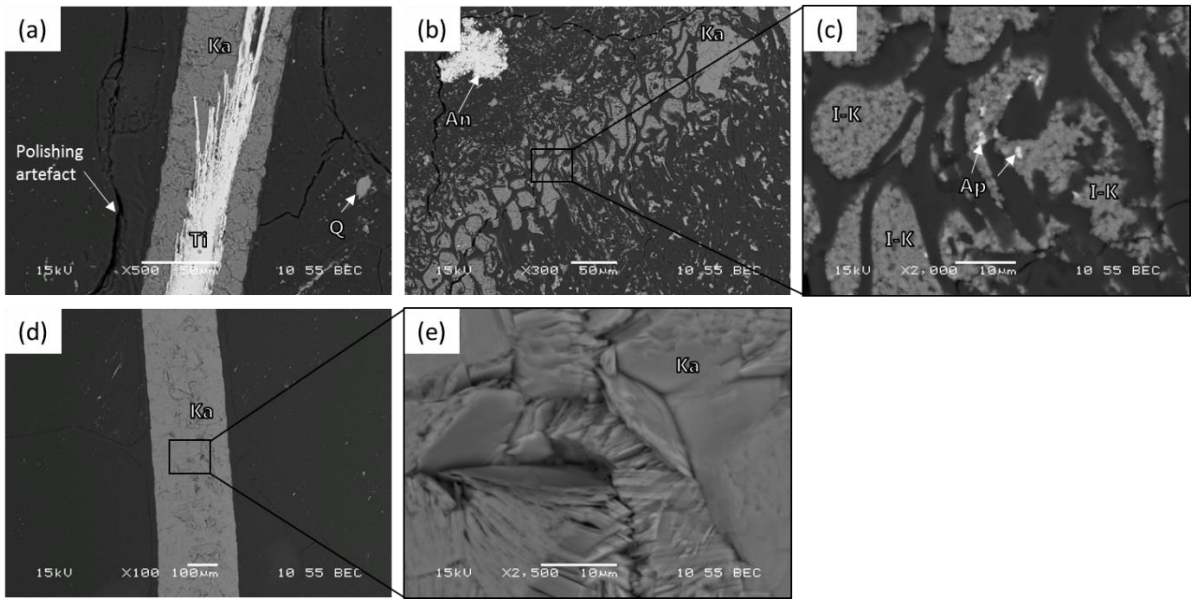

Figure 6-34 SEM images of 15 2/3 block 1. Ti = anatase, Ka = kaolinite, Q = quartz, An = ankerite, I-K = illite (K) and Ap = apatite. The micro-fractures in (a) were likely the result stresses formed during the polishing method.

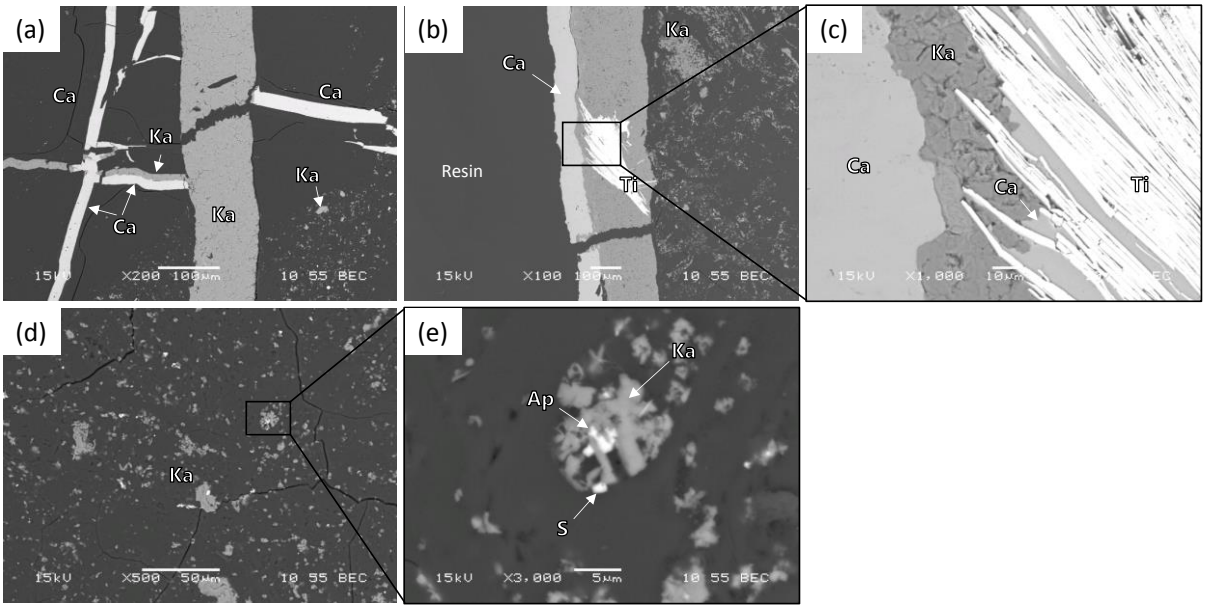

Figure 6-35. SEM images of 11 1/3 block 2. Ti = anatase, Ka = kaolinite, Q = quartz, An = ankerite, Ap = apatite and S = sulphide, variable composition.

Face cleats in 15 2/3 were predominantly kaolinite filled (Figure 6-34 d,e) with minor occurrences of anatase (Figure 6-34 a). No butt cleats in 15 2/3 were identified in the block investigated. They may still be present in alternative regions. The coal matrix of 15 2/3 contained predominantly kaolinite, with moderate ankerite, quartz and illite-K (Figure 6-34 b). Minor apatite was also visible within illite-K rich zones (Figure 6-34 c).

Face cleats in 11 1/3 were predominantly kaolinite-rich and contained some minor anatase (Figure 6-35 b, c). Butt cleats in and major secondary cleats in 11 1/3 contained mixed layer calcite and kaolinite (Figure 6-35 a). The mixed layer kaolinite/calcite mineralogy was also visible in larger face cleats (Figure 6-35 b).

It is possible that secondary cleat opening, caused by changes to the in-situ stress field, may have resulted in the intrusion of a calcite rich fluid and consequent calcite precipitation in 11 1/3. Matrix mineralisation in 11 1/3 was mostly kaolinite (Figure 6-35 d), though trace apatite and Pb-sulphides were also observed (Figure 6-35 e).

The cleat filling with kaolin is not thought to be an artefact from sealing the rubber sleeve around the sample when it has been tested in the triaxial cell (see chapter 5.2.2), as the coating has been removed in a sonicator and fragments from the centre of the core have been used for analysis.

6.4.4 Porosity

Porosity measurements for block samples from 15 2/3 and 11 1/3 are summarised in Table 6-4. Cumulative mercury intrusion and log differential intrusion profiles are shown in Figure 6-36. Pore volume distribution profiles are shown in Figure 6-37.

Table 6-4. Summary of measured porosity from helium pycnometry and mercury porosimetry.

Sample	Mass [g]	ρ_{He} [g/cm^3]	ρ_{Hg} [g/cm^3]	ϕ [%]
15 2/3 Block 1	2.335	1.53	1.39	8.97
15 2/3 Block 2	2.234	1.55	1.42	8.05
Average		1.54	1.41	8.52
11 1/3 Block 1	2.370	1.40	1.31	6.77
11 1/3 Block 2	2.022	1.39	1.31	6.25
Average		1.40	1.31	6.51

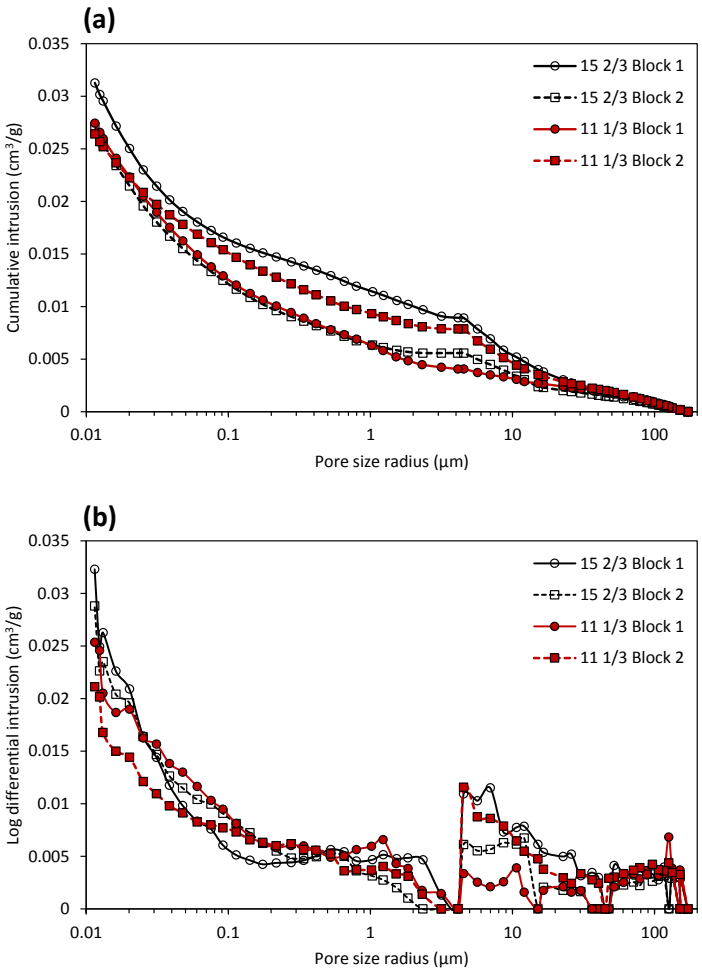

Figure 6-36 a. Cumulative mercury intrusion and b. log differential intrusion profiles for block samples

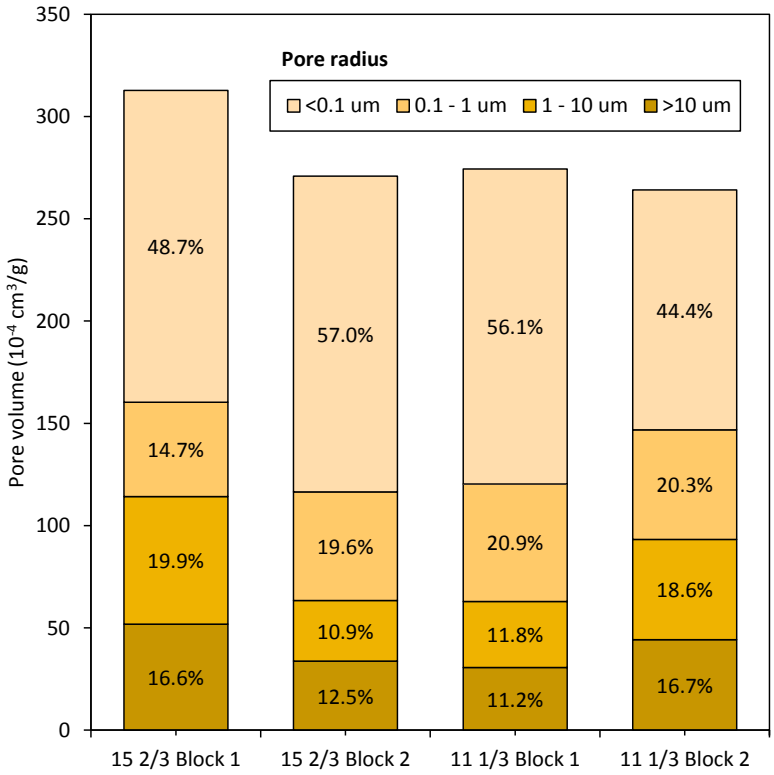

Figure 6-37 Pore volume distribution for 15 2/3 and 11 1/3 block samples

The intrusion profiles in Figure 6-36 show a tilt around a pore size radius of 4 – 5 µm. This is identified as the transition from matrix to cleat porosity, based on the SEM images (Figure 6-38). The majority of the cleats is heavily mineralised, so mercury intrusion into the cleats was relatively low, starting from 4 -5 µm. The SEM images have been used as evidence of cleat and matrix mercury intrusion rates for example by Klaver et al. (2012) and Ramandi et al. (2015).

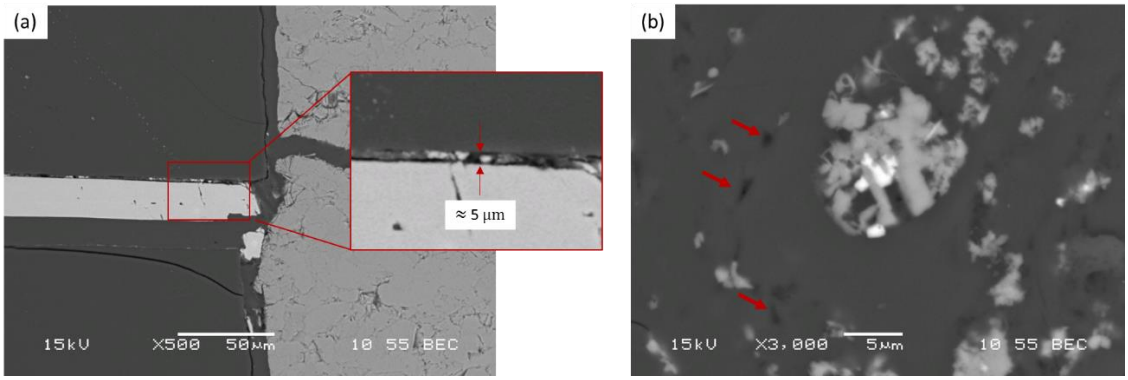

Figure 6-38 Evidence of mercury intrusion rates representing the sizes of a. Cleat porosity with values > 5µm and b. Matrix porosity with values < 5 µm. The image is showing sample 11 1/3 Block 1.

Based on this distinction, the porosities of cleats and matrix are determined. The ratio of the cumulative intrusion that accounts for the cleats to the total intrusion represents the ratio of the cleat porosity to the total porosity. Similarly, the ratio of the cumulative intrusion

into the matrix represents the ratio of the matrix porosity to the total porosity. The data is shown in Table 6-5.

Table 6-5. Summary of cleat and matrix porosity distinction

Sample	Total ϕ [%]	Type	Intrusion [%]	ϕ [%]
15 2/3 Block 1	8.97	Cleats	71.5	6.41
		Matrix	28.5	2.56
15 2/3 Block 2	8.05	Cleats	79.4	6.39
		Matrix	20.6	1.66
Average	8.51	Cleats	75.5	6.42
		Matrix	24.5	2.08
11 1/3 Block 1	6.77	Cleats	86.4	5.85
		Matrix	13.6	0.92
11 1/3 Block 2	6.25	Cleats	70.2	4.39
		Matrix	29.8	1.86
Average	6.51	Cleats	78.3	5.09
		Matrix	21.7	1.41

From these results, the following conclusions can be drawn. The average porosity of 15 2/3 was larger than 11 1/3. The average measured porosity of 15 2/3 was 8.51 %, compared to 6.51 % for 11 1/3. The cleat porosity for sample 15 2/3 is 6.4%, the matrix porosity is 2.01 %. For sample 11 1/3 the cleat porosity is 5.1%, the matrix porosity is 1.4%. The difference in measured porosity between adjacent block samples was larger in 15 2/3. The vast majority of sample porosity is below 0.1 μm and is similar for all samples (Figure 6-36). The porosity values explain the low intrinsic permeability of the samples that has been measured in the triaxial cell (see chapter 5).

Further characterisation methods such as N_2 adsorption would be required to determine the pore size distribution below 0.01 μm. Additional interpretation methods for mercury intrusion data are discussed by Webb (2001).

6.5 CONCLUSION

The structural characterisation of one sample of the Elphinstone seam and the Hynds seam included a two-dimensional image processing method, as well as scanning electron microscopy and energy dispersive spectroscopy (SEM-EDS) to determine the mineral occurrence in the core samples. Furthermore, cleat and matrix porosity have been measured.

Two network types of coal cleats have been described based on CT-scans taken from coal samples. The Elphinstone coal sample 11 1/3 reveals a coal network similar to the classic

butt/face cleat model. The sample of the Hynds seam shows parallel face cleats only. Cleat aperture has been found to follow a power law distribution, for butt as well as face cleats. Apertures were found in the range of 0.3 mm to 2.5 mm for butt cleats and 0.25 to 0.75 mm for face cleats. These values are in the same range as the results by Permana (2012) who found cleat aperture of Bowen Basin coals in the range from 0.3 mm to 1.5 mm in a CT-scan analysis with a resolution of down to 2 µm, but did not make a distinction between face and butt cleats

These values are larger than the results of similar studies by Karacan & Okandan (2000) and by Weniger et al. (2016). For two different coals from north-western Turkey, coal cleat aperture was found in a polished surface analysis to fall into the range of 40–60 µm (mean value 47.1 µm) and 10–30 µm (mean value 20.2 µm) (Karacan & Okandan, 2000). For a set of 17 samples from various international sites with varying degrees of coalification apertures in the range of 2 µm to 2 mm (median value of 29 µm) was measured (Weniger et al., 2016). This discrepancy might be due to the different methods used and the different resolution of the obtained images. While in this study a pixel size of 53 µm is used, the pixel sizes range between 2.3 µm and 45.1 µm for the study of Weniger et al. (2016). However, the similarities with the results of the study by Permana (2012) hint at the possibility that the differences are due to rank and type of coal.

No clear relationship between spacing and aperture could be established. A large range of the cleat spacings that have been measured are smaller than the range of 10 -25 mm given in the literature. This might be due to the fact that the cited study (Wang et al., 2009) was focused upon large-scale major cleats. The image processing based method captured the more common small-scale cleats with spacings of less than a millimetre, as have been described by Dawson and Esterle (2010). This observation points out the usefulness of high resolution CT-scans, but also the fact that spacing measurements are limited by the diameter of the core sample. The maximum spacings have been found to be smaller for face cleats (max. 13 mm) than for butt cleats (max. 27 mm).

In all cases the total number of face cleats outweighed the total number of butt cleats, as did the total length of the face cleats. Gridline frequencies of face cleats are higher than those of the butt cleats. The same holds true for the area sizes, which always follow a power law distribution. While density of face cleats is generally larger than those for butt cleats, intensity values follow no clear pattern when comparing face cleats and butt cleats. As butt cleats are formed to accommodate relaxation of the stress which originally lead to the formation of the face cleat structure, the lack of a clear pattern regarding cleat intensity

could be due to the relaxation of the sample after coring. However, since in this study mineralised cleats are investigated, this can be excluded.

Two approaches have been tested to describe the connectivity of the cleat networks: the number of branchpoints, as well as the Euler number. The number of branch points for the Elphinstone sample is 197. The Euler characteristics sums up to -12.

Face cleats in 15 2/3 were predominantly kaolinite filled (Figure 6-34 d, e) with minor occurrences of anatase (Figure 6-34 a). No butt cleats in 15 2/3 were identified in the block investigated. They may still be present in alternative regions. The coal matrix of 15 2/3 contained predominantly kaolinite, with moderate ankerite, quartz and illite-K (Figure 6-34 b). Minor apatite was also visible within illite-K rich zones (Figure 6-34 c). Face cleats in 11 1/3 were predominantly kaolinite-rich and contained some minor anatase (Figure 6-35 b, c). Butt cleats in and major secondary cleats in 11 1/3 contained mixed layer calcite and kaolinite (Figure 6-35 a). The mixed layer kaolinite/calcite mineralogy was also visible in larger face cleats (Figure 6-35 b).

The average porosity of 15 2/3 was larger than 11 1/3. The average measured porosity of 15 2/3 was 8.51 %, compared to 6.51 % for 11 1/3. The cleat porosity for sample 15 2/3 is 6.4%, the matrix porosity is 2.01 %. For sample 11 1/3 the cleat porosity is 5.1%, the matrix porosity is 1.4%. The porosity in cleats is decisive for the resulting permeability in cleat structures.

7. Numerical Modelling

7.1 INTRODUCTION

The behaviour of fluid flow is strongly influenced by the geotechnical features defining the fracture system, like orientation, aperture, and geometry of fractures which usually exhibit large variabilities. In order to quantify these heterogeneities of samples on the micro-scale, the CT-scans of the coal samples introduced in Chapter 6.3 are used. Based on the CT-scans, the cleat network is reconstructed in three dimensions. Blocks of centimetre sizing representing the cleat network are obtained in a micrometre resolution with a voxel size of 53 µm.

In order to assess the relations of permeabilities across the micro-scales, the artificial blocks representing the cleat network are segmented into smaller partitions covering a range of 0.02 cm^3 to 95.28 cm^3. After breaking the samples down into smaller subsamples, the permeability tensor is determined using a LBM based code for each subsample, and the permeability results across scales are analysed. The fluid flow modelling is based on the definition of a heterogeneous system of interconnected cleats, as introduced in chapter 2.4.1 and shown in Figure 2-11c. Based on the literature that reports the matrix of coal to be effectively impermeable (see chapter 2.2.4) and the core mineralogy of the cleats observed in chapter 6.4. The lowest permeabilities are assumed to be in bed normal direction (z-direction).

The aim of the numerical modelling is to assess the permeability variation across a range of scales that becomes accessible by modelling the cleat structure and numerically breaking the samples into smaller partitions. The insight into the distributions of permeabilities across the range of volumes of 0.02 cm^3 to 95.28 cm^3 helps to establish the representative element volume.

To facilitate the distinction, the results for the Elphinstone sample (11 1/3) are plotted in blue, results for the Hynds sample (15 2/3) are shown in a green colour scheme.

7.2 MODELLING FLUID FLOW AND PERMEABILITIES USING LBM

The preparation of data sets to be imported into the LBM model consists of three different stages. Coal samples need to be taken first (see 4.3) and prepared to allow further investigations. These samples are scanned using X-Ray (see 6.1) and the resulting data

are further analysed based on an image processing workflow. The full cleat network is reconstructed and fluid flow is simulated within the cleat network in three dimensions. The workflow for the Lattice Boltzmann modelling and the analysis of the results is shown in Figure 7-1 and the individual steps are introduced in more detail in the following.

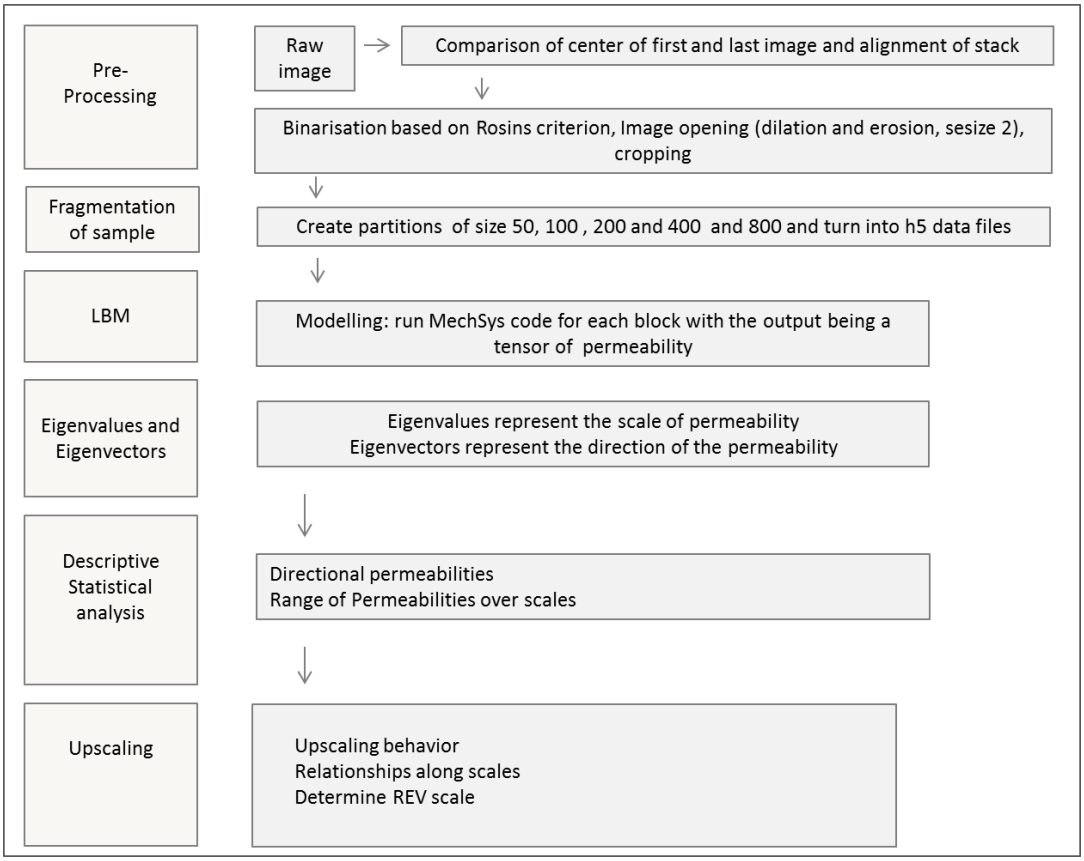

Figure 7-1 Workflow of modelling efforts and data analysis

7.2.1 Pre-processing

The CT-scans that were acquired in an earlier stage (6.1) are used as a basis for the numerical modelling. An image processing method was developed based on MatLab Image processing toolbox. A sequence of basic image processing steps were implemented consisting of reading the raw image that is similar to the two-dimensional method explained in chapter 6.3.2, with the difference that in this case a stack of images in used to create a three-dimensional dataset. The images obtained during the CT-scans are representing the inner structure of the sample in a 53 µm resolution. That is, images are taken at intervals of 53 µm in z-direction of the samples (Figure 6-2).

After cropping, the dimensions of each two-dimensional image are 800 x 800 pixels^2, showing an image region of 4.24 x 4.24 cm^2. For the numerical simulations the coal sample is reconstructed in three dimension of a stack of 1000 images, therefore the total

length of the reconstructed sample is 5.3 cm. Binarisation of the stack is based on the grayscale distribution by Rosin (2001) (see Figure 6-7). The grayscale distribution is calculated for each of the 1000 images and the average of all is applied to the whole stack of images. Filtering of small clusters and image opening to bridge possible blur in the scan is done with a circular structural element of 2 pixel size radius. To ensure that the sample is aligned along its main axis, the first and the last image are compared and the centre of the sample is imaged (Figure 7-2). If there is a deviation between the centres, the angle of the deviation is calculated and the each image is aligned so it centred based on the centre of the first image.

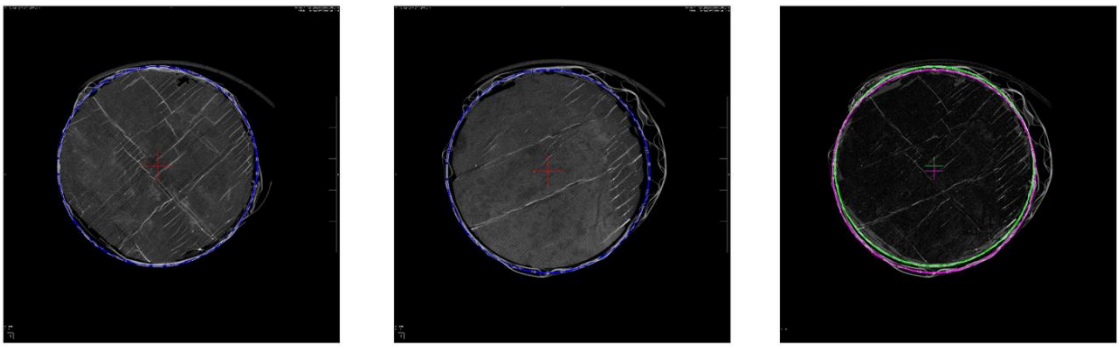

Figure 7-2 Centre of a. first and b. last scan and c. their overlap (Sample 11 1/3)

7.2.2 Partition of the sample

First, a square-shaped column is digitally extracted from the cylindrical sample, which is then further divided into five cubes of 800 x 800 x 200 voxel size. Each of these can then be further divided four times to finally receive a cube with 50-pixel side-length. The partition of the sample is shown in Figure 7-3. The image shows the sub-segmentation of the first of the five blocks of a size of 800 x 800 x 200 voxel. The same is done for the following four partitions, so that altogether, each sample is broken down into 5865 subsamples.

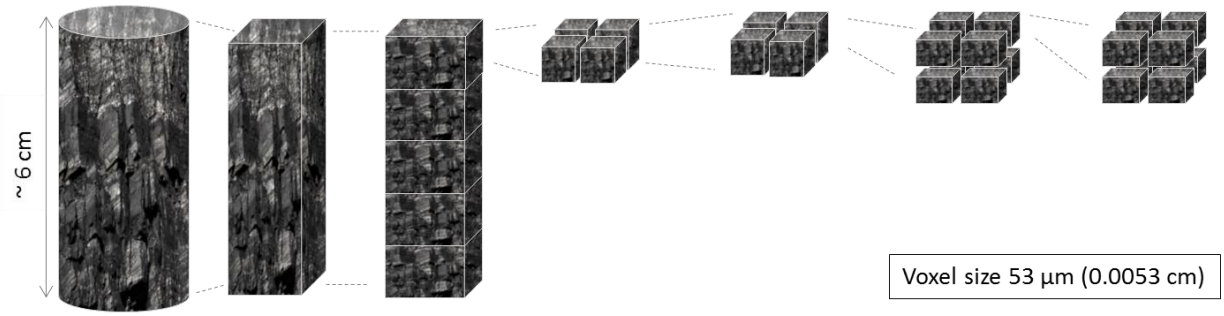

Partition	1	5	4	4	8	8
Voxel dimension	800×800×1000	800×800×200	400×400×200	200×200×200	100×100×100	50×50×50
Number of cells	640,000,000	128,000,000	32,000,000	8,000,000	1,000,000	125,00
Block size [cm]	4.24×4.24×5.3	4.24×4.24×1.06	2.12×2.12×1.06	1.06×1.06×1.06	0.53×0.53×0.53	0.27×0.27×0.27
Block size [cm^3]	95.281	19.056	4.764	1.191	0.149	0.0197
Total nr of blocks	1	5	20	80	640	5120

Figure 7-3 Sample segmentation and resulting block sizes

A naming convention allows identifying the sub-samples of each sample. It includes a coding of the block size (e.g. cutTDM050 or cutTDM800) and consists of five blocks of numbers that represent the x, y and z position of the block of each stage of segmentation. Figure 7-4 shows the naming based on the example of a block of 200 voxel side length that is divided into eight blocks of 100 voxel side length.

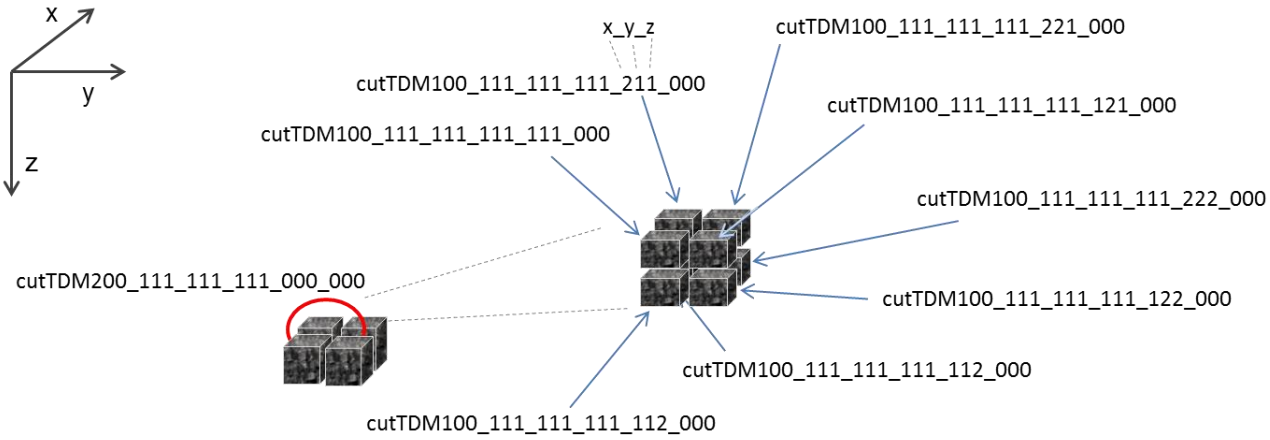

Figure 7-4 Naming convention to identify derivation of sub-samples

Lattice - Boltzmann based simulations are conducted with each subsample, as well as the whole block. For a better understanding, a visual example of a binarised sample of 200-pixel side length with its eight sub-samples is shown in Figure 7-5. The numbers represent short versions following the naming convention. Because the aim of this work is to establish the representative element volume, the analysis in the following is expressed in cm^3 volumes rather than voxel dimensions.

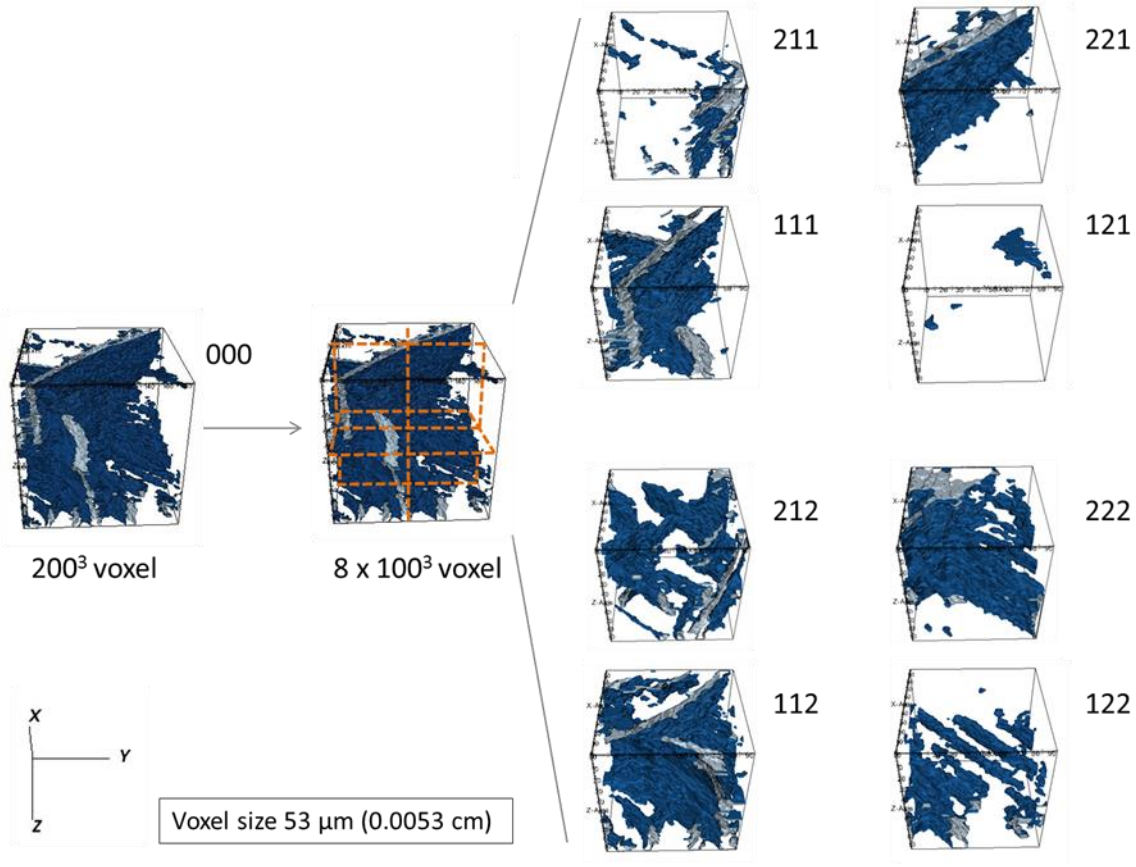

Figure 7-5 An example of a binarised sample (200 x 200 x 200 voxel) and its eight partitions

7.2.3 Modelling fluid flow with MechSys Code

7.2.3.1 Assumptions

Fractured geo-materials can be distinguished by the permeabilities of matrix and fractures, as has been introduced in chapter 2.4.1. The fluid flow modelling is based on the definition of a heterogeneous system, as shown in Figure 2-11c. That the matrix of coal can be effectively treated as impermeable is shown in chapter 2.2.4. The core mineralogy of the cleats observed in chapter 6.4 supports the decision to treat the cleat-matrix system as a heterogeneous one, with a reduced cleat permeability due to filling of the cleats. The permeability anisotropy, that is discussed in chapter 2.2.4, is represented in three principal directions of permeability that are results of the calculation. Based on the literature, it is

assumed that the highest permeability values occur parallel to the face cleats, which are by definition longer than the butt cleats. It has been reported that the bed-normal permeability is lowest and can be almost non-existent.

Therefore, the following assumptions are made:

- The matrix is is impermeable
- The cleats are filled and the cleat permeability is reduced.
- Lowest permeabilities are in bed-normal direction (z-direction)

The assumed system is represented in Figure 7-6.

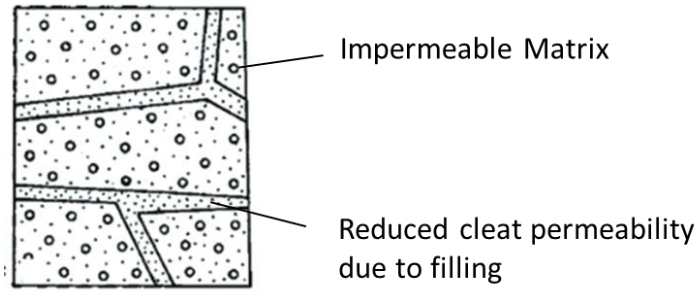

Figure 7-6 Assumptions for modelling of permeability within the cleat system

7.2.3.2 Simulations

The binary information (representing coal cleats and matrix) of each three-dimensional block gained by the CT-scan is fed into the Lattice Boltzmann Method based code MechSys as explained by Galindo-Torres et al. (2012) to determine the full permeability tensor.

The Lattice Boltzmann Method solves the Navier-Stokes equations and pressure boundary conditions are applied. The Lattice Boltzmann Method has an excellent accuracy with few cells representing the opening of the fractures, outperforming other Computational Fluid Dynamic methods.

The simulations were carried out on the flashlite high performance computing cluster within the School of Civil Engineering at the University of Queensland. The cluster could handle sample size of up to 640,000,000 cells. However, due to memory constrains, the whole sample cannot be simulated. Therefore, an analysis on the Representative Element Volume was done for this study. It is presented in chapter 7.5, and discusses the tensor statistics as a function of the sample size.

To determine the permeability tensor, the fluid's velocity field is calculated. The simulation runs until a steady state is reached and then the average velocity vector v [m/s] is obtained. This average velocity is used with the imposed pressure gradient vector for 3 to 8 cases to determine the nine independent components of the permeability tensor. To find the nine components of the tensor, three different simulations are carried out per sample. With three cases, enough equations exist to determine the nine components of the permeability tensor. This is done for the whole sample, as well as its 5865 subsamples.

The basic idea is the implementation of a pressure gradient, ∂P, over the domain in three directions as shown by equation 7-1.

$$\frac{\partial P}{\partial x}, \frac{\partial P}{\partial y}, \frac{\partial P}{\partial z} \qquad (7\text{-}1)$$

Assuming that the fluid is compressible, pressure, P [N/m^2], and density, ρ [kg/m^3], are related linearly in equation 7-2 to get the speed of sound c_s [m/s].

$$c_s = \sqrt{\frac{\partial P}{\partial \rho}} \qquad (7\text{-}2)$$

The speed of sound c_s in air at sea level is 340.29 m/s (20°C), in fresh water it is 1497 m/s (25°C). However, for the simulations, we are not taking a realistic speed of sound. By keeping the densities close to 1.0 with small variations, the Mach number, which is the ratio between the fluid mean speed and the speed of sound, stays small.

Based on the information gained in the CT-scan, the domain is divided into a grid of cells that are either assigned as coal matrix or cleats. The D_3Q_{19} scheme is used. The cleats are treated as open and non-mineralised. The boundary condition is a prescribed density that is set between the outer cells (Figure 7-7). For the inner cells, density and velocity are calculated. The density gradient between ρ^0 and ρ^1 in x direction over the length, l, of the domain in the respective direction is applied according to the pressure gradient, ∇P, that is needed to obtain the flow characteristic of the sample as represented by equation 7-3.

$$\vec{\nabla} P = \left(\frac{{c_s}^2({\rho_x}^1 - {\rho_x}^0)}{lx}\hat{x} + \frac{{c_s}^2({\rho_y}^1 - {\rho_y}^0)}{ly}\hat{y} + \frac{{c_s}^2({\rho_z}^1 - {\rho_z}^0)}{lz}\hat{z}\right. \qquad (7\text{-}3)$$

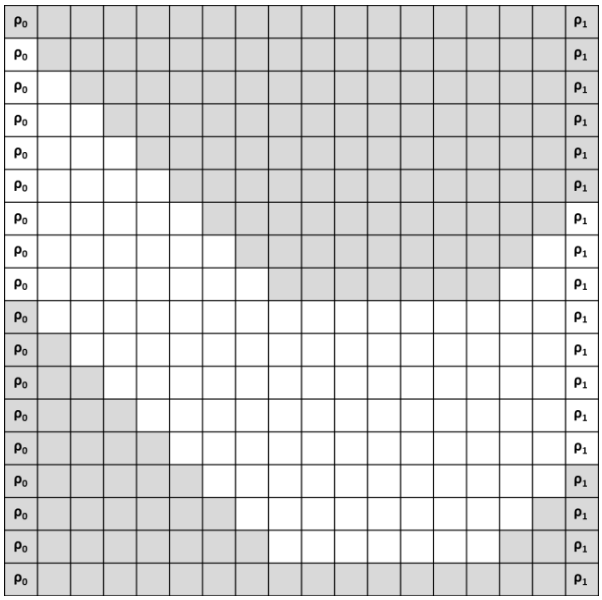

Figure 7-7 Two-dimensional binary representation of fracture (grey – solid, white – void) in the domain with boundary conditions ρ^0 and ρ^1

The output is the average density ρ_{avg} [kg/m^3] and velocity v [m/s] in three directions for each cell over the domain. With the pressure gradient ∇P and the average velocity obtained with this code, as well as the viscosity of the fluid, the equation 7-4 can be fulfilled and solved for the value of interest, which is the permeability, k [m^2].

$$k * \vec{\nabla} P = \rho_{avg} * \vec{v} \qquad (7\text{-}4)$$

Three simulations are run with three different pressure gradients to solve the permeability tensor, which has nine unknowns (Bear, 1972). The result is a tensor of second rank, that is, a 3x3 matrix (Figure 7-8).

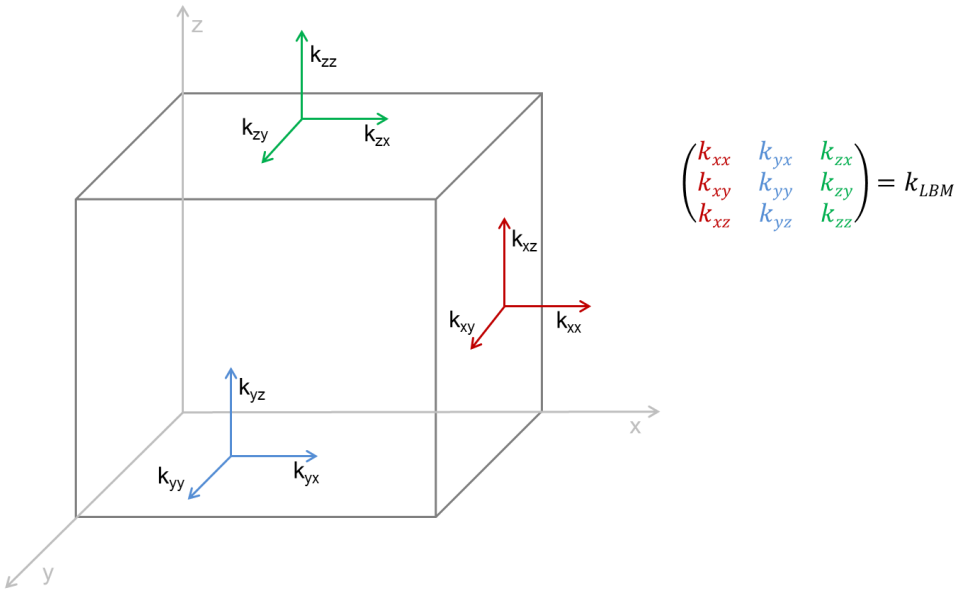

Figure 7-8 Permeability tensor in a three-dimensional coordinate system, the components form the matrix

7.2.3.3Verification of simulation result

In the following, permeability tensors of sample 11 1/3 that have been obtained for three different angle combinations are shown. The results are in m^2, the values are comparably high, since they represent open, unfilled cleats. For the angles 60˚, 240˚ and 360˚ it is shown in equation 7-5

$$k_{60,240,360} = \begin{pmatrix} 1.5045037^{-9} & -1.6938467^{-9} & 2.6024973^{-10} \\ -7.1608708^{-10} & 3.2047253^{-9} & 2.1165201^{-10} \\ -1.9297175^{-11} & 4.7612378^{-10} & 3.0326042^{-9} \end{pmatrix} \quad (7\text{-}5)$$

for the angles 90˚, 180˚ and 270˚ it is shown in equation 7-6

$$k_{90,180,270} = \begin{pmatrix} 1.5327740^{-9} & -1.6926428^{-9} & 3.8939272^{-10} \\ -7.3105340^{-10} & 3.2037575^{-9} & 1.3678948^{-10} \\ 4.4243615^{-11} & 4.7643436^{-10} & 3.3465315^{-9} \end{pmatrix} \quad (7\text{-}6)$$

for the angles 90˚, 240˚ and 360˚ it is shown in equation 7-7.

$$k_{90,240,360} = \begin{pmatrix} 1.5049443^{-9} & -1.6926428^{-9} & 2.5984651^{-10} \\ -7.1644132^{-10} & 3.2037575^{-9} & 2.1197616^{-10} \\ -1.9183498^{-11} & 4.7643436^{-10} & 3.0325002^{-9} \end{pmatrix} \quad (7\text{-}7)$$

The consistency of the resulting tensors allows the conclusion that any combination of three different angles can be chosen for the simulations. In the following, the combination of the angles 60˚, 240˚ and 360˚ is used. Notice that the values along the matrix diagonal are larger than the non-diagonal values, which is signifying an orientation that is close to the principal directions of the system.

7.2.4 Analysis of simulation results

For the permeability tensors, the eigenvectors and eigenvalues are calculated. The eigenvectors represent the principal directions of permeability. The eigenvalues represent the corresponding permeabilities in m^2. The permeability tensor results are multiplied by $1.013449 * 10^{15}$ to get the values in mD. Based on their value, they are ranked in descending order into major, medium and minor eigenvectors (Komura, 2008). Negative eigenvalues depict cases where there is no connection from one end of the domain to the other. Those are replaced by a zero matrix.

The total number of cells, as well as the secondary porosity, are additional output of the simulation. Secondary porosity is the ratio of voxels representing cleats to the total voxel

size of the sample. The underlying assumption is that the coal is completely solid and impermeable and matrix permeability is negligible.

The resulting cleat permeabilities represent the case for open, unfilled cleats. Therefore, the ratio of total volume taken up by cleats to the total bulk volume of the sample is shown as equation 7-8

$$\Phi_{oc} = \Phi_{LBM} = \frac{Total\ cleat\ volume}{Total\ bulk\ volume} \quad (7\text{-}8)$$

however, as the cleats of the scanned coal samples are filled by calcite the results have to be corrected by the porosity of the filling (see assumptions made in 7.2.3). The porosity is added based on the Kozeny - Carman model (Costa, 2006) where the permeability is related to the porosity, φ, by the porosity function, fφ, as shown in equation 7-9.

$$f\phi = \frac{\phi^3}{(1-\phi)^2} \quad (7\text{-}9)$$

The simulation results are corrected by multiplying the permeability tensor obtained with the calcite porosity to get equation 7-10.

$$k = k_{LBM} \frac{{\phi_c}^3}{(1-\phi_c)^2} \quad (7\text{-}10)$$

Typical calcite porosity, φ_c, used in modelling are given in the literature research in chapter 2.2.3. For this project, the porosity is used as a fitting parameter to obtain modelling results on the whole block that are similar to the permeability value obtained in the laboratory (chapter 5).

The laboratory testing measures the vertical permeability perpendicular to the bedding. Because of the anisotropic structure of coal, this is the direction of the lowest permeability (see Chapter 2.2.4). Out of the three permeability values that are resulting as major, medium and minor eigenvalue, the smallest one is fitted to the laboratory results. For the example of sample number 11 1/3, which has been tested to a vertical permeability of 1.41 mD in the lab, the stepwise fitting of calcite porosity φ_c delivers the permeability results given in the following Table 7-1.

Table 7-1 Permeability results based on different calcite porosities φ_c

φ_c	Permeability [mD]		
[%]	Major	Medium	Minimum
2.00	32.18	25.22	7.95
1.50	13.44	10.53	3.32
1.25	7.74	6.06	1.90
1.20	6.84	5.36	1.69
1.15	6.01	4.71	1.49
1.13	5.70	4.47	1.41
1.11	5.26	4.12	1.30

Given the fit of a minimum permeability of 1.41 mD when applying a calcite porosity of 1.13%, this value is used and applied on each of the permeability tensors for the 5866 blocks.

This porosity value fits the reported values for cleat porosities (see chapter 2.2.3) and values used in earlier numerical studies that range from 1 to 5%. However, these values do not match the porosities measured using helium pycnometry and mercury intrusion as reported in chapter 6.4.4. The cleat porosity measured for the sample 11 1/3 is 5.1%, the matrix porosity 1.4%.

Since the focus of this thesis is on the permeability distributions across scales, the modelling results have been fitted to represent the permeabilities measured for the samples 11 1/3 and sample 15 1/3 as they have been obtained for the respective samples in the laboratory (see chapter 5.2.3).

7.3 PERMEABILITY DATA OBTAINED IN SIMULATIONS

7.3.1 Numerically obtained permeability Sample 11 1/3

The permeabilities for the porous cleat network are calculated on a range of scales under the assumption that fluid flow is occurring within the cleat network only and the coal matrix is impermeable. The calcite porosity used for the Elphinstone coal sample 11 1/3 is 1.13%, as introduced in Chapter 7.3. Using this porosity value, the minor eigenvalue on the 95.28 m^3 scale equals the value measured in the laboratory (1.31 mD).

Figure 7-9 a and Figure 7-9 b provide an overview about the permeabilities obtained across scales for sample 11 1/3. With increasing volume the number of subsamples decreases, as well as the range of permeability values obtained (Figure 7-9 a). The maximum value within the data set is 93.41 mD. The averages of the permeabilities, shown in Figure 7-9 b, show overall an increasing trend with increasing volumes (from 0.02 cm^3 to 95.28 cm^3), with a tilt in the major eigenvalues at 1.19 cm^3. The arithmetic means of the permeability values range from 0.38 mD on the smallest scale to 6.77 mD on a medium scale (1.19 cm^3).

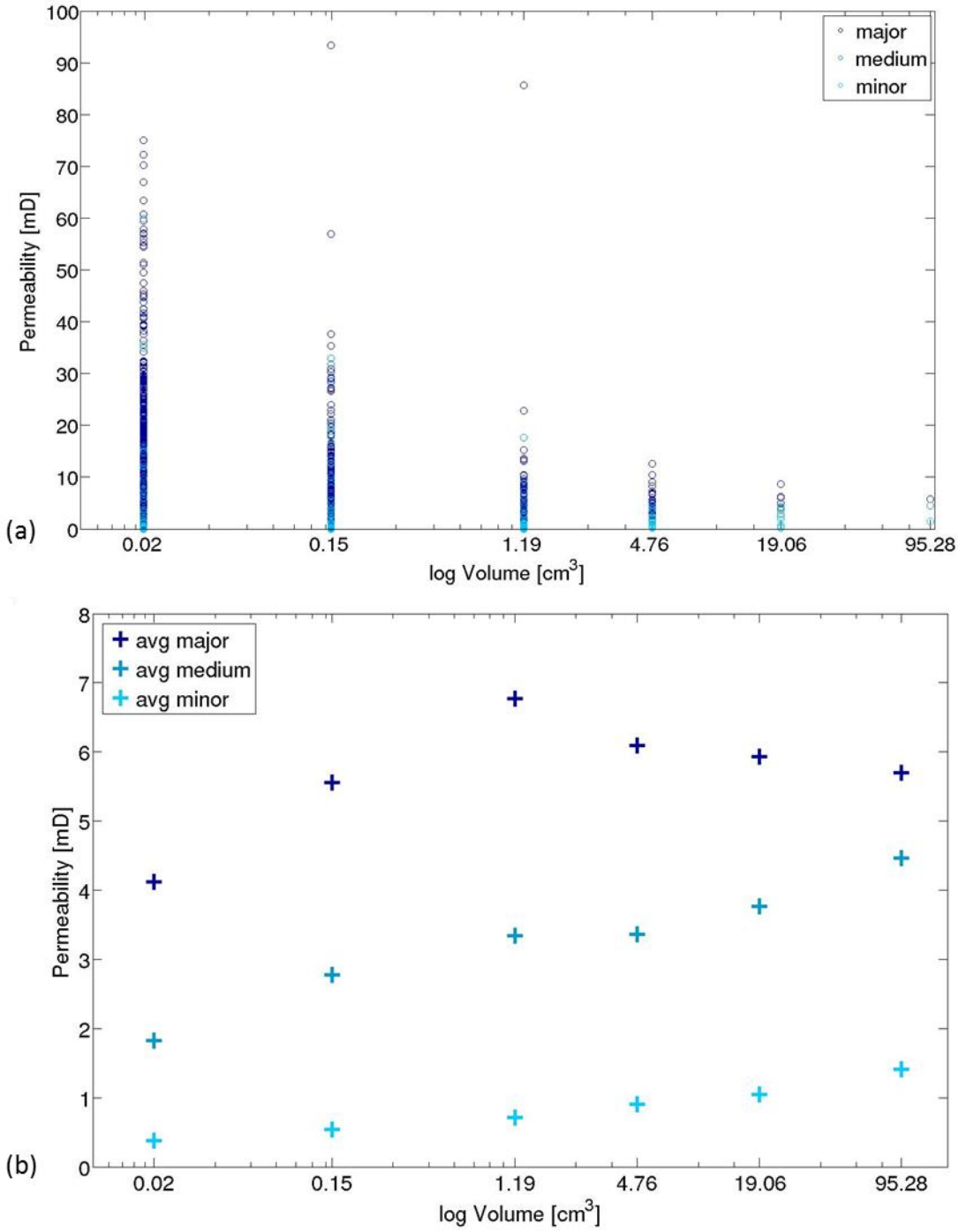

Figure 7-9 a. Absolute permeabilities and b. average permeabilities calculated for sample 11 1/3

7.3.2 Numerically obtained permeability Sample 15 2/3

An overview about the permeabilities obtained across scales for the Hynds coal sample 15 2/3 is shown in the following. The calcite porosity used to fit the numerical permeability value on the whole block to the laboratory derived permeability of 0.53 mD is 0.675%. With increasing volume the number of subsamples decreases, as well as the range of permeability values obtained (Figure 7-10 a). The maximum value is 61.57 mD.

The averages of the permeabilities, shown in Figure 7-10 b, overall show an increasing trend with increasing volume (from 0.02 cm^3 to 95.28 cm^3), with a tilt in the major eigenvalues around 4.76 cm^3. The arithmetic average permeability values range from 0.21 mD to 9.01 mD.

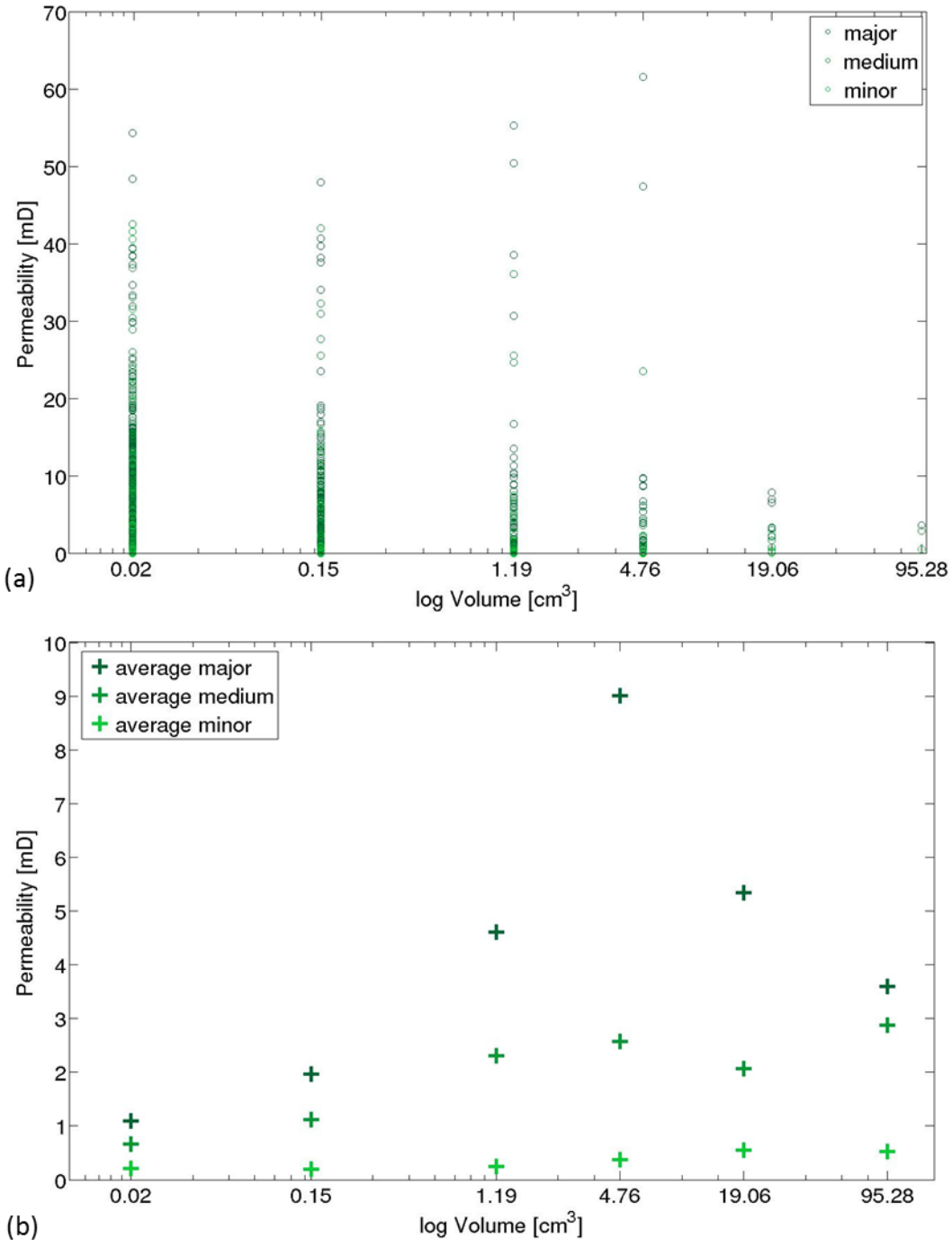

Figure 7-10 a. Absolute permeabilities and b. average permeabilities calculated for sample 15 2/3

7.4 RELATIONS BETWEEN PERMEABILITIES OF SAMPLES AND SUBSAMPLES

7.4.1.1 Samples and subsamples

Based on the naming convention that has been introduced in 7.2.2 the relations between samples and subsamples can be established. The name includes a coding for the size of the sample and affiliation to the larger sample that is referred to as supersample in the following. Table 7-2 shows the number p of partitions of each sample, sizes are given in cm^3.

Table 7-2 Number p of subsamples of each supersample

		Size Supersample [cm^3]				
		0.15	**1.19**	**4.76**	**19.0**	**95.28**
Size Subsample [cm^3]	**0.02**	8	64	256	1024	5120
	0.15		8	32	128	640
	1.19			4	16	80
	4.76				4	20
	19.06					5

Based on this partition, the relations between subsamples and supersamples can be further distinguished by their order. Subsamples of first order are thus those samples that are the direct partitions of the supersample. Subsamples of second order are the partition of the partition, and so on. This way, five orders of subsamples are distinguished. The number of relations decreases with increasing order.

For example, the smallest blocks of 0.02 cm^3 form the first order partition of the 0.15 cm^3 sample, the second order partition of the 1.19 cm^3 blocks, the third order partition of the 4.76 cm^3, the fourth order partition of the 19.06 cm^3 and the fifth order partition of the whole sample with a volume of 95.28 cm^3. Figure 7-11 presents an overview of the definition of order of the partition.

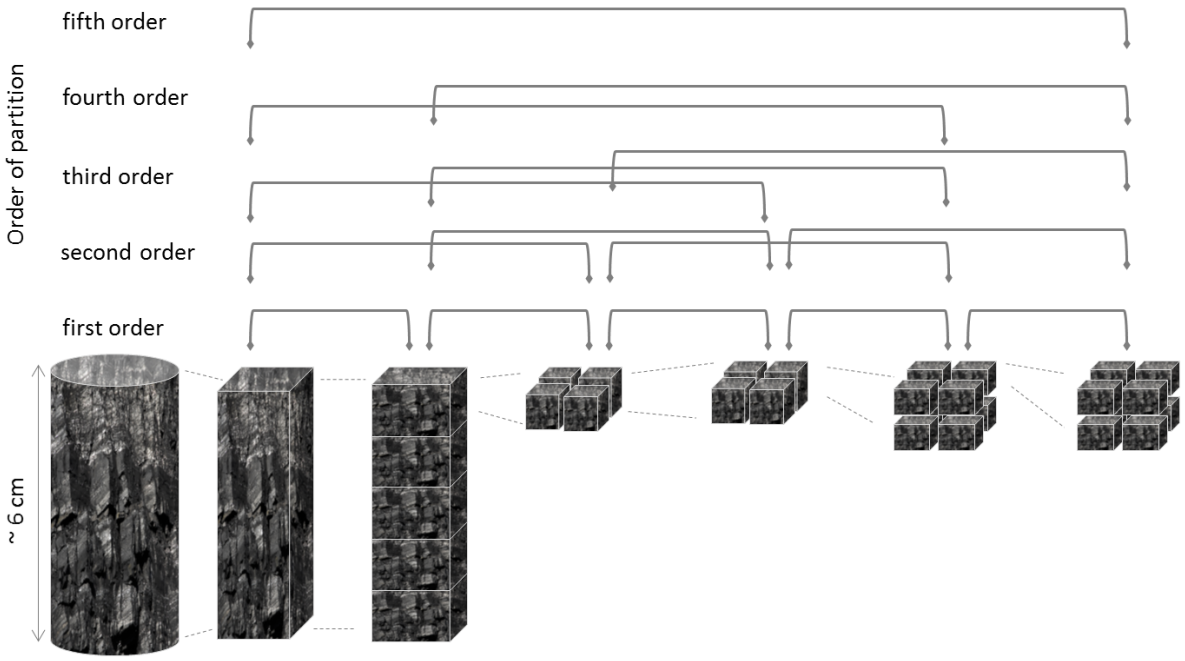

Partition	1	5	4	4	8	8
Block size [cm]	4.24×4.24×5.3	4.24×4.24×1.06	2.12×2.12×1.06	1.06×1.06×1.06	0.53×0.53×0.53	0.27×0.27×0.27
Block size [cm^3]	95.28	19.06	4.77	1.19	0.15	0.02
Total nr of blocks	1	5	20	80	640	5120

Figure 7-11 Definition of relationships between samples along scales depending on the order of partition

7.4.1.2 Analysis of permeability relations across scales

Different types of averages of the permeability tensors of the p subsamples are calculated and the results compared to the permeability of the supersample (see chapter 2.5.4). The best fit between the combined permeability of the subsamples and the permeability of the supersample is approached.

In the following, the approach is introduced using the example of the relationship between the first order subsamples of 0.15 cm^3 and their 1.19 cm^3 large supersamples that are formed by eight subsamples each. Eighty supersamples are divided into each eight subsamples. The presented blocks belong to the sample 11 1/3 of the Elphinstone seam. As introduced in chapter 7.2.4, the permeabilites are represented by the eigenvalues of the permeability tensors and are ranked in descending order into major, medium and minor eigenvalues. Plotting the ranked permability values of each subsample against the respective ranked permeability values of the supersamples, no clear relationship can be established (Figure 7-12).

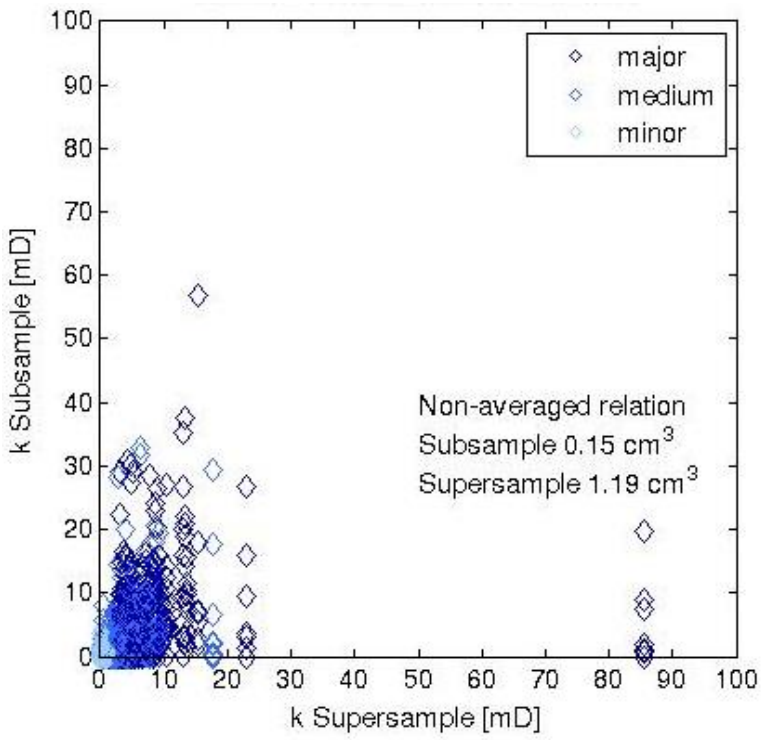

Figure 7-12 Ratio between ranked permeability values of subsamples (0.15 cm^3) and the ranked permeability values of their respective supersamples (1.19 cm^3)

Permeability averaging for up-scaling is introduced in 2.5.4. Based on the findings of the literature research, the average, the harmonic mean and the geometric mean of each group of subsamples are tested first to find a better fit for the relation between the permeabilities of the eight subsamples and the supersamples.

The average, harmonic mean and geometric mean of the tensors are calculated. Then, eigenvalues of the tensors are calculated and ranked into major, medium and minor. Based on their rank, the eigenvalues are plotted against the eigenvalue of the supersample with the respective rank. Figure 7-13 shows that none of this averaging methods results in a linear relation between the values. Therefore, averaging, harmonic mean and geometric mean are found to be insufficient to display the up-scaling behaviour between subsample and supersample (see Figure 7-13 a, b and c, respectively).

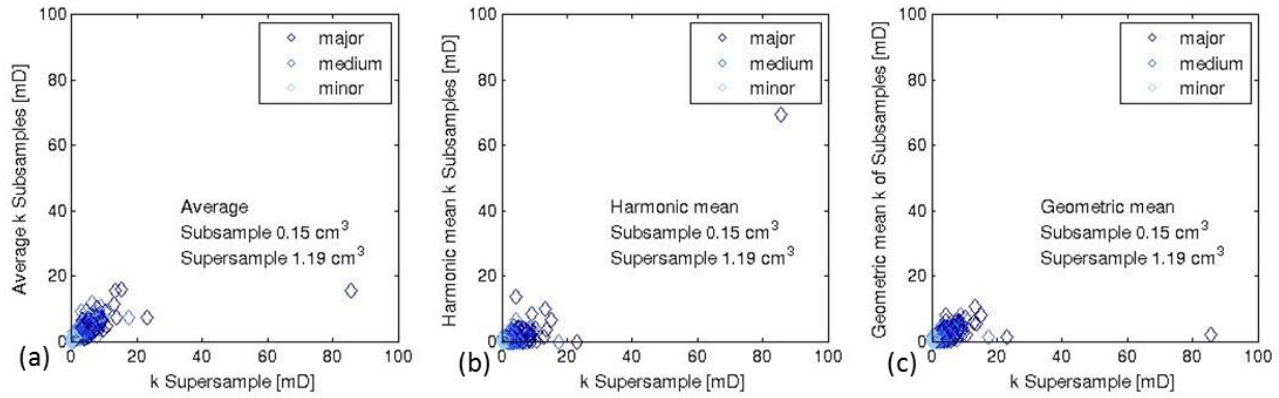

Figure 7-13 a. Average, b. harmonic mean and c. geometric mean of subsamples (0.15 cm^3) plotted against the ranked permeability values of their respective supersamples (1.19 cm^3)

As introduced earlier (chapter 2.5.4), the power average has been proposed for permeability upscaling by Desbarats (1992). With the power average exponent α = -1 the harmonic mean, with α = 1 the arithmetic mean is represented by equation 7-11

$$k_{power\ average} = \left(\frac{\sum_{i=1}^{n} {k_i}^{\alpha}}{n}\right)^{\frac{1}{\alpha}} \qquad (7\text{-}11)$$

For the geometric mean, α equals to 0 and the power average is defined as equation 7-12

$$k_{power\ average} = \left(\prod_{i=1}^{n} k_i\right)^{\frac{1}{n}} \qquad (7\text{-}12)$$

Therefore, by varying α, the ideal solution of a power average of the permeability of the subsamples that match the permeability of the supersamples is approximated. As the permeability data of the blocks are in tensorial form, the calculations are done both, elementwise and non-elementwise. To find the ideal alpha, values between α = -5 and α = 5 in increments of 0.05 are tested. While α should typically vary between -1 and 1 this range is chosen in order to capture any possible outliers.

Firstly, the power average of the subsamples is calculated as shown in equation 7-11 and 7-12. Next, the difference between the permeability tensor of the supersample and the permeability tensor of the power-averaged subsamples is determined. The norm of this difference is divided by the norm of the supersamples. The resulting value is defined as the error between the averaged permeability of the subsamples and the permeability of the supersample using equation 7-13.

$$error = \frac{norm\left(k_{supersample} - k_{power\ average\ of\ subsamples}\right)}{norm\ (k_{supersample})} \qquad (7\text{-}13)$$

Finally, the errors of all eighty cases are averaged. Using the mentioned range of alphas of -5 to +5, the smallest average error is approximated. The plot in Figure 7-14 shows the average errors for their respective alpha values for both the elementwise and the non-elementwise calculation around the minimum average errors.

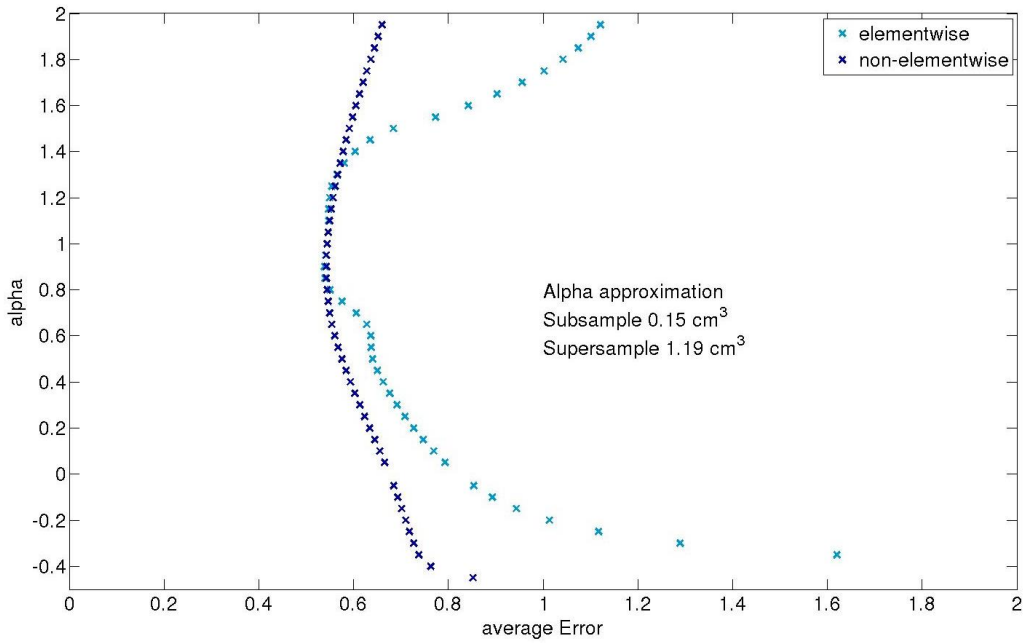

Figure 7-14 Approximation to the ideal alpha to form the power law of subsamples (0.15 cm^3)

For the example of subsamples of 15 cm^3 and supersamples of 1.19 cm^3, the ideal power average exponent for both the elementwise and non-elementwise calculation is $\alpha = 0.9$. These two ideal power average exponents are used to calculate the powermeans of the permeabilities of the subsamples and are displayed against the permeabilities of the respective supersample (Figure 7-15).

As the results for the non-elementwise and the elementwise calculation appear to be similar, they are plotted against each other in Figure 7-16. The same ideal alphas are used: 0.9 for the non-elementwise calculation, as well as for the elementwise calculated powermean. The linear relation between the results allows for the conclusion that they are similar. Therefore, in the following, only the elementwise averaging is pursued. The results of the relations between samples and subsamples across scales for partitions of all orders are presented in the next chapters.

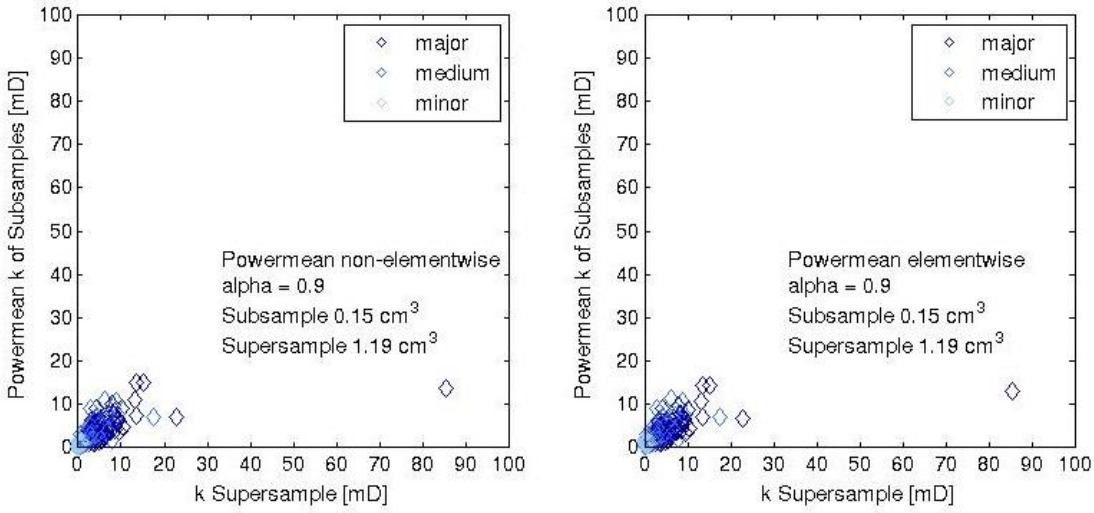

Figure 7-15 Ranked power-averaged of subsamples (0.15 cm^3) calculated both a. non-elementwise and b elementwise plotted against the permeabilities of the supersamples (1.19 cm^3)

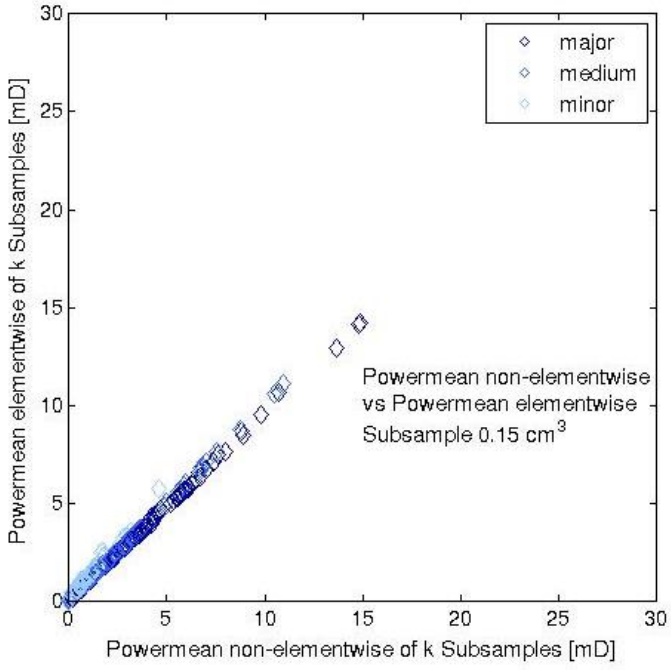

Figure 7-16 Comparison of results for elementwise (α = 0.9) and non-elementwise (α = 0.9) calculation

7.4.2 Relations between results on different scales Sample 11 1/3

7.4.2.1 First order partition

The relations between the major, medium and minor permeability values of subsamples and and the major, medium and minor permeabilities of their respective supersamples of first order are shown in the Figure 7-17. The image on the left shows the respective ratio before averaging, and the image on the right shows the ratio after power averaging with the ideal alpha. The letter of the subplots refer to the size of subsample and the size of

supersample as follows: a) 0.02 cm^3 : 0.15 cm^3 blocks b) 0.15cm^3 :1.19 cm^3 blocks, c) 1.19 cm^3 : 4.76 cm^3 blocks, d) 4.76 cm^3 : 19.06 cm^3, e) 19.06 cm^3 : 95.28 cm^3 blocks.

a)

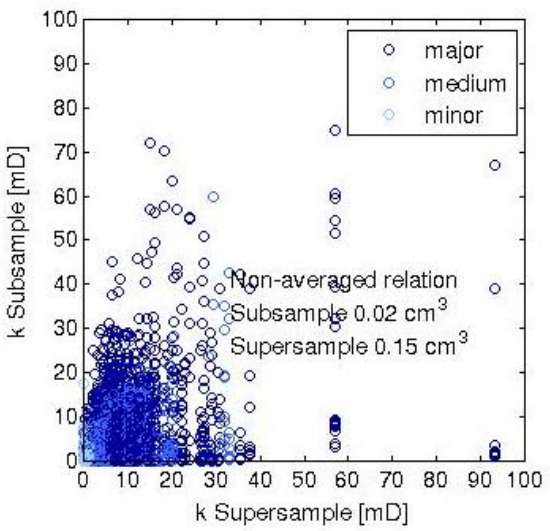

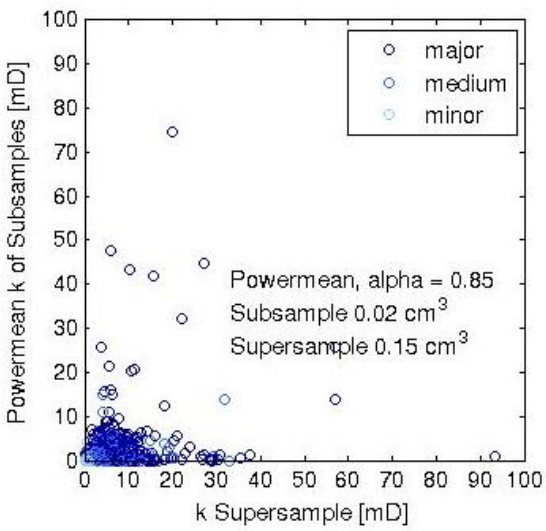

b)

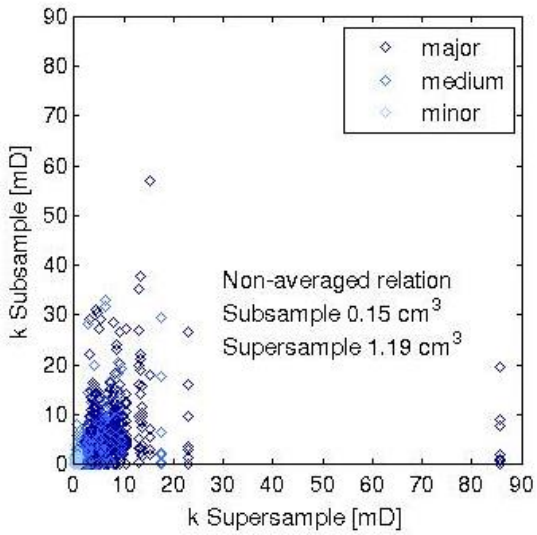

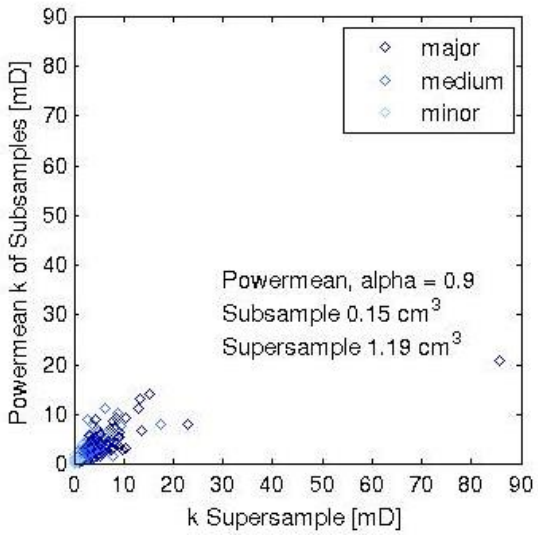

c)

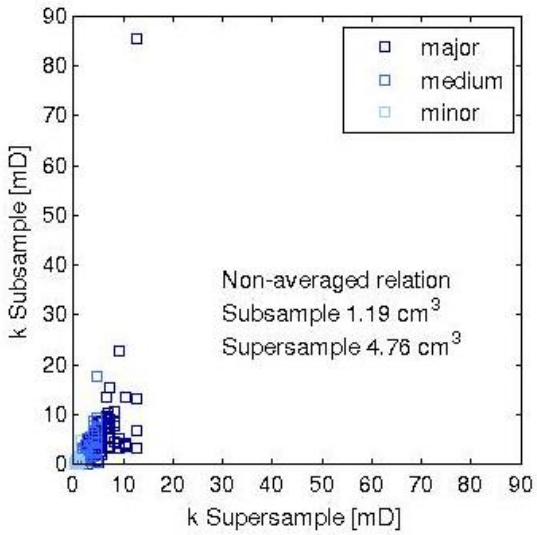

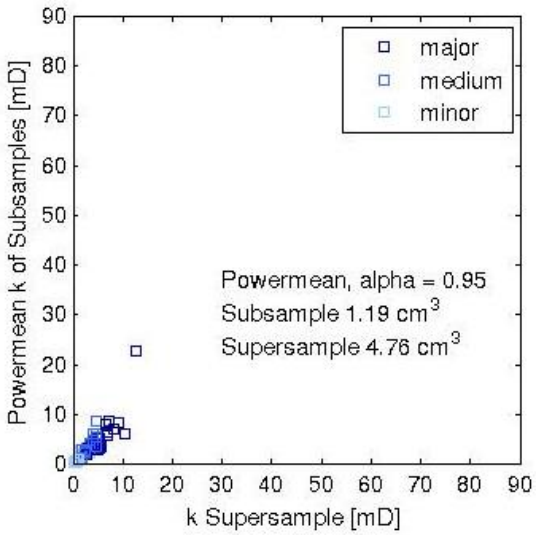

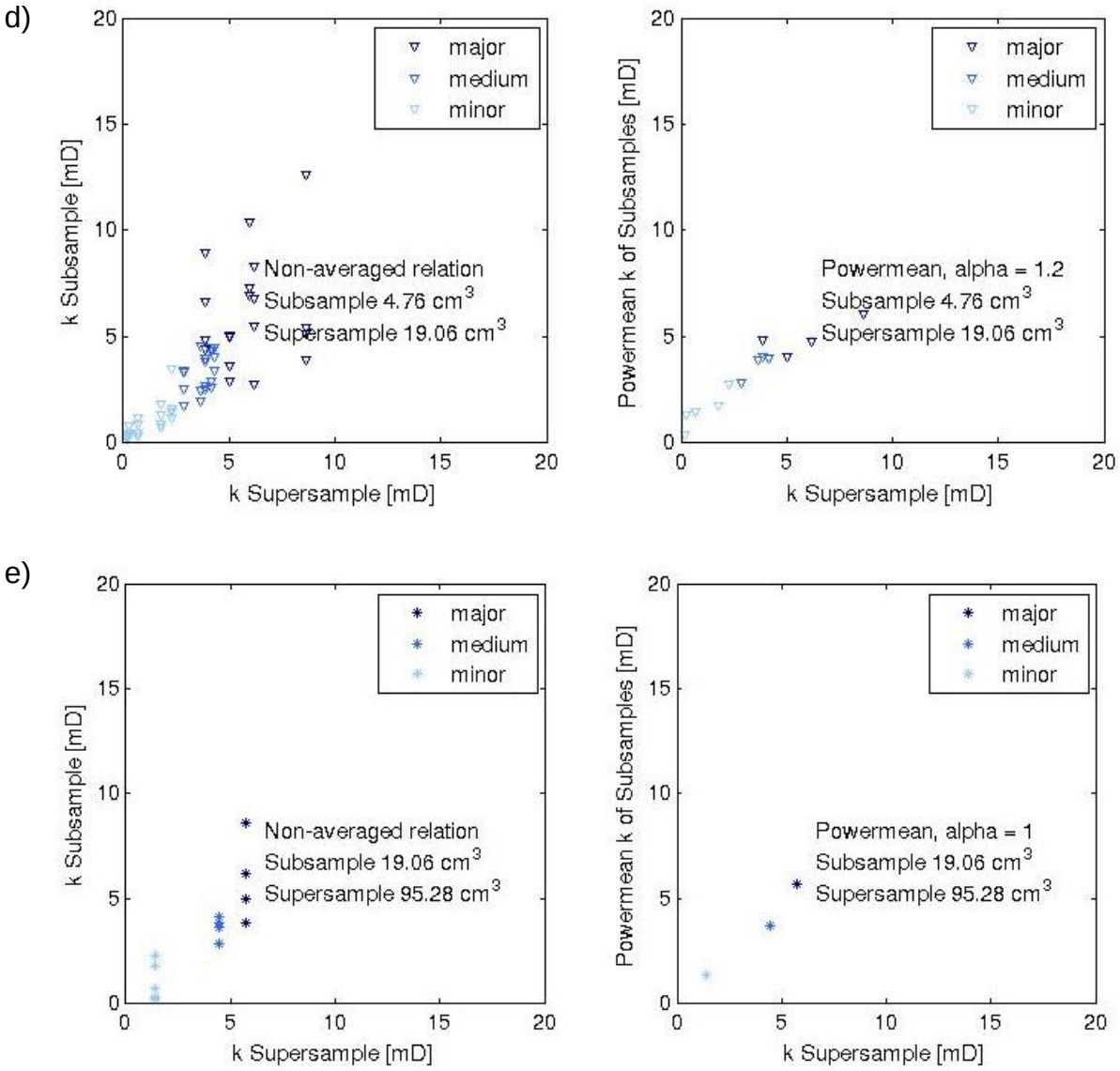

Figure 7-17 Ratio of non-averaged and power-averaged permeabilities of subsamples to permeabilities of supersamples for partitions of first order for sample 11 1/3. Displayed are the size of subsample : size of supersample: a) 0.02 cm^3 : 0.15 cm^3 blocks b) 0.15 cm^3 :1.19 cm^3 blocks, c) 1.19 cm^3 : 4.76 cm^3 blocks, d) 4.76 cm^3 : 19.06 cm^3, e) 19.06 cm^3 : 95.28 cm^3 blocks

The average error for a range of power average exponents alpha for each of the first order partitions are shown in Figure 7-18. The ideal alphas with the smallest average error are shown in Table 7-3. For the sample representing the cleat network of the coal sample 11 1/3 taken at the Elphinstone seam the ideal alpha used for the power law relation between samples and subsamples approaches $\alpha = 1$ with increasing size of subsamples. That is, from subsample size 1.19 cm^3 the average of the subsamples provides the best estimation of the permeability of the samples.

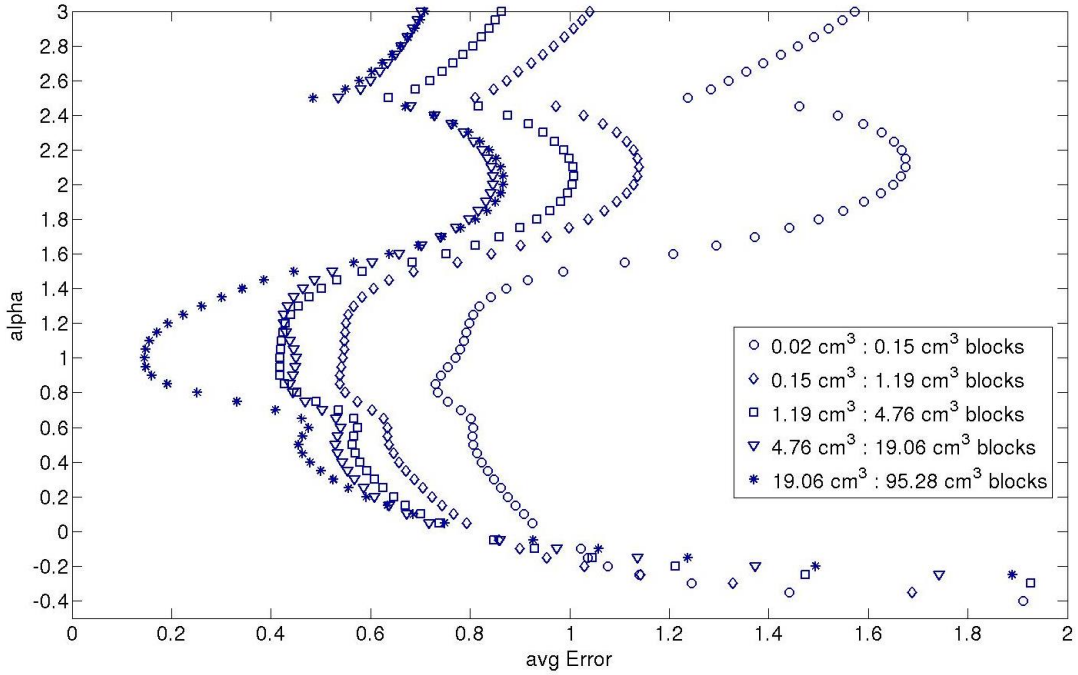

Figure 7-18 Average error for alpha in the range of α=-0.5 to 3 for the first order partitions

Table 7-3 Ideal alphas for first order partitions of sample 11 1/3

Size Subsample [cm^3]	Size Supersample [cm^3]	Ideal Alpha
0.02	0.15	0.85
0.15	1.19	0.90
1.19	4.76	0.95
4.76	19.06	1.20
19.06	95.28	1.00

7.4.2.2 Higher order partitions

The partitions of second to third order are presented in the appendix, chapter A1. The ideal power law coefficient α for each relation is shown in Table 7-4. The ideal power law coefficient is increasing with increasing order, with values from 0.85 up to 1.3.

Table 7-4 Ideal alpha for the different relations between subsamples of each supersample for sample 11 1/3

		Size Supersample [cm^3]				
		0.15	**1.19**	**4.76**	**19.06**	**95.28**
Size Subsample [cm^3]	**0.02**	0.85	1.15	1.20	1.30	1.30
	0.15		0.90	1.10	1.25	1.20
	1.19			0.95	0.85	0.95
	4.76				1.20	1.05
	19.06					1.00

7.4.3 Relations between results on different scales Sample 15 2/3

7.4.3.1 First order partition

The relations between the major, medium and minor permeability values of subsamples and the major, medium and minor permeabilities of their respective supersamples of first order are shown in the Figure 7-19.

The image on the left shows the respective ratio before averaging, and the image on the left shows the ratio after power averaging with the ideal alpha. The letter of the subplots refer to the size of subsample and the size of supersample as follows: a) 0.02 cm^3 : 0.15 cm^3 blocks b) 0.15cm^3 :1.19 cm^3 blocks, c) 1.19 cm^3 : 4.76 cm^3 blocks, d) 4.76 cm^3 : 19.06 cm^3, e) 19.06 cm^3 : 95.28 cm^3 blocks.

a)

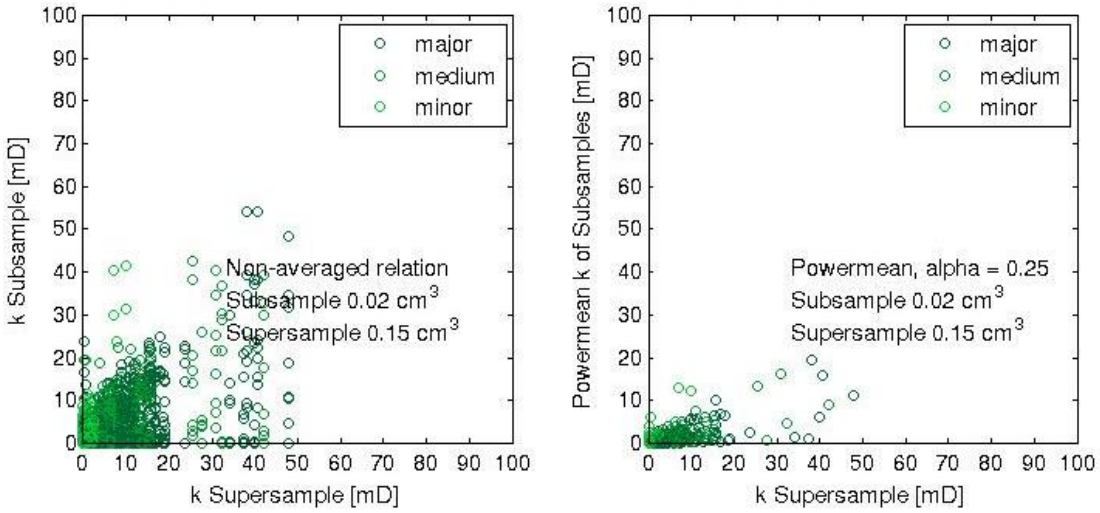

b)

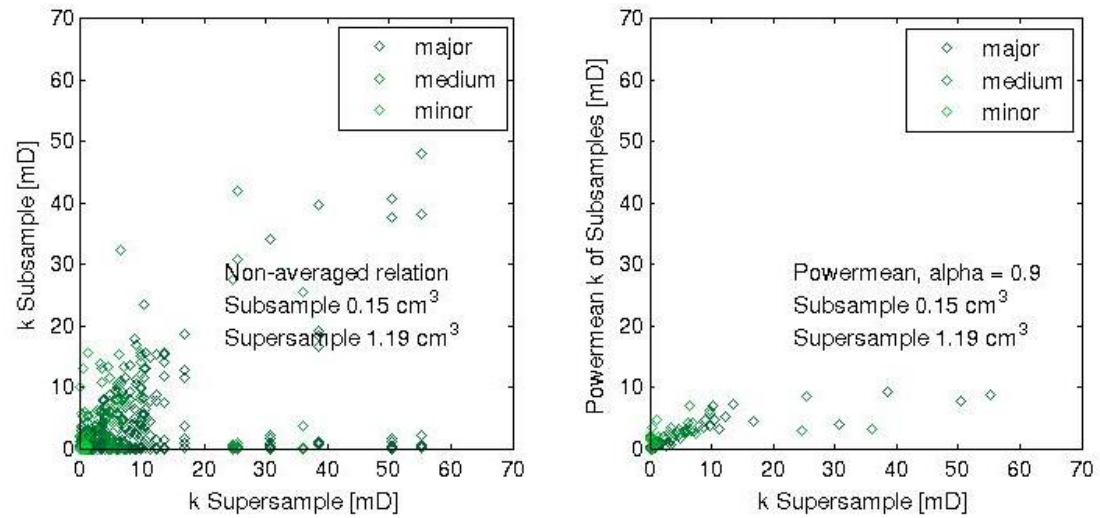

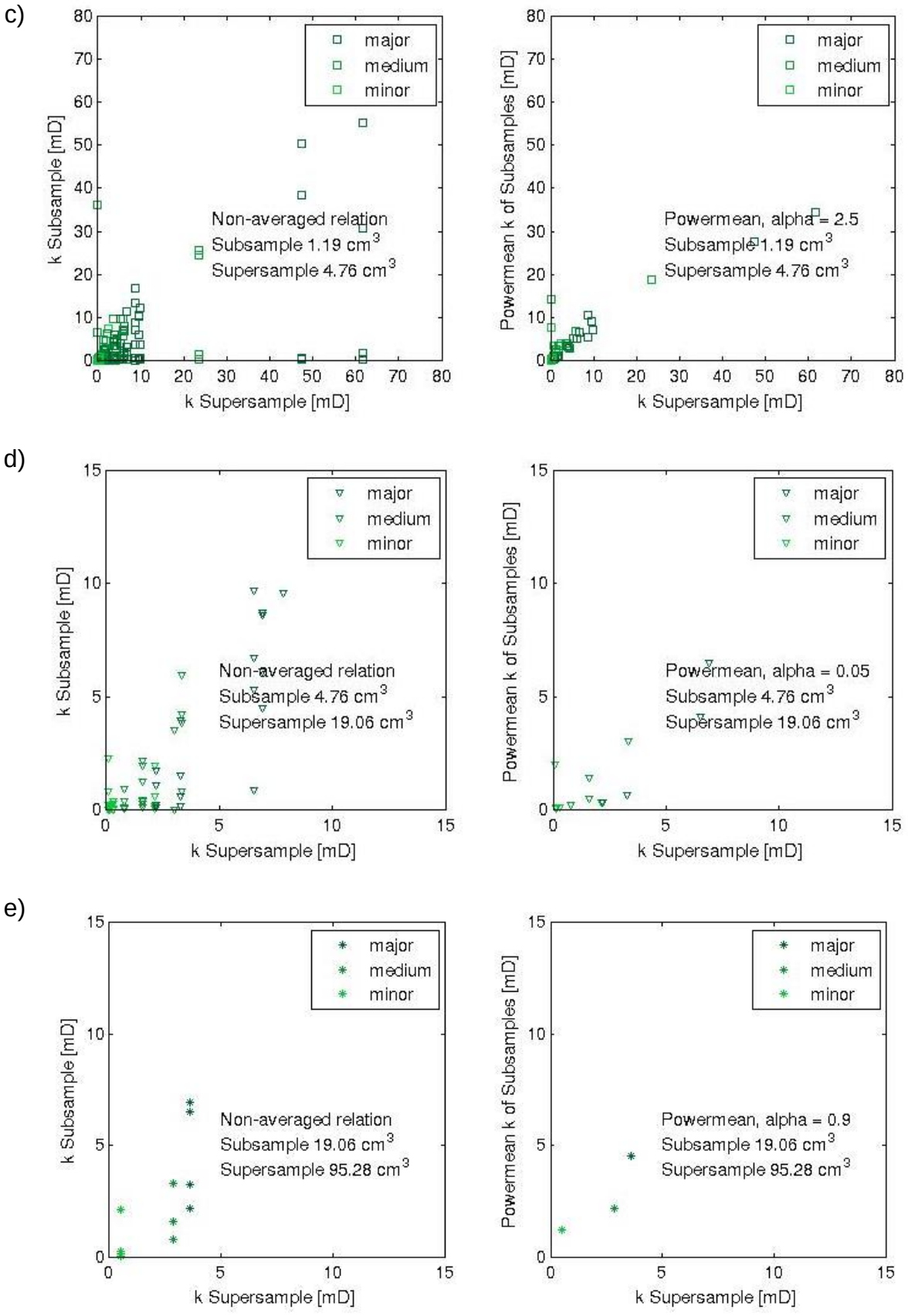

Figure 7-19 Ratio of non-averaged and power-averaged permeabilities of subsamples to permeabilities of supersamples for partitions of first order for sample 15 2/3. Displayed are the size of subsample : size of supersample: a) 0.02 cm^3 : 0.15 cm^3 blocks b) 0.15cm^3 :1.19 cm3 blocks, c) 1.19 cm^3 : 4.76 cm^3 blocks, d) 4.76 cm^3 : 19.06 cm^3, e) 19.06 cm^3 : 95.28 cm^3 blocks

The average error for a range of power average exponents alpha for each of the first order partitions are shown in Figure 7-20. The ideal alphas with the smallest average error are shown in Table 7-5. For this sample (15 2/3) taken at the Hynds seam, the ideal alpha is varying between 0.05 and 0.9 across the scales.

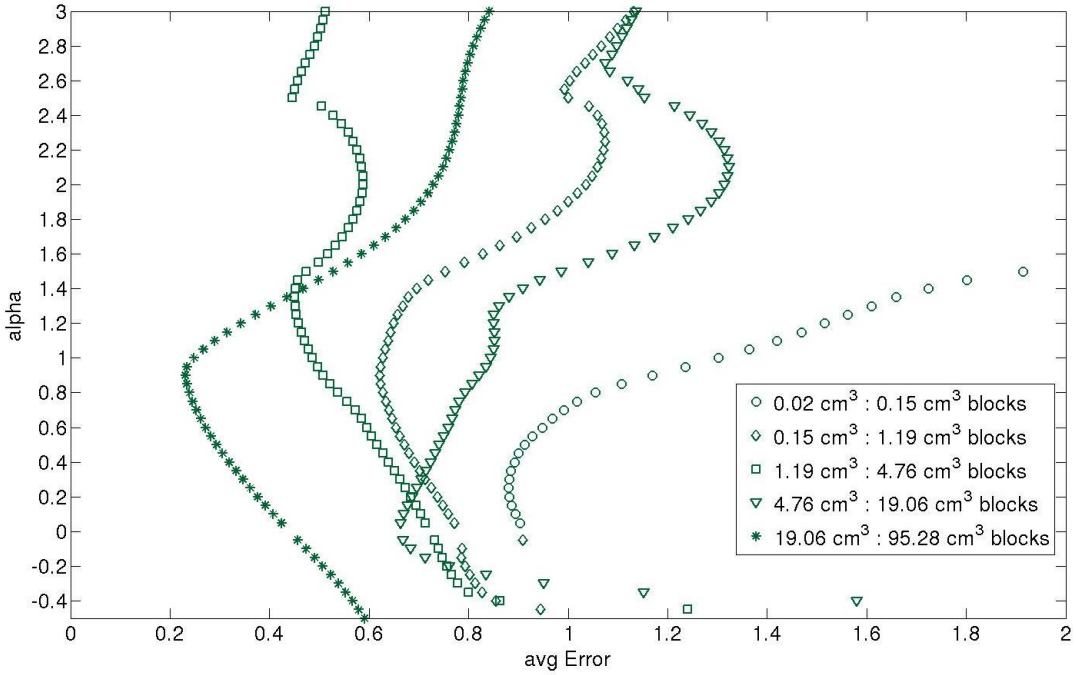

Figure 7-20 Average error for alpha in the range of α=-0.5 to 3 for the first order partitions

Table 7-5 Ideal alphas for first order partitions of sample 15 2/3

Size Subsample [cm^3]	Size Supersample [cm^3]	Ideal Alpha
0.02	0.15	0.25
0.15	1.19	0.90
1.19	4.76	2.50
4.76	19.06	0.05
19.06	95.28	0.90

7.4.3.2 Higher order partitions

The partitions of second to third order are presented in the appendix, chapter A2. The ideal power law coefficient for each relation is shown in Table 7-6. No trend between ideal alpha and order of partition is apparent.

Table 7-6 Ideal alpha for the different relations between subsamples of each supersample for sample 15 2/3

		Size Supersample [cm^3]				
		0.15	**1.19**	**4.76**	**19.0**	**95.2**
Size Subsample [cm^3]	**0.02**	0.25	1.00	1.40	2.60	1.75
	0.15		0.90	1.35	2.55	1.45
	1.19			2.50	0.85	0.90
	4.76				0.05	0.65
	19.06					0.90

7.5 DETERMINATION OF REPRESENTATIVE ELEMENT VOLUME

The concept of the REV is introduced in chapter 2.5.3. The REV is illustrative of the behaviour of the medium as a whole. As shown in Figure 2-17, any property of the medium can vary among the scales and REVs can be identified for each of these scales. The numerical modelling of the permeabilities on the micro-scale captures this behaviour.

The relations that are shown in the Figure 7-17 and Figure 7-19 can also be expressed as a ratio between the power-average of the permeability of the subsamples over the permeability of the supersample using equation 7-14

$$Power\ average\ factor = \frac{k_{power\ average\ of\ subsamples}}{k_{supersample}} \qquad (7\text{-}14)$$

A power average factor of 1 therefore would represent a case where the power average of the permeabilities of the subsamples equals the permeability of the supersample. The distribution of the power average factors should converge around 1 when close to the REV scale. It is to be noted, that in each case the major, medium and minor permeabilities of the subsamples are compared with the permeabilities of their respective order. However, the anisotropy of the medium might result in the change of these orders for a certain direction. For example, while for a smaller subsample the major permeability might be in x-direction, in the large supersample it is part of, the major permeability might be directed along the y-axis.

7.5.1 Power-average factors Sample 11 1/3

7.5.1.1 First order partition

Displays of the distribution of the power average factors between 0 and 2 are shown in Figure 7-21. Note that the values beyond 2 are summarised in the last bin of the histogram. While a larger range of power average factors is present for the smaller block sizes, the power average factors start to converge towards 1 for the blocks of 95.28 cm^3 size. It can therefore be concluded, that the REV is met at this scale. On the smaller scales within the range of 0.15 cm^3 to 19.06 cm^3 the power averaging of the permeabilities of the subsamples can only be seen as an approximation to the permeability of the super samples.

a)

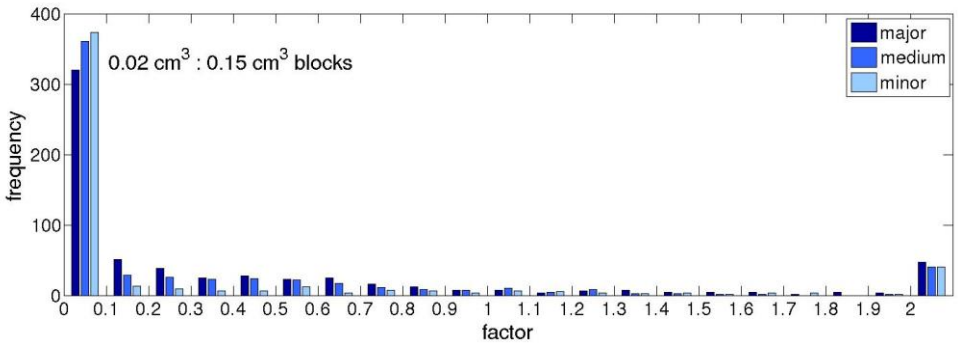
0.02 cm3 : 0.15 cm3 blocks
major
medium
minor
frequency
factor

b)

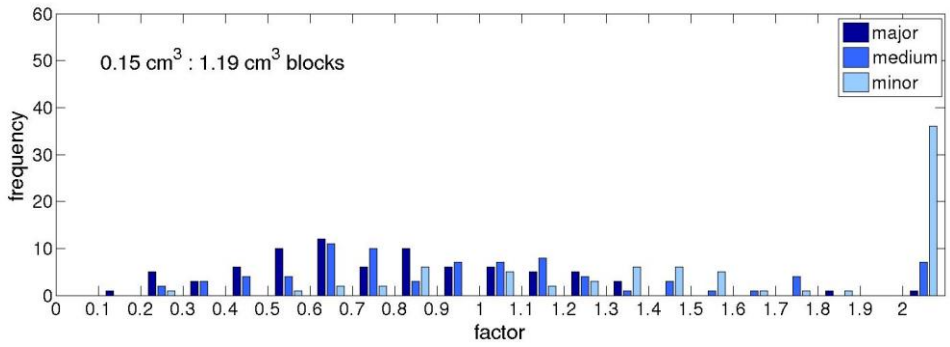
0.15 cm3 : 1.19 cm3 blocks
major
medium
minor
frequency
factor

c)

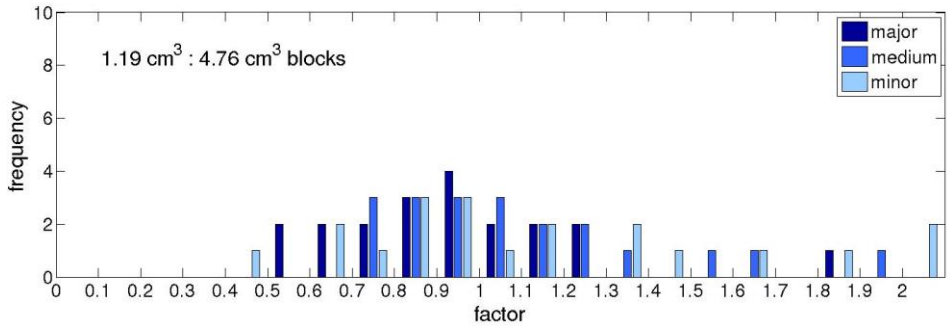
1.19 cm3 : 4.76 cm3 blocks
major
medium
minor
frequency
factor

d)

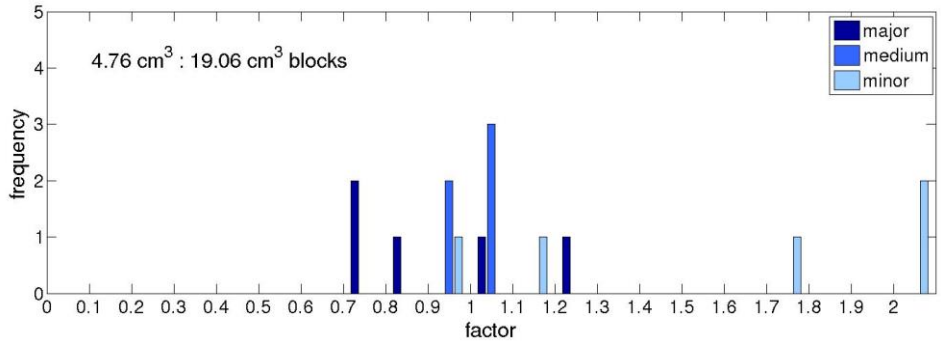
4.76 cm3 : 19.06 cm3 blocks
major
medium
minor
frequency
factor

e)

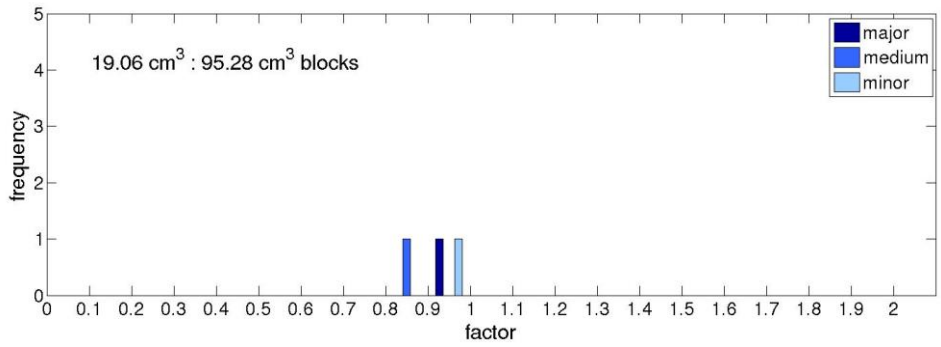

Figure 7-21 Power-average factors for the first order partitions of sample 11 1/3.Displayed are factors for the size of subsample : size of supersample: a) 0.02 cm^3 : 0.15 cm^3 blocks b) 0.15cm^3 :1.19 cm3 blocks, c) 1.19 cm^3 : 4.76 cm^3 blocks, d) 4.76 cm^3 : 19.06 cm^3, e) 19.06 cm^3 : 95.28 cm^3 blocks

7.5.1.2 Higher order partitions

The power average factors for higher order partitions of sample 11 1/3 are shown in the appendix, chapter A1. Up until the fourth order, the power-averaging of the permeabilities of smaller blocks represents the permeability of the block of 95.28 cm^3 size quite well with the power average factors being in the range of 0.8 to 1.1 (Figure A3 d, Figure A6 c, and Figure A9 b). However, the power-average of permeability of the 5120 subsamples with a block size of 0.02 cm^3 cannot be averaged adequately to fit the permeability of the 95.28 cm^3 supersample.

7.5.2 Power average factors Sample 15 2/3

7.5.2.1 First order partition

In the same way, the results for the Hynds sample 15 2/3 are given. Figure 7-22 shows the distribution of the power average factors. Note that the values beyond 2 are summarised in the last bin of the histogram. For this sample no convergence towards a power average factor of 1 is taking place at any size. For this data set, the power averaging is not suitable to express relation between the permeability values across scales.

a)

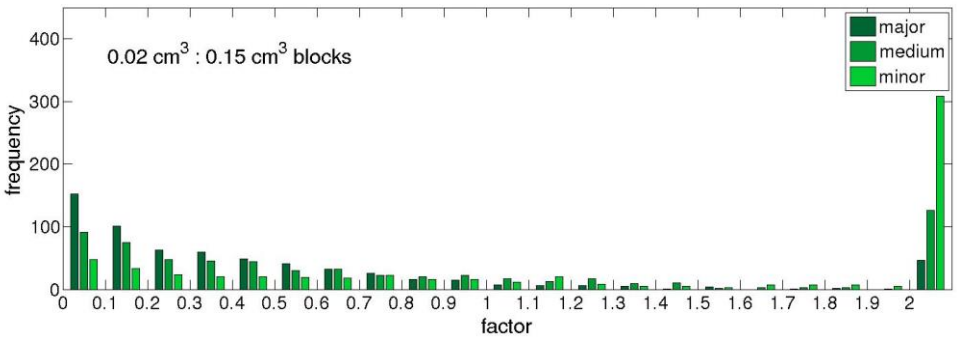

b)

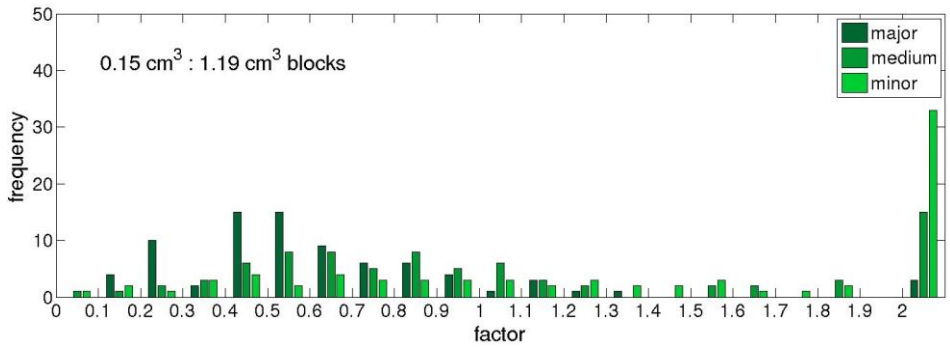

c)

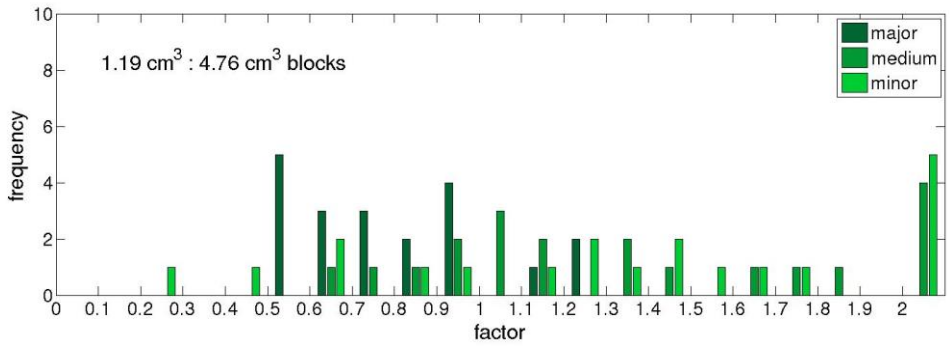

d)

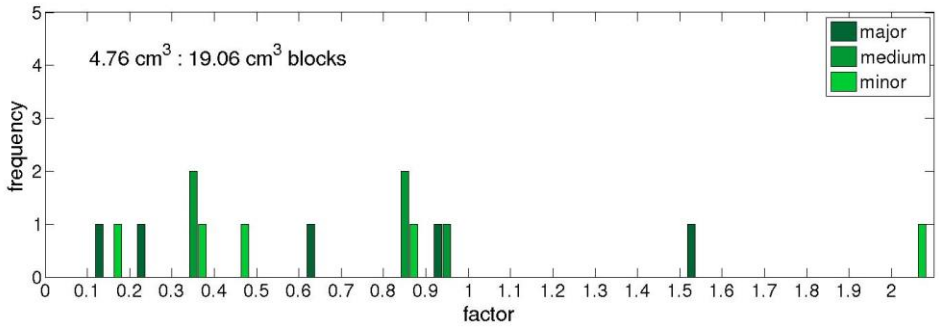

e)

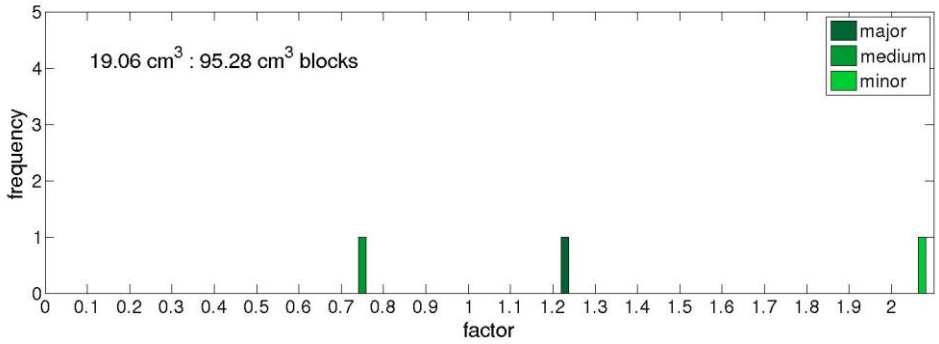

Figure 7-22 Power-average factors for the first order partitions of sample 15 2/3.Displayed are factors for the size of subsample : size of supersample: a) 0.02 cm^3 : 0.15 cm^3 blocks b) 0.15cm^3 :1.19 cm3 blocks, c) 1.19 cm^3 : 4.76 cm^3 blocks, d) 4.76 cm^3 : 19.06 cm^3, e) 19.06 cm^3 : 95.28 cm^3 blocks

7.5.2.2 Higher order partitions

The power average factors for higher order partitions of sample 15 2/3 are shown in the appendix, chapter A2. As for the first order partition, the distributions of the power average factor is random across all scales (Figure A15, Figure A 18, Figure A21 and Figure A24). The power averaging is not suitable to up-scale permeabilities for this sample.

7.6 CONCLUSION

Permeabilities have been modelled for a range of volumes across the micro-scale. This has been achieved by the partition of the artificial samples that are reconstructed based on CT-scans of the samples 11 1/3 of the Elphinstone seam and the sample 15 2/3 of the Hynds seam.

The averages of the permeabilities of the Elphinstone coal sample (11 1/3), shown in Figure 7-9, overall show an increasing trend with increasing volume from 0.02 cm^3 to 95.28 cm^3, with a tilt in the major eigenvalues at 1.19 cm^3. The average permeability values range from 0.38 mD on the smallest scale to 6.77 mD. The averages of the permeabilities, of the Hynds coal sample (15 2/3) shown in Figure 7-10, also show an increasing trend with increasing volume, with a tilt in the major eigenvalues around 4.76 cm^3. The average permeability values range from 0.21 mD to 9.01 mD. For both samples the range of values obtained decreases with increasing sample size. The maximum value within the Elphinstone coal data set is 93.41 mD. The maximum value for the artificial cleat network of Hynds coal is 61.57 mD.

Using a power averaging approach, up-scaling behaviour across scales was tested. This worked quite well for the sample 11 1/3 (Elphinstone seam), with the power law averages for the major, medium and minor permeabilities of smaller blocks on all scales being very similar to the major, medium and minor permeabilities of the whole block (95.25 cm^3). Therefore, this volume is assumed as the REV for the micro- scale. As this volume represents the size of the whole sample that has been tested in the laboratory tests (see chapter 5), it can be assumed that the laboratory measurements are done at REV scale and are therefore a good approximation to the permeability of the coal cleat system. However, for the sample 15 2/3 (Hynds seam), the upscaling using a power averaging method did not result in an appropriate fit on any scale. This is assumed to be due to possible blur in the segmentations of the images, see Figure 6-4. It has therefore to be highlighted that segmentation is one of the keys steps when working with image processing techniques. As pointed out in chapter 6.3.1.3, the scans show a more

homogeneous Elphinstone coal and more heterogeneous structure for the Hynds coal. As a consequence, results from the image analysis and subsequent structure based modelling are more representative for sample 11 1/3 of the shallower and younger Elphinstone seam than for 15 2/3, which has been taken at the Hynds seam.

The anisotropy of the material further influences the results, as the directionality of the permeabilities is, based on the cleat structure model, expressed by the order of the permeability (major, medium or minor permeability). However, for a certain block the major permeability might occur in a different direction that for its supersample.

8. Permeabilities across scales

8.1 OBSERVATION SCALES

One aim of this project is to compare the results from different permeability measuring methods, taking scaling issues into account and to try to identify scale transitions indicating the REV size for fractured samples. To achieve this goal, permeability is examined on multiple spatial scales: borehole flow measurements cover the macro-scale subject to influences from the field of up to several hundreds to thousands of metre, triaxial cell tests are done on a meso-scale of several decimetres, and the micro-scale is covered by the results of the CT-scans of blocks of centimetre sizing that are displayed in micrometre resolution. The definition of the observation scales and the methods used to investigate permeability within these scales is shown in Figure 8-1.

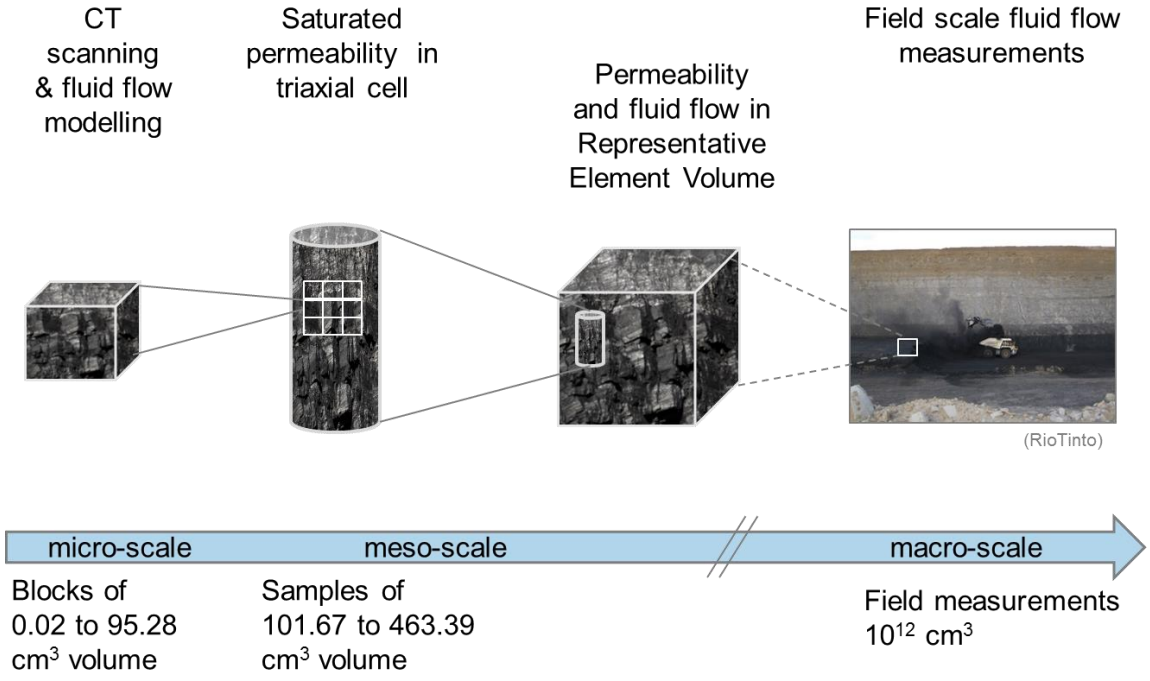

Figure 8-1 Scale definition of the present study

8.2 PERMEABILITIES OBTAINED ACROSS SCALES

8.2.1 Micro-scale: Numerical modelling

The numerical simulations conducted on the scans of samples cover a range of 0.02 cm^3 to 95.28 cm^3. The range of permeability values obtained during numerical modelling, decreases with increasing sample volume. The maximum value within the Elphinstone

coal data set is 93.41 mD. The maximum value for the artificial cleat network of Hynds coal is 61.57 mD. For the simulated blocks largest range of k values was determined.

8.2.2 Meso-scale: Laboratory testing

The meso-scale of this investigation covers the bulk permeability of present cleats and other porous structures. A range of sample volumes from 101.97 cm^3 to 463.39 cm^3 has been investigated in the laboratory testing. There is no apparent relation between sample size and measured permeability value (see Figure 5-8). The range of permeability values observed in the laboratory is greater for the Hynds seam than for the Elphinstone seam. While for the Elphinstone seam samples values from 0.023 mD (sample 4 2/2) to 1.408 mD (sample 11 1/3) have been obtained, the results for the Hynds seam samples are in the range of 0.011 mD (sample 13 2/3) to 20.62 mD (sample 24 1/1).

8.2.3 Macro-scale: Field testing

The field results are influenced by a range of structural parameters: besides the influence of small-scale cleat structures, the permeability on the field-scale is dominated by faults structures, large scale coal fractures and dykes and sills that are present at the Hail Creek Mine field (see chapter 3.2). On the field-scale the deeper Hynds seam comprises of zones of higher permeability than the Elphinstone seam (chapter 4.2.5). The zone thickness ranges from 0.0007 m to 14.415 m (see Table 4-3). The results have been corrected by the thickness of the seams. For the Elphinstone seam, permeabilities in the range of 0.17 mD to 70.46 mD, for the Hynds seam in the range of 3.04 mD to 88.31 mD have been observed.

8.3 SUMMARY OF RESULTS

In the following, all results conducted within the framework of this research are presented in a comparable manner. Figure 8-2 a and Figure 8-2 b give an overview of all data points on a linear and a log scale, respectively. Results for the Elphinstone seam are displayed in blue, results for Hynds seam are displayed green. By plotting the data on a log–scale (Figure 8-2 b), the large number of very small permeability values obtained in the numerical modelling becomes obvious. Permeabilities in the small range of up to 10^{-34} mD have been obtained through numerical values which are of course strongly influenced by the underlying assumption of a non-permeable matrix. No laboratory or field instrument could obtain results for permeability in this range. The laboratory results are generally smaller than the data retrieved using the Heat Pulse Flow Meter. Compared to the field

results (0.17 mD to 70.46 mD), the laboratory data for samples of the Elphinstone seam are one order of magnitude smaller (0.023 mD to 1.408 mD). The lowest laboratory results for the Hynds samples (0.011 mD) are two orders of magnitude lower than the field data of the Hynds seams (3.04 mD), while the maximum laboratory value of 20.64 mD is in the same order of magnitude as the maximum field value of 88.31 mD.

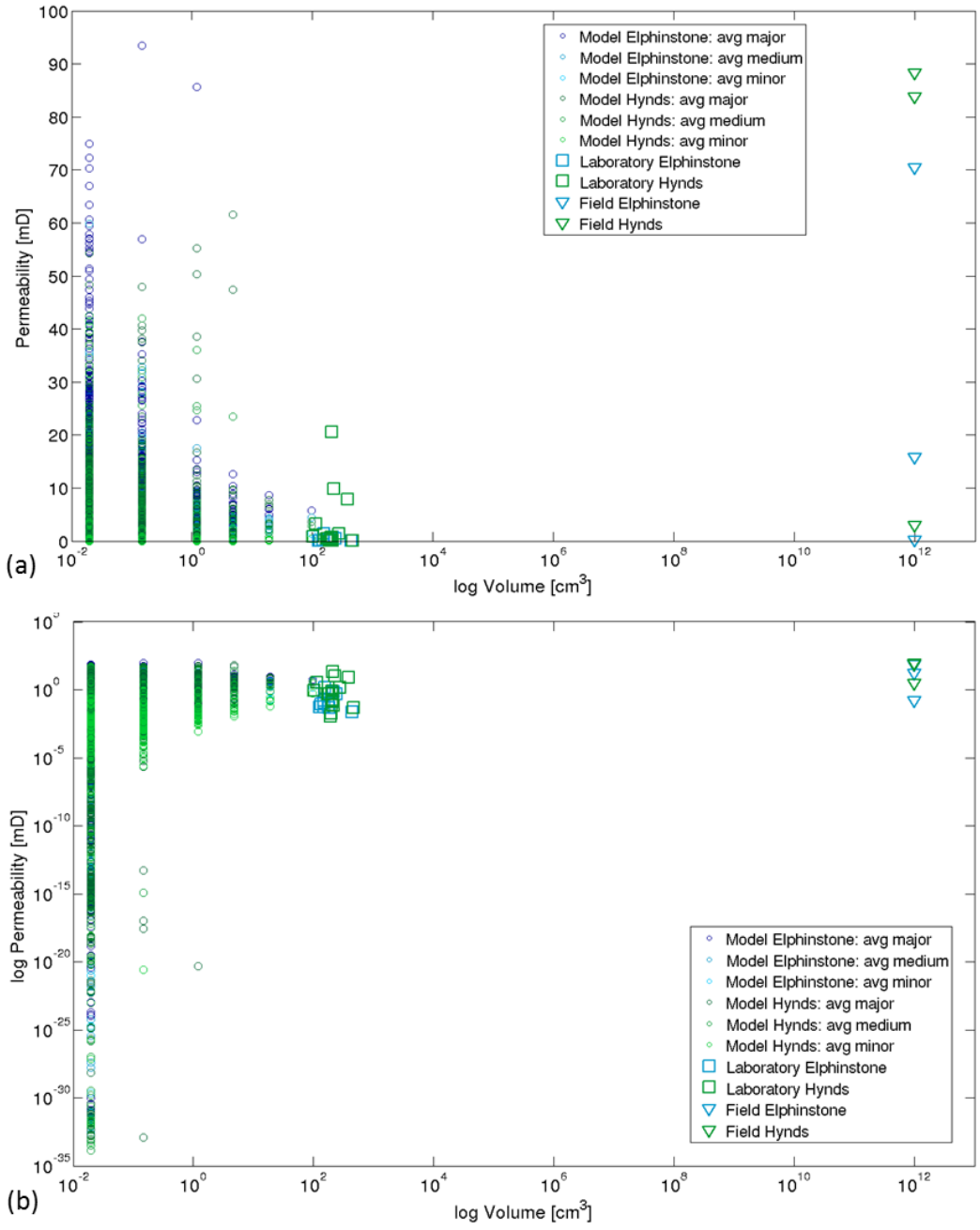

Figure 8-2 a. Absolute and b. logarithmic distribution of permeability values measured by the different methods: Elphinstone (blue) and Hynds (green) seam

Plots with only the averages of the modelling data for each block scale size are shown in Figure 8-3 a and Figure 8-3 b. Using the average numerical data, an increasing trend of permeability values with increasing scale can be deduced. While the averages of the

numerically obtained data are all below 10 mD, the laboratory value span 0.023 mD to 1.408 mD for the Elphinstone seam and 0.011 mD to 20.62 mD for the Hynds seam. In this comparison, the largest range of results is obtained for the field values (Elphinstone seam: 0.17 mD to 70.46 mD, Hynds seam: 3.04 mD to 88.31 mD), which reflects the expected evolution of permeabilities over the scales.

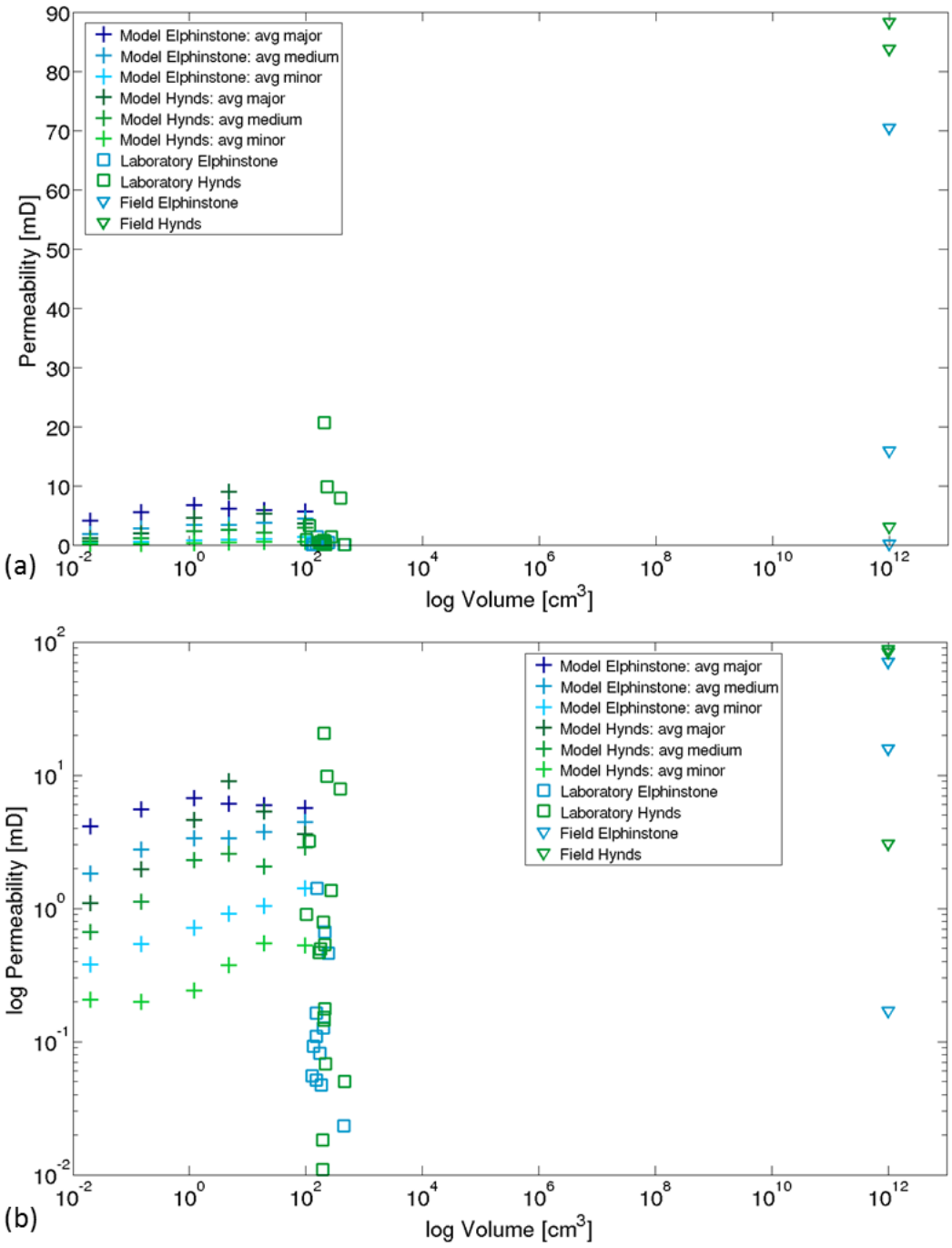

Figure 8-3 a. Absolute and b. logarithmic distribution of permeability values measured by the different methods with the average modelled values displayed: Elphinstone (blue) and Hynds (green) seam

8.3.1 Distributions of results

Figure 8-4 and Figure 8-5 show the distributions of permeabilities for each of the scales for the Elphinstone and the Hynds seam. These distributions are of course strongly influenced by the number of results observed in each scale. However, the comparison of the distributions effectively visualises the range of measured values for the permeability, which gives an indication to whether the measurements have taken place within the REV. Only few data exist for the field scale, which is one scale beyond the scale covered with the laboratory experiments. The inclusion of the field scale results in the comparison highlights the strong influence of fractures and faults on the fluid flow within the coal seams and thus the permeability of the system. The presence of large scale coal fractures and faults seem to have increased the permeabilities locally for both the Elphinstone and Hynds seam, as can be seen at the measured permeabilities in the range from 70 mD to 90 mD.

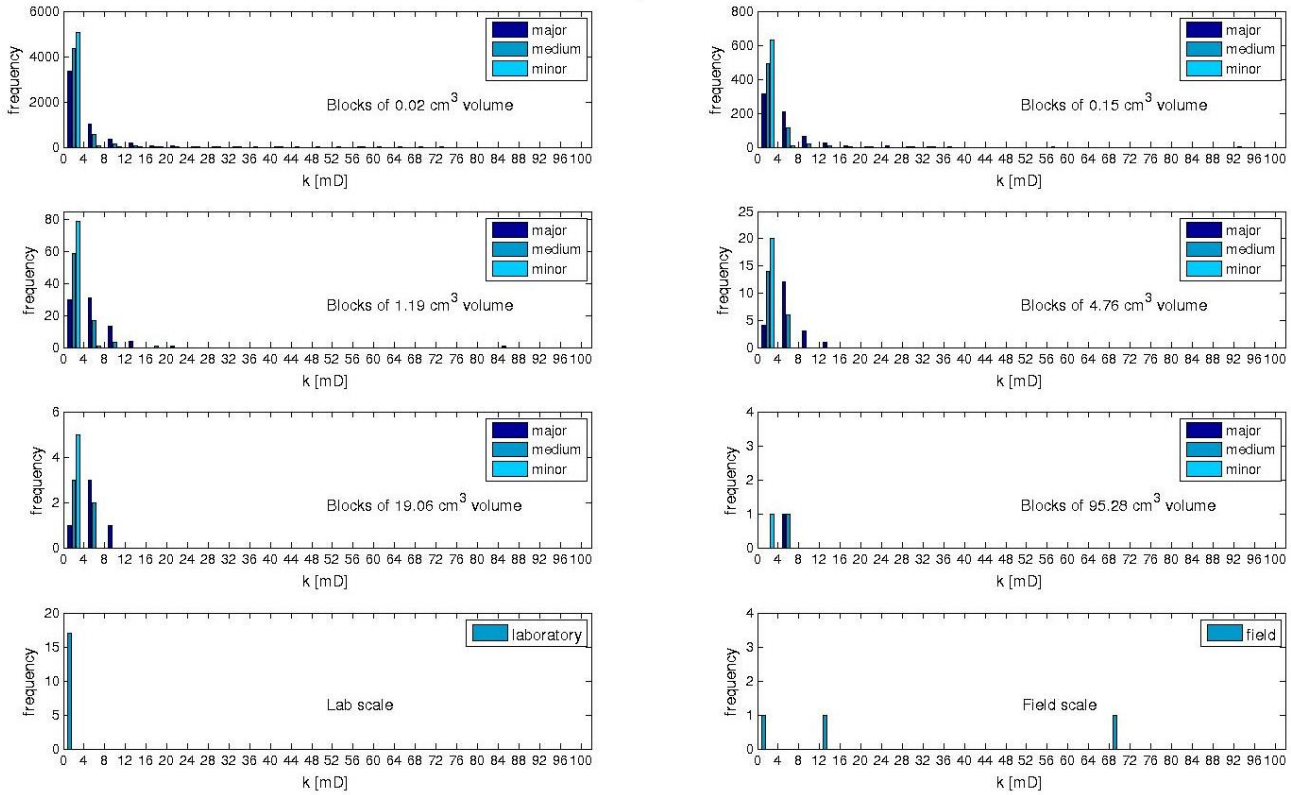

Figure 8-4 Overview of the results collected in the field, in the lab and modelled for Elphinstone seam

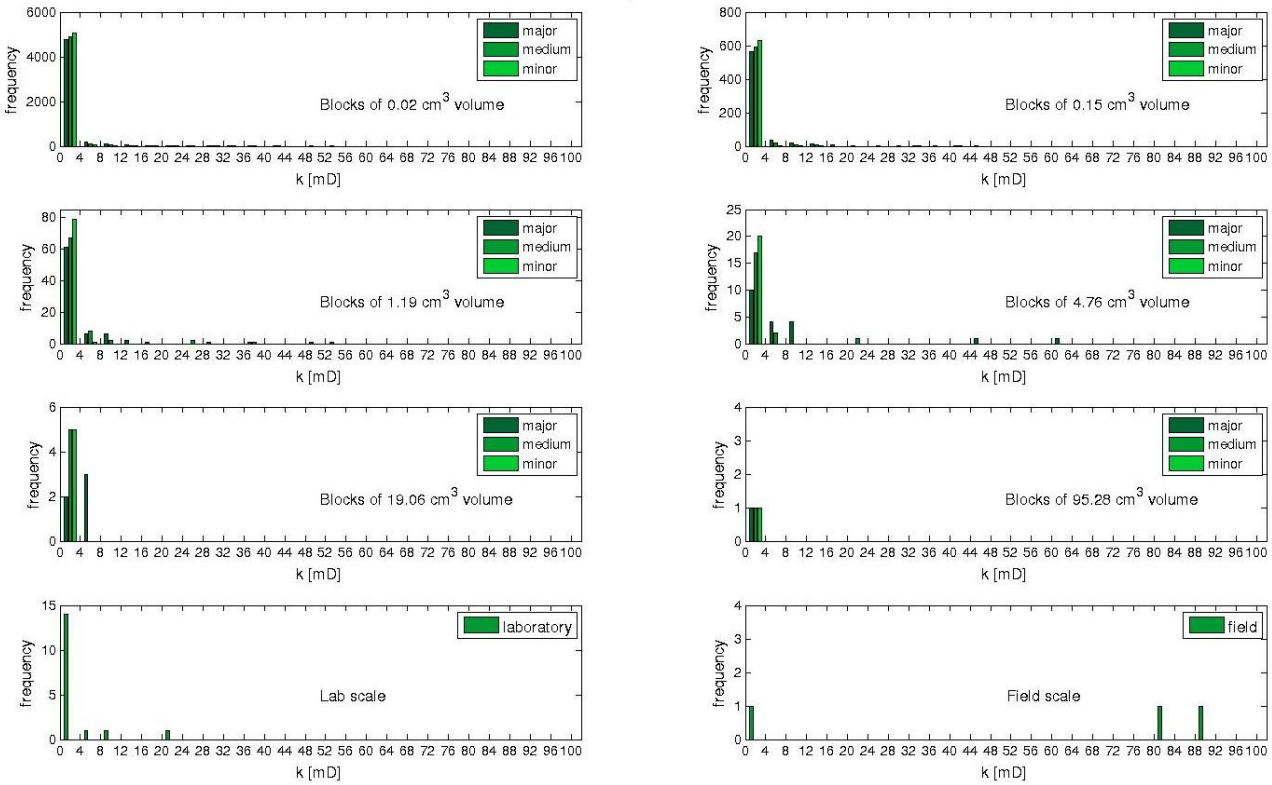

Figure 8-5 Overview of the results collected in the field, in the lab and modelled for Hynds seam

8.4 REPRESENTATIVE ELEMENT VOLUMES

As introduced in chapter 2.5.3, the heterogeneity of a material leads to the variation of any property across scales. For the multi-scale permeability of coal, two systems mainly influence this behaviour: coal fractures on the macro scale and cleats on the meso- and micro-scale.

A small sample of the coal fails to capture the heterogeneity of coal permeability and neglects the influence of discontinuities on the field scale, however it represents the bulk cleat permeability well. As shown on the example of the Elphinstone coal in chapter 7.5.1, laboratory tests on core samples can be assumed to capture the bulk permeability of the cleats and, therefore, potentially represent the REV for the permeability of the cleat system. This is supported by the fact that there is no apparent relation between sample size and measured permeability value (Figure 5-8). At the REV a change in sample volume does not lead to a dramatic change of the measured property. For the Elphinstone sample 11 1/3 the relations between subsamples and supersamples are found to fit a power averaging approach with the power law coefficient α varying between 0.85 and 1.3. For the Hynds sample 15 2/3, the upscaling approach proved to be unsuccessful.

Once the upper boundary of the REV scale is reached, an increase of the volume leads to oscillation of the property again. In this thesis it is shown that indeed the field values are by several orders of magnitude larger than the laboratory values.

To capture and quantitatively characterise the variation in permeability influenced by the heterogeneity of the coal system, scales from the centimetre to kilometre range, therefore, have to be investigated. Figure 8-6 shows all results taken under the framework of this research and visualises the dual scale system governed by coal cleats and coal fractures.

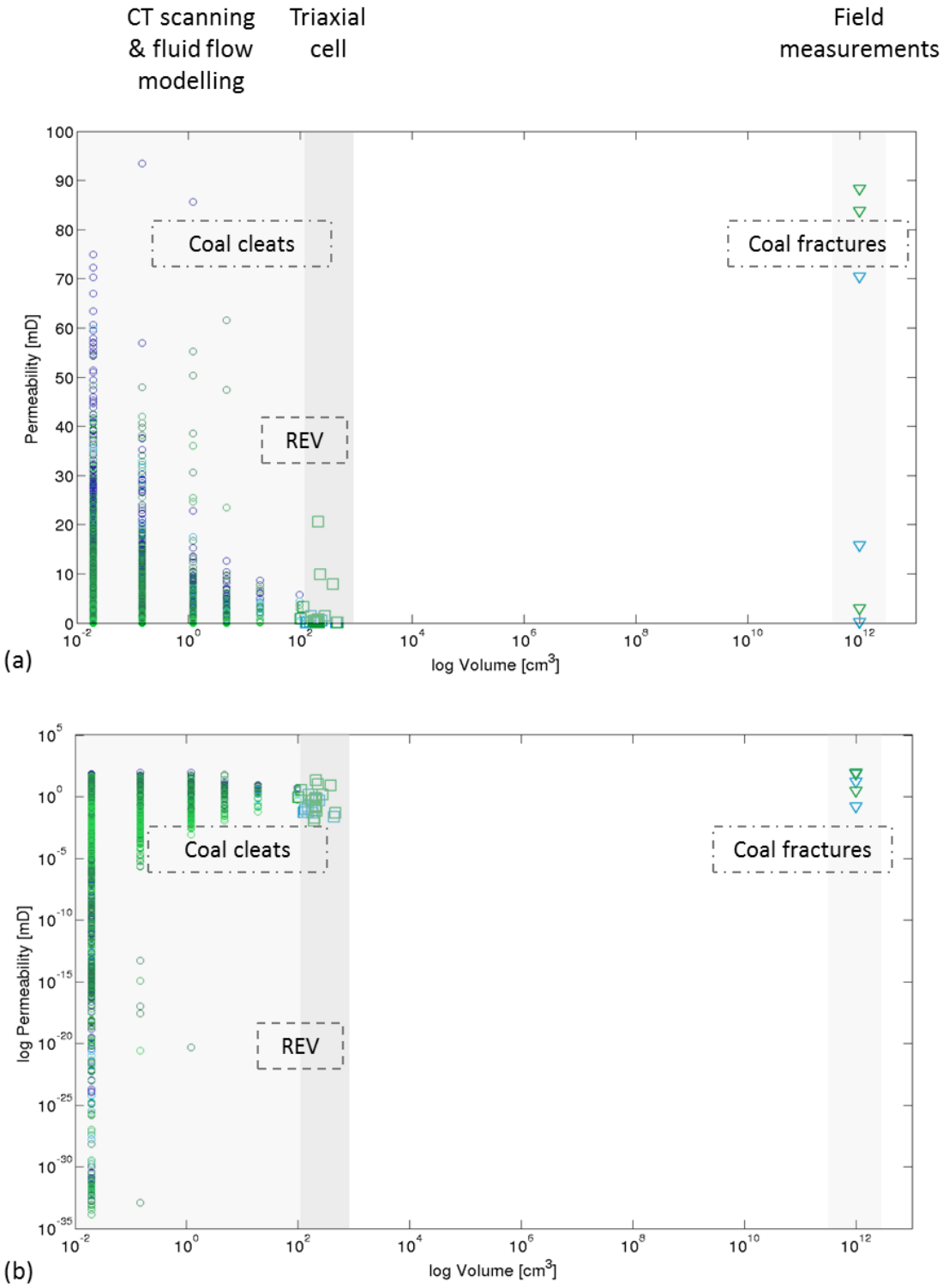

Figure 8-6 Scale dependency of permeability governed by coal fractures and cleats (blue symbols represent data for Elphinstone coal, green symbols represent data for Hynds coal): a. absolute and b. logarithmic distribution of permeability values

9. Discussion

9.1 FIELD TESTING

As part of this project, a paper on the field performance of the Heat Pulse Flow Meter has been published (Busse et al., 2016). The method is useful to delineate flow zones along the borehole and to calculate permeabilities.

However, some limitations have been encountered during the field campaign. The accuracy of the permeability estimates is limited by the accuracy of the tool. Compared to other geophysical flow measurements the heat pulse flow meter allows the tracking of relatively low flow rates. In laboratory tests done by the manufacturer the measuring range has been estimated to be between 0.113 l/min and 3.815 l/min with an accuracy of 5% to 15%. Many of the values obtained during the field testing were below that lower limit, which raises doubts in the accuracy of the results, although field experience has shown that the flow meter can be reliable down to measurements of about 0.05 l/min (Hess, 1986). While the high accuracy of the tool is promising under controlled conditions, the quality of the field data is highly influenced by the circumstances in the field that are deviating from the ideal.

Indeed, the influences on the field results are manifold. Firstly, there is a possibility of disturbance by near well influences on the flow, also known as the skin effect (Sevee, 1991). Besides that, the flow behaviour around the thermistors is uncertain and not well defined. Although the diverter is used to guide all (or most of all) flow through the measurement section and a factor to account for the bypass is introduced (see chapter 4.2.3), it is not certain that the measured value represents the actual total flow at that depth.

For uncased boreholes as present at the Hail Creek Mine site subject to this study, possible outbreak zones result in a larger borehole diameter which can lead to bypass or turbulence around the sensors producing scatter in the data. A time-variant degassing of the coal seams was encountered as well that influence borehole flow. On the one hand, this observation offers the opportunity to quantify the degassing process of seams when the water pressure is disturbed by the drilling of a borehole. On the other hand, when intrinsic permeabilities need to be measured, a period for degassing needs to be introduced which did not happen during the field investigations. Additionally, the presence

of a highly transmissive feature made it difficult to characterise other fractures in the same borehole especially when they are located in a larger depth. Generally, no results can be obtained for the lower parts of the borehole, when high transmissive features dominate in the upper part of the borehole. In these cases, high transmissive features need to be isolated e.g. through packers to enable further measurements in deeper regions. Within the frame of this project, it was not possible to test this idea.

9.2 LABORATORY TESTING

The laboratory testing in the triaxial cell has shown high repeatability of the results. However, there are limitations which need to be kept in mind evaluating these results.

As the image analysis found cleat lengths with a maximum below 30 mm and spacings of up to 18 mmm, the samples that have core diameters of 59 mm to 83 mm are considered to be large enough to incorporate the influence of cleats sufficiently. However, the full connectivity of the cleat system might still be underestimated.

De-ionised and de-aired water is used for testing, with the consequence that desorption and adsorption processes have been apparent during the testing: saturating the samples took time with permeability constantly decreasing over several days before reaching equilibrium.

No true triaxial cell was available for testing, so that the values measured represent the vertical, uni-directional permeability and therefore represent the direction with the lowest values. The triaxial testing was not undertaken at formation pressure. With sample depths of up to 300 m underground, the equipment available to the Geotechnical Engineering Centre, was not able to reproduce corresponding in-situ pressures. The difference in results when comparing the laboratory permeability data with in-situ observed borehole permeability test data might therefore not only be a result of scale effects. The inclusion of a method to adjust test permeability data for in-situ pressures could be subject to further studies. For this study, however, it was the aim to allow for a direct comparison between the laboratory measured permeability values and the permeabilities simulated with the LBM model based on CT-scans that have been taken at unloaded conditions.

9.3 IMAGE PROCESSING

The image processing was used to get an insight into the coal structure in two dimensions, as well as for the reconstruction of the cleat networks in three dimensions for one sample

of the Elphinstone and the Hynds seam each. The main limitation of image processing based methods is the segmentation of image features gained from X-ray computed tomography. Inadequate image segmentation may result in misclassification of coal features that subsequently cause numerical instabilities and wrong results when the structures are used for computational modelling of the flow conditions in the cleat system.

9.3.1 Two-dimensional cleat structure characterisation

A paper on the two dimensional image processing based characterisation of three different coal cleat networks has been published as part of this research (Busse et al., 2017).

The simplicity of the image processing based approach to characterise the two-dimensional features allows high reproducibility. However, there are some sources of uncertainty that may impact on the result. As only two dimensions are used, the common biases truncation, censoring and trace disconnection are still a concern. The region of interest most likely is smaller than the longest cleat occurring. Therefore, the sampling size is a serious limitation.

The distributions and derived power law exponents can be used as input to geo-mechanical and hydraulic computational models. The common approach for the modelling of fluid flow in fractures is to randomly generate artificial sets of fractures based on commonly known distributions (De Dreuzy et al., 2001).

However, CT-scans can only give an insight into the cleat pattern of coal after they have been recovered. To date it is still a matter of discussion, if and to what extend the cleats are created during the coring process or if they are already formed in-situ. Generally, straight and systematic cleats are considered to be of natural origin. It is considered that due to relaxation, apertures ex-situ are larger than at depth. The relaxation might also influence the ovality of the core samples and therefore influenced the similarity/difference between face and butt cleat apertures. However, since this study focuses on mineralised cleats, they can be considered as not drilling-induced. Of importance to the practitioner is the preservation of the core sample orientation during image acquisition and processing. To allow for cleat mapping in the field that could be subject to an up-scaling, the accurate sampling orientation would have to be noted already in the field.

In the context of this thesis, the two-dimensional characteristics are only used to get an insight into the structure of the cleats. However, to derive conclusions between cleat geometry and permeability, the image processing method needs to be expanded to three dimensions.

9.3.2 Three-dimensional reconstruction of cleat network

Based on the stack of the two-dimensional CT-images, the three-dimensional representation of the cleat networks is generated and used for the computational investigation of the permeability. As for the two-dimensional analysis, the resulting cleat networks are highly influenced by the quality and resolution of the images used for the analysis. Significant improvement can be achieved by using other techniques for capturing the internal structure of samples. One possible method is the use of micro-CT-scans. However, the use of higher resolved measuring techniques comes with the cost of being able to investigate only small sample sizes. One possible solution for this dilemma could be the combination of different methods.

9.4 NUMERICAL MODELLING

The modelling of fluid flow within an accurate representation of a real cleat network presented in this thesis is novel. Due to computational restrictions, to date this is commonly done on synthetically generated fracture networks based on the distribution of geometrical parameters.

The numerical modelling is based on a range of assumptions (chapter 7.2.3). One assumption for the modelling part is that the coal matrix is impermeable and flow is conducted within the mineralised cleats that are filled with materials of a certain porosity. The porosities used to fit the modelling results to the laboratory permeability values are smaller than the porosities determined using the laboratory values.

The laboratory-derived cleat porosity for sample 15 2/3 is 6.4 %, the matrix porosity is 2.01 %. For sample 11 1/3 the cleat porosity is 5.1 % (see chapter 6.4.4). The calcite porosity used in the modelling for sample 11 1/3 is 1.13 %, for sample 15 2/3 it is 0.675 %. This discrepancy has been accepted because the focus of this thesis is on the permeability distributions across scales rather than the porosities. Therefore, the modelling results have been fitted to represent the permeabilities measured for the samples 11 1/3 and sample 15 1/3 as they have been obtained for the respective samples in the laboratory (see chapter 5).

Table 9-1 Cleat porosities from laboratory testing and calcite porosities from modelling

Sample	φ_{cleat} [%]	$\varphi_{calcite}$ [%]
11 1/3	5.10	1.13
15 2/3	6.40	0.68

Power law averaging has been found to be a valid upscaling approach for the example of the Elphinstone sample 11 1/3. The power averaging of the permeability of subsamples of a block proved to fit the permeability of the supersample of the size of 95.28 cm^3 with sufficient accuracy. However, for the Hynds sample 15 2/3, the upscaling approach proved to be unsuccessful, which is accounted to an inadequate segmentation of the cleats and coal matrix during the image processing stage. A limitation of the approach is the ranking of major, medium and minor permeabilities as an approximation for the directionality. The anisotropy of the medium might result in the change of these orders for a certain direction. For example, while for a smaller subsample the major permeability might be in the x-direction, in the large supersample it is part of, the major permeability might be directed along the y-axis.

9.5 COMPARISON OF PERMEABILITIES

Permeability heterogeneities are observed at each scale. Using the average numerical data, a general trend is found that shows an increase in permeability with an increase in scale. The quantitative comparison of the resulting permeabilities measured at the different scales show an expected evolution for the Elphinstone coal sample.The variability of the permeabilities decrease with increasing scale up to the meso scale used for the experimental investigation in the triaxial cell, even suggesting that the REV could be around this sample scale (Figure 8–6).

For the Hynds seam, however, a large variability in the determined permeability values is noted up until the sample scale, and a REV beyond the volumes subject to the laboratory studies is assumed. This is related to the degree of inhomogeneity inherent to the coal samples of the Hynds seam.

The variability of the permeabilities in the field is large over a broad range suggesting the existence of another larger REV. It will be the task of future research projects to close the gap between laboratory and field observations and to quantify the REVs for each scale based on the observations made on the accessible scales both in the field and the laboratory.

Generally, coal permeability is determined by both the structure and the stress condition. The structural effects can be said as scale-dependent while the stress effects have to be considered separately. As pointed out in the literature review (chapter 2.2.4.3), permeability is sensitive to the effective stress. When permeabilities are compared across scales, the influence of effective stresses should be taken into account.

Recommendations for future research projects are given in the following chapter 10.2.

.

10. Conclusion and Recommendations

10.1 CONCLUSION

The main objective of the presented thesis is the quantification of the permeability of coal on different scales and the identification of the REV representing the permeability conditions for a coal specific system of face and butt cleats. To achieve this aim, investigations have been realised in the field, in the laboratory, and by computational modelling and image analysis to enable the analysis of the influence of the cleat system on the permeability. The resulting permeabilities are compared and evaluated to provide a complete picture of the permeability conditions for the selected Hail Creek Mine site.

Generally, the scale effect of permeability in fractured rock is controlled by the connectivity of the fluid conducting fractures and therefore increases with scale with local variations (Illman, 2006). In particular, the permeability of coal is influenced by its unique structure that is characterised by coal fractures and cleats. The connectivity of coal fractures and cleats is a directional quantity based on the complex structure of coal that has been developed as a response to the stresses that were present during coalification and changing stresses during subsequent tectonic processes and mining activities.

This results in a dual-scale system of permeability in coal. Coal fractures are present on the macro-scale and influence field measurements. They are forming the major pathways on the macro-scale, which results in larger permeability values. On smaller scales, these large scale structures are not present. Instead, here the permeability is highly dependent on the presence of coal cleats and their geometrical properties. Laboratory measurements capture permeability values as a bulk measurement of all cleats present in a core. Using numerical methods, the permeabilities can be quantified on the micro-scale. The influence of each single cleat on the permeability can be determined using a CT-scan based cleat network model that displays the geometric features of each cleat with high accuracy.

The main conclusions on permeability of coal fractures and coal cleats are:

- Laboratory values on the meso-scale are representing the bulk measurement of micro-scale cleat permeability.
- Field-scale values represent the macro-scale permeability and these permeabilities are governed by larger coal fractures.
- Permeability heterogeneities are observed at each scale.

Permeability measurement techniques need to be chosen by intended scale of use. This research combined the results over a range of scales from a centimetre to a kilometre range. The dual-scale permeability system is shown in Figure 10-1.

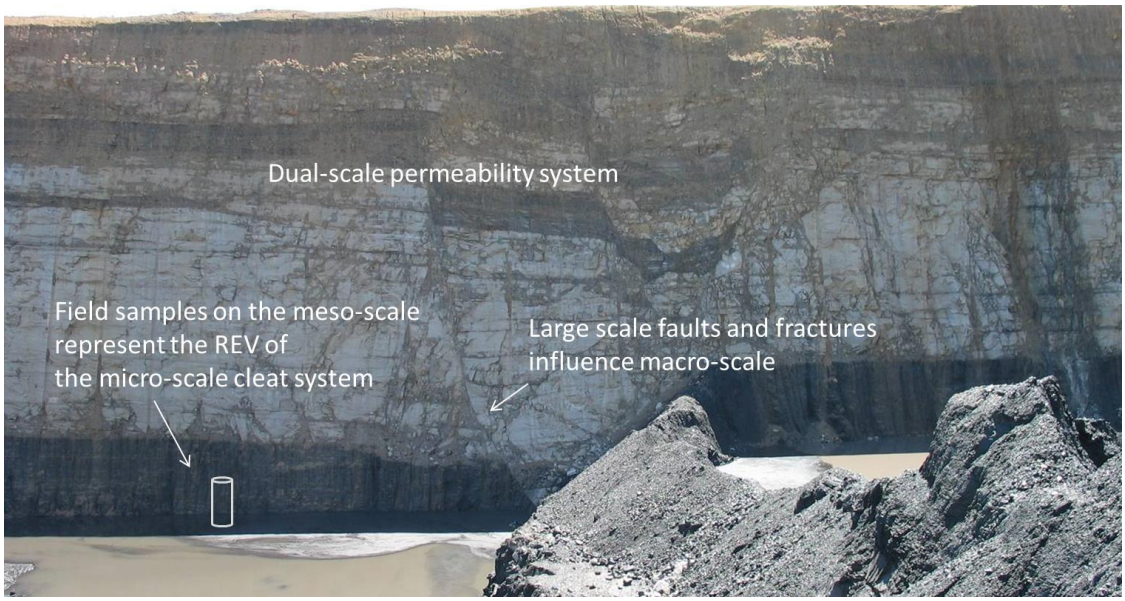

Figure 10-1 Elphinstone seam at the Hail Creek mine and the structures that influence permeability on two scales (photo by Holwell, 2007)

The different techniques used on different scales result in experimental bias, However, it is difficult to measure permeability with the same instrument at multiple scales. Furthermore, by its anisotropic nature, coal shows a high structural variability from one sampling point to the next. The large scale field testing done by means of the Heat Pulse Flow Meter captures high conductive features, like coal fractures and faults that are not present on the smaller scales and therefore cannot be preserved in the laboratory measurements. The field data collected with the Heat Pulse Flow Meter represent the average non-directional horizontal permeability. Based on the world wide average of permeability anisotropy ratio of 4:1 (k_{max} : k_{min}), these values will be off the maximal horizontal permeability by an average of 1.6. Furthermore, field data is influenced by near well effects, as the skin effect and de-stressed conditions around the borehole. These do result in the measurements of

higher permeabilities than the ones actually present in the far field (Massarotto, Rudolph, et al., 2008).

While core sampling was used to give an insight into the smaller coal cleat structure, the core samples might underestimate the coal cleats, as the diameter is smaller than the maximum length of the cleats. Lama & Bodziony (1998) point out that laboratory permeability data is often lower by 1 to 3 orders of magnitude as compared to in situ test results. This is because cleats are not filled with gas and water after removal from the site and might add to experimental bias.

The image resolution is the main limitation when using CT-scans as the basis for numerical analysis of the flow in cleat or fracture systems. The resolution determines the scale at which insight into the material is obtained. Eker & Akin (2006) found that permeability values found in LBM simulations were smaller than the ones obtained with cubic law estimates.

The main influences that affect the investigation of permeability of coal across scales are:

- The heterogeneity and anisotropic nature of coal govern the permeability on different scales.
- On the large-scale: Coal fractures and discontinuities govern the permeability in the field.
- On the meso- and micro-scale: Directional effects based on coal structure with face cleats and butt cleats lead to permeability tensors with distinctly different permeabilities in different directions without the existence of an orthogonal permeability tensor.
- Permeability values are experimentally biased when different techniques are used on the various scales with different initial and different boundary conditions.
- The comparison of the permeability conditions derived from studies done by different professionals can lead to misinterpretation of the real conditions as different measurement techniques and analysis methods are commonly used.

The presented work was successful in quantifying the permeabilities on different scales with sophisticated measurement methods in the field, as well as by novel analysis methods based on image analysis and computational models. The results clearly show the challenges linked to the investigation of scale dependent permeabilities and highlight the importance to determine the REVs of this important parameter. The comprehensive study

not only covers multiple scales but also very different analysis and measurement methods that can be considered for future investigations in this field.

10.2 RECOMMENDATIONS

The investigation of the permeability of coal needs to take the complexity of the medium into account. Coal is characterised by its unique microstructure of a porous matrix intersected by a network of face and butt cleats. Together with faults caused by geological activities and mining-induced fractures, these small scale cleats provide the principal source of permeability for groundwater and gas flow within a coal seam. To capture the heterogeneity of permeability of coal across the scales, investigations have to be focused on the scale of the intended use. The techniques to capture permeability, therefore, have to be chosen bearing in mind the use of the respective study.

While this study focuses on the structural influences on coal permeability, the ability to allow for fluid flow is further determined by the present stress conditions. While the structural effects are scale-dependent, the influence of stress should be considered separately in a future project. To take this into account, a permeability model could be used to transform all permeability measurements into values that would be expected under the same effective stress condition, i.e., 0.45 MPa. Equal stress conditions would guarantee a higher comparability of laboratory, field and numerical permeability values and the influence of stresses on the results can be excluded (Liu et al., 2011).

Each experimental method and analysis approach used as part of this research has its advantages and limitations. In the following, the gaps of knowledge that have been identified and recommendations for further research are presented for each method or approach, respectively. The findings presented in this thesis, as well as the encountered challenges, shall provide guidance for future studies aiming at the quantitative characterisation of the permeability of structured geo-materials.

10.2.1 Field testing

While the Heat Pulse Flow Meter allows for a very accurate zoning of groundwater flow along the borehole and can detect flow rates as small as 0.113 l/min, the method has several major limitations that have been published in Busse et al. (2016). While near well influences due to the skin effect cannot be completely eliminated, the outcome of future field campaigns using the Heat Pulse Flow Metre can be improved when implementing some of the lessons learned.

It is recommended not to use the method in cased or back-filled boreholes, as these structural condition leads to further turbulence around the borehole. The borehole diameter needs to be large enough to allow for the use of a diverter to seal the fluid flow against the borehole wall. Furthermore, when mapping borehole flow in coal seams, a waiting period needs to be served to allow for degassing after drilling.

A highly transmissive feature, for example the overburden or a large fault, can dominate the flow conditions along the borehole. As a consequence, the quantification of the flow in lower areas along the borehole below this dominating feature and thus the determination of transmissivities can be at least much restricted and even be made impossible. The effect of injection or pumping that is necessary in order to collect two subsequent sets of data under two different hydraulic conditions on lower less transmissive parts of the borehole can be diminished or overlain by the influence of the highly transmissive feature. This can be resolved by the use of packers to delineate zones of interest, which should be integrated in the field set-up in future measuring campaigns.

10.2.2 Laboratory testing

To measure the permeabilities on the meso-scale within this research project, a conventional triaxial cell system has been used. This system allowed the measurement of the permeability of the coal core samples along the z-axis, that is, perpendicular to the bedding plane. For future research, the use of a true-triaxial would be desirable. In a true-triaxial cell, the permeability could be measured for the three mutually orthogonal directions and stresses could be applied and varied independently for each direction. In a larger machine, larger samples could be tested, allowing the incorporation of the full influence of the connectivity of the cleat network, which might be under-represented with the sample sizes used within this study. Even with the triaxial cell available at the School of Civil Engineering, future research could focus on the influence of different effective stresses on the permeability of coal cleats.

10.2.3 Image processing

Image processing for geo-materials is an ongoing research topic, with the potential to be constantly improved by a growing community sharing ideas (Busse et al., 2017). By comparing different current approaches to depict cleat network characteristics, issues related to representability, reproducibility and resolution can be minimised. For example, to test the quality of the cleat segmentation and clustering described, results of other segmentation techniques (e.g., manual, sobel edge detection, watershed segmentation)

could be used. While not in the framework of this study, the generation of multiple cleat networks based on different segmentation and the influence on the permeability results could be tested to analyse and quantify uncertainties in the permeability determination.

Future improvement of the image processing efforts should concentrate on extending the two-dimensional characterisation method to 3D to provide a more detailed and realistic quantification of the three-dimensional structure of cleats in coal. This would allow for the investigation of the relationship of the two-dimensional cleat network statistics with the three-dimensional structure. The derived data can be used for permeability estimations and are therefore useful to the engineering practitioner. The distributions and derived power law exponents can be used as input parameters for geo-mechanical and hydraulical models. The common approach for the modelling of fluid flow in fractures is to randomly generate artificial sets of fractures based on commonly known distributions (De Dreuzy et al., 2001).

While the constantly growing computing resources allow for the increase of the volume of interest, the capturing of cleat and fracture structures is also limited by the field of view of the scanner used. The use of higher resolved measuring techniques comes with the cost of being able to investigate only small sample sizes. One possible solution for this dilemma could be the combination of different measuring systems. Small scale structures could be captured in a higher resolution, and larger scale structures scanned in a machine with a lower resolution. The results could then be merged in a multi-scale model.

10.2.4 Numerical modelling

A novel framework to quantify the directional permeability based on CT scans and to investigate the statistical distributions of permeabilities across the micro-scale was implemented in the frame of this project. While reasonable conclusions could be drawn for the Elphinstone coal (sample 11 1/3) no apparent relationship between the permeabilities across the investigated scales could be found for the Hynds coal (sample 15 2/3). The reason for this outcome is most probably caused by the fact that the structure of the investigated Hynds coal sample not only varied within the sample, but also led to an insufficient distinction between coal matrix and cleats (see Figure 6–4). In order to verify the computational method, it should be tested using a different segmentation method of the input images, as well as on other data sets of structured geo-materials.

Future research using the proposed approach should focus on an analysis of the eigenvectors that are resulting from the Lattice Boltzmann based fluid modelling. The

eigenvectors depict the direction of the eigenvalues and therefore the direction of the permeabilities. In this thesis, the results have been simplified to three main directions according to the rank of their permeability (major, medium and minor). The chosen approach represents a simplification, yet allowed to quantify the relationships between permeabilities on different scales. Nevertheless, with the cleat structure of coal being highly complex, the inclusion of the eigenvectors of the permeability across scales has great potential to deliver further interesting insights into the scale dependent behaviour of permeability and its directionality.

Appendix

Table of Figures in Appendix

List of Tables in Appendix

A.1 HIGHER ORDER PARTITION SAMPLE 11 1/3

A.1.1 *Second order partition*

a)

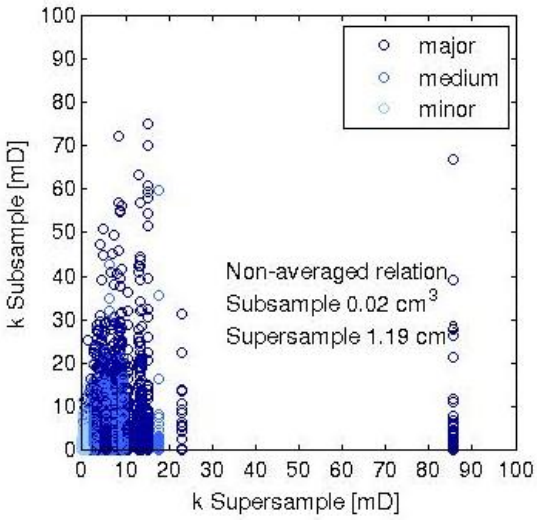

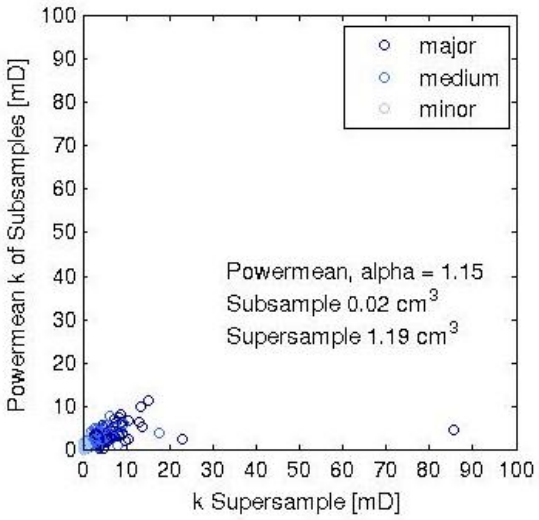

b)

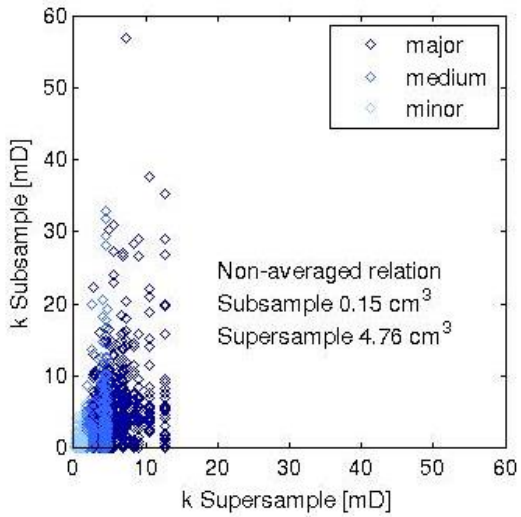

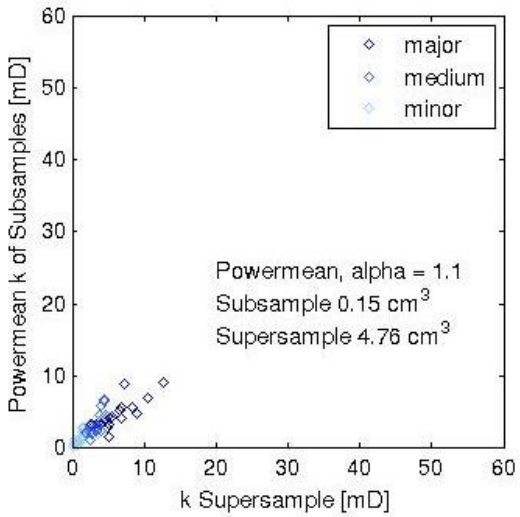

c)

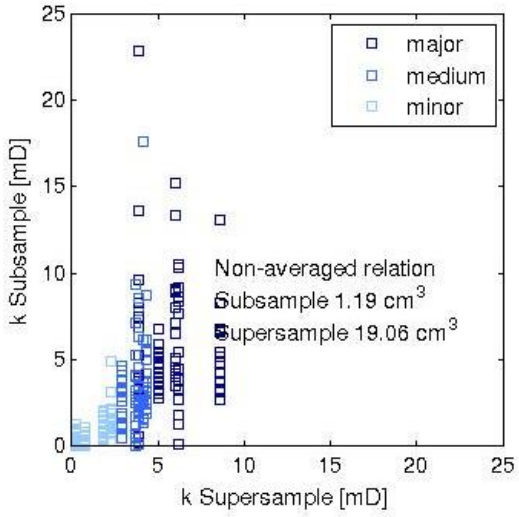

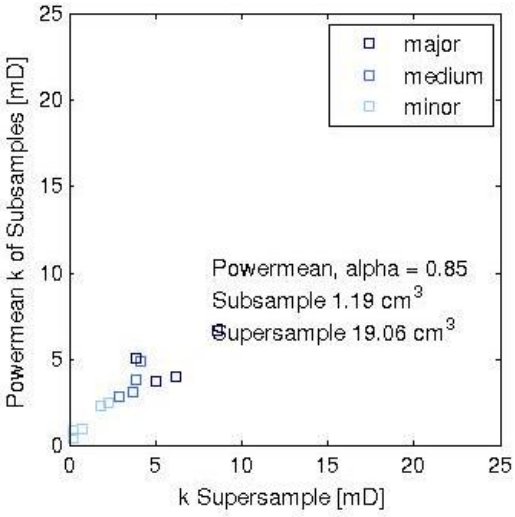

d)

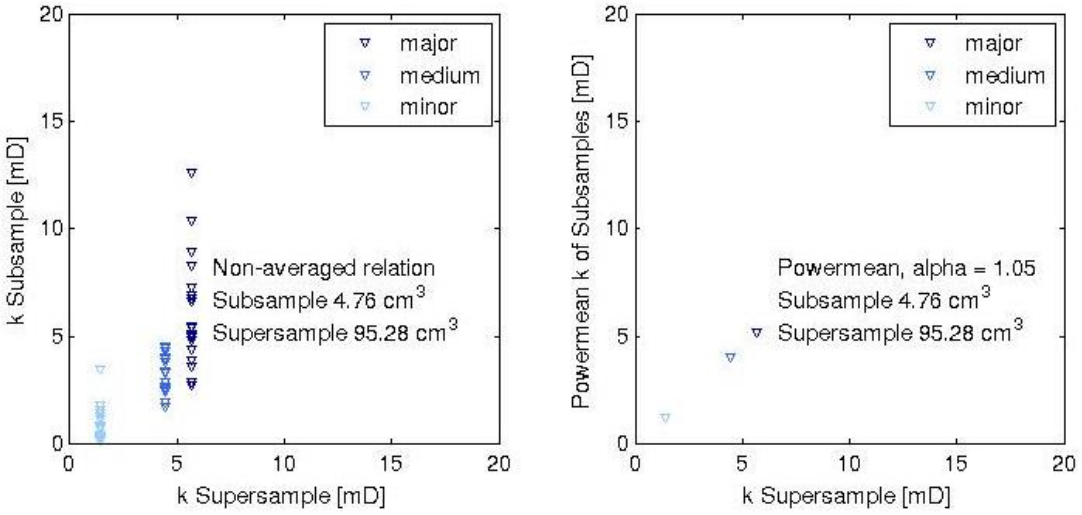

Figure A 1 Ratio of non-averaged and power-averaged permeabilities of subsamples to permeabilities of supersamples for partitions of second order for sample 11 1/3. Displayed are the size of subsample to the size of supersample: a) 0.02 cm^3 : 1.19 cm^3 blocks b) 0.15cm^3 : 4.76 cm3 blocks, c) 1.19 cm^3 : 19.06 cm^3 blocks, d) 4.76 cm^3 : 95.28 cm^3

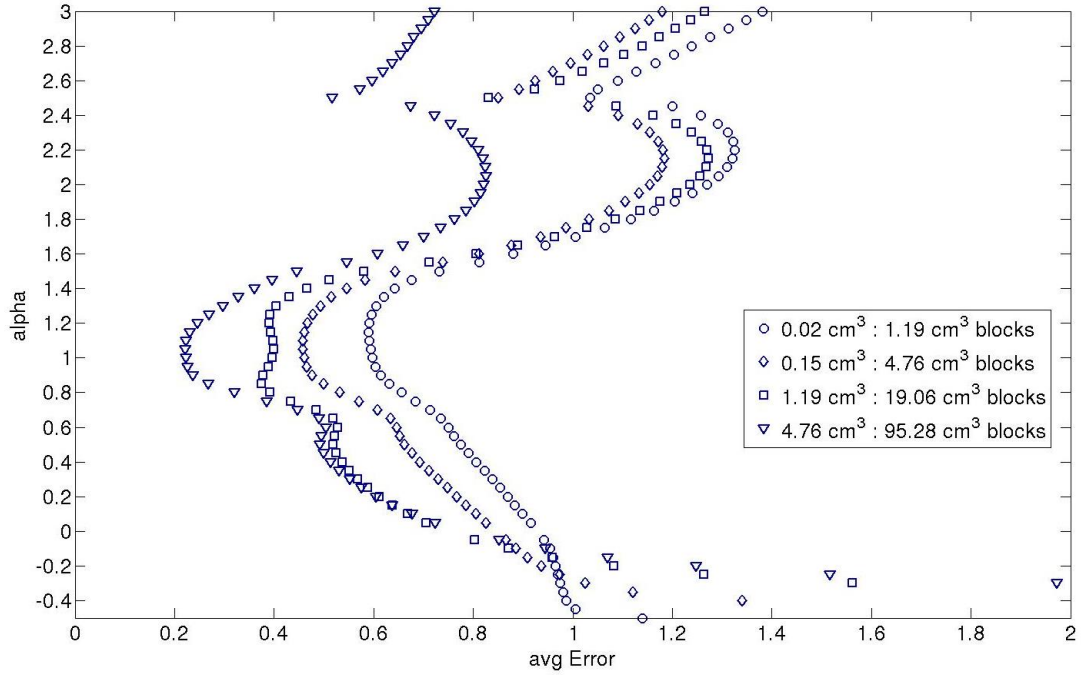

Figure A 2 Average error for alpha in the range of α=-0.5 to 3 for the second order partitions of sample 11 1/3

Table A 1 Ideal alphas for second order partitions of sample 11 1/3

Size Subsample [cm^3]	Size Supersample [cm^3]	Ideal Alpha
0.02	1.19	1.15
0.15	4.76	1.10
1.19	19.06	0.85
4.76	95.28	1.05

a)

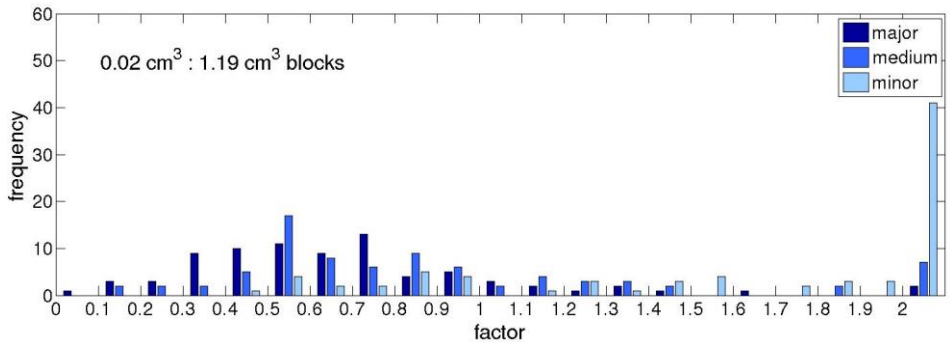

b)

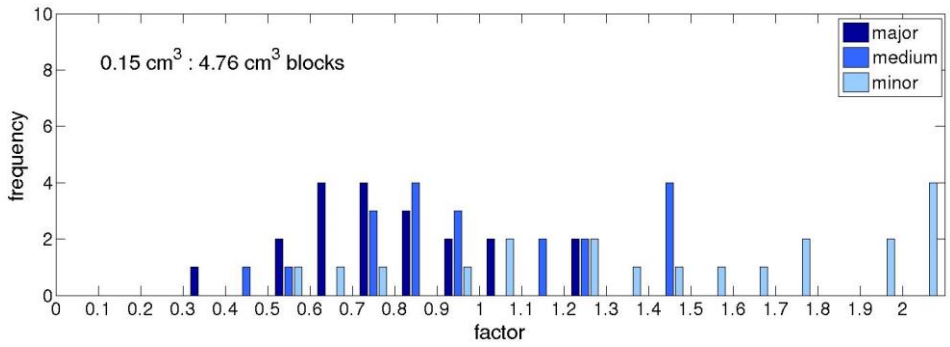

c)

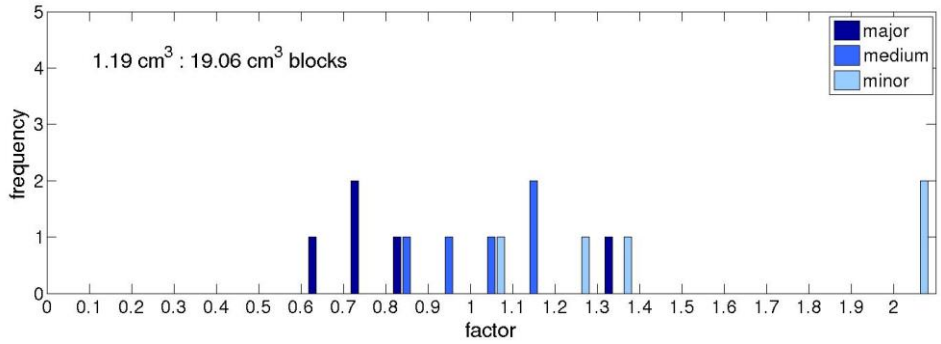

d)

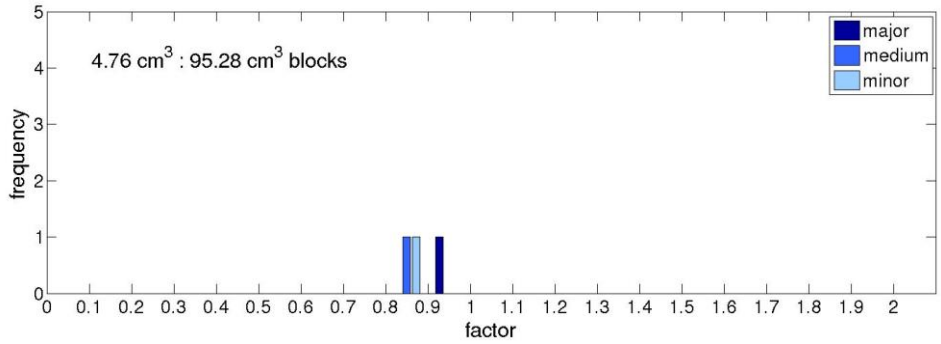

Figure A 3 Power-average factors for the second order partitions of sample 11 1/3. Displayed are the size of subsample to the size of supersample: a) 0.02 cm^3 : 1.19 cm^3 blocks b) 0.15cm^3 : 4.76 cm3 blocks, c) 1.19 cm^3 : 19.06 cm^3 blocks, d) 4.76 cm^3 : 95.28 cm^3

A.1.2 *Third order partition*

a)

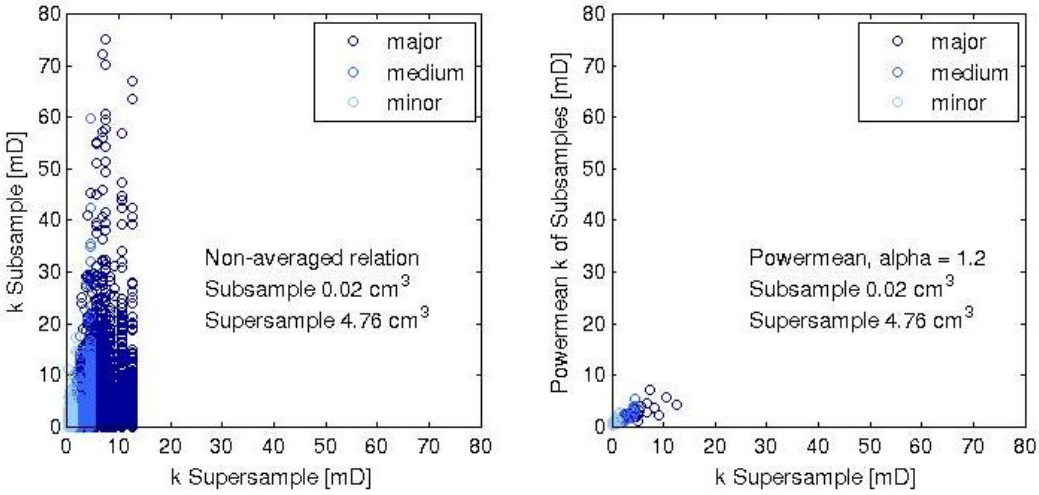

b)

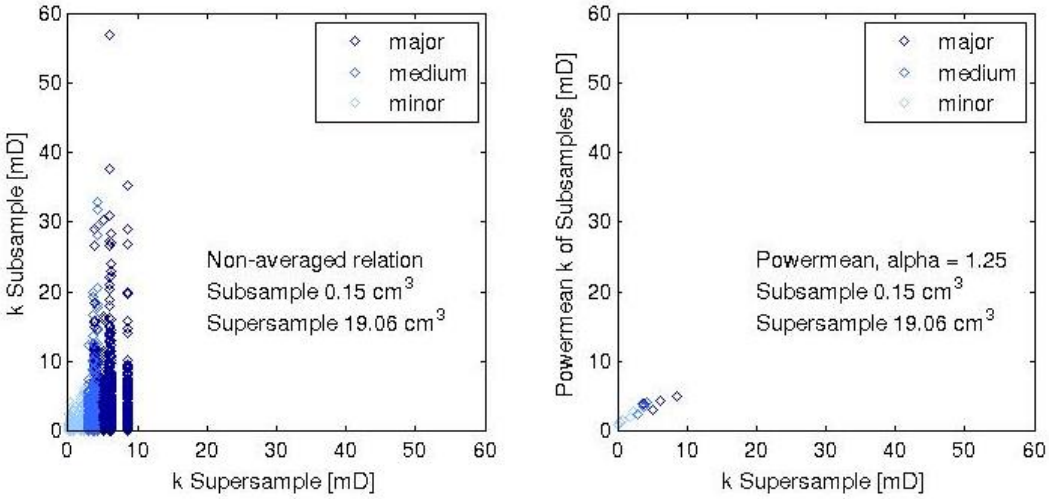

c)

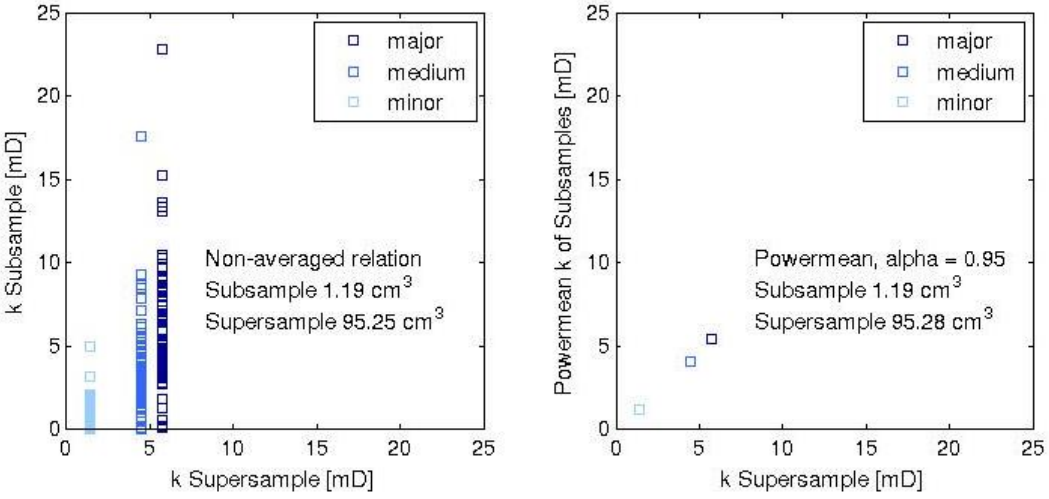

Figure A 4 Ratio of non-averaged and power-averaged permeabilities of subsamples to permeabilities of supersamples for partitions of third order for sample 11 1/3. Displayed are the size of subsample to the size of supersample: a) 0.02 cm^3 : 4.76 cm^3 blocks b) 0.15cm^3 : 19.06 cm3 blocks, c) 1.19 cm^3 : 95.28 cm^3 blocks

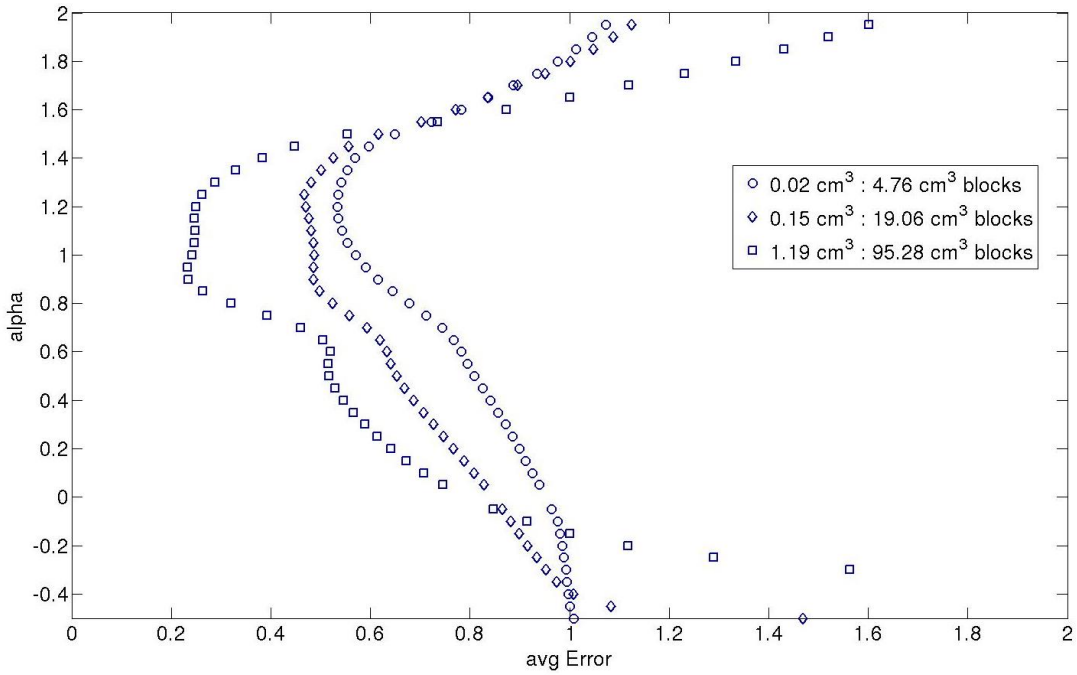

Figure A 5 Average error for alpha in the range of α=-0.5 to 3 for the third order partitions

Table A 2 Ideal alphas for third order partitions of sample 11 1/3

Size Subsample [cm^3]	Size Supersample [cm^3]	Ideal Alpha
0.02	4.76	1.20
0.15	19.06	1.25
1.19	95.28	0.95

a)

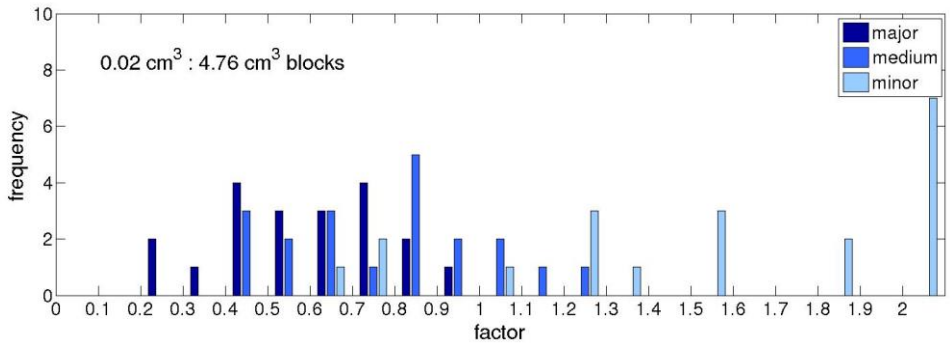

b)

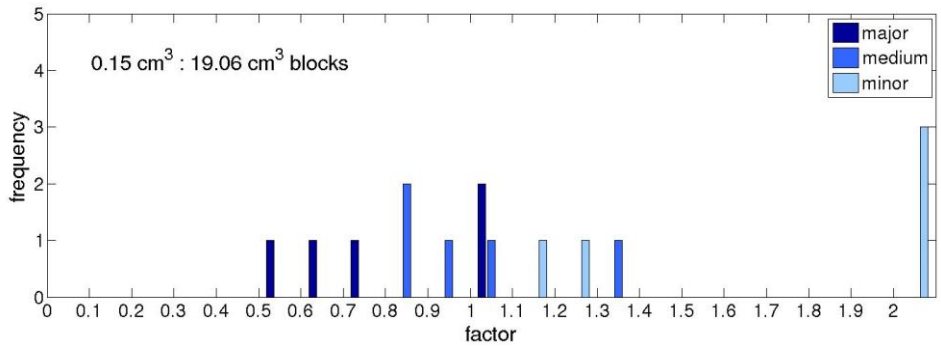

c)

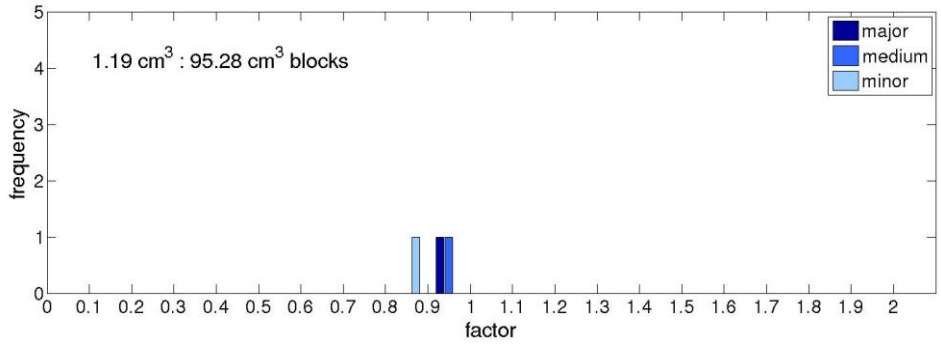

Figure A 6 Power-average factors for the third order partitions of sample 11 1/3. Displayed are the size of subsample to the size of supersample: a) 0.02 cm^3 : 4.76 cm^3 blocks b) 0.15cm^3 : 19.06 cm3 blocks, c) 1.19 cm^3 : 95.28 cm^3 blocks

A.1.3 *Fourth order partition*

a)

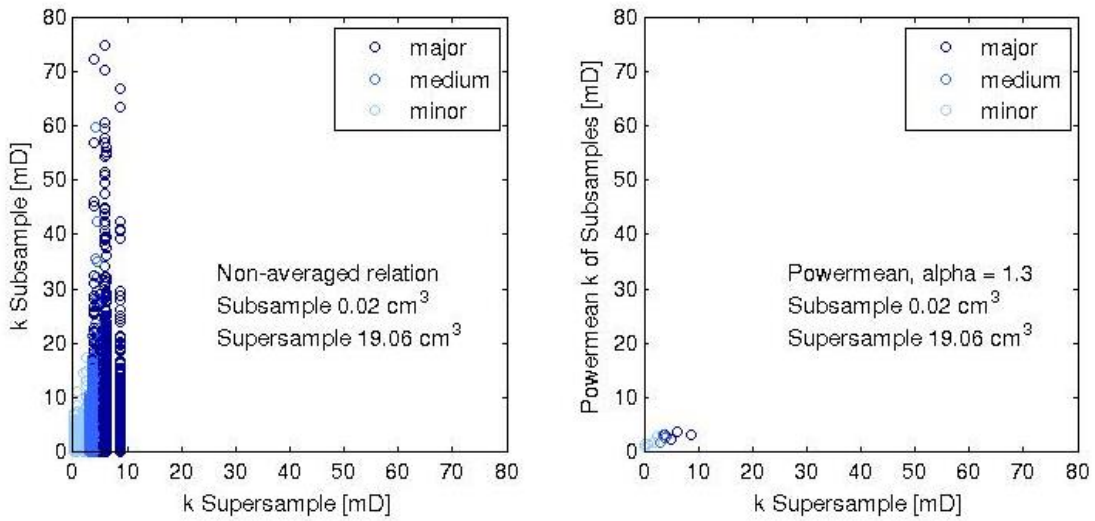

b)

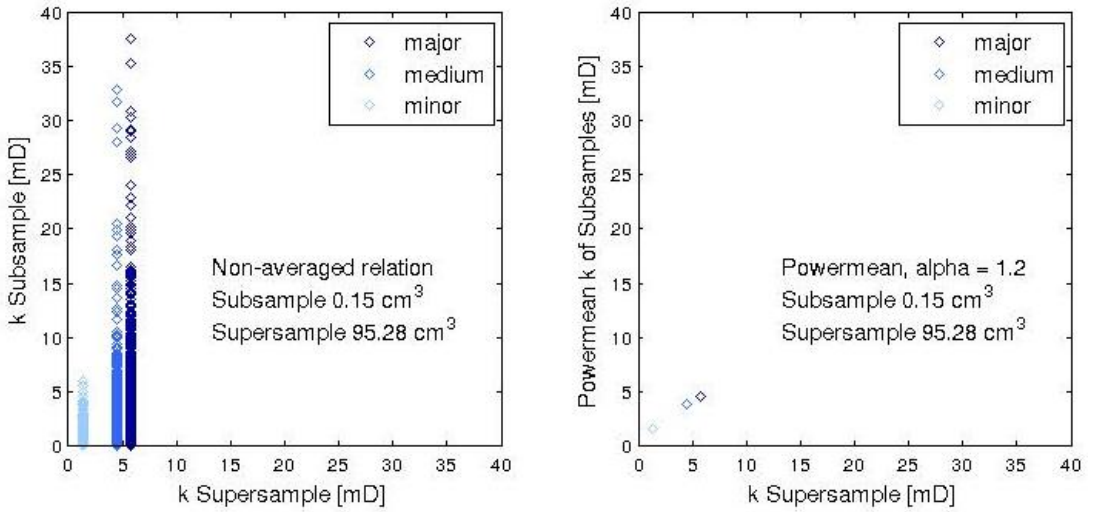

Figure A 7 Ratio of non-averaged and power-averaged permeabilities of subsamples to permeabilities of supersamples for partitions of fourth order for sample 11 1/3. Displayed are the size of subsample to the size of supersample: a) 0.02 cm^3 : 19.06 cm^3 blocks b) 0.15cm^3 : 95.28 cm^3 blocks

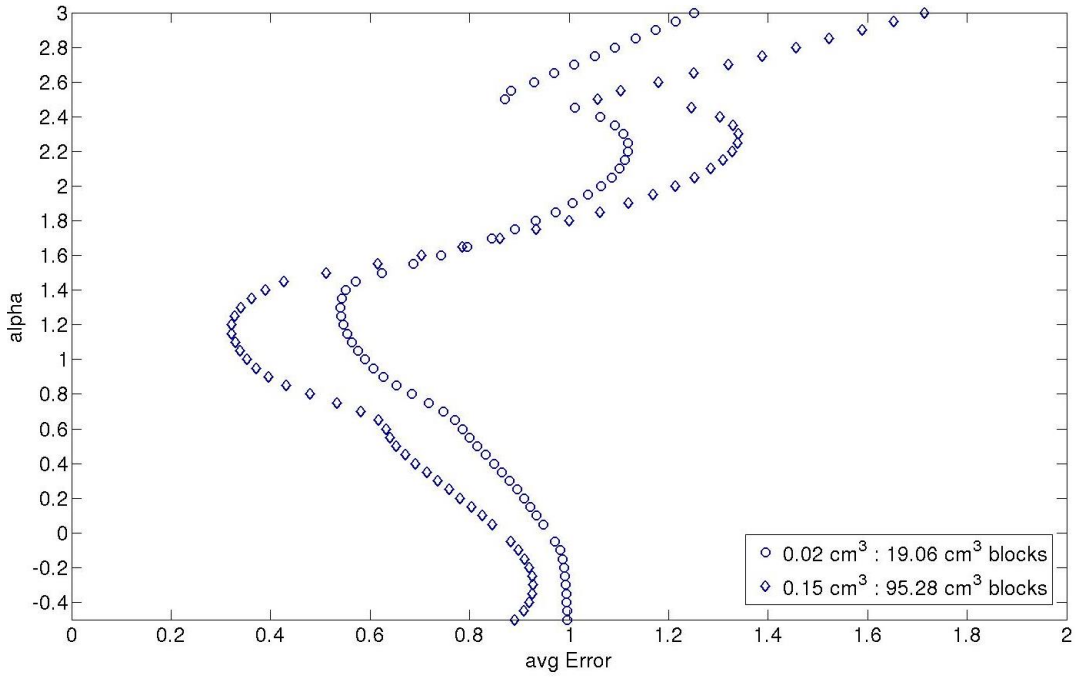

Figure A 8 Average error for alpha in the range of α=-0.5 to 3 for the fourth order partitions

Table A 3 Ideal alphas for fourth order partitions of sample 11 1/3

Size Subsample [cm^3]	Size Supersample [cm^3]	Ideal Alpha
0.02	19.06	1.3
0.15	95.28	1.2

a)

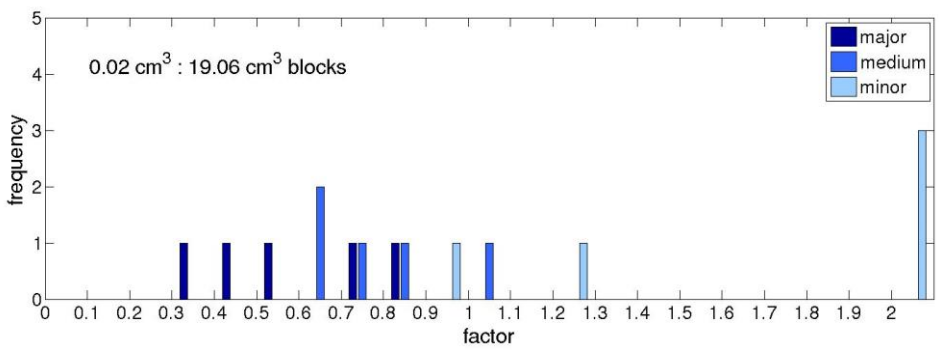

b)

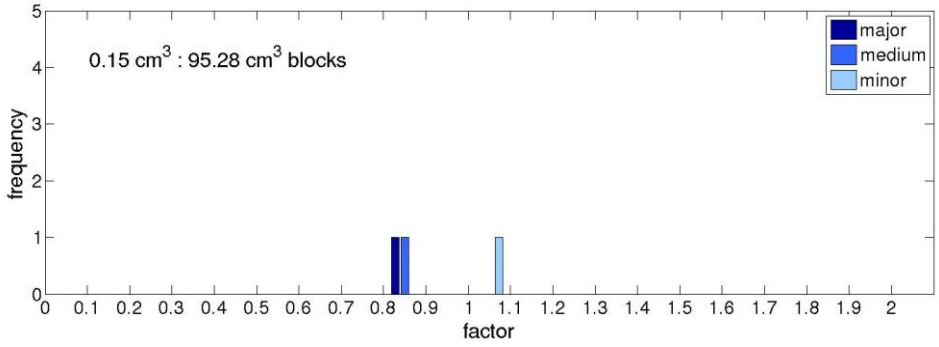

Figure A 9 Power-average factors for the fourth order partitions of sample 11 1/3. Displayed are the size of subsample to the size of supersample: a) 0.02 cm^3 : 19.06 cm^3 blocks b) 0.15cm^3 : 95.28 cm^3 blocks

A.1.4 *Fifth order partition*

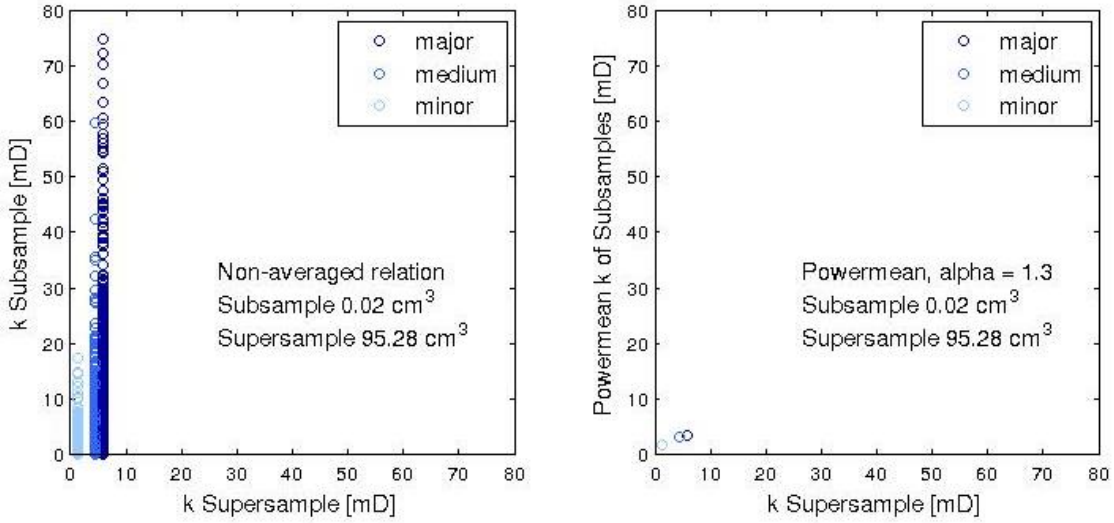

Figure A 10 Ratio of non-averaged and power-averaged permeabilities of subsamples to permeabilities of supersamples for partitions of fifth order for sample 11 1/3. Displayed is the size of subsample to the size of supersample: 0.02 cm^3 : 95.28 cm^3 blocks

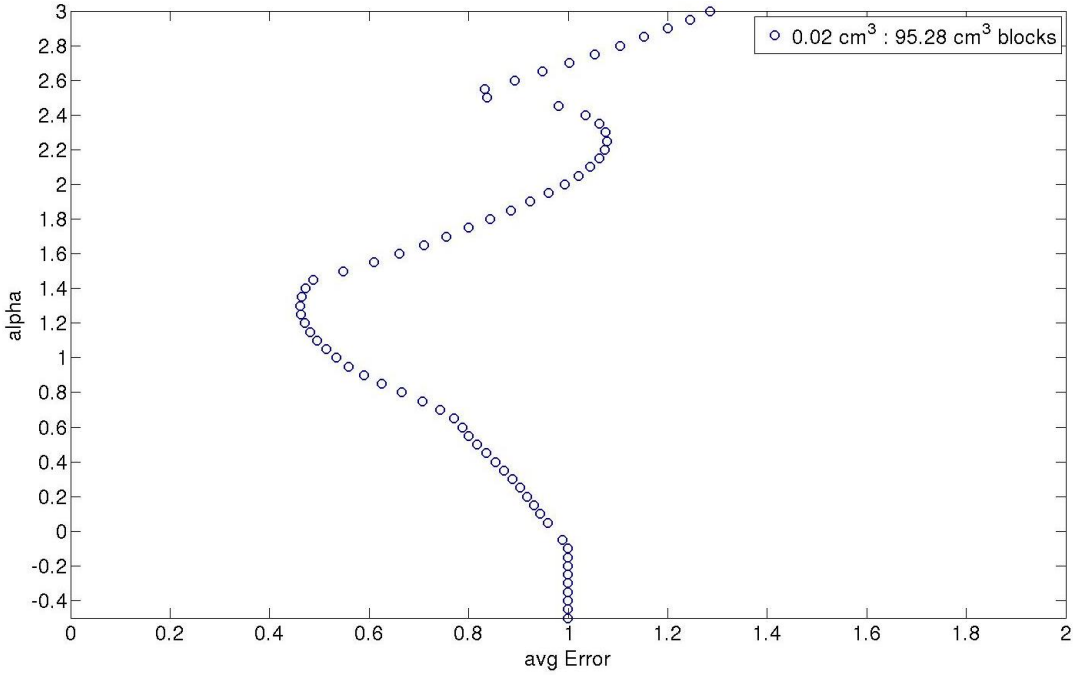

Figure A 11 Average error for alpha in the range of α=-0.5 to 3 for the fifth order partitions

Table A 4 Ideal alpha for fifth order partitions of sample 11 1/3

Size Subsample [cm^3]	Size Supersample [cm^3]	Ideal Alpha
0.02	95.28	1.3

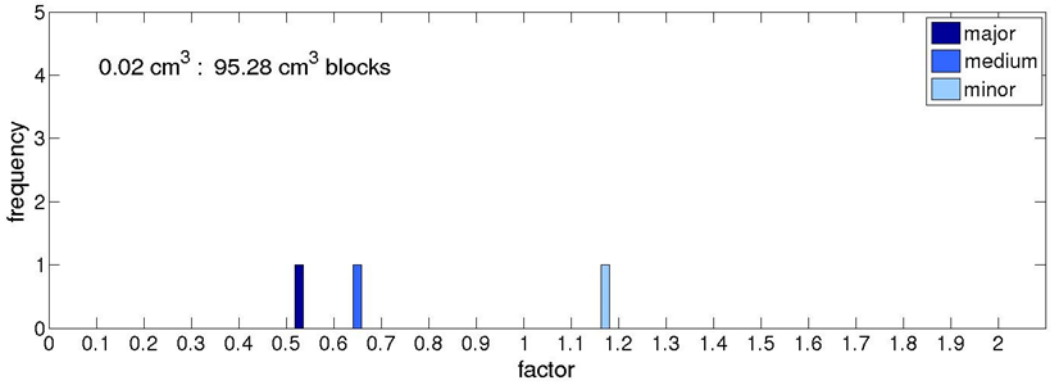

Figure A 12 Power-average factors for the fifth order partitions of sample 11 1/3. Displayed is the size of subsample to the size of supersample: 0.02 cm^3 : 95.28 cm^3 blocks

A.2 HIGHER ORDER PARTITION SAMPLE 15 2/3

A.2.1 *Second order partition*

a)

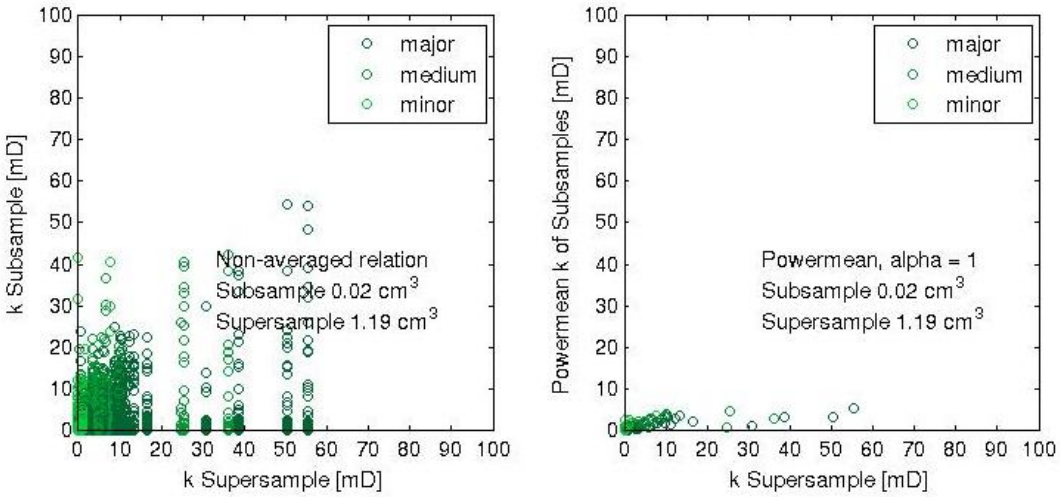

b)

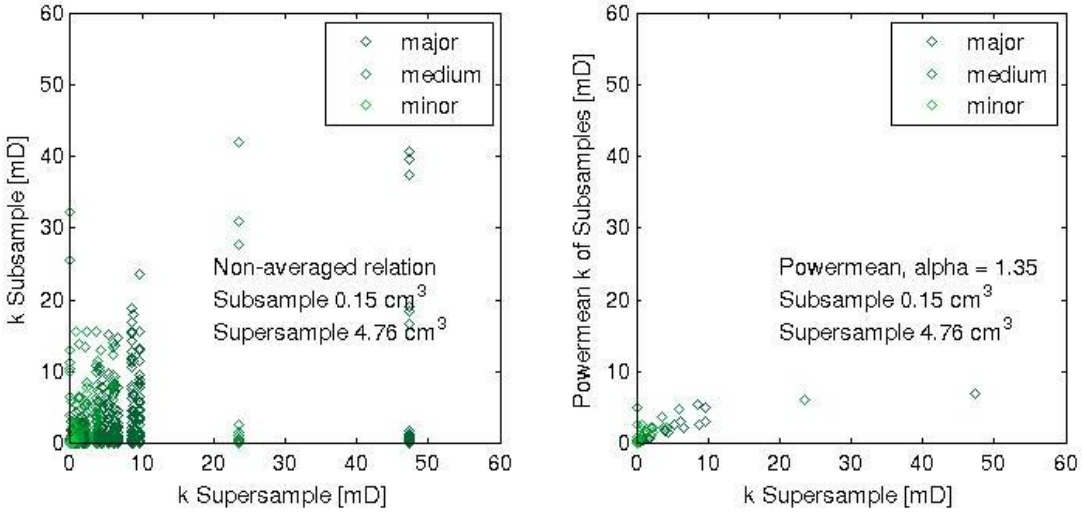

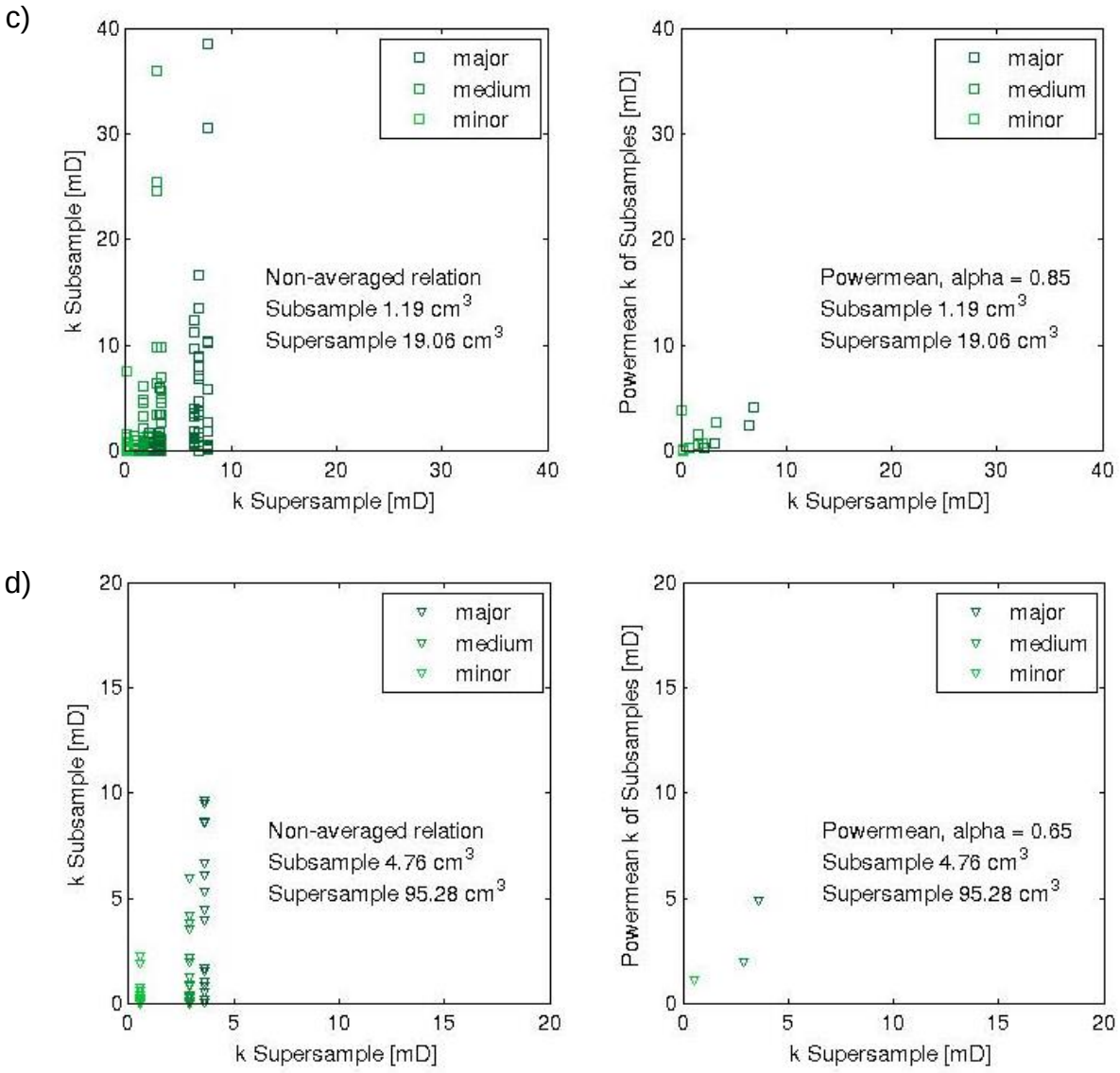

Figure A 13 Ratio of non-averaged and power-averaged permeabilities of subsamples to permeabilities of supersamples for partitions of second order for sample 15 2/3. Displayed are the size of subsample to the size of supersample: a) 0.02 cm^3 : 1.19 cm^3 blocks b) 0.15cm^3 : 4.76 cm3 blocks, c) 1.19 cm^3 : 19.06 cm^3 blocks, d) 4.76 cm^3 : 95.28 cm^3

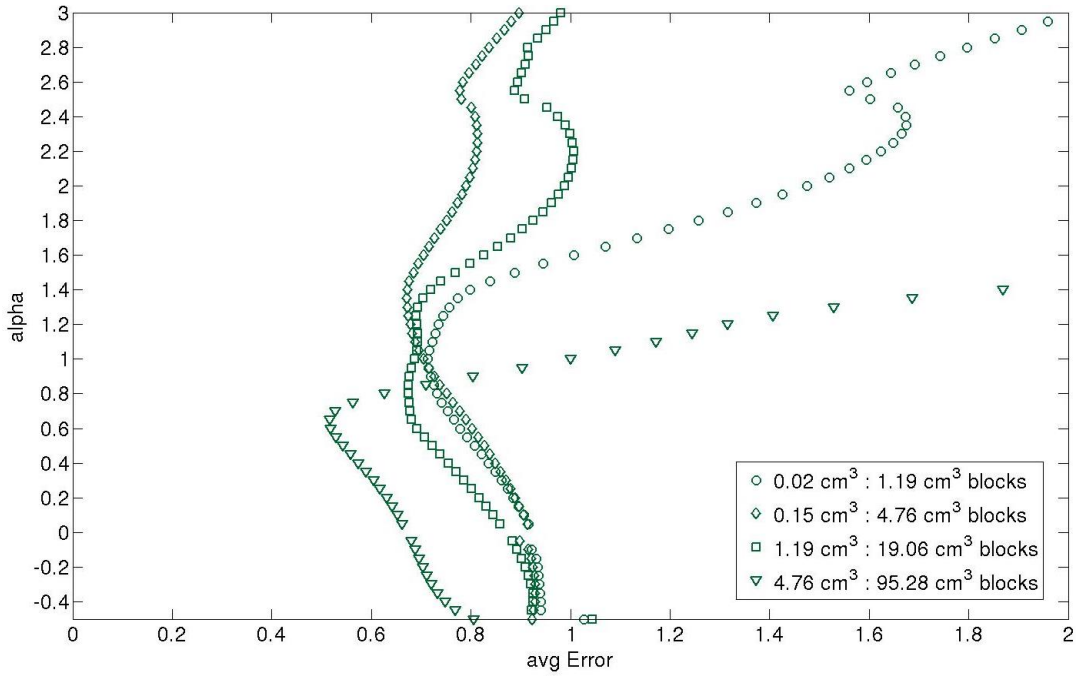

Figure A 14 Average error for alpha in the range of α=-0.5 to 3 for the second order partitions of sample 15 2/3

Table A 5 Ideal alphas for second order partitions of sample 15 2/3

Size Subsample [cm^3]	**Size Supersample [cm^3]**	**Ideal Alpha**
0.02	1.19	1.00
0.15	4.76	1.35
1.19	19.06	0.85
4.76	95.28	0.65

a)

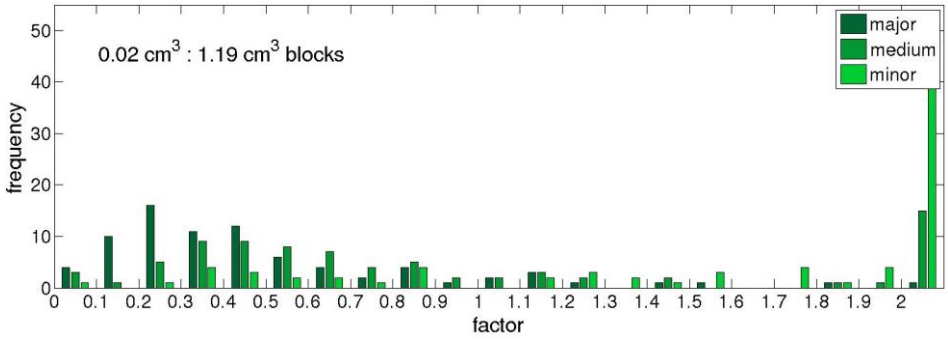

b)

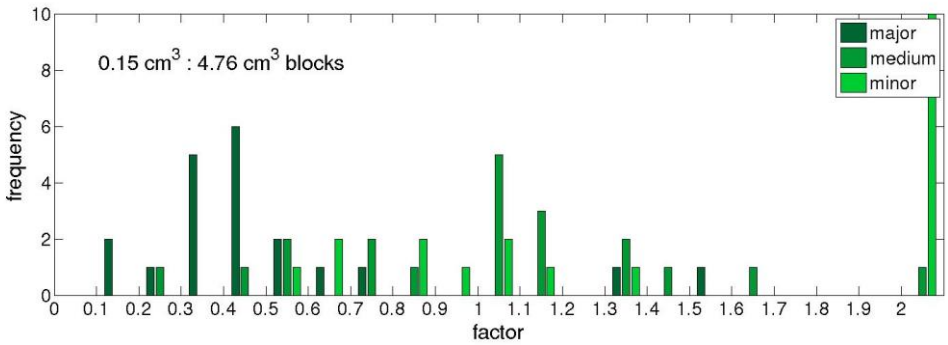

c)

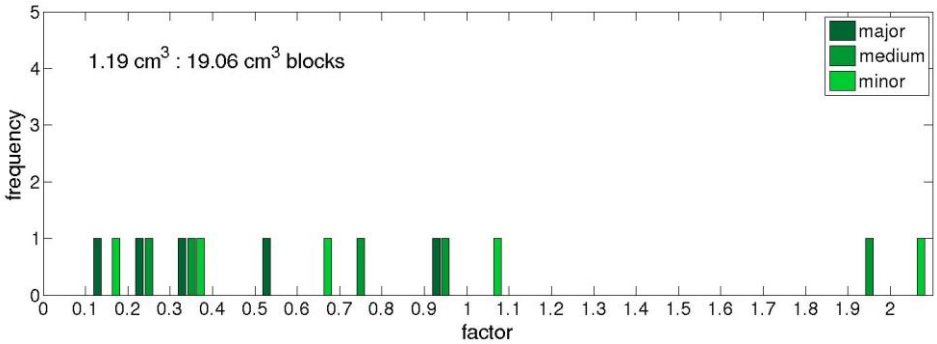

d)

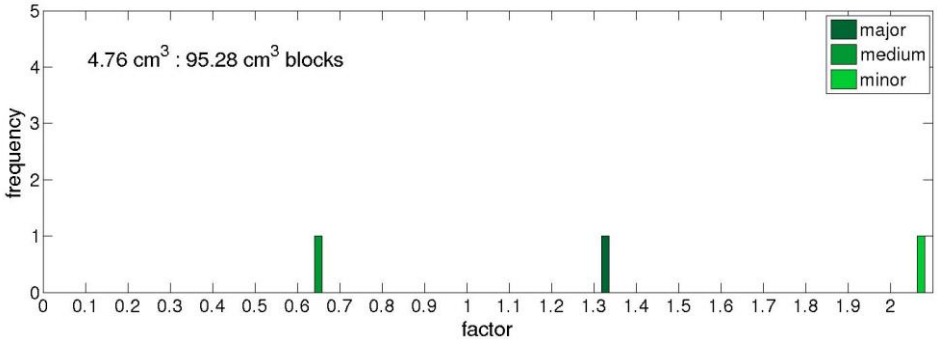

Figure A 15 Power-average factors for the second order partitions of sample 15 2/3. Displayed are the size of subsample to the size of supersample: a) 0.02 cm^3 : 1.19 cm^3 blocks b) 0.15cm^3 : 4.76 cm3 blocks, c) 1.19 cm^3 : 19.06 cm^3 blocks, d) 4.76 cm^3 : 95.28 cm^3

A.2.2 *Third order partition*

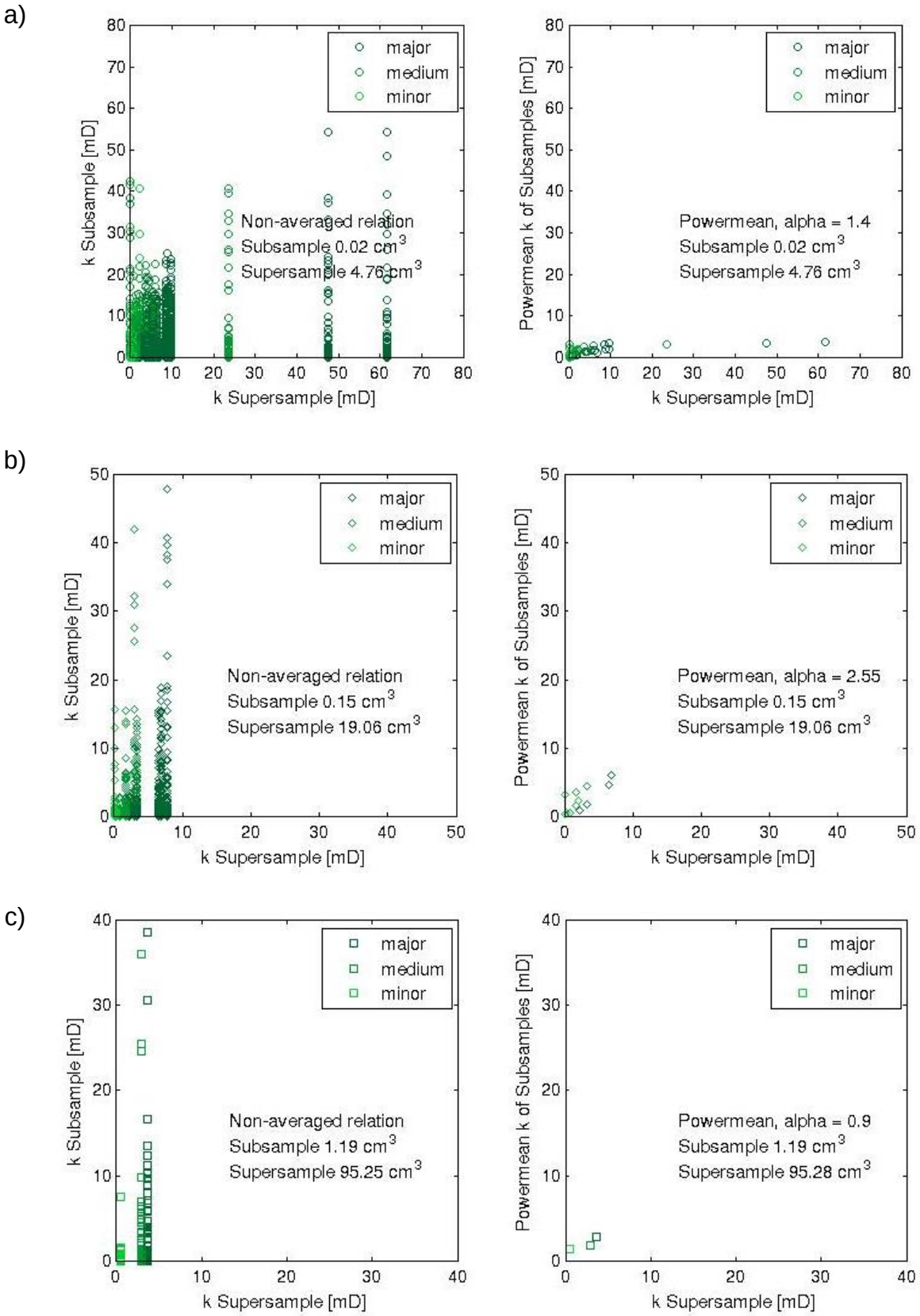

Figure A 16 Ratio of non-averaged and power-averaged permeabilities of subsamples to permeabilities of supersamples for partitions of third order for sample 15 2/3. Displayed are the size of subsample to the size of supersample: a) 0.02 cm^3 : 4.76 cm^3 blocks b) 0.15cm^3 : 19.06 cm3 blocks, c) 1.19 cm^3 : 95.28 cm^3 blocks

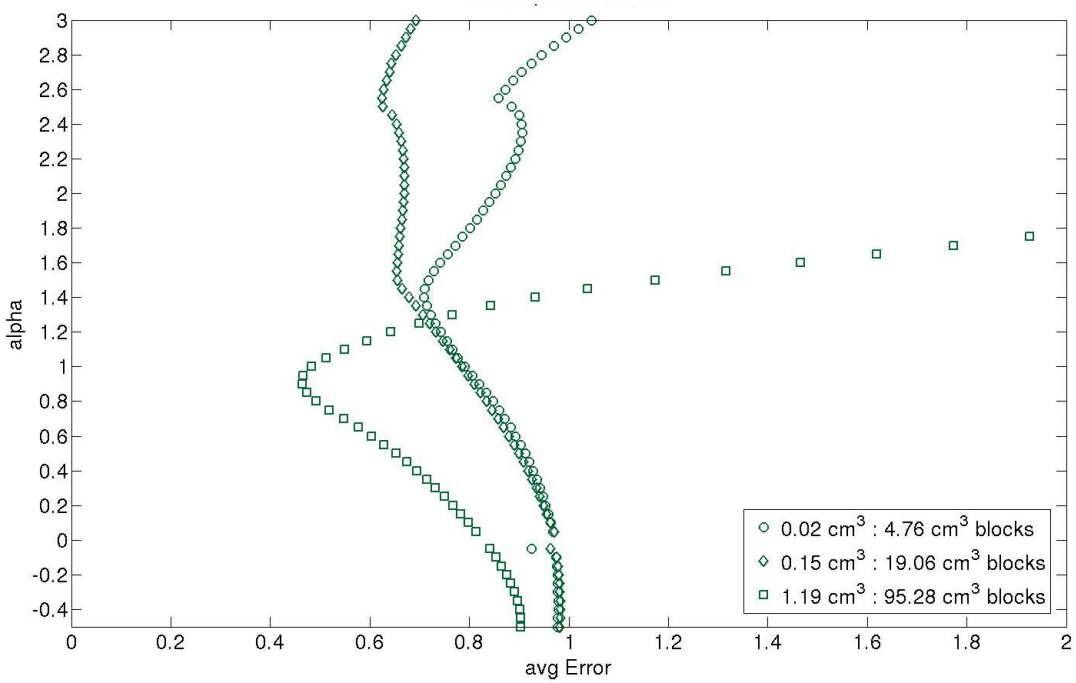

Figure A 17 Average error for alpha in the range of α=-0.5 to 3 for the third order partitions

Table A 6 Ideal alphas for third order partitions of sample 15 2/3

Size Subsample [cm^3]	Size Supersample [cm^3]	Ideal Alpha
0.02	4.76	1.40
0.15	19.06	2.55
1.19	95.28	0.90

a)

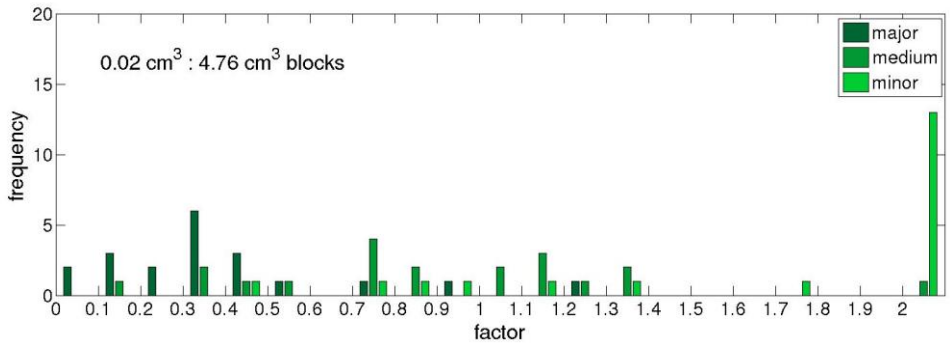

b)

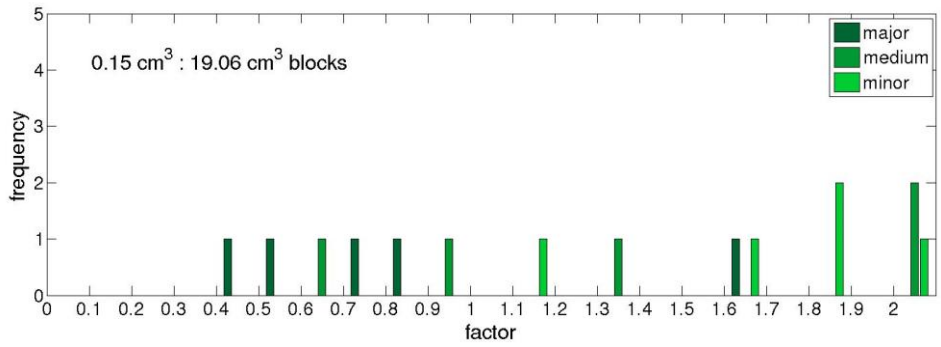

c)

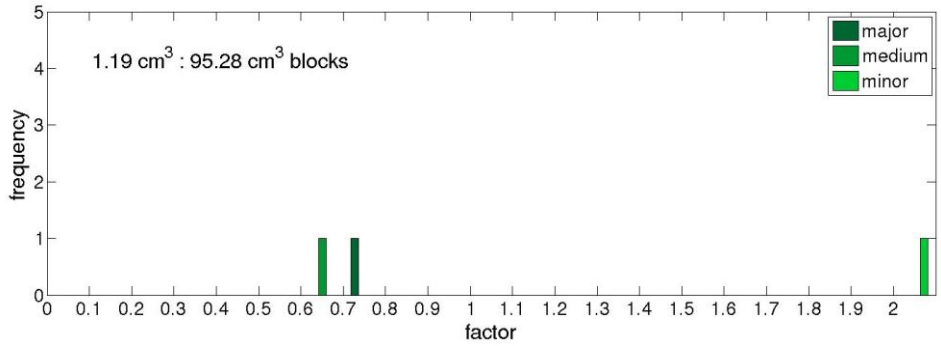

Figure A 18 Power-average factors for the third order partitions of sample 15 2/3. Displayed are the size of subsample to the size of supersample: a) 0.02 cm^3 : 4.76 cm^3 blocks b) 0.15cm^3 : 19.06 cm3 blocks, c) 1.19 cm^3 : 95.28 cm^3 blocks

A.2.3 *Fourth order partition*

a)

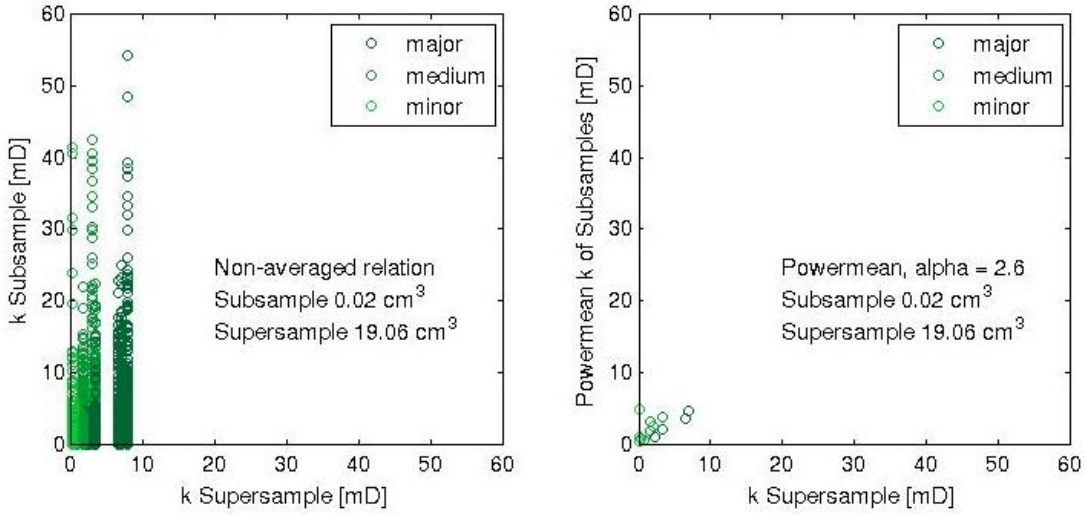

b)

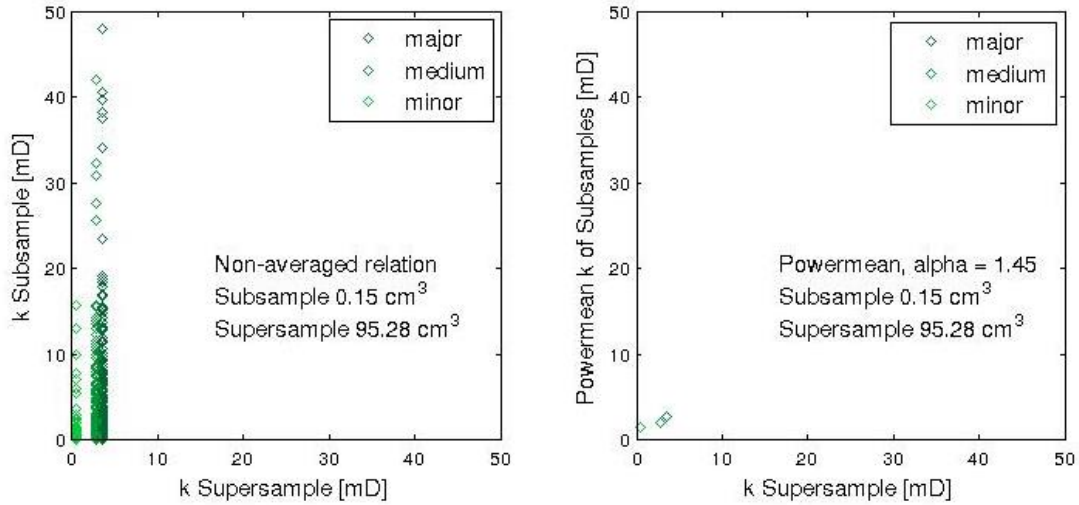

Figure A 19 Ratio of non-averaged and power-averaged permeabilities of subsamples to permeabilities of supersamples for partitions of fourth order for sample 15 2/3. Displayed are the size of subsample to the size of supersample: a) 0.02 cm^3 : 19.06 cm^3 blocks b) 0.15cm^3 : 95.28 cm^3 blocks

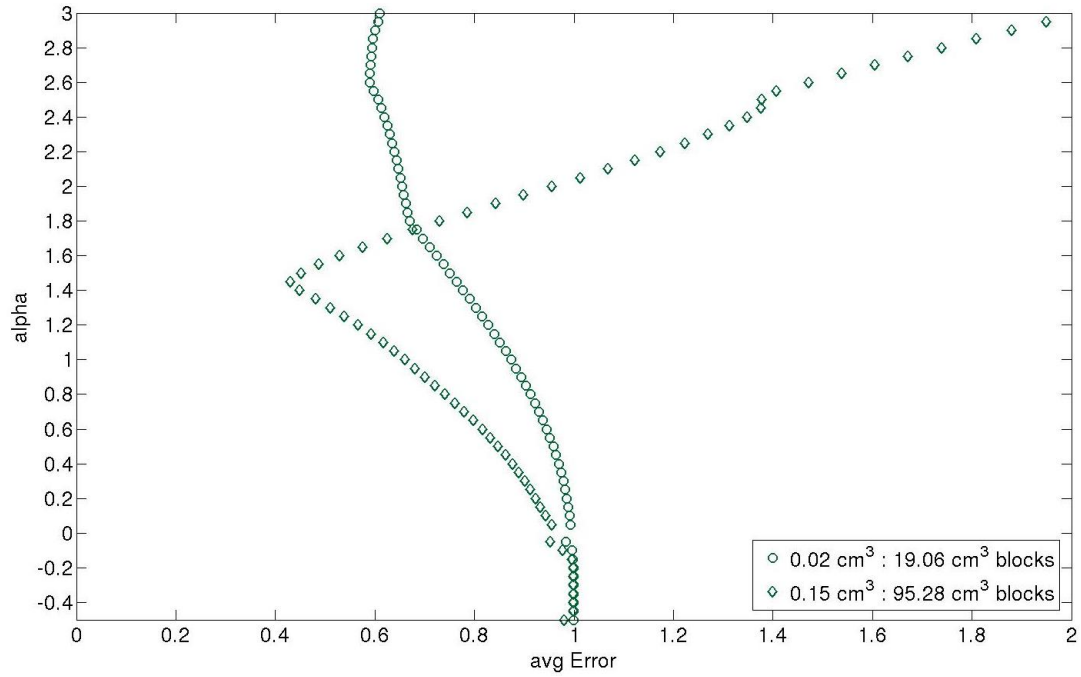

Figure A 20 Average error for alpha in the range of α=-0.5 to 3 for the fourth order partitions

Table A 7 Ideal alphas for fourth order partitions of sample 15 2/3

Size Subsample [cm^3]	Size Supersample [cm^3]	Ideal Alpha
0.02	19.06	2.60
0.15	95.28	1.45

a)

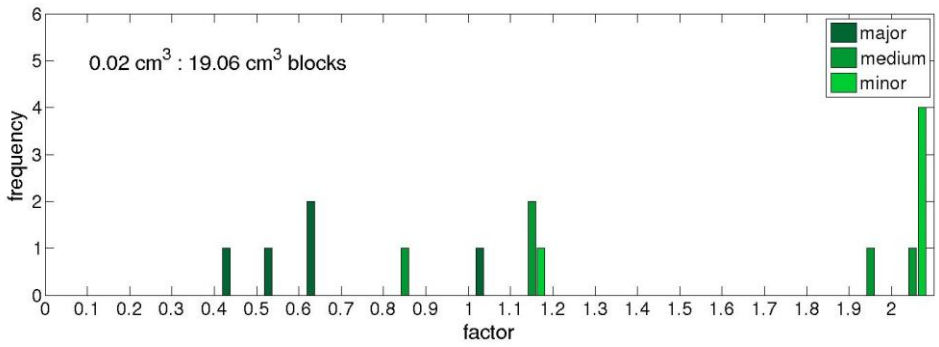

b)

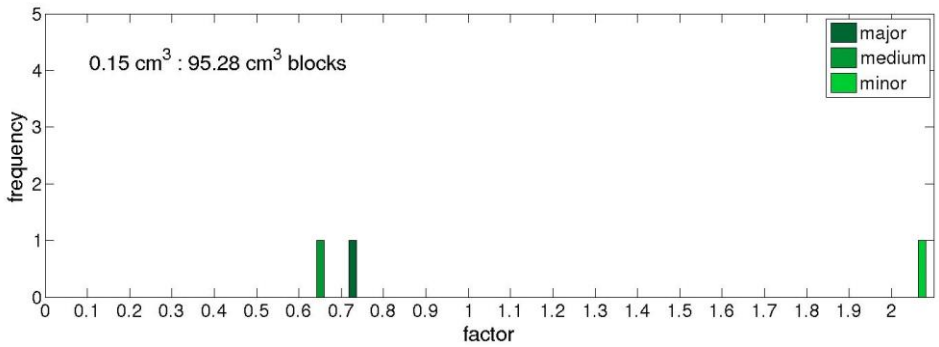

Figure A 21 Power-average factors for the fourth order partitions of sample 15 2/3. Displayed are the size of subsample to the size of supersample: a) 0.02 cm^3 : 19.06 cm^3 blocks b) 0.15 cm^3 : 95.28 cm^3 blocks

A.2.4 *Fifth order partition*

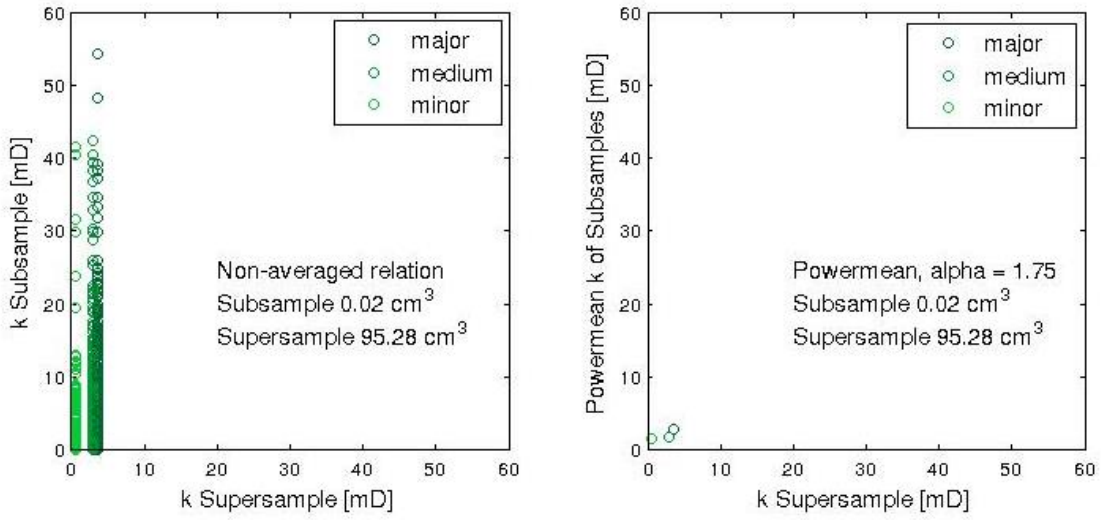

Figure A 22 Ratio of non-averaged and power-averaged permeabilities of subsamples to permeabilities of supersamples for partitions of fifth order for sample 11 1/3. Displayed is the size of subsample to the size of supersample: 0.02 cm^3 : 95.28 cm^3 blocks

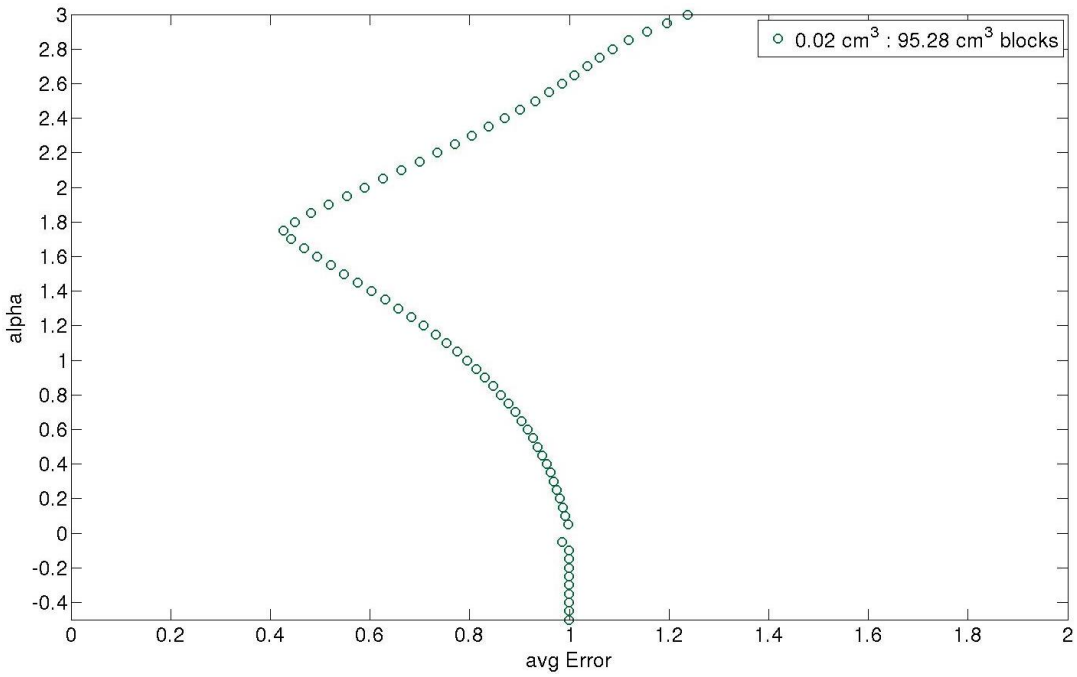

Figure A 23 Average error for alpha in the range of α=-0.5 to 3 for the fifth order partitions

Table A 8 Ideal alpha for fifth order partitions of sample 15 2/3

Size Subsample [cm^3]	Size Supersample [cm^3]	Ideal Alpha
0.02	95.28	1.75

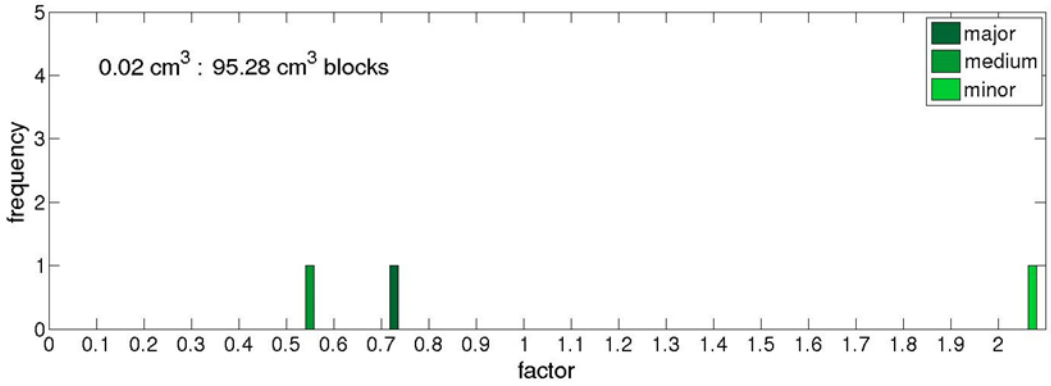

Figure A 24 Power-average factors for the fifth order partitions of sample 15 1/3. Displayed is the size of subsample to the size of supersample: 0.02 cm^3 : 95.28 cm^3 blocks

References

Abell, A., Willis, K., & Lange, D. (1999). Mercury Intrusion Porosimetry and Image Analysis of Cement-Based Materials. *Journal of Colloid and Interface Science*, *211*(1), 39–44. doi:10.1006/jcis.1998.5986

Adeboye, O. O. (2011). Effects of Coal Composition and Fabric on Porosity , Sorption Capacity and Gas Flow Properties in Western Canada Sedimentary Basin Coals. Vancouver: The University of Bristish Columbia.

Ali, M., Sarkar, A., Sagar, R., Klimentos, T., & Basu, I. (2008). Cleat Characterization in CBM wells for completion Optimization. *Society of Petroleum Engineers*, (SPE 113600).

Baecher, G. B., Lanney, N. A., & Einstein, H. H. (1977). Statistical Description Of Rock Properties And Sampling. *18th U.S. Symposium on Rock Mechanics*, 1–8.

Bai, T., Chen, Z., Aminossadati, S. M., Pan, Z., Liu, J., & Li, L. (2015). Characterization of coal fines generation: A micro-scale investigation. *Journal of Natural Gas Science and Engineering*, *27*, 862–875. doi:10.1016/j.jngse.2015.09.043

Barenblatt, G. I., Zheltov, I. P., & Kochina, I. N. (1960). Basic concepts in the theory of seepage of homogeneous liquids in fissured rocks [strata]. *Journal of Applied Mathematics and Mechanics*, *24*(5), 1286–1303.

Barton, C. A., Zoback, M. D., & Moos, D. (1995). Fluid flow along potentially active faults in crystalline rock. *Geology*. doi:10.1130/0091-7613(1995)023<0683:FFAPAF>2.3.CO

Bear, J. (1972). *Dynamics of fluids in porous media*. Courier Dover Publications.

Bear, J. (1979). *Hydraulics of groundwater*. Courier Dover Publications.

Beck, M. B. (1985). *Water quality management: A review of the development and application of mathematical models*. Springer-Verlag Berlin, Heidelberg, New York, Tokyo.

Beeston, J. W. (1986). Coal rank variation in the Bowen Basin, Queensland. *International Journal of Coal Geology*, *6*(2), 163–179. doi:10.1016/0166-5162(86)90019-4

Blacka, B., & MacGregor, S. (2014). *Hail Creek Underground Project – Geotechnical Characterisation for Pre Feasibility Study*. Brisbane.

Bonnet, E. (1997). *La localisation de la deformation dans les milieux fragiles-ductiles: Approche experimentale et application a la lithosphere continentale*. PhD thesis, University of Rennes 1, France.

Bonnet, E., Bour, O., Odling, N. E., Davy, P., Main, I., Cowie, P., & Berkowitz, B. (2001). Scaling of fracture systems in geological media. *Reviews of Geophysics*, *39*(3), 347–383.

Boyle, R. (1662). New experiments physico-mechanical, touching the air: Whereunto is added a defence of the authors explication of the experiments, against the objections of Franciscus Linus and Thomas Hobbes. *Oxford: Printed by H. Hall for T. Robinson.*

Busse, J., de Dreuzy, J. R., Galindo Torres, S., Bringemeier, D., & Scheuermann, A. (2017). Image processing based characterisation of coal cleat networks. *International Journal of Coal Geology*, *169*, 1–21. doi:10.1016/j.coal.2016.11.010

Busse, J., de Dreuzy, J. R., Scheuermann, A., Bringemeier, D., Galindo Torres, S., Davy, P., & Li, L. (2015). Detection and description of fracture networks in coal samples for micro-scale flow simulations. In *Assembly of the International Union of Geodesy and Geophysics*. Prague. doi:10.1016/S0031-3203(00)00136-9

Busse, J., Paillet, F. L., Hossack, A., Bringemeier, D., Scheuermann, A., & Li, L. (2016). Field performance of the heat pulse flow meter: Experiences and recommendations. *Journal of Applied Geophysics*, *126*, 158–171. doi:10.1016/j.jappgeo.2016.01.021

Cacas, M., Ledoux, E., Marsily, G., Tillie, B., Barbreau, A., & Durand, E. (1990). Modeling fracture flow with a stochastic discrete fracture network: calibration and validation: 1. The flow model. *Water Resources Research*, *26*, 479–489.

Carbotte, S., & Macdonald, K. (1994). Comparison of seafloor tectonic fabric at intermediate, fast, and super fast spreading ridges: Influence of spreading rate, plate motions, and ridge segmentation on fault. *Journal of Geophysical Research: Solid Earth*, *99(B7)*, 13609–13631. Retrieved from http://onlinelibrary.wiley.com/doi/10.1029/93JB02971/full

Central Queensland University. (2003). Bowen Basin Mining Communities Research Exchange. Retrieved January 14, 2017, from www.bowenbasin.cqu.edu.au

Chen, G., Illman, W. A., Thompson, D. L., Vesselinov, V. V., & Neuman, S. P. (2000). Geostatistical, Type Curve, and Inverse Analyses of Pneumatic Injection Tests in Unsaturated Fractured Tuffs at the Apache Leap Research Site Near Superior, Arizona. *Dynamics of Fluids in Fractured Rock*, 73–98.

Clarke, G. (2007). *Documentation of Significant Geological Features evident within Rio Tinto's Hail Creek Coal Mine*. Queensland.

Clarkson, C. R., & Bustin, R. M. (2011). Coalbed Methane: Current Field-Based Evaluation Methods. *SPE Reservoir Evaluation & Engineering*, *14*(1).

Clauser, C. (1992). Permeability of crystalline rocks. *Eos, Transactions American Geophysical Union*, *73*(21), 233–238. doi:10.1029/91EO00190

Close, J. C. (1993). Natural fractures in coal. In B. E. Law Rice, D.D. (Ed.), *Hydrocarbons from coal* (Vol. 38, pp. 119–132). Tulsa, Oklahoma, U.S.A.: The American Association of Petroleum Geologists.

Cnudde, V., & Boone, M. N. (2013). High-resolution X-ray computed tomography in geosciences: A review of the current technology and applications. *Earth-Science Reviews*, *123*, 1–17. doi:10.1016/j.earscirev.2013.04.003

Cooper, H. H., Bredehoeft, J. D., & Papadopulos, I. S. (1967). Response of a finite-diameter well to an instantaneous charge of water. *Water Resources Research*, *3*(1), 263–269. doi:10.1029/WR003i001p00263

Costa, A. (2006). Permeability-porosity relationship: A reexamination of the Kozeny-Carman equation based on a fractal pore-space geometry assumption. *Geophysical Research Letters*, *33*(2), 1–5. doi:10.1029/2005GL025134

Cvetkovic, V., Painter, S., Outters, N., & Selroos, J. O. (2004). Stochastic simulation of radionuclide migration in discretely fractured rock near the Äspö Hard Rock Laboratory. *Water Resources Research*, *40*(2).

Darcel, C. (2003). Connectivity properties of two-dimensional fracture networks with stochastic fractal correlation. *Water Resources Research*, *39*(10), 1–13. doi:10.1029/2002WR001628

Darcel, C., Bour, O., Davy, P., & de Dreuzy, J. R. (2003). Connectivity properties of two-dimensional fracture networks with stochastic fractal correlation. *Water Resources Research*, *39*(10), 1–13. doi:10.1029/2002WR001628

Darcy, H. P. G. (1856). *Dètermination des lois d'ècoulement de l'eau à travers le sable*. Dijon, France.

Dawson, G. K. W., & Esterle, J. S. (2010). Controls on coal cleat spacing. *International Journal of Coal Geology*, *82*(3-4), 213–218. doi:10.1016/j.coal.2009.10.004

De Dreuzy, J. R., Davy, P., & Bour, O. (2001). Hydraulic properties of two-dimensional random fracture networks following a power law length distribution 1. Effective connectivity. *Water Resources Research*, *37*(8), 2065–2078. doi:10.1029/2001WR900011

De Haan, M. F. E. (1999). *Enhanced coalbed methane production by carbon dioxide injection; theory, experiments and simulation*. Novem-TUD Technical Report, Contr. Nr. 222103/2008.

De Marsily, G., Delay, F., Gonçalvès, J., Renard, P., Teles, V., & Violette, S. (2005). Dealing with spatial heterogeneity. *Hydrogeology Journal*, *13*, 161–183. doi:10.1007/s10040-004-0432-3

DeAngelis, D. L., Yeh, G. T., Huff, D. D., & Laboratory, O. R. N. (1984). *An Integrated Compartmental Model for Describing the Transport of Solute in a Fractured Porous Medium*. Oak Ridge National Laboratory, Environmental Sciences Division. Retrieved from http://books.google.com.au/books?id=VJvNGwAACAAJ

Deisman, N., Mas Ivars, D., Darcel, C., & Chalaturnyk, R. J. (2010). Empirical and numerical approaches for geomechanical characterization of coal seam reservoirs. *International Journal of Coal Geology*, *82*(3-4), 204–212. doi:10.1016/j.coal.2009.11.003

Dershowitz, W. (1984). *Rock joint systems*. Massachusetts Institute of Technology, Cambridge. Retrieved from http://dspace.mit.edu/handle/1721.1/27939

Dershowitz, W. S., & Einstein, H. H. (1988). Characterizing rock joint geometry with joint system models. *Rock Mechanics and Rock Engineering*, *21*(1), 21–51. doi:10.1007/BF01019674

Desbarats, A. J. (1992). Spatial averaging of hydraulic conductivity in three-dimensional heterogeneous porous media. *Mathematical Geology*, *24*(3), 249–267. doi:10.1007/BF00893749

Deutsch, C. V, & Journel, A. G. (1998). *Geostatistical software library and user's guide*. New York: Oxford University Press.

Deza, M. M., & Deza, E. (2009). *Encyclopedia of distances*. Heidelberg: Springer Berlin. Retrieved from http://link.springer.com/content/pdf/10.1007/978-3-642-00234-2_1.pdf

Dmyterko, A. S. K. (2014). *Variability of coal seam gas reservoir parameters in the Leichhardt Seam, Rangal Coal Measures, Bowen Basin, Central Queensland*. University of Queensland.

Einstein, H., & Baecher, G. (1983). Probabilistic and statistical methods in engineering geology. *Rock Mechanics and Rock Engineering*, *16.1*, 39–72. Retrieved from http://link.springer.com/article/10.1007/BF01030217

Eker, E., & Akin, S. (2006). Lattice Boltzmann simulation of fluid flow in synthetic fractures. *Transport in Porous Media*, *65*(3), 363–384. doi:10.1007/s11242-005-6085-4

Elmouttie, M. K., & Poropat, G. V. (2011). Uncertainty propagation in structural modeling. *Slope Stability 2011*.

Esterle, J. (2012). Coal Macerals [Power point slides]. Brisbane: School of Earth Sciences, Energy Resources ERTH 3202, The University of Brisbane.

Esterle, J. S., Golding, S. D., Massarotto, P., & Angle, I. (2011). Cleat and Joint Intersections and Mineralisation of a Coal Core from the Bowen Basin , Queensland , Australia, (051).

Faiz, M., & Aziz, N. (1992). Porosity and gas sorption capacity of some eastern Australian coals in relation to coal rank and composition. In *Coalbed Methane Symposium, Townsville*. Retrieved from http://www.undergroundcoal.com.au/outburst/presentations_publications/coal_methane_1992/Naj Aziz.PDF

Faraj, B. S. M., Fielding, C. R., & Mackinnon, I. D. R. (1996). Cleat mineralization of Upper Permian Baralaba/Rangal Coal Measures, Bowen Basin, Australia. *Coalbed Methane and Coal Geology*, *109*(1), 151–164. doi:10.1144/GSL.SP.1996.109.01.11

Faybishenko, B., Witherspoon, P., & Benson, S. (2000). *Dynamics of fluids in fractured rock* (Vol. 122.). Washington, DC: American geophysical Union. Retrieved from https://publications.lbl.gov/islandora/object/ir%3A122471/datastream/PDF/download/Session-8.pdf

Fetter, C. (2000). *Applied hydrogeology*. Prentice Hall. Retrieved from http://e2m-lao.com/e-learning/books/Applied Hydrogeology (4th Edition) by C. W. Fetter (Hardcover).pdf

Flores, R. M. (2013). *Coal and Coalbed Gas: Fueling the Future*. Newnes. Retrieved from https://books.google.com/books?hl=en&lr=&id=F3otuH4Ld2QC&pgis=1

Fu, J., Axness, C. L., & Gomez-Hernandez, J. J. (2011). Upscaling transmissivity in the near-well region for numerical simulation: A comparison on uncertainty propagation. *Engineering Applications of Computational Fluid Mechanics*, *5*(1), 49–66.

Galindo-Torres, S. A., Molebatsi, T., Kong, X., Scheuermann, A., Bringemeier, D., & Li, L. (2015). Scaling solutions for connectivity and conductivity of continuous random networks. *Physical Review E.*, *92*(4), 1–5.

Galindo-Torres, S. A., Scheuermann, A., & Li, L. (2012). Numerical study on the permeability in a tensorial form for laminar flow in anisotropic porous media. *Physical Review E*, *86*(4), 46306. Retrieved from http://link.aps.org/doi/10.1103/PhysRevE.86.046306

Gamson, P., Beamish, B., & Johnson, D. (1996). Coal microstructure and secondary mineralization: their effect on methane recovery, (109), 165–179.

Gamson, P. D., & Beamish, B. B. (1992). Coal type, microstructure and gas flow behaviour of Bowen Basin coals. *Coalbed Methane Symposium*, 43–66. Retrieved from file:///R:/LITERATURE/Angela/Gamson and Beamish 1992.PDF

Gamson, P. D., Beamish, B. B., & Johnson, D. P. (1993). Coal microstructure and micropermeability and their effects on natural gas recovery. *Fuel*, *72*(1), 87–99. doi:http://dx.doi.org/10.1016/0016-2361(93)90381-B

Gao, F., Stead, D., & Kang, H. (2014). Numerical investigation of the scale effect and anisotropy in the strength and deformability of coal. *International Journal of Coal Geology*, *136*, 25–37. doi:10.1016/j.coal.2014.10.003

Gash, B. W., Volz, R. F., Potter, G., & Corgan, J. M. (1992). The effects of cleat orientation and confining pressure on cleat porosity, permeability and relative permeability in coal. *Paper*, *9321*, 17–21.

Gash, B. W., Volz, R. F., Potter, G. & Corgan, J. M. (1993). The effects of cleat orientation and confining pressure on cleat porosity, permeability and relative permeability in coal. In *Procs. 1993 Intl. CBM Symp.* Univ. Alabama, Tuscaloosa.

Gelhar, L. W., & Axness, C. L. (1983). Three-dimensional stochastic analysis of macrodispersion in aquifers. *Water Resources Research*, *19*(1), 161–180. doi:10.1029/WR019i001p00161

Ghaffari, H., Nabovati, A., Sharifzadeh, M., & Young, R. P. (2011). Fluid flow anlaysis in a rough fracture (type II) using complex networks and lattice Boltzmann method. Pan-Am CGS Geotechnical Conference.

Ghaffari, H. O., Nasseri, M. H. B., & Young, R. P. (2011). Fluid Flow Complexity in Fracture Networks: Analysis with Graph Theory and LBM. *arXiv Preprint*, *arXiv:1107*. Retrieved from http://arxiv.org/abs/1107.4918

Golab, A., Ward, C. R., Permana, A., Lennox, P., & Botha, P. (2013). High-resolution three-dimensional imaging of coal using microfocus X-ray computed tomography, with special reference to modes of mineral occurrence. *International Journal of Coal Geology*, *113*(0), 97–108. doi:http://dx.doi.org/10.1016/j.coal.2012.04.011

Golder Associates Pty Ltd. (2013). *Factual Report on Hydrogeological Investigations at the Hail Creek Mine Site*. Rio Tinto Coal Australia Pty Ltd.

Gómez-Hernández, J. J., & Wen, X.-H. (1998). To be or not to be multi-Gaussian? A reflection on stochastic hydrogeology. *Advances in Water Resources*, *21*(1), 47–61. doi:10.1016/S0309-1708(96)00031-0

Gong, B., Zhang, Y., Fan, Y., & Qin, G. (2014). A novel approach to model enhanced coal bed methane recovery with discrete fracture characterizations in a geochemical simulator. *Journal of Petroleum Science and Engineering*, *124*, 198–208. doi:10.1016/j.petrol.2014.09.035

Gonzales, R. C., Woods, R. E., & Eddins, S. L. (2004). Digital image processing using MatLab [Power point slides]. Swiss Federal Institute of Technology, Zurich.

Google Maps. (2014). Map of Hail Creek Mine, Rio Tinto Coal Australia. Retrieved from https://www.google.com.au/maps/place/Hail+Creek+Mine+(Rio+Tinto+Coal+Australia/@-21.4907319,148.3296071,15234m/data=!3m1!1e3!4m5!3m4!1s0x6bd081fb98b9d4c5:0x7a401dd46adffd71!8m2!3d-21.4907391!4d148.3646375

Groenland, S. (2007). Geophysical Interpretation and Correction of Borehole Data Using Geophysical Logs. BHP Bililton Mitsubishi Alliance.

Guo, X., Yao, Y., & Liu, D. (2014). Characteristics of coal matrix compressibility: An investigation by mercury intrusion porosimetry. *Energy and Fuels*, *28*(6). doi:10.1021/ef5004123

Gutjahr, A. L., Gelhar, L., Bakr, A., & MacMillan, J. (1978). Stochastic Analysis of Spatial Variability in Subsurface Flows: 2. Evaluation and Application. *Water Resources Research*, *14*(5), 953–959.

Hamzehpour, H., Mourzenko, V. V., Thovert, J. F., & Adler, P. M. (2009). Percolation and permeability of networks of heterogeneous fractures. *Physical Review E - Statistical, Nonlinear, and Soft Matter Physics*, *79*, 1–12. doi:10.1103/PhysRevE.79.036302

Han, F., Busch, A., van Wageningen, N., Yang, J., Liu, Z., & Krooss, B. M. (2010). Experimental study of gas and water transport processes in the inter-cleat (matrix) system of coal: Anthracite from Qinshui Basin, China. *International Journal of Coal Geology*, *81*(2), 128–138. doi:10.1016/j.coal.2009.11.001

Harpalani, S. (1999). Compressibility of coal and its impact on gas production from coalbed reservoirs.

Hess, A. E. (1986). Identifying hydraulically conductive fractures with a slow-velocity borehole flowmeter. *Canadian Geotechnical Journal*, *23*(1), 69–78. doi:10.1139/t86-008

Hirono, T., Takahashi, M., & Nakashima, S. (2003). In situ visualization of fluid flow image within deformed rock by X-ray CT. *Engineering Geology*, *70*, 37–46. doi:10.1016/S0013-7952(03)00074-7

Hoek, E., & Franklin, J. A. (1967). *A simple triaxial cell for field or laboratory testing of rock*. Imperial College of Science and Technology, University of London.

Hölting, B., & Coldewey, W. G. (2005). *Einführung in die Allgemeine und Angewandte Hydrogeologie* (Vol. 6.). Elsevier Spektrum Akademischer Verlag.

Holwell, M. (2007). Geology at Hail Creek [Power Point slides]. Brisbane: Rio Tinto Coal Australia Pty Ltd.

Hooker, J. N., Laubach, S. E., & Marrett, R. (2013). Fracture-aperture size, frequency, spatial distribution, and growth processes in strata-bounded and non-strata-bounded fractures, cambrian mesón group, NW Argentina. *Journal of Structural Geology*, *54*, 54–71. doi:10.1016/j.jsg.2013.06.011

Hough, P. V. C. (1962). *Method and means for recognising complex patterns*. U.S. Patent No. 3,069,654, U.S.A. Retrieved from http://www.osti.gov/scitech/biblio/4746348

Hounsfield, G. N. (1973). Computerized transverse axial scanning (tomography): Part 1. Description of system. *The British Journal of Radiology*, *46*(552), 1016–1022. doi:10.1259/0007-1285-46-552-1016

Huy, P. Q., Sasaki, K., Sugai, Y., & Ichikawa, S. (2010). Carbon dioxide gas permeability of coal core samples and estimation of fracture aperture width. *International Journal of Coal Geology*, *83*(1), 1–10. doi:10.1016/j.coal.2010.03.002

Illman, W. A. (2006). Strong field evidence of directional permeability scale effect in fractured rock. *Journal of Hydrology*, *319*(1), 227–236.

Illman, W. A. (2013). Hydraulic Tomography Offers Improved Imaging of Heterogeneity in Fractured Rocks. *Groundwater*. doi:10.1111/gwat.12119

International Energy Agency. (2008). *Coal Information 2008*. *IEA Statistics*. Organisation for Economic Cooperation & Development.

Jalal, J., & Mohaghegh, S. D. (2004). A Coalbed Methane Reservoir Simulator Designed and Developed for the Independent Producers. *SPE Eastern Regional Meeting*, (1), 1–7. doi:10.2118/91414-MS

Ji, S. H., Park, Y. J., & Lee, K. K. (2011). Influence of Fracture Connectivity and Characterization Level on the Uncertainty of the Equivalent Permeability in Statistically Conceptualized Fracture Networks. *Transport in Porous Media*, *87*(2), 385–395. doi:10.1007/s11242-010-9690-9

Jiang, Z., Dijke, M. I. J., Sorbie, K. S., & Couples, G. D. (2013). Representation of multiscale heterogeneity via multiscale pore networks. *Water Resources Research*, *49*(9), 5437–5449.

Jin, Y., Song, H., Hu, B., Zhu, Y., & Zheng, J. (2013). Lattice Boltzmann simulation of fluid flow through coal reservoir's fractal pore structure. *Science China Earth Sciences*, *56*(9), 1519–1530. doi:10.1007/s11430-013-4643-0

Jing, L. (2003). A review of techniques, advances and outstanding issues in numerical modelling for rock mechanics and rock engineering. *International Journal of Rock Mechanics and Mining Sciences*, *40*(3), 283–353. doi:10.1016/S1365-1609(03)00013-3

Jing, L., & Stephansson, O. (2007). Fundamentals of Discrete Element Methods for Rock Engineering - Theory and Applications. In *Developments in Geotechnical Engineering* (Vol. 85, pp. 365–398). Elsevier. doi:10.1016/S0165-1250(07)85010-3

Jing, Y., Armstrong, R. T., Ramandi, H. L., & Mostaghimi, P. (2016). Coal cleat reconstruction using micro-computed tomography imaging. *Fuel*, *181*, 286–299. doi:10.1016/j.fuel.2016.04.127

Journel, A. G., & Deutsch, C. V. (1993). Entropy and spatial disorder. *Mathematical Geology*, *25*(3), 329–355. doi:10.1007/BF00901422

Kadanoff, L. P. (1986). On two levels. *Physics Today*, *39*(7). Retrieved from http://adsabs.harvard.edu/abs/1986PhT....39i...7K

Karacan, C. Ö., & Okandan, E. (2000). Fracture/cleat analysis of coals from Zonguldak Basin (northwestern Turkey) relative to the potential of coalbed methane production. *International Journal of Coal Geology*, *44*(2), 109–125. doi:10.1016/S0166-5162(00)00004-5

Kasteel, R., Vogel, H. J., & Roth, K. (2000). From local hydraulic properties to effective transport in soil. *European Journal of Soil Science*, *51*, 81–91. doi:10.1046/j.1365-2389.2000.00282.x

Kentwell, D. J., Bloom, L. M., & Comber, G. A. (1999). Geostatistical conditional fractal simulation with irregularly spaced data. *Mathematics and Computers in Simulation*, *48*(4), 447–456.

Ketcham, R. A., & Iturrino, G. J. (2005). Nondestructive high-resolution visualization and measurement of anisotropic effective porosity in complex lithologies using high-resolution X-ray computed tomography. *Journal of Hydrology*, *302*(1-4), 92–106. doi:10.1016/j.jhydrol.2004.06.037

King, I., & Hair, A. (2009). *Hydrogeological assessment of Hail Creek coal mine*. Brisbane.

Kirsch, R. (2006). *Groundwater geophysics* (Vol. 493). Heidelberg: Springer Berlin.

Klaver, J., Desbois, G., Urai, J. L., & Littke, R. (2012). BIB-SEM study of the pore space morphology in early mature Posidonia Shale from the Hils area, Germany. *International Journal of Coal Geology*, *103*, 12–25. doi:10.1016/j.coal.2012.06.012

Klawitter, M., Collins, S., & Esterle, J. (2013). *Coal density and fracture charcterisation by X-ray computerised tomography scanning: a case study of Bowen Basin, Queensland, Australia*. Brisbane: University of Queensland.

Klepikova, M. V, Le Borgne, T., Bour, O., & de Dreuzy, J.-R. (2013). Inverse modelling of flow tomography experiments in fractured media. *Water Resources Research*. doi:10.1002/2013wr013722

Knackstedt, M. A., Sheppard, A. P., & Sahimi, M. (2001). Pore network modelling of two-phase flow in porous rock: The effect of correlated heterogeneity. *Advances in Water Resources*, *24*, 257–277. doi:10.1016/S0309-1708(00)00057-9

Komura, T. (2008). Tensor Visualisation [Power point slides]. *University Lecture, Institute of Perception, Action & Behaviour*. Edinburgh: School of Informatics, University of Edinburgh.

Kong, X., Ma, Y., Busse, J., Bringemeier, D., Scheuermann, A., & Li, L. (2015). Hydraulic connectivity between mines and adjacent river and groundwater systems in the Hunter River Valley. Brisbane.

Kumar, M., Senden, T. J., Sheppard, A. P., Middleton, J. P., & Knackstedt, M. A. (2010). Visualizing and quantifying the residual phase distribution in core material. *Petrophysics*, *51*(5), 323.

Kural, O. C. (1994). *Coal: resources, properties, utilization, pollution*. Istanbul, Turkey: Istanbul Technical University. Retrieved from http://uq.summon.serialssolutions.com/2.0.0/link/0/eLvHCXMwY2AwNtIz0EUrE0ySDVNTkoA9HzNjk6SUNGPjJBOzZGAEJVsAqwdT8CUm2IY_4DO7hRhDFxaW5gag22qZzQ1MIAc6A_tcluamlqbmoDY-5GwdON8CaZcjuOZwE2RgAe0mEGJgSs0TYWBxzk_MEWWQdnMNcfbQLS2Mhw6exMMssjASY-BNBC06zysBb05LkWBQSE4z

Lama, R. D., & Bodziony, J. (1998). Management of outburst in underground coal mines. *International Journal of Coal Geology*, *35*, 83–115. doi:10.1016/S0166-5162(97)00037-2

Laubach, S. E., Marrett, R. A., Olson, J. E., & Scott, A. R. (1998). Characteristics and origins of coal cleat: A review. *International Journal of Coal Geology*, *35*(1–4), 175–207. doi:http://dx.doi.org/10.1016/S0166-5162(97)00012-8

Laubach, S. E., Olson, J. E., & Gale, J. F. W. (2004). Are open fractures necessarily aligned with maximum horizontal stress? *Earth and Planetary Science Letters*, *222*(1), 191–195. doi:10.1016/j.epsl.2004.02.019

Law, B. E. (1993). The relationship between coal rank and cleat spacing: implications for the prediction of permeability in coal. In *Proceedings of the 1993 International Coalbed Methane Symposium.* Tuscaloosa, Alabama: University of Alabama.

Li, Z., Katsumi, T., Inui, T., & Takai, A. (2013). Fabric effect on hydraulic conductivity of kaolin under different chemical and biochemical conditions. *Soils and Foundations*, *53*(5), 680–691. doi:10.1016/j.sandf.2013.08.006

Liu, J., Chen, Z., Elsworth, D., Qu, H., & Chen, D. (2011). Interactions of multiple processes during CBM extraction: A critical review. *International Journal of Coal Geology*, *87*(3-4), 175–189. doi:10.1016/j.coal.2011.06.004

Long, J. C. S., Remer, J. S., Wilson, C. R., & Witherspoon, P. A. (1982). Porous media equivalents for networks of discontinuous fractures. *Water Resources Research*, *18*(3), 645–658.

Long, J. C. S., & Witherspoon, P. A. (1985). The relationship of the degree of interconnection to permeability in fracture networks. *Journal of Geophysical Research: Solid Earth*, *90*(B4), 3087–3098. doi:10.1029/JB090iB04p03087

Lorig, L. J., Darcel, C., Damjanac, B., Pierce, M., & Billaux, D. (2015). Application of discrete fracture networks in mining and civil geomechanics. *Mining Technology*, *124*(4), 239–254. doi:10.1179/1743286315Y.0000000021

Lucia, F. (1983). Petrophysical Parameters Estimated From Visual Descriptions of Carbonate Rocks: A Field Classification of Carbonate Pore Space. *Journal of Petroleum Technology*, 629–637. doi:10.2118/10073-PA

Madadi, M., & Sahimi, M. (2003). Lattice Boltzmann simulation of fluid flow in fracture networks with rough, self-affine surfaces. *Physical Review E*, *67*(2), 1–12. doi:10.1103/PhysRevE.67.026309

Mahajan, O. P., & Walker, P. L. (1978). *Porosity of Coals and Coal Products*. Pennsylvania.

Mandelbrot, B. B. (1983). The Fractal Geometry of Nature. *American Journal of Physics*. doi:10.1119/1.13295

Martin, P. J., & Frind, E. G. (1998). Modeling a Complex Multi-Aquifer System: The Waterloo Moraine. *Ground Water*, *36*(4), 679–690.

Massarotto, P., Golding, S. D., Bae, J. S., Iyer, R., & Rudolph, V. (2010). Changes in reservoir properties from injection of supercritical CO2 into coal seams - A laboratory study. *International Journal of Coal Geology*, *82*(3-4), 269–279. doi:10.1016/j.coal.2009.11.002

Massarotto, P., Golding, S. D., & Rudolph, V. (2003). *Anisotropic permeability characterisation of permian coals*. Brisbane.

Massarotto, P., Iyer, R. S., & Bae, J.-S. (2008). Porosity and compressibility of core coal samples using helium pycnometry and mercury porosimetry. Retrieved from http://espace.library.uq.edu.au/view/UQ:196731#.WISzSjCzDdE.mendeley

Massarotto, P., Rudolph, V., Golding, S., Wang, F., & Iyer, R. (2008). Scaleup of laboratory measured coal permeability. In *2008 Asia Pacific Coalbed Methane Symposium*. The University of Queensland.

Matheron, G. (1967). *Eléments pour une théorie des milieux poreux*. Paris: Masson. Retrieved from http://infoscience.epfl.ch/record/27350

Mathews, J. P., & Chaffee, A. L. (2012). The molecular representations of coal - A review. *Fuel*, *96*, 1–14. doi:10.1016/j.fuel.2011.11.025

Matthäi, S., & Nick, H. (2009). Upscaling two-phase flow in naturally fractured reservoirs. *AAPG Bulletin*, *93*(11), 1621–1632.

Mauldon, M. (1998). Estimating Mean Fracture Trace Length and Density from Observations in Convex Windows. *Rock Mechanics and Rock Engineering*, *31*, 201–216. doi:10.1007/s006030050021

Mavor, M. J., & Robinson, J. R. (1993). Analysis of Coal Gas Reservoir Interference and Cavity Well Tests. In *Low Permeability Reservoirs Symposium*. Society of Petroleum Engineers.

Mazumder, S., Wolf, K. H. A. A., Elewaut, K., & Ephraim, R. (2006). Application of X-ray computed tomography for analyzing cleat spacing and cleat aperture in coal samples. *International Journal of Coal Geology*, *68*(3-4), 205–222. doi:10.1016/j.coal.2006.02.005

McClure, J., Gray, W., & Miller, C. (2010). Beyond anisotropy: Examining non-Darcy flow in asymmetric porous media. *Transport in Porous Media*, *84.2*, 535–548. Retrieved from http://link.springer.com/article/10.1007/s11242-009-9518-7

McLaren, R. G., Sudicky, E. A., Park, Y.-J., & Illman, W. A. (2012). Numerical simulation of DNAPL emissions and remediation in a fractured dolomitic aquifer. *Journal of Contaminant Hydrology*, *136*, 56–71.

Meng, Z., & Li, G. (2013). Experimental research on the permeability of high-rank coal under a varying stress and its influencing factors. *Engineering Geology*, *162*(0), 108–117. doi:http://dx.doi.org/10.1016/j.enggeo.2013.04.013

Molz, F. J., Boman, G. K., Young, S. C., & Waldrop, W. R. (1994). Borehole flowmeters: field application and data analysis. *Journal of Hydrology*, *163*(3–4), 347–371. doi:http://dx.doi.org/10.1016/0022-1694(94)90148-1

Molz, F. J., Morin, R. H., Hess, A. E., Melville, J. G., & Güven, O. (1989). The Impeller Meter for measuring aquifer permeability variations: Evaluation and comparison with other tests. *Water Resources Research*, *25*(7), 1677–1683. doi:10.1029/WR025i007p01677

Monier-Williams, M., Davis, R. K., Paillet, F. L., Turpening, R. ., Sol, S. J. Y., & Schneider, G. W. (2009). *Review of Borehole Based Geophysical Site Evaluation Tools and Techniques* (Vol. TR-2009–25). Nuclear Waste Management Organization, Toronto, Ontario, Canada. Retrieved from http://www.nwmo.ca/uploads_managed/MediaFiles/1770_nwmotr-2009-25boreholebasedgeophysicaltools_r0d.pdf

Moore, C. R. (2006). The use of regularized inversion in groundwater model calibration and prediction uncertainty analysis, 1–300. doi:10.1007/978-0-387-76896-0

Moreno, L., Tsang, Y. W., Tsang, C. F., Hale, F. V., & Neretnieks, I. (1988). Flow and tracer transport in a single fracture: A stochastic model and its relation to some field

observations. *Water Resources Research*, *24*(12), 2033. doi:10.1029/WR024i012p02033

Munson, B. R., Young, D. F., & Okiishi, T. H. (1990). *Fundamentals of fluid mechanics* (5th ed.). New York: John Wiley & Sons, Inc.

Murray, E. J. (2002). *Procedure for the Determination of the Permeability of Clayey Soils in a Triaxial Cell Using the Accelerated Permeability Test*. Bristol, UK.

Neuman, S. (1988). Stochastic Continuum Representation of Fractured Rock Permeability as an Alternative to the REV and Fracture Network Concepts. *Groundwater Flow and Quality Modelling*, 331–362. doi:10.1007/978-94-009-2889-3_19

Neuman, S. (2005). Trends, prospects and challenges in quantifying flow and transport through fractured rocks. *Hydrogeology Journal*, *13*(1), 124–147.

Neuville, A., Toussaint, R., & Schmittbuhl, J. (2010). Hydrothermal coupling in a self-affine rough fracture. *Physical Review E*, *82*(3), 36317.

Nick, K., Conway, M. W., & Fowler, K. S. (1995). The Relation of Diagenetic Clays and Sulfates to the Treatment of Coalbed Methane Reservoirs. In *SPE Annual Technical Conference and Exhibition*. Society of Petroleum Engineers.

Nordahl, K., & Ringrose, P. S. (2008). Identifying the representative elementary volume for permeability in heterolithic deposits using numerical rock models. *Mathematical Geosciences*, *40*(7), 753–771. doi:10.1007/s11004-008-9182-4

Norouzi Apourvari, S., & Arns, C. H. (2015). Image-based relative permeability upscaling from the pore scale. *Advances in Water Resources*, *000*, 1–15. doi:10.1016/j.advwatres.2015.11.005

NSW Department of Planning. (2008). *Impacts of underground coal mining on natural features in the Southern Coalfield: strategic review.* Sydney.

Nur, A. (1982). The origin of tensile fracture lineaments. *Journal of Structural Geology*, *4.1*, 31–40. Retrieved from http://www.sciencedirect.com/science/article/pii/0191814182900049

O'Keefe, J. M. K., Bechtel, A., Christanis, K., Dai, S., DiMichele, W. A., Eble, C. F., … Hower, J. C. (2013). On the fundamental difference between coal rank and coal type. *International Journal of Coal Geology*, *118*, 58–87. doi:10.1016/j.coal.2013.08.007

Odgaard, A., & Gundersen, H. J. (1993). Quantification of connectivity in cancellous bone, with special emphasis on 3-D reconstructions. *Bone*, *14*(2), 173–182. doi:10.1016/8756-3282(93)90245-6

Odling, N. E., Gillespie, P., Bourgine, B., Castaing, C., Chiles, J. P., Christensen, N. P., … Watterson, J. (1999). Variations in fracture system geometry and their implications for fluid flow in fractures hydrocarbon reservoirs. *Petroleum Geoscience*, *5*(4), 373–384. doi:10.1144/petgeo.5.4.373

Odsæter, L. V. (2013). *Numerical Aspects of Flow Based Local Upscaling*. Norwegian University of Science and Technology, Trondheim.

Olafuyi, A. O., Sheppard, A. P., Arns, C. H., Sok, R. M., Cinar, Y., Knackstedt, M. A., & Pinczewski, W. V. (2006). Experimental Investigation of Drainage Capillary Pressure Computed From Digitized Tomographic Images. In *Symposium on Improved Oil Recovery*. Tulsam Oklahoma: Society of Petroleum Engineers.

Ortega, O. J., Marrett, R. A., & Laubach, S. E. (2006). A scale-independent approach to fracture intensity and average spacing measurement. *AAPG Bulletin*, *90*(2), 193–208. doi:10.1306/08250505059

Ortega, O., & Marrett, R. (2000). Prediction of macrofracture properties using microfracture information, Mesaverde Group sandstones, San Juan basin, New Mexico. *Journal of Structural Geology*, *22*(5), 571–588. doi:10.1016/S0191-8141(99)00186-8

Paillet, F. L. (1998). Flow modeling and permeability estimation using borehole flow logs in heterogeneous fractured formations. *Water Resources Research*, *34*(5), 997–1010. doi:10.1029/98wr00268

Paillet, F. L. (2004). Borehole flowmeter applications in irregular and large-diameter boreholes. *Journal of Applied Geophysics*, *55*(1–2), 39–59. doi:http://dx.doi.org/10.1016/j.jappgeo.2003.06.004

Paillet, F. L., Hess, A. E., Cheng, C. H., & Hardin, E. (1987). Characterization of Fracture Permeability with High-Resolution Vertical Flow Measurements During Borehole Pumping. *Ground Water*, *25*(1), 28–40. doi:10.1111/j.1745-6584.1987.tb02113.x

Paillet, F., Williams, J., Urik, J., Lukes, J., Kobr, M., & Mares, S. (2012). Cross-borehole flow analysis to characterize fracture connections in the Melechov Granite, Bohemian-Moravian Highland, Czech Republic. *Hydrogeology Journal*, *20*(1), 143–154. doi:10.1007/s10040-011-0787-1

Pan, J., Meng, Z., Hou, Q., Ju, Y., & Cao, Y. (2013). Coal strength and Young's modulus related to coal rank, compressional velocity and maceral composition. *Journal of Structural Geology*, *54*(0), 129–135. doi:http://dx.doi.org/10.1016/j.jsg.2013.07.008

Pan, Z., & Connell, L. D. (2012). Modelling permeability for coal reservoirs: A review of analytical models and testing data. *International Journal of Coal Geology*, *92*, 1–44. doi:10.1016/j.coal.2011.12.009

Pant, L. M., Huang, H., Secanell, M., Larter, S., & Mitra, S. K. (2015). Multi scale characterization of coal structure for mass transport. *Fuel*, *159*, 315–323. doi:10.1016/j.fuel.2015.06.089

Park, Y. J., Sudicky, E. a., McLaren, R. G., & Sykes, J. F. (2004). Analysis of hydraulic and tracer response tests within moderately fractured rock based on a transition probability geostatistical approach. *Water Resources Research*, *40*, 1–14. doi:10.1029/2004WR003188

Paterson, L. (1986). A model for outbursts in coal. *International Journal of Rock Mechanics and Mining Sciences & Geomechanics Abstracts*, *23*(4), 327–332. doi:http://dx.doi.org/10.1016/0148-9062(86)90644-3

Pattison, C. I., Fielding, C. R., McWatters, R. H., & Hamilton, L. H. (1996). Nature and origin of fractures in Permian coals from the Bowen Basin, Queensland, Australia. *Geological Society, London, Special Publications*, *109*(1), 133–150. doi:10.1144/GSL.SP.1996.109.01.10

Pekot, L. J., & Reeves, S. R. (2002). *Modeling coal matrix shrinkage and differential swelling with CO2 injection for enhanced coalbed methane recovery and carbon sequestration applications*. *Topical Report*. Washington, DC.

Permana, A. K. (2012). 3-D Imaging of Cleat and Micro-cleat Characteristics, South Walker Creek Coals, Bowen Basin, Australia: Microfocus X-ray Computed Tomography Analysis. *Indonesian Journal of Geology*, *7*(1), 1–9.

Petchsingto, T., & Karpyn, Z. (2009). Deterministic modeling of fluid flow through a CT-scanned fracture using computational fluid dynamics. *Energy Sources, Part A: Recovery, Utilization, and Environmental Effects*, *31:11*, 897–905. Retrieved from http://www.tandfonline.com/doi/abs/10.1080/15567030701752842

Philip, Z. G., Jennings, J. W., Olson, J. E., Laubach, S. E., & Holder, J. (2005). Modeling Coupled Fracture-Matrix Fluid Flow in Geomechanically Simulated Fracture Networks. In *Society of Petroleum Engineers Annual Technical Conference and Exhibition* (pp. 300–309). San Antonio, Texas. doi:10.2118/77340-PA

Pitrak, M., Mares, S., & Kobr, M. (2007). A simple borehole dilution technique in measuring horizontal ground water flow. *Ground Water*, *45*(1), 89–92.

Pratt, W. K. (2001). *Processing Digital Image Processing* (Third Edit., Vol. 5). Los Altos, California: John Wiley & Sons, Inc.

Price, D. G. (2009). *Engineering geology : principles and practice*. (M. H. De Freitas, Ed.). Berlin: Springer.

Priest, S. D., & Hudson, J. A. (1976). Discontinuity spacings in rock. *International Journal of Rock Mechanics and Mining Sciences and*, *13*(5), 135–148. doi:10.1016/0148-9062(76)90818-4

Priest, S., & Hudson, J. (1981). Estimation of discontinuity spacing and trace length using scanline surveys. *International Journal of Rock Mechanics and Mining Sciences & Geomechanics Abstracts*, *18*(3). Retrieved from http://www.sciencedirect.com/science/article/pii/0148906281909736

Puri, R., Evanoff, J., & Brugler, M. (1991). Measurement of coal cleat porosity and relative permeability characteristics. In *SPE Gas Technology Symposium* (pp. 93–104). Houston, Texas: Society of Petroleum Engineers. Retrieved from https://www.onepetro.org/conference-paper/SPE-21491-MS

Ramandi, H. L., Mostaghimi, P., Armstrong, R. T., Saadatfar, M., & Val Pinczewski, W. (2015). Porosity and permeability characterization of coal – a micro-computed

tomography study. *International Journal of Coal Geology*. doi:10.1016/j.coal.2015.10.001

Rees, S. (2013). Introduction to triaxial testing. GDS Instruments. Retrieved from www.gdsinstruments.com

Renard, P., & De Marsily, G. (1997). Calculating equivalent permeability: a review. *Advances in Water Resources*, *20*(5), 253–278.

Rio Tinto. (2010). *Hail Creek Coal Mine. Deposit Geology. [Power Point slides]*. Brisbane.

Robertson, E., & Christiansen, R. (2006). A Permeability Model for Coal and Other Fractured Sorptive-Elastic Media. In *Society of Petroleum Engineers Eastern Regional Meeting* (pp. 11–13). doi:10.2118/104380-PA

Rosin, P. L. (2001). Unimodal thresholding. *Pattern Recognition*, *34*(11), 2083–2096. doi:10.1016/S0031-3203(00)00136-9

Rouleau, A., & Gale, J. (1985). Statistical characterization of the fracture system in the Stripa granite, Sweden. *International Journal of Rock Mechanics and Mining*. Retrieved from http://www.sciencedirect.com/science/article/pii/0148906285900014

Roy, S. G., & Pyrak-Nolte, L. J. G. (1995). The effect of drying and re-saturation on the gas permeability of coal. In *The 35th US Symposium on Rock Mechanics*. Reno, Nevada: American Rock Mechanics Association.

Rude, T. J., & Strait, L. H. (2000). Measurement of Fiber Density by Helium Pycnometry. *Journal of Composite Materials*, *34*.

Russ, J. C. (1999). *The image processing handbook* (3rd ed.). Boca Raton, Florida: CRC Press.

Rutqvist, J., & Stephansson, O. (2003). The role of hydromechanical coupling in fractured rock engineering. *Hydrogeology Journal*, *11*(1), 7–40.

Sánchez-Vila, X., Carrera, J., & Girardi, J. P. (1996). Scale effects in transmissivity. *Journal of Hydrology*, *183*(1–2), 1–22. doi:http://dx.doi.org/10.1016/S0022-1694(96)80031-X

Scholtes, L., Donze, F. V., & Khanal, M. (2011). Scale effects on strength of geomaterials, case study: Coal. *Journal of the Mechanics and Physics of Solids*, *59*(5), 1131–1146. doi:10.1016/j.jmps.2011.01.009

Schwarz, J. O., & Enzmann, F. (2013). Simulation of Fluid Flow on Fractures and Implications for Reactive Transport Simulations. *Transport in Porous Media*, *96*(3), 501–525. doi:10.1007/s11242-012-0103-0

Şen, Z. (1995). *Applied hydrogeology for scientists and engineers*. Boca Raton: Lewis Publishers.

Serra, O. E. (1983). Fundamentals of well-log interpretation. Elsevier Science Pub. Co., Inc.,New York, NY.

Sevee, J. (1991). Methods and procedures for defining aquifer parameters. *Practical Handbook of Ground-Water Monitoring. Lewis Publishers, Chelsea, MI*, 397–447.

Singhal, B. B. S. (2008). Nature of hard rock aquifers: hydrogeological uncertainties and ambiguities. In *Groundwater Dynamics in Hard Rock Aquifers* (pp. 20–39). Springer.

Singhal, B. B. S., & Gupta, R. P. (1999). *Applied Hydrogeology of Fractured Rocks*. Kluwer Academic Publishers. Retrieved from http://books.google.com.au/books?id=ut3JmJ-h-lgC

Speight, J. G. (2005). Handbook of coal analysis (Google eBook), 222. doi:10.1080/10426919008953291

Stadter, M., & Hair, I. (2014). *Report on Groundwater Flow Modelling for the Hail Creek Underground Project Feasibility Study*. Hail Creek Coal Mine via Nebo, North Queensland.

Stumm, F. (2001). *Use of advanced borehole geophysical techniques to delineate fractured-rock ground-water flow and fractures along water-tunnel facilities in northern Queens County, New York*. US Department of the Interior, US Geological Survey.

Suuberg, E. M., Deevi, S. C., & Yun, Y. (1995). Elastic behaviour of coals studied by mercury porosimetry. *Fuel*, *74*(10), 1522–1530. doi:10.1016/0016-2361(95)00110-Q

Szabo, T. L. (1981). A representative Poisson's ratio for coal. In *International Journal of Rock Mechanics and Mining Sciences & Geomechanics Abstracts* (Vol. 18, pp. 531–533). Pergamon.

Ting, F. T. C. (1977). Origin and spacing of cleats in coal beds. *Journal of Pressure Vessel Technology*, *99*(4), 624–626.

Tsang, C.-F., & Neretnieks, I. (1998). Flow channeling in heterogeneous fractured rocks. *Reviews of Geophysics*, *36*(2), 275–298. doi:10.1029/97rg03319

Tu, J., Yeoh, G. H., & Liu, C. (2007). *Computational fluid dynamics: a practical approach*. Butterworth-Heinemann.

Turner, L. G. (2015). *Chemical Stimulation Techniques for Increasing the Permeability of Coal Seams*. PhD thesis, School of Chemical Engineering, The University of Queensland.

Tyson, R., Killops, S., & Killops, V. (2006). Introduction to Organic Geochemistry. *Geological Magazine*, *143*(2), 250.

University at Buffallo. (2016). SEM/EDS : Scanning Electron Microscopy with X-ray microanalysis. Retrieved January 22, 2017, from https://wings.buffalo.edu/faculty/research/scic/sem-eds.html

Van der Heijde, P. K., Rosswall, T., Woodmansee, R. G., & Risser, P. G. (1988). *Spatial and Temporal Scales in Groundwater Modeling*. John Wiley & Sons, Inc. Retrieved from http://www.scopenvironment.org/downloadpubs/scope35/chapter11.html

Van Krevelen, D. (1993). *Coal-typology, physics, chemistry, constitution*. Amsterdam: Elsevier Science.

Walsh, J. J., & Watterson, J. (1993). Fractal analysis of fracture patterns using the standard box-counting technique : valid and invalid methodologies, *15*(12), 1509–1512.

Wang, G. X., Massarotto, P., & Rudolph, V. (2009). An improved permeability model of coal for coalbed methane recovery and CO2 geosequestration. *International Journal of Coal Geology*, *77*(1–2), 127–136. doi:http://dx.doi.org/10.1016/j.coal.2008.10.007

Washburn, E. W. (1921). The dynamics of capillary flow. *Physical Review*, *17*(3), 273–283. doi:10.1103/PhysRev.17.273

Weeks, E. P. (1969). Determining the Ratio of Horizontal to Vertical Permeability by Aquifer-Test Analysis. *Water Resources Research*, *5*(1), 196–214.

Weniger, S., Weniger, P., & Littke, R. (2016). Characterizing coal cleats from optical measurements for CBM evaluation. *International Journal of Coal Geology*, *154-155*, 176–192. doi:10.1016/j.coal.2015.12.005

Wildenschild A. P., D. . S. (2013). X-ray imaging and analysis techniques for quantifying pore-scale structure and processes in subsurface porous medium systems. *Advances in Water Resources*, *51*, 217–246.

Wildenschild, D., Vaz, C. M. P., Rivers, M. L., Rikard, D., & Christensen, B. S. B. (2002). Using X-ray computed tomography in hydrology: systems, resolutions, and limitations. *Journal of Hydrology*, *267*(3–4), 285–297. doi:http://dx.doi.org/10.1016/S0022-1694(02)00157-9

Wille Geotechnik. (2013). Soil Catalogue. (APS Antriebs- Prüf- und Steuertechnik GmbH, Ed.). Rosdorf, Germany. Retrieved from www.wille-geotechnik.com

Witherspoon, P. A., Wang, J. S. Y., Iwai, K., & Gale, J. E. (1979). Validity of cubic law for fluid flow in a deformable rock fracture. *Water Resources Research*.

Wold, M. B., & Jeffrey, R. G. (1999). A Comparison of Coal Seam Directional Permeability as Measured in Laboratory Core Tests and in Well Interference Tests. In *SPE Rocky Mountain Regional Meeting*. Gillette, Wyoming: Society of Petroleum Engineers.

Wolf, K. H. A. A., van Bergen, F., Ephraim, R., & Pagnier, H. (2008). Determination of the cleat angle distribution of the RECOPOL coal seams, using CT-scans and image analysis on drilling cuttings and coal blocks. *International Journal of Coal Geology*, *73*(3-4), 259–272. doi:10.1016/j.coal.2007.06.001

Xue, S., Yuan, L., Wang, J., Wang, Y., & Xie, J. (2015). A coupled DEM and LBM model for simulation of outbursts of coal and gas. *International Journal of Coal Science and Technology*, *2*(1), 22–29. doi:10.1007/s40789-015-0063-4

Yeh, T. C. J., & Liu, S. (2000). Hydraulic tomography: Development of a new aquifer test method. *Water Resources Research*, *36*(8), 2095–2105. doi:10.1029/2000wr900114